THERMAL, ELECTRICAL AND MECHANICAL PROPERTIES OF THREE-DIMENSIONAL FUNCTIONAL MATERIALS

BY

JIN GU KANG

DISSERTATION

Submitted in partial fulfillment of the requirements
for the degree of Doctor of Philosophy in Materials Science and Engineering
in the Graduate College of the
University of Illinois at Urbana-Champaign, 2018

Urbana, Illinois

Doctoral Committee:

Professor Paul V. Braun, Chair and Director of Research
Professor David G. Cahill
Associate Professor Sanjiv Sinha
Assistant Professor Daniel P. Shoemaker

ABSTRACT

Colloidal assembly is a dynamic phenomenon where the particulates dispersed in fluids, with the size over tens of nms to several μms, form into specific spatial organization resulting from the variations in the surroundings. The general hard sphere colloids with charged surfaces can be self-assembled into the periodic arrays during the drying process of the fluids. These static periodic arrays, namely, colloidal crystals do not possess any dynamic functionalities, but serve as a sacrificial template for the fabrication of various classes of 3D functional materials. On the other hand, some colloids themselves have their own dynamic functionalities, so that they can be directed-assembled in response to external triggering forces. These particles serve as an active element that offers dynamic changes in the properties of the material systems.

The inorganic 3D functional meso/nanostructures were developed for the potential uses in thermal management applications using the self-assembled colloidal crystals as the template. Especially, the Fe_3O_4 was epitaxially grown through the complex 3D colloidal templates, after which the single crystal Fe_3O_4 3D porous structures were obtained. These materials have the multiple nanosized 3D interfaces to deter the phonon transport, and at the same time consist of the single crystals to enhance the electron transport. Through various kinds of analysis tools, we thoroughly characterized the materials, particularly focusing on the crystallinity, the density, the thermal conductivity, and the electrical conductivity. The epitaxial Fe_3O_4 nanoporous structures including the pores with 40 nm in diameter were identified to be thermally insulating and electrically conductive at the same time.

The dynamically reconfigurable colloidal assembly in the viscoelastic fluids was investigated with the ultimate goals of the energy harvesting. As the first step, two different methods of integrating the colloids into the viscoelastic media were developed. The PNIPAM colloids, which intrinsically possess the thermo-responsive functionality, were synthesized by two kinds of polymerization routes, and then incorporated into the fibrin networks hydrogels using the method developed. The PNIPAM microgels/fibrin networks hydrogel composites demonstrated the reversibly switchable mechanical property, which is multifold jump in the storage modulus due to the strain-stiffening of fibrin networks, in response to the external temperature changes.

ACKNOWLEDGEMENTS

Most of all, I would like to express my sincere gratitude to my adviser, Prof. Paul Braun. I feel so fortunate that I have had the opportunity to work for him over the past 6 years, which was one of the most important periods in my life. I appreciate him so much for his patience and endless support toward the slow progress in my project. Every time I met with bottlenecks, I could get them through wisely thanks to his surprising insight and professional advice on how to figure out the problems and to his constant availabilities for the individual interactions. I am also very grateful for the numerous opportunities to be involved in the diverse kinds of projects covering both hard materials and soft materials as well as the mechanical engineering fields. These collaborative works indeed helped me to broaden my perspectives towards the research and the collaborators, which I strongly believe will be the valuable assets for my future careers. I am sure that my Ph.D. life would have been far less satisfactory if I had not been mentored by an adviser like him.

I would also like to thank Prof. David Cahill, who is one of my committee members. After taking the preliminary exam, I have been working with him for about 2 years. I am so grateful for his helpful advice and clear guidance toward my work. Meeting with him was always educational and stimulating. Thanks to him, I was able to experience the highest level of research in the thermal science field and to learn more in-depth about it, which I have always appreciated so much. Without his help, I could not have obtained such solid results as what I have now.

My entrance into the thermal conductivity measurement was aided by Prof. Sanjiv Sinha, another member of my committee. Thanks to his consideration, I could keep utilizing the measurement setup, learn the underlying principle and the way of operation in more detail, and hence make steady progress in my work without any big difficulties, which I was so grateful to. I also appreciate Prof. Daniel Shoemaker for his insight and feedback after my preliminary exam. His advice was critical and helpful, leading me to perform more focused and refined research.

I'd also like to thank Braun group members past and present for their help, support, and friendship throughout my time in the group, including Dr. Hyungjoon Koo, Dr. Sungkon Kim, Dr. Jiung Cho, Dr. Jaewon Yoon, Dr. Junjie Wang, Dr. Runyu Zhang, Kaitlin Tyler, Julia Kohanek, Ashshi Kulkarni, Sanghyun Kim, Jungwoo Shin, Osman Safa Cifci, Shuqi Lai, Daniel Bacon-Brown, Dr. Pengcheng Sun, Dr. Akkisetty Bhaskar, Dr. Eric Epstein, Shiyan Zhang, Prof. Marta

Hatzell, Jongmin Ju, Dr. Junhee Choi, Prof. Chaeryong Cho, Prof. Jongho Kim, Dr. Jaewon Choi, Dr. Minho Yang, Zhao Li, Arghya Patra, Michael Caple, and Christian Ocier.

The support from Erica Malloch was also greatly and sincerely appreciated. She always helped me in many ways from purchasing supplies to handling administrative matters. Without her efforts, I would have suffered from numerous difficulties in taking care of these works.

A number of my collaborators deserve acknowledgement for their contributions to my research and discussions. I have had numerous opportunities to interact with intelligent and talented people, particularly, Prof. Jian-Min Zuo, Prof. William King, Prof. Nenad Miljkovic, Prof. Kenneth Goodson, Prof. Kenneth Schweizer, Prof. Jeffrey Moore, Prof. Randy Ewoldt, Dr. Jun Ma, Tianyu Yang, Tanya Liu, Prof. Patricia Weisensee, Dr. Bharadwaj Ashwin, Dr. Khalid Hattar, Dr. Qun Yang, Gaurav Chaudhary, Ashesh Ghosh, and Prof. Kristin Hutchins.

I'm also grateful to the staff members in MRL, MNTL, and Beckman Institute, where I have learnt how to operate the instruments by myself, especially for Dr. Mauro Sardela, Dr. Tao Shang, Dr. Xiaoli Wang, Dr. Fubo Rao, Dr. Honghui Zhou, Dr. Timothy Spila, and Dr. Julio Soares.

Furthermore, I gratefully acknowledge the Power Optimization of Electro-thermal System (POETS), the Air Force Office of Scientific Research (AFOSR), the Department of Energy (DOE), and the Kwanjeong Educational Foundation for their consistent financial supports during my doctorate period.

Another greatest assets that I have obtained here in Urbana-Champaign were those I met with outside the ESB building. I have been blessed with so many wonderful friends who have made my time truly memorable. Thanks to their support and help, I was able to get through every difficult moment, and enjoy this doctorate period. I especially appreciate Dr. Jonglo Park, Dr. Jaejun Lee, Dr. Taeann Kim, Hyejin Jang, Dr. Taewook Lim, Dr. Junmin Lee, Dr. Hojun Kim, Dr. Minjee Kang, Sehyun Park, Jaeyoung Heo, Dr. Keonmook Seong, Dr. Youngsoo Kim, Yukyung Ko, Dr. Honggyu Kim, Dr. Jaeyeol Lee, Dr. Gyungmin Choi, and Dr. Sungki Lee.

Finally, I would like to express my sincere gratitude to my family in hometown. Over the past 6 years, they have been always on my side and encouraged me with unwavering support. Their trust and patience toward me has driven me to work harder and to aim higher whenever I felt it very hard to do research. Without them, I am certain that I could not have completed this long and tough doctorate period. I greatly appreciate them again for their infinite support and love toward me from the time I was very young to the present.

To my family

for your endless support and love

TABLE OF CONTENTS

LIST OF ABBREVIATIONS

1D	one-dimensional
2D	two-dimensional
3D	three-dimensional
3ω	three-omega
4pp	4-point probe
ATRP	atom transfer radical polymerization
CML	carboxylate modified polystyrene/latex
DLS	dynamic light scattering
FCC	face-centered cubic
FIB	focused ion beam
FT-IR	Fourier-transform infrared spectroscopy
HEPES	4-(2-hydroxyethyl)-1-piperazineethanesulfonic acid
HRSTEM	high-resolution scanning transmission electron microscope
HRTEM	high-resolution transmission electron microscope
LAOS	large amplitude oscillatory shear
PECVD	plasma-enhanced chemical vapor deposition
PNIPAM	poly(N-isopropylacrylamide)
PS	polystyrene
RBS	Rutherford backscattering spectrometry
SEM	scanning electron microscope
SEND	scanning electron nano-diffraction
SFEP	surfactant-free emulsion polymerization
TCR	temperature coefficient of resistance
TDTR	time-domain thermo-reflectance
TEM	transmission electron microscope
TEA	triethanolamine
THF	tetrahydrofuran
XRD	X-ray diffraction
XRF	X-ray fluorescence

CHAPTER 1.

INTRODUCTION AND BACKGROUND

The structure of three-dimensional (3D) functional materials depends on the shapes of 3D template, e.g. sphere or cubic, and the methods of fabrication, e.g. lithography or building-block assembly. The function of 3D materials is determined by the physical and chemical properties of their constituents, such as compositional stoichiometry, thermal conductivity, electrical conductivity, optical constants, and elastic/loss moduli. Self-assembled colloids can serve a structural template for the fabrication of 3D functional materials. On the other hand, they can be an active constituent that functions directly in 3D materials.

This chapter deals with two introductory subjects. In the first section, we give an overview of the usage of the colloidal self-assembly as an effective way of providing structural templates of 3D functional materials applicable to diverse areas ranging from photonics, energy storage, solar energy harvesting, sensing to thermal management. In the following section, we introduce functional colloidal assemblies that dynamically and reversibly reconfigure their spatial organizations and hence alter the properties of 3D functional materials in response to a variety of external triggering forces including the changes in chemical environment, temperature variation, electric/magnetic fields, and optical actuations.

1.1 Self-assembled Colloidal Crystals for 3D Functional Materials

1.1.1 Colloidal self-assembly

Functional three-dimensional (3D) materials have been diversifying their applications from photonics[1-6] to energy storage[7-12], solar cells[13,14], thermophotovoltaics (TPVs)[15-19], sensors[20,21], and thermal transport[22-24] over the past years. As a way of incorporating the desired functionalities into 3D structures, either top-down or bottom-up approach has been employed, as illustrated in **Figure 1.1**. The top-down techniques accompany complex and costly processes including optical lithography, gas-phase deposition, and reactive-ion etching[25]. On the other hand, the bottom-up

approaches offer the potential for easier fabrication and manipulation when designing 3D functional materials[26].

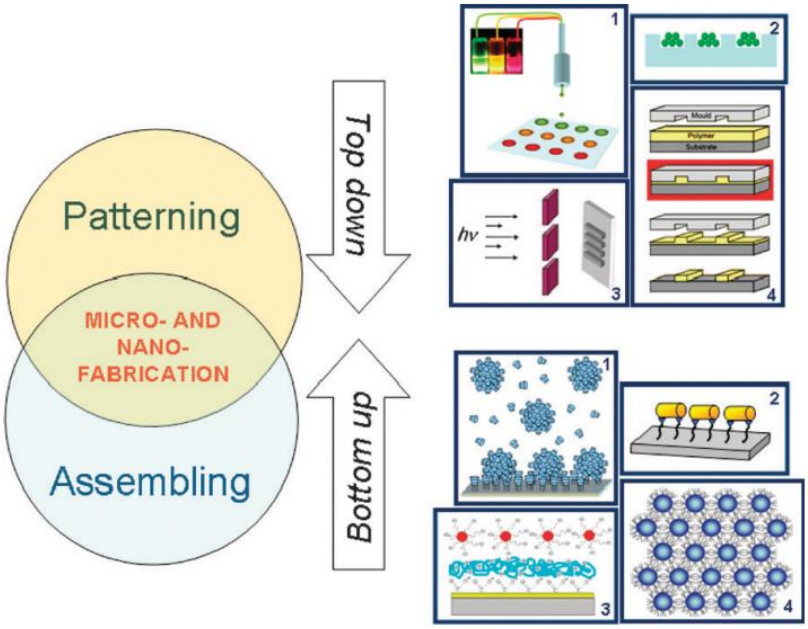

Figure 1.1 – Schematics of top-down and bottom-up approaches for the fabrication of the functional 3D materials. Top-down: (1) ink jet printing, (2) capillary assembly, (3) photolithography, (4) nanoimprinting lithography. Bottom-up: (1) host-guest chemistry, (2) covalent immobilization onto substrate, (3) electrostatic layer-by-layer deposition, (4) self-assembly. Adapted from ref. 27.

Colloidal self-assembly, one of the bottom-up methods, is extensively used for the fabrication of 3D porous materials[25,26,28-31]. In colloidal suspensions, amorphous inorganic particles, or polymeric particles with specific geometries (sphere, cube, cylinder, etc) are dispersed in liquid solvents performing Brownian motion. During self-assembly process, these particles are packed into the ordered arrays, resulting in the formation of so-called colloidal crystals that are used as templates of 3D porous architectures. The colloidal crystallization is a complex process affected by multiple thermodynamic and kinetic factors that interfere with each other[32-36]. Amongst them, it is well known that there are three critical factors of determining the quality of the crystallization[25], which are detailed in the following section.

1.1.2 Requirements of colloidal crystallization

Figure 1.2 demonstrates two types of particle-particle interactions that predominantly govern the colloidal crystallization: repulsions and van der Waals attractions[37]. High-quality

colloidal crystals can be obtained only when there are large enough repulsive forces compared to the van der Waals attractions so that the colloids do not stick to each other in the disordered form. The repulsive forces required for preventing premature aggregation upon particle assembly are the same forces that provide stability of colloidal suspensions. This indicates the stable colloidal suspension is essential for achieving highly-ordered crystals. The repulsive forces can be categorized into two examples, electrostatic repulsions in polar solvents[38] and steric repulsions in universal solvents[39]. The electrostatic ones are enabled by making colloidal particle surfaces positively or negatively charged. The surface charges are counterbalanced by the presence of oppositely charged ionic species dissolved in the liquid solvent[40]. The steric repulsions are realized by physically attaching adsorbed layers such as polymers or nonionic surfactants, to the surfaces of the particles. The primary origin of the steric stabilization is known to be entropic[40].

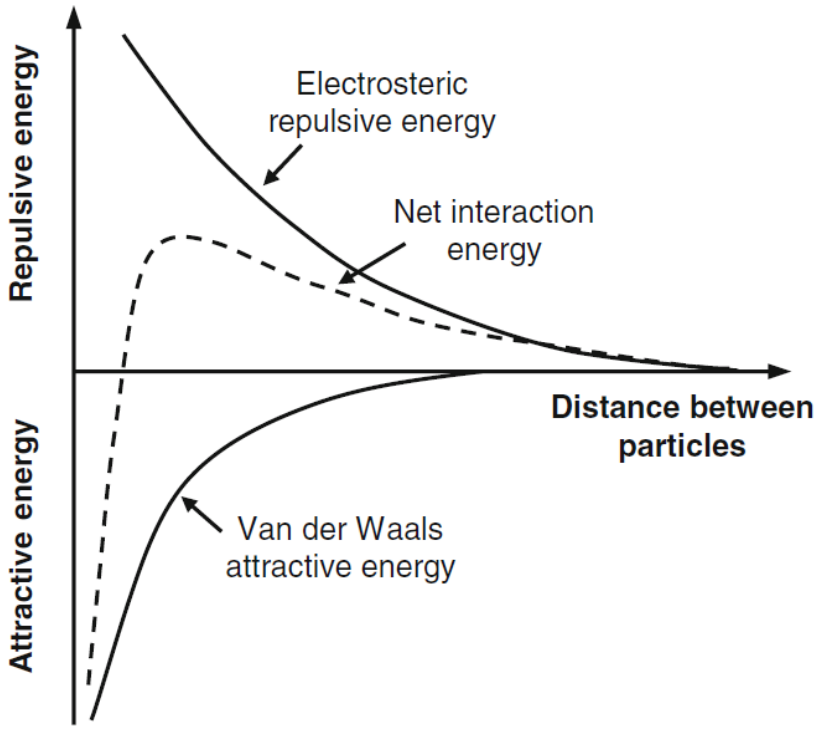

Figure 1.2 – Two kinds of particle-particle interactions that determine the colloidal crystal quality as well as the colloidal suspension stability: electrostatic (or steric) repulsion and van der Waals attraction. The total potential energy is described as the sum of these two energies. Adapted from ref. 37.

Another important factor required for attaining highly-ordered colloidal crystals is external driving forces acting on the colloids during self-assembly process[25]. Representative examples include the gravitation/centrifugal forces that lead particles to sediment, the evaporative capillary

forces that drag particles to compact at the crystal growth front, and the electric fields that attract oppositely charged colloids onto conductive electrodes. These forces are closely related with the colloidal crystal growth techniques which will be discussed later in more detail.

Last critical factor is monodispersity of colloidal particles in the size and the shape to achieve highly-ordered packing of colloids[25]. This is to increase the entropy of the system during self-assembly process, thereby minimizing the total free energy[41,42]. In the system that is lack of the monodispersity, particles tend to pack into disordered arrays rather than into ordered ones to maximize the configurational entropy.

1.1.3 Colloidal crystal growth techniques

As mentioned above, the growth technique of colloidal crystals is primarily determined by choice of the external driving forces. **Figure 1.3** shows various types of deposition techniques utilizing such forces ranging from gravitational force[43-45], capillary force[26,29,46-48], electric field[49-55], magnetic field[56-58], and shear flow[59]. The most popular ones are the gravitational force and the evaporative-capillary force as they are scalable and simple. The sedimentation method is a representative example of using the gravitational field[43-45]. Colloidal particles can be assembled by sedimentation when particle density is different from that of a liquid solvent. The larger the difference is, the faster sedimentation is. The main drawback of the sedimentation technique is that it takes quite long periods of time to completely settle sub-μm sized particles. Centrifugation, which also employs the gravitational force, offers the solution to this issue[25]. Centrifugal force with high inertia is imposed to colloidal suspension to accelerate the deposition rate of the particles.

Of various capillary force-induced crystallizations, the vertical deposition is the most widely used technique, where a liquid solvent evaporation plays a key role during convective self-assembly[48,60-63]. A charged substrate is vertically immersed into a colloidal suspension, and then a liquid solvent of the suspension is left to evaporate over a certain period of times, leaving a dried colloidal film on the substrate. This technique is basically operated based on the convective flow dragging the particles as the liquid solvent evaporates at an evaporating front called the meniscus. The evaporative-pressure generated at the meniscus attracts a suspension toward the meniscus and then forces the colloids to pack into the ordered arrays on the already-deposited layers. This method has many advantages over the sedimentation. It requires a smaller amount of colloidal suspension, creates less amounts of defects, and offers easier sample handling. One drawback of

the vertical deposition is sedimentation of the colloids during slow evaporation, especially for large heavy particles.

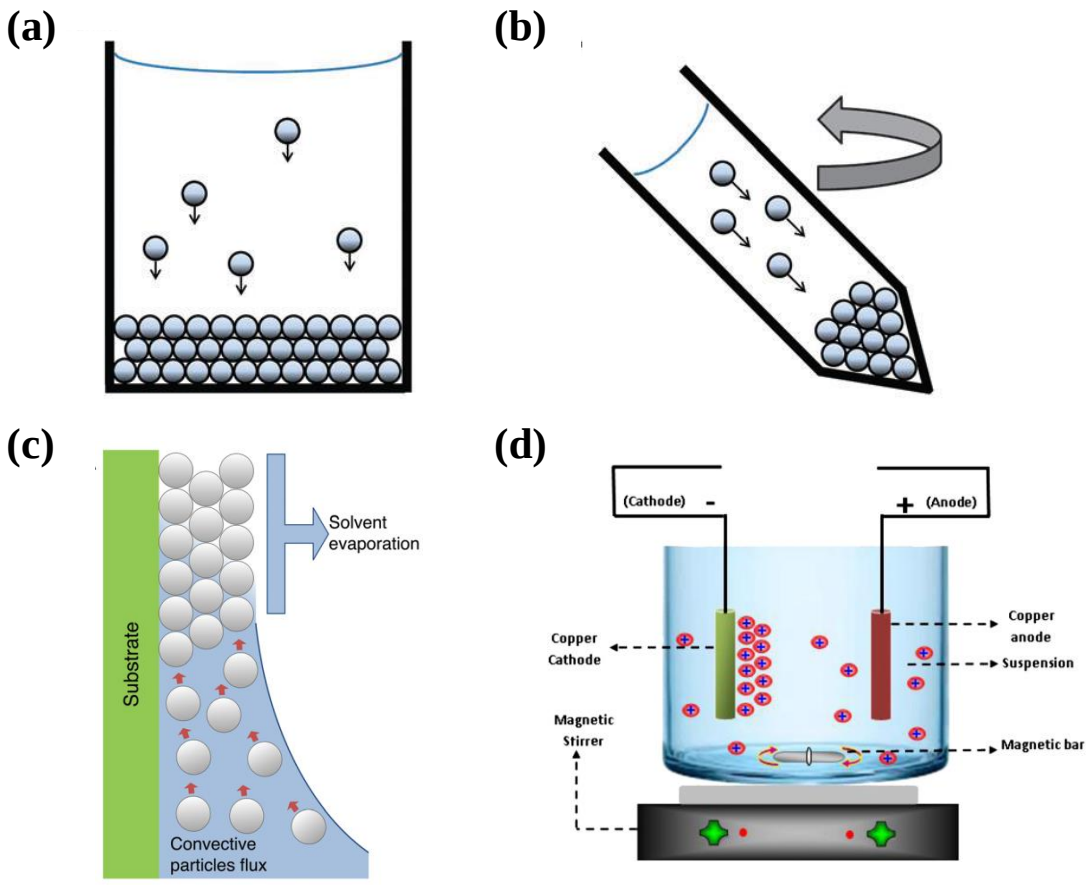

Figure 1.3 – Schematics of colloidal crystal growth techniques: (a) sedimentation, (b) centrifugation, (c) evaporative-capillary vertical deposition, (d) electrophoretic deposition. Adapted from refs. 64-66.

Nucleation and growth of colloidal crystals can be induced by an electric field and conductive electrodes immersed in a colloidal suspension. Electric-field driven colloidal crystallization is categorized into three types such as electrophoresis, dielectrophoresis, and electroosmosis[49]. The electrophoretic deposition is the most widely used technique. Under an external electric field, charged particles in a suspension are attracted to an oppositely charged electrode and then form periodic crystalline arrays. The dielectrophoresis, on the other hand, does not require the particles to be charged. Instead, an inhomogeneous electric field exerts driving forces on the dielectric particles to assemble in the desired forms such as straight single microwires, multiply branched microwires, or parallel arrays of microwires[53-55]. The

electroosmosis utilizes the motion of liquid along charge surfaces of colloids induced by an electric potential. This phenomenon has proven to be significant for colloidal organization under an electric field[49].

Magnetic fields can also drive the motion of magnetic colloids to self-assemble[57,58]. Paramagnetic colloidal particles were readily guided by a magnetic field[57]. Colloidal arrays with ring structures were also attained[58]. These were induced by assembling a mixture of diamagnetic and paramagnetic spherical particles within a magnetized ferrofluid comprised of Fe_3O_4 nanoparticles suspended in water. The shapes of colloidal arrays were controllable, including flowers, Saturn-like rings, and other multi-polar architectures. Rather than extensive crystallization, these individual structures were preferentially developed because of self-limiting assembly[58].

1.1.4 Pore-filling methods

Functional 3D materials can be eventually realized by filling the pores inside the colloidal crystal with a material possessing the desired functionality and then removing the colloidal particles with etchants. Due to the structural complexity of colloidal crystals, the key issue of infiltration is a filling fraction of the material. The most productive way is the potentiostatic or galvanostatic electrochemical deposition that has been first demonstrated for the fabrication of the 3D photonic crystals consisting of semiconductors such as CdSe and CdS[67], as shown in **Figure 1.4a**. In electrodeposition technique, two or three conductive electrodes are immersed in a liquid electrolyte dissolving ionic precursors. Imposed by an electric field between the conductive electrodes, ionic precursors are dragged to an oppositely charged electrode to subsequently nucleate and grow on the electrode. If this electrode has colloidal crystals on the surface, the ionic precursors will travel through colloidal crystals and then fill the pores from the bottom. This is the reason this technique enables high filling fraction. Through electrodeposition, we can obtain highly dense and rigid structures that are not prone to shrinkage upon template removal. A variety of 3D porous materials comprised of Fe_2O_3[12], Cu_2O[68], Cu[24], Ni[7], or polypyrrole[10] have been fabricated by the electrochemical methods for a variety of applications such as energy storage, optoelectronics or thermal managements. A challenge in templated electrodeposition is that the colloidal crystals need to be grown on top of a conducting substrate which limits some of the

optical template fabrication methods (for example, holography on a reflective substrate is challenging)[30].

Gas-phase deposition is another powerful way of filling the voids inside colloidal templates (**Figure 1.4b)**. The two most widely used gas phase deposition methods are chemical vapor deposition (CVD) and atomic layer deposition (ALD). Typically, the colloidal crystals grown on a substrate that is thermally and chemically stable under the process condition, are first loaded into the temperature-controllable vacuum chamber. A mixture of gas-phase precursors of target materials are injected to the reactor and then allowed to go through the pores of the templates. Once the precursors meet with any nucleation sites such as colloid surfaces or substrate surface, they react with one another to form the nuclei on the surfaces and grow until completely filling the surrounding pores. In 2000, Si photonic crystal[2] was fabricated by CVD technique using disilane (Si_2H_6) gas as a precursor. A similar disilane-based CVD process was employed to fabricate Si porous materials for nanoscale thermal transport studies[23]. Ge photonic crystal was also enabled by the CVD procedure using digermane (Ge_2H_6) gas as a precursor[69]. Whereas these photonic crystals are polycrystalline, III-V semiconductor GaAs photonic crystal has been for the first time fabricated as single crystal or epitaxy by metal-organic CVD (MOCVD) process[3]. Other than the CVD processes, the operating principle of ALD is a self-limited surface reaction between species formed by the discretely pulsed precursor vapors and the reaction site, which makes ALD suitable for the conformal deposition of materials on the colloids. A wide range of materials including dielectrics, semiconductors and metals were fabricated in the inverse form of colloidal crystals using ALD methods[70].

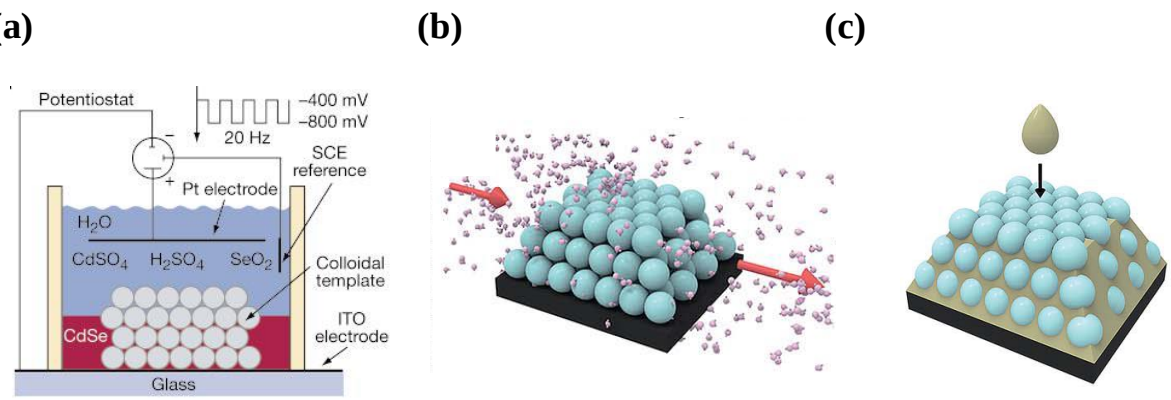

Figure 1.4 – Schematics of representative pore-filling methods: (a) electrochemical deposition, (b) gas-phase deposition, (c) liquid-precursor infiltration. Adapted from refs. 67,71.

Infiltrating liquid precursors of interest through colloidal crystal templates gives us another option to realize functional 3D porous materials **(Figure 1.4c)**. This approach can be classified into two big categories depending on the types of precursors that are initially injected into colloidal crystals. One is to infiltrate sol-gel precursors[1,72,73]. Inside the pores, they transform into the solid material through a classical sol-gel process consisting of hydrolysis, condensation, drying, and calcination, in serial. In general, multiple rounds of infiltration and reaction steps need to be repeated to fully fill the pores. This technique has been first proposed for making TiO_2 inverse opals[1]. They suffered from the large shrinkage and cracking during the whole process, ended up with obtaining very low filling fraction of 12 ~ 20 %. Sol-gel-mediated method was especially excellent when it comes to making metal oxide structures such as SiO_2, Al_2O_3, ZrO_2, and Y_2O_3[1,73-76]. The other route is to utilize pre-prepared nanoparticles as an injecting material [77-79]. Typical size of nanoparticles is ~10 % of the pore diameter. After the infiltration, sintering process is required so that nanoparticle networks can convert into robust crystalline matters possessing enhanced electrical and optical properties. The major advantage of this method is the flexibility in the choice of the chemical composition of the target material as the composition is controllable during nanoparticle synthesis.

1.1.5 Applications

Photonics is the main area where 3D porous materials that are realized by so-called colloidal crystal templating method, which is comprised of sequential steps of colloidal crystal growth, infiltration, and template removal, can be applied[1-3,80]. The TiO_2 photonic crystals with radii between 120 ~ 1000 nm have been first realized using liquid precursor infiltration method[1]. They confirmed that the crystals made from templates comprised of colloids with radii of 292 nm demonstrated much stronger photonic behaviors than any other colloidal crystals which were reported until that time. Afterwards, Si inverse opal photonic crystal, depicted in **Figure 1.5**, was reported to form complete photonic band gap at around 1.5 μm wavelength[2]. At this wavelength regime, Si has a high refractive index of 3.45, which is well above the theoretical threshold for a photonic band gap formation, 2.8 in an FCC lattice of air spheres. This crystal has also proven to allow the coherent localization of light. Another hallmark in photonics is the development of single crystalline photonic crystal enabled by selective area epitaxy through a 3D colloidal crystal template[3]. Nelson et al. have demonstrated that epitaxially grown GaAs semiconducting photonic

crystal showed high-performance in optoelectronic devices because of low charge recombination rate and high charge carrier mobilities induced by single crystalline nature containing lower defect density. Filling complex 3D colloidal crystals with eutectic melts would open another opportunity of designing advanced optical materials, such as metamaterials[6]. As an initial attempt, AgCl-KCl eutectic melts have been successfully incorporated through the colloidal templates using directional solidification method recently[81].

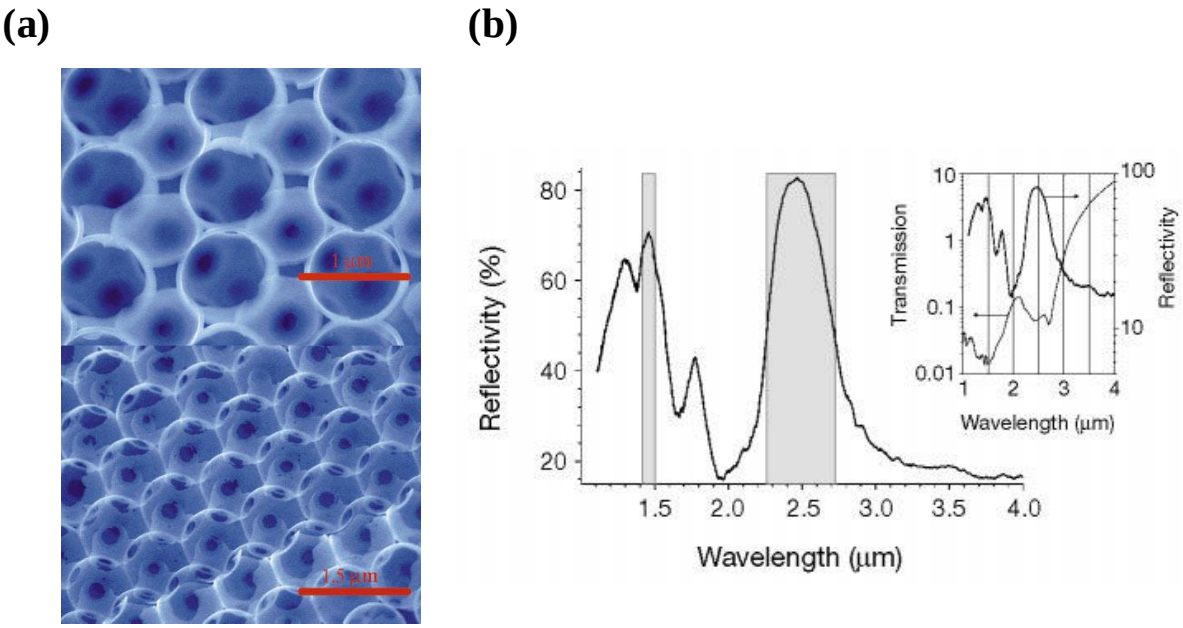

Figure 1.5 – Si inverse opal photonic crystal fabricated by CVD process. (a) SEM images of Si inverse opal. (b) Optical reflectance spectrum demonstrating the formation of photonic band gap at the wavelength of 1.5 μm. Adapted from ref. 2.

Colloidal crystal templated 3D porous materials can be also applied to the multiple energy storage devices including rechargeable batteries and supercapacitors[7-12]. Using Ni inverse opal as an electrically conducting scaffold, bicontinuous battery electrodes have been first proposed recently **(Figure 1.6)**[7]. Since all the active materials directly contacted with the Ni scaffold, superior rate performance and cycle stability were accomplished. Combining colloidal crystal templating method with a classical microfabrication process, microbattery which employed the bicontinuous scaffolds in both anode and cathode, has been demonstrated to deliver high power density[8]. In addition, a number of battery electrodes have been fabricated based on the bicontinuous strategy aiming at delivering high capacity and ensuring long-term cycle stability[11,12]. Electrochemical capacitors, so called supercapacitors also introduced colloidal crystal templating

method to design novel electrodes[10]. Electro-polymerization of polypyrrole in colloidal crystal template enabled the mesostructured 3D pseudo-supercapacitor electrode. The catechol derivative was sufficiently bound to the polypyrrole through noncovalent interactions to provide a volumetric capacitance as high as 130 F cm^{-3} and a capacitance retention of 75 % over 10000 charging/discharging cycles.

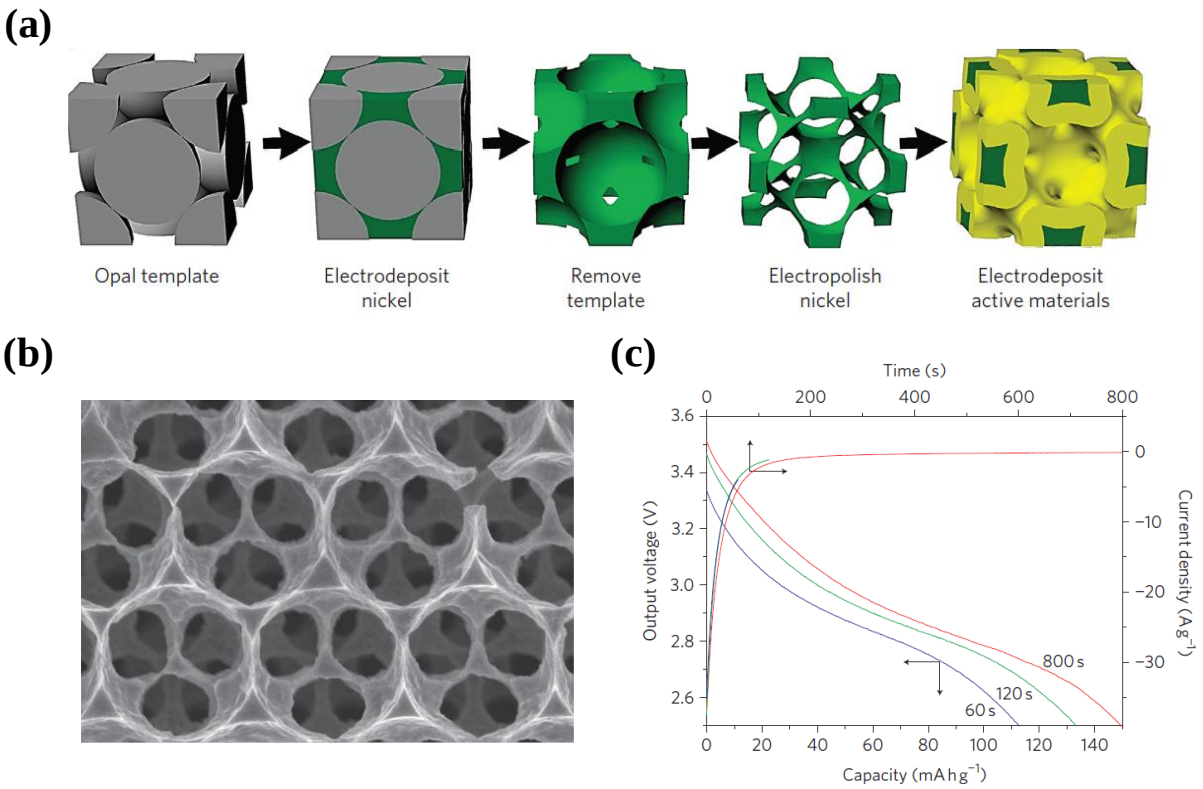

Figure 1.6 – Bicontinuous battery electrodes enabled by colloidal crystal templating and electrodeposition. (a) Fabrication schematics of bicontinuous electrodes. (b) SEM image of Ni inverse opal serving as a conducting scaffold. (c) Lithium-ion battery ultrafast charge behavior. Adapted from ref. 7.

Solar energy harvesting[13,14] and hydrogel sensors have been also considered suitable areas where the colloidal templated 3D porous structures play a key role. In dye-sensitized solar cells (DSSCs) of **Figure 1.7**, the templated 3D structures were identified to be able to facilitate electrolyte transport through the pores as well as to enhance the photo-conversion efficiency[13]. There have been increasing interests in the development of thermophotovoltaics (TPVs) based on 3D metallodielectric architectures[15-17,19]. The key issue when it comes to applying these templated porous materials to this area is whether they can meet the thermal and optical requirements[30].

Hydrogel sensors based on the inverse opal structure that are sensitive to pH and glucose were demonstrated[20,21]. Mesoporous hydrogels based on the copolymers consisting of 2-hydroxy-ethyl methacrylate (HEMA) and acrylic acid (AA), exhibited pH-dependent shifts in optical diffraction, the magnitude of which can be controlled by changing the AA concentration[20]. Similarly, inverse opal hydrogels functionalized with phenylboronic acid within microfluidic channels, showed diffraction shift response as a function of glucose concentration or ionic strength of glucose solution[21].

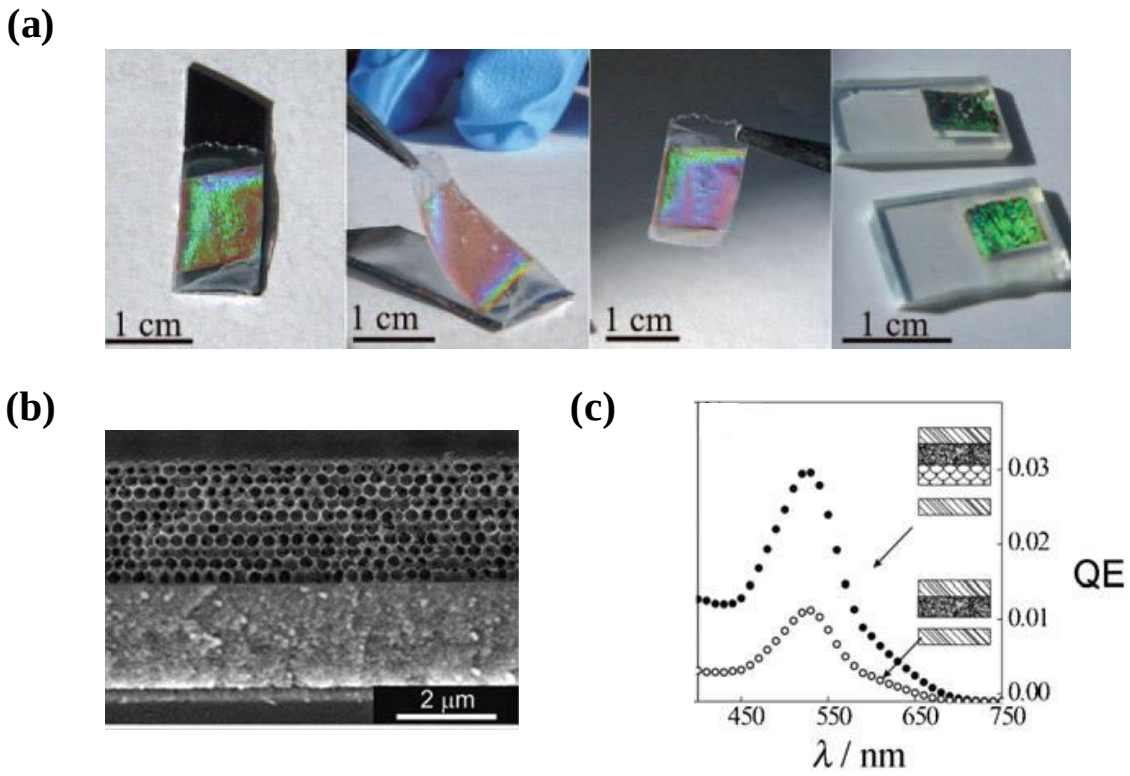

Figure 1.7 – Transferred 3D photonic crystals onto DSSC. (a) Photographs of solar cell fabrication procedure. (b) Cross-section SEM image of inverse Si photonic crystals on nanocrystalline TiO_2 layer. (c) Quantum efficiency plots of control (gray open circles) and inverse silicon coupled (black filled circles) DSSCs. Adapted from ref. 13.

Most recently, colloidal crystal templated 3D architectures have been expanding their applications to thermal management field where precise regulation of heat transport is required. Thermal management is a broad concept that refers to temperature control of any system, for example, power electronics, mobile vehicles, and batteries, using an appropriate heating or cooling process. The 3D porous materials can provide versatility in regulating thermal transport. If we fill the pores with a material with high thermal conductivity and heat capacity such as metals, the

porous material can be used as an effective coolant owing to large surface area-to-volume ratio of the 3D structure. If we fill the pores with a material with semiconductors or insulators, where electronic contribution to total thermal conductivity is very low, this porous material can be utilized as a thermal insulator to block the heat conduction. Even though colloidal crystal templated 3D structures have great potential for regulating thermal transport, the study on these is still in its infancy. Ma et al. have first reported the heat transport behavior in Si inverse opal structure using silica colloidal template and CVD method[23]. They observed low thermal conductivities compared to a typical bulk value, which they attributed to coherent phonon scattering at inter-grain boundaries. Another fundamental study has been conducted on the Ni and Cu inverse opals that could potentially serve as cooling media[24]. As the pore diameter decreased, they observed quasi-ballistic phonon transport behavior.

1.2 Reconfigurable Colloidal Assembly for 3D Responsive Materials

1.2.1 Reconfigurable colloidal assembly

In **Chapter 1.1**, we discussed the colloidal self-assembly as a medium for making colloidal crystals that serve a template in the fabrication of 3D porous structures. The main concerns lied on the way of assembling colloids in a more elegant way to well-crystallize, the way of filling the pores with functional materials, and the way of removing colloids selectively. For these applications, dynamic response of colloidal assemblies themselves is beyond our interests. Instead, providing well-ordered, chemically stable, and mechanically robust scaffold is the most important aspect to be considered.

In contrast, there have been a broad range of areas, for example sensing, transduction, and actuation in biomimetics, biorobotics and soft-mechanics[82-86], where the understanding and the control of a time-dependent optical, structural, or mechanical response of soft materials are essential. Of various geometric forms of soft matters, colloidal assembly that possesses dynamically reconfigurable and reversible behaviors, has been attracting great attention due to its versatility in designing size, shape, and functions of colloids. Depending on where to use, we choose and assemble colloids with desired functionalities and geometries, after which dynamically

regulate configuration of the assembly, so that functions of the assembly can switch reversibly under varying external stimulus.

M. Solomon defined the reconfigurable colloidal assembly as following three statements[87]: (1) It involves reversible, back-and-forth transitions between two different equilibrium states of a colloidal system by temporally manipulating thermodynamic variables (e.g. temperature, pressure, electric/magnetic field) or colloidal properties (e.g. particle size, shape, particle-particle interactions). (2) It accompanies a functional change in microstructure or property of the assembly, for example, phase transition, lattice spacing modulation, and shape or position of the assembly. (3) It includes structural transitions that are in the thermodynamic limit (e.g. bulk phase transition), as well as those beyond the limit (e.g. spatially localized, small-number of particles that function in microscale).

Study on the dynamically reversible and reconfigurable behavior has not been limited to the colloidal assemblies only. Many polymer-based soft materials have unique responsive characteristics to external trigger forces including pH, solvent composition, ionic strength, temperature, electric/magnetic field, light, and pressure[88-93]. For instance, poly(N-isopropylacrylamide) (PNIPAM) is a representative and most extensively studied thermo-responsive soft material. Below lower critical solution temperature (LCST), PNIPAM is hydrophilic, but above LCST it becomes hydrophobic due to conformational change of polymer chains, which is entropic[93]. The matrix expels the water inside, so that the volume or size of PNIPAM dramatically shrinks. **Table 1.1** summarizes various stimuli-responsive polymers and corresponding triggers[91].

In principle, reconfigurable colloidal assembly and reconfigurable polymeric thin films are not completely dissimilar, as well illustrated in **Figure 1.8**[94]. Depending on the shape of a polymer determines dynamics and reconfiguration of a soft material. If a polymer is synthesized in the form of spherical colloids, it will reconfigure in time following particle dynamics and polymer chemistry. If its form is linear chain or cross-linked mesh, the dynamics would differ from that of the colloidal form.

Table 1.1 – Reconfigurable polymers reacting to various external stimuli. Adapted from ref. 91.

	Polymer	Type of stimulus
BIS	Bisacrylamide	
PAA	Poly(acrylic acid)	pH
PAAEM	Poly(acetoacetoxyethyl methacrylate)	
PAm	Poly(acryalamides)	
PBA	Poly(butyl acrylate)	
PDEA	Poly[2-(diethylamino)ethyl methacrylate]	pH
PDMS	Poly(dimethylsiloxane)	[a]E-field, [b]T-field
PDPA	Poly[2-(diisopropylamino)ethyl methacrylate]	pH
PEO	Poly(ethylene oxide)	T-field
PGMA	Poly(glycerol monomethacrylate)	
PHEMA	Poly(hexyl ethyl methacrylate)	
PHFBMA	Poly(hexafluorobutylmethacrylamide)	T-field
PLG	Poly(glutamic acid)	pH
PLLA	Poly(L-lactides)	
PMMA	Poly(methyl)methacrylate	
PMPC	Poly[2-(methacryloyloxy)ethyl phosphorylcholine]	E-field, T-field
PNaA	Poly(sodium acrylate)	pH
PNaVBA	Poly(sodium-4-vinylbenzoate)	pH
PNCL	Poly(*N*-vinylcaprolactone)	T-field, pH
PNIPAM	Poly(*N*-isopropylacrylamide)	T-field
PPO	Poly(propylene oxide)	T-field
PSMA	Poly(stearyl methacrylate)	
PVIm	Poly(*N*-vinylimidazole)	pH

[a] Electrical field. [b] Thermal field.

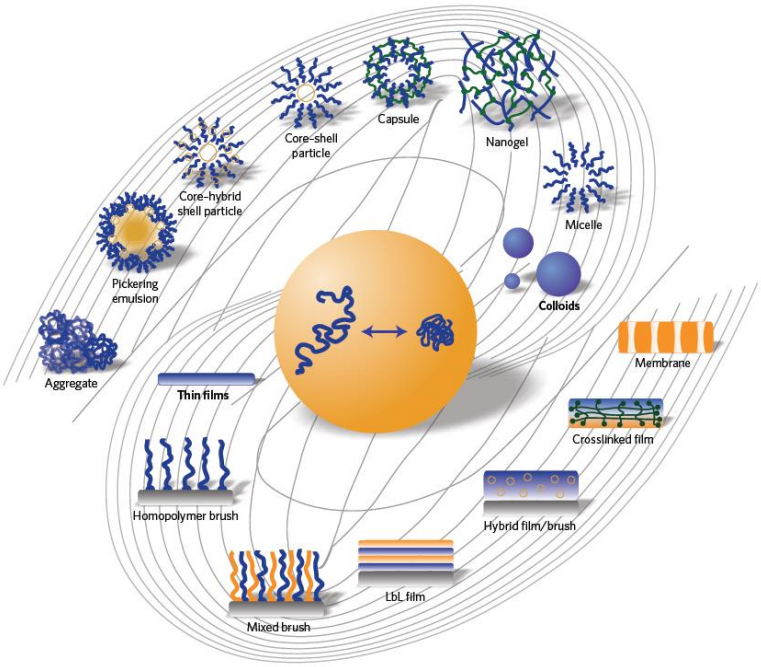

Figure 1.8 – Stimuli-responsive polymer materials in diverse geometries which can be categorized into two representative forms: thin films and particulates. Depending on the geometry of polymers, phase and dynamic behavior of macromolecule assemblies vary. Adapted from ref. 94.

1.2.2 Trigger forces

Responsive functional materials reconfigure themselves and hence exhibit switchable properties in a response to trigger forces, which is often called stimuli. This section exemplifies a variety of dynamically reconfigurable colloid systems reported to date.

First, changes in chemical environment can trigger the reconfiguration and response of a colloidal assembly[95-98]. **Figure 1.9a** represents pH-dependent dynamics of colloidal particles consist of a poly(acrylic acid) (PAA) hydrogel and poly(vinyl cinnamate) (PVCi) organogel, either freestanding (bottom row) or tethered to silica spheres (top row)[95]. The PAA swells and contracts with pH changes but the PVCi is pH-inactive. Particles are observed in their original configurations in pH 5 buffer and in their inverted configurations in pH 6. In **Figure 1.9b**, we observe that a crystalline colloidal array of polystyrene spheres (~100 nm diameter) polymerized within a hydrogel that swells and shrinks reversibly in the presence of certain analytes, here, metal ions[96,97]. The hydrogel contains either a molecular-recognition group that binds the analyte selectively (crown ethers for metal ions), or a molecular-recognition agent that reacts with the analyte selectively. These recognition events cause the hydrogel to swell because of an increased osmotic pressure, which in turn increases the mean separation between the colloidal particles and so shifts the Bragg reflection peaks to longer wavelengths. Similarly, **Figure 1.9c** shows the images of 2D monolayer colloidal crystal arrays with dynamic responsiveness to chemical environments[98]. The colloidal arrays attached on the functional hydrogels change the spacing between the colloids, in response to changes in pH and solvent composition of the hydrogel**.**

Another distinct type of switchable dynamic response can be realized using temperature changes of colloidal assembly functionalized with thermo-responsive components[99-101]. **Figure 1.10a** includes the images of dynamic reconfiguration of colloidal assembly of multi-scale structures that combines thermo-responsive depletion attraction with topographically patterned surface features[99]. As the temperature increases, depletion attraction becomes negligible, and particles diffuse freely except for the small gravitational energy difference inside and outside features. This indicates that changing both the temperature and topography can reversibly induce colloidal reconfigurations between two well-defined states: multi-scale periodic structures and disordered fluid states.

Figure 1.10b demonstrates reversible solid–solid phase transition of colloidal superballs dispersed in depletant mixture of poly(ethylene oxide) (PEO) and PNIPAM[100]. At 27.5°C, colloids assemble into a square lattice, but at 31°C, energetic contribution of PNIPAM becomes negligible, whereas that of PEO stays fixed, so that resulting in the transition into the other densest lattice form, Λ1.

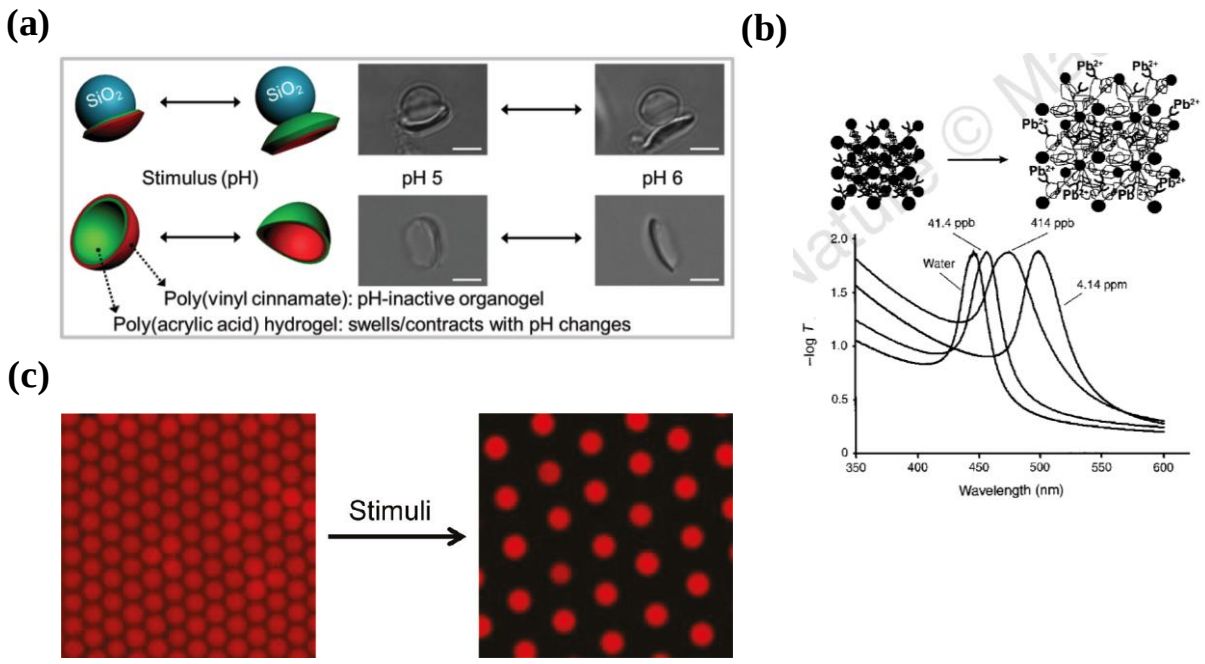

Figure 1.9 – Dynamic response of colloidal configuration triggered by chemical environment. (a) pH-responsive bi-stable colloids consisting of PAA and PVCi. (b) Colloidal crystals polymerized in hydrogel that respond to surrounding chemical species or analytes. (c) Reconfiguration of 2D colloidal crystal arrays actuated by pH and solvent composition. Adapted from refs. 95,96,98.

Reconfigurable colloid assembly that responds to temperature change can in turn activate the dynamic response of optical properties, as depicted in **Figure 1.10c**[101]. PNIPAM microgel colloids can assemble into 2D periodic arrays, which can be used for the optical devices, etalons. The etalons are composed of two reflective, semitransparent, and thin Au layers, sandwiching a 2D monolithic microgel layers, on a glass substrate. This structure allows light to enter the dielectric cavity and resonate between two reflective layers. This resonating light yields constructive and destructive interference, allowing certain wavelengths of light to be reflected. The optical reflectance peak shifts accordingly in response to colloidal reconfiguration induced by temperature change.

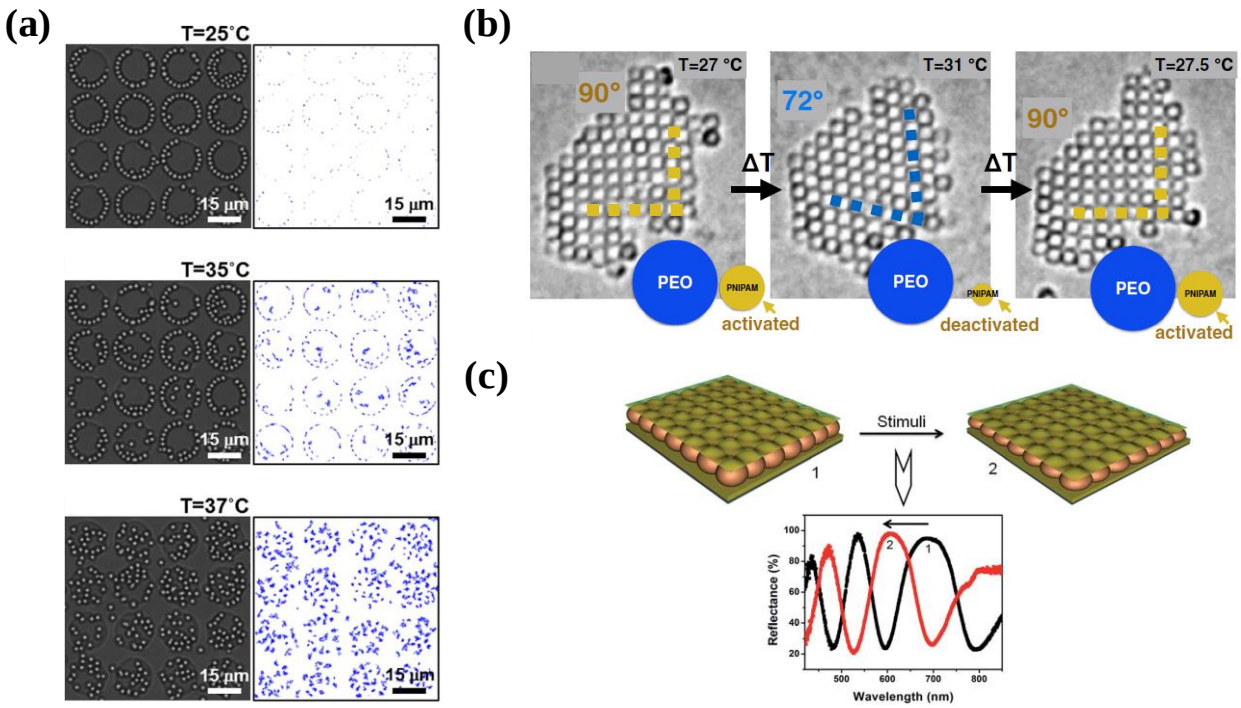

Figure 1.10 – Thermo-responsive reconfigurable colloidal assembly. (a) Colloidal reconfigurations between multi-scale periodic states and disordered fluid states. (b) Reversible solid–solid phase transition of colloidal superballs between two densest lattice forms. (c) PNIPAM microgel 2D periodic array-based optical device, etalons. Adapted from refs. 99-101.

Electric field or magnetic field can also trigger dynamic reconfiguration of a variety of colloidal assemblies[102-104]. **Figure 1.11a** shows the fluorescence microscopy images of elliptical colloids arrays at two distinctive configurations[102]. Under light-assisted electrophoretic deposition, the homogeneous ellipsoids undergo an order-disorder transition. At applied voltages between 1.75 ~ 2.1 V, and light intensities < 250 W m^{-2}, a liquid crystal phase characterized by highly dense structures, with a high degree of positional and orientational ordering was observed over large domains. Another example of dynamic switching between colloidal configurations triggered by electric field is represented in **Figure 1.11b**[103]. Charged rod-like colloidal particles form three-dimensional plastic crystals and glasses if their repulsions extend significantly beyond their length. These plastic phases can be reversibly and dynamically switched to full crystals by an AC electric field. Laser diffraction shows a field-induced order-disorder transition in the sphero-cylinder colloidal arrays. Smoukov et al. have demonstrated Janus magnetic particles could reversibly switch their configurations using repeated magnetization and demagnetization processes as shown

in **Figure 1.11c**[104]. The Janus colloids in the disordered arrays in the absence of magnetic field, have become the ordered ones by external magnetic field.

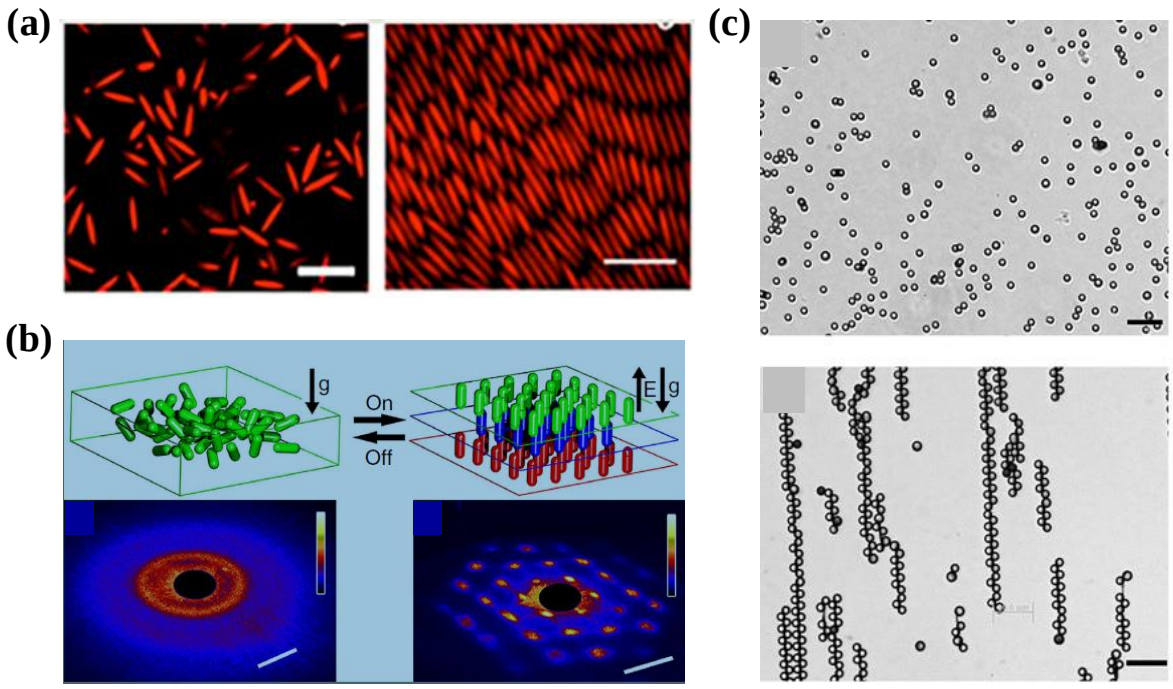

Figure 1.11 – Electric and magnetic fields-driven reconfigurations. (a) Light-assisted electrophoretic triggering for order-disorder transition. (b) Laser diffraction patterns of crystal switching by an AC electric field. (c) Reversible dynamics of Janus magnetic colloids by magnetic field. Adapted from refs. 102-104.

Light-triggered colloidal rearrangements also offer distinctive and exciting dynamics-property-structure relationships[105,106]. **Figure 1.12a** represents time lapse images of functionalized PMMA colloidal particles under optical field excitation[105]. The photo-induced assembly process occurs rapidly, and accumulated particles display a close-packed crystallization. This dynamic behavior was attributed to electrophoresis of colloids generated by photochemistry at an indium tin oxide-coated substrate. **Figure 1.12b** demonstrates a light-activated form of self-organization in a suspension containing synthetic photoactivated colloidal particles[106]. Under the illumination, the particles assemble into two-dimensional living crystals, which form, break, explode, and re-form elsewhere. It was revealed that the dynamic reconfiguration resulted from a competition between self-propulsion of particles and an attractive force caused respectively by osmotic and phoretic effects and activated by light.

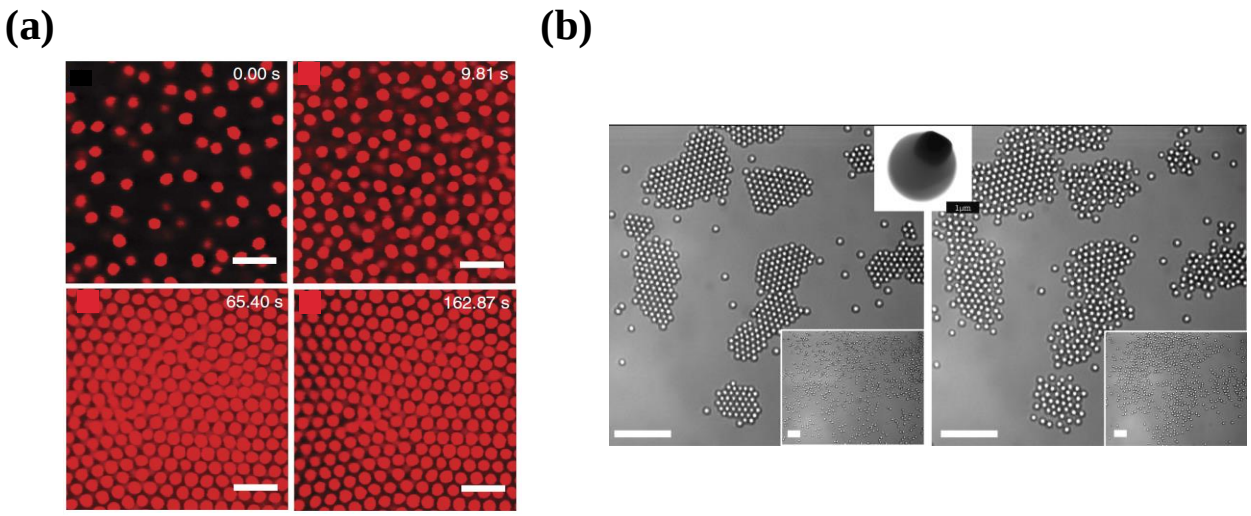

Figure 1.12 – Light-triggered reconfigurable colloidal dynamics. (a) Photo-induced self-assembly process leads to complete crystallization. (b) Living colloidal crystals that form, break, explode, and reform, all of which are actuated by light. Adapted from refs. 105,106.

1.2.3 3D colloid/polymeric network gel hybrids

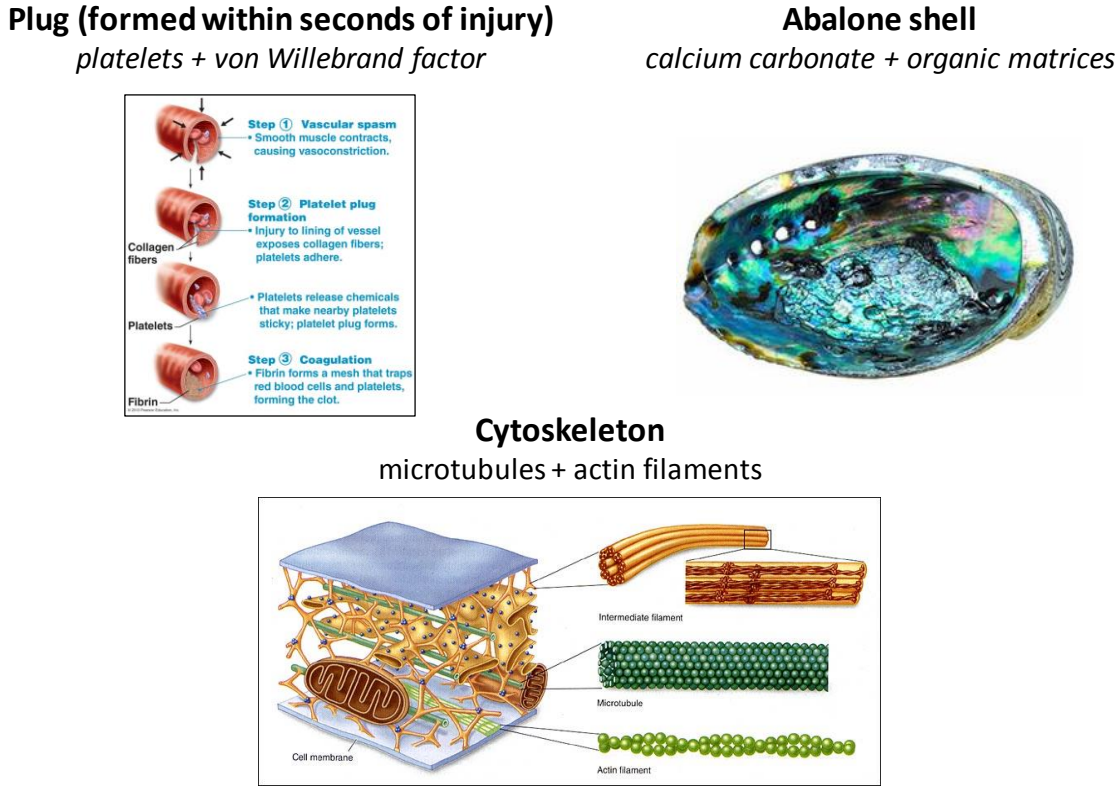

Figure 1.13 – Colloid/polymer gel composites in nature. Adapted from online.

We have discussed so far dynamic reconfigurations of colloidal assembly in low viscosity liquids without time-dependent memory nor dynamic viscoelastic responses[107]. In nature, however, particles in viscoelastic polymer gels are everywhere in functional 3D biological assemblies, as shown in **Figure 1.13**. For instance, a blood clot, which is formed when we are injured, consists of colloidal platelets and polymeric von Willebrand factor. Abalone shell is also comprised of calcium carbonate surrounded by organic matrices. Cytoskeleton is another example of colloid/polymer gel composites whose components are microtubules and actin filaments. In this context, a fundamental understanding of the physics lying behind the dynamic responsiveness of colloids in 3D viscoelastic meshes is essential for designing novel material functionality in a broad range of areas such as biotechnology and biomedicine[108,109].

Despite the importance, the study of such 3D hybrid materials is in its infancy due to the complexity of the systems[110,111]. Significant theoretical progress for the equilibrium amorphous assembly of spherical particles and homopolymers has been recently achieved[112-114]. Three distinct statistical microstructural regimes have been proposed[112], as shown in **Figure 1.14**, which were largely verified experimentally[115-117]. Reconfiguration dynamics of particles-polymers strongly depends on the effective attraction energy between particles and between polymers and colloids, and their magnitudes relative to thermal energy, k_BT[112]. With increasing net colloid-polymer attraction energy (left to right in **Figure 1.14**), three states of organization can be formed: i) contact particle aggregation driven by depletion attraction and/or van der Waals attraction, ii) steric stabilization, and full dispersion due to discrete adsorbed layer formation, and iii) polymer-particle bridging complexes. There have been another simulation works on predicting dynamics of colloid-gels assemblies.

Figure 1.15a illustrates flow-driven self-assembly of colloid/polymer 3D composite, which is a blood clot[118]. The system became aggregated above a certain critical shear rate. Cross-linking density of polymer matrix is crucial factor of determining colloid-colloid interactions and colloid-network structuring[110]. As depicted in **Figure 1.15b**, Di Michele et al. also investigated spatial organization and dynamics of silica colloids surrounded by the polyacrylamide matrix and revealed the relationships between cross-linking density and reconfiguration dynamics.

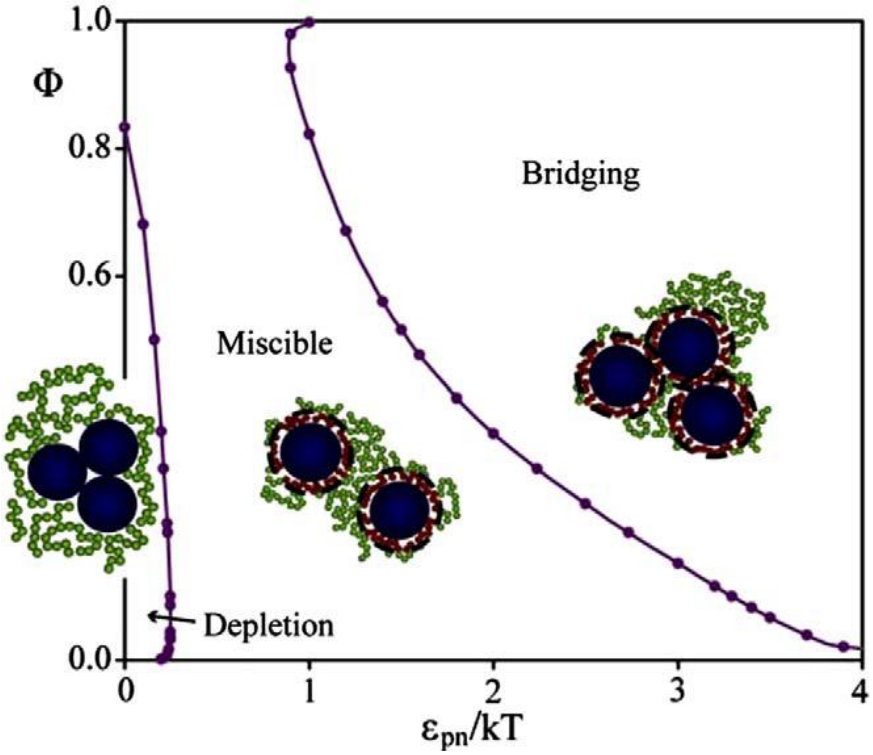

Figure 1.14 – Three states of organization in melt polymer nanocomposites with increasing net polymer-particle attraction energy. Adapted from ref. 112.

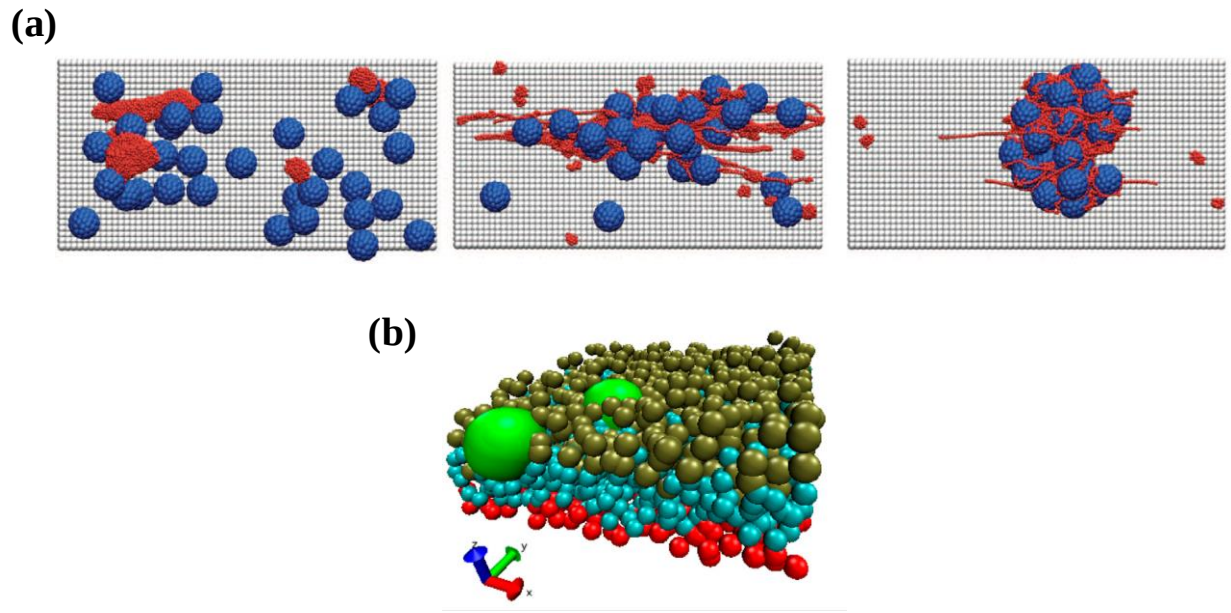

Figure 1.15 – Theoretical frameworks on spatial distribution and dynamics of colloid/polymer gel hybrids. (a) Flow-driven self-assembly in the blood clot, during blood clotting. (b) Effects of cross-linking density on colloids distribution in polymer networks. Adapted from refs. 110,118.

Based on these previous theoretical works, well-designed experimental studies on colloids-polymeric fiber gels can be performed to answer following fundamental questions. How will colloid-colloid interaction and colloid-polymer interaction affect dynamics and spatial reorganization of colloids in viscoelastic polymeric mesh gels? How can we realize reversible and switchable behavior of colloidal assemblies in viscoelastic fiber gels in response to external triggers? Can we mimic the nature to fabricate novel materials with specific responsive functionality? As illustrated in **Figure 1.16**, from this understanding we can deduce relationships between spatial organization and dynamics under varying external fields, which will enable dynamic and reversible control of the electrical, mechanical, and sensing properties of the 3D colloid/polymer mesh composites.

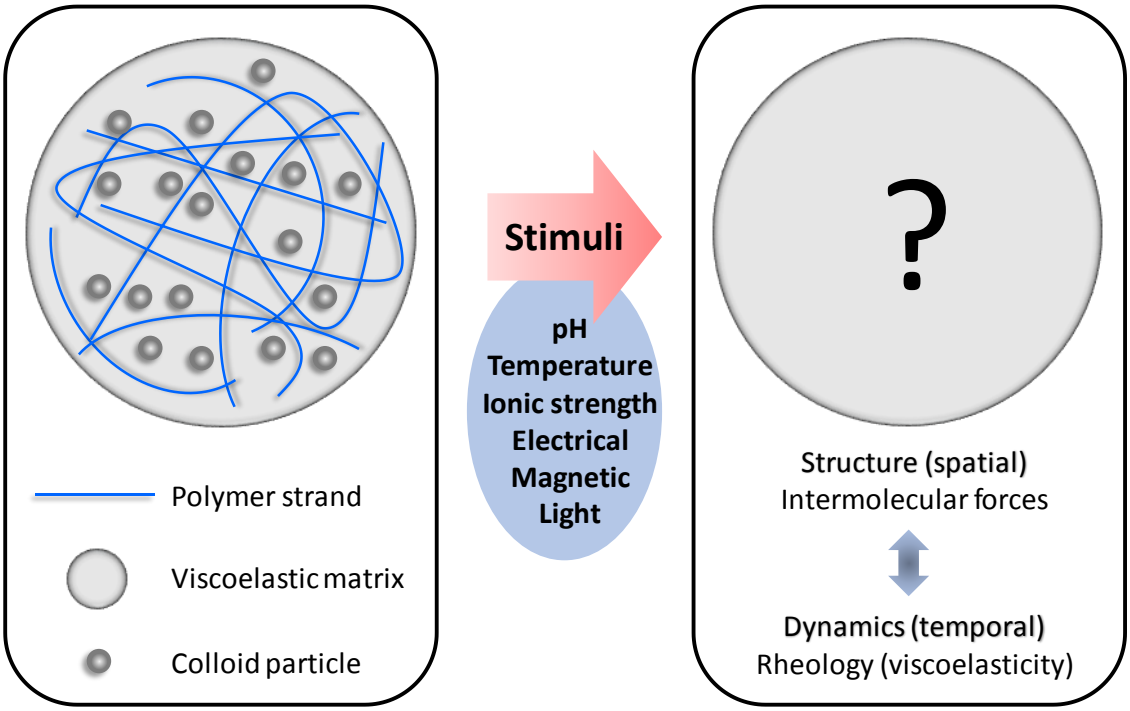

Figure 1.16 – Schematics of stimuli-responsive 3D colloid/polymer viscoelastic matrices to understand the spatial organization and temporal dynamics.

1.3 Thesis Overview

This thesis can be divided into two big categories: i) thermal and electrical transport properties of inorganic 3D porous meso/nanostructures, which is related with **Chapter 1.1**, and ii)

viscoelastic properties of 3D colloid/polymeric fiber hydrogel composites, which is related with **Chapter 1.2**.

Chapters 2, **3**, and **4** explore the first topic, i). **Chapter 2** focuses on the fabrication and characterization of functional 3D porous structures made of inorganic materials such as Bi_2Te_3, PbS, and Fe_3O_4 realized by colloidal crystal templated electrodeposition techniques. In **Chapter 3**, we discuss thermal conductivity measurement and analysis of epitaxial Fe_3O_4 3D porous structures. **Chapter 4** handles the electrical conductivity measurement of epitaxial Fe_3O_4 3D porous structures.

Chapters 5 and **6** cover the second topic, ii). **Chapter 5** mainly discusses two methods of integration of hard sphere polystyrene colloids into fibrin large mesh gels and their viscoelastic properties. **Chapter 6** deals with the fabrication of 3D thermo-responsive PNIPAM microgel/fibrin large mesh hydrogel composites that demonstrate dynamic reconfiguration of colloid assemblies and switchable viscoelastic properties.

Chapter 7 includes summaries and conclusions of this thesis, and future directions based on the previous works.

1.4 References

1 Wijnhoven, J. E. G. J. & Vos, W. L. Preparation of photonic crystals made of air spheres in titania. *Science* **281**, 802-804, doi:DOI 10.1126/science.281.5378.802 (1998).

2 Blanco, A. *et al.* Large-scale synthesis of a silicon photonic crystal with a complete three-dimensional bandgap near 1.5 micrometres. *Nature* **405**, 437, doi:10.1038/35013024 (2000).

3 Nelson, E. C. *et al.* Epitaxial growth of three-dimensionally architectured optoelectronic devices. *Nature Materials* **10**, 676-681, doi:10.1038/Nmat3071 (2011).

4 Rinne, S. A., García-Santamaría, F. & Braun, P. V. Embedded cavities and waveguides in three-dimensional silicon photonic crystals. *Nature Photonics* **2**, 52-56, doi:10.1038/nphoton.2007.252 (2007).

5 Yu, X., Lee, Y. J., Furstenberg, R., White, J. O. & Braun, P. V. Filling Fraction Dependent Properties of Inverse Opal Metallic Photonic Crystals. *Advanced Materials* **19**, 1689-1692, doi:10.1002/adma.200602792 (2007).

6 Kulkarni, A. A. *et al.* Template-Directed Solidification of Eutectic Optical Materials. *Advanced Optical Materials*, 1800071, doi:10.1002/adom.201800071 (2018).

7 Zhang, H., Yu, X. & Braun, P. V. Three-dimensional bicontinuous ultrafast-charge and -discharge bulk battery electrodes. *Nat Nanotechnol* **6**, 277-281,

doi:10.1038/nnano.2011.38 (2011).
8 Pikul, J. H., Gang Zhang, H., Cho, J., Braun, P. V. & King, W. P. High-power lithium ion microbatteries from interdigitated three-dimensional bicontinuous nanoporous electrodes. *Nat Commun* **4**, 1732, doi:10.1038/ncomms2747 (2013).
9 Taberna, P. L., Mitra, S., Poizot, P., Simon, P. & Tarascon, J. M. High rate capabilities Fe3O4-based Cu nano-architectured electrodes for lithium-ion battery applications. *Nature Materials* **5**, 567, doi:10.1038/nmat1672 (2006).
10 Kim, S.-K., Cho, J., Moore, J. S., Park, H. S. & Braun, P. V. High-Performance Mesostructured Organic Hybrid Pseudocapacitor Electrodes. *Advanced Functional Materials* **26**, 903-910, doi:10.1002/adfm.201504307 (2016).
11 Liu, J. *et al.* Graphene Sandwiched Mesostructured Li-Ion Battery Electrodes. *Adv Mater* **28**, 7696-7702, doi:10.1002/adma.201600829 (2016).
12 Wang, J., Zhou, H., Nanda, J. & Braun, P. V. Three-Dimensionally Mesostructured Fe2O3 Electrodes with Good Rate Performance and Reduced Voltage Hysteresis. *Chemistry of Materials* **27**, 2803-2811, doi:10.1021/cm504365s (2015).
13 Mihi, A., Zhang, C. & Braun, P. V. Transfer of preformed three-dimensional photonic crystals onto dye-sensitized solar cells. *Angew Chem Int Ed Engl* **50**, 5712-5715, doi:10.1002/anie.201100446 (2011).
14 Suezaki, T., Chen, J. I. L., Hatayama, T., Fuyuki, T. & Ozin, G. A. Electrical properties of p-type and n-type doped inverse silicon opals - towards optically amplified silicon solar cells. *Applied Physics Letters* **96**, 242102, doi:10.1063/1.3447374 (2010).
15 Han, S. E., Stein, A. & Norris, D. J. Tailoring Self-Assembled Metallic Photonic Crystals for Modified Thermal Emission. *Physical Review Letters* **99**, 053906, doi:10.1103/PhysRevLett.99.053906 (2007).
16 Denny, N. R., Han, S. E., Norris, D. J. & Stein, A. Effects of Thermal Processes on the Structure of Monolithic Tungsten and Tungsten Alloy Photonic Crystals. *Chemistry of Materials* **19**, 4563-4569, doi:10.1021/cm071228p (2007).
17 Arpin, K. A., Losego, M. D. & Braun, P. V. Electrodeposited 3D Tungsten Photonic Crystals with Enhanced Thermal Stability. *Chemistry of Materials* **23**, 4783-4788, doi:10.1021/cm2019789 (2011).
18 Nagpal, P., Han, S. E., Stein, A. & Norris, D. J. Efficient Low-Temperature Thermophotovoltaic Emitters from Metallic Photonic Crystals. *Nano Letters* **8**, 3238-3243, doi:10.1021/nl801571z (2008).
19 Arpin, K. A. *et al.* Three-dimensional self-assembled photonic crystals with high temperature stability for thermal emission modification. *Nat Commun* **4**, 2630, doi:10.1038/ncomms3630 (2013).
20 Lee, Y. J. & Braun, P. V. Tunable Inverse Opal Hydrogel pH Sensors. *Advanced Materials* **15**, 563-566, doi:10.1002/adma.200304588 (2003).
21 Lee, Y.-J., Pruzinsky, S. A. & Braun, P. V. Glucose-Sensitive Inverse Opal Hydrogels: Analysis of Optical Diffraction Response. *Langmuir* **20**, 3096-3106, doi:10.1021/la035555x (2004).
22 Lee, J. H., Galli, G. A. & Grossman, J. C. Nanoporous Si as an efficient thermoelectric material. *Nano Lett* **8**, 3750-3754, doi:10.1021/nl802045f (2008).
23 Ma, J. *et al.* Coherent phonon-grain boundary scattering in silicon inverse opals. *Nano Lett* **13**, 618-624, doi:10.1021/nl304190s (2013).
24 Barako, M. T. *et al.* Quasi-ballistic Electronic Thermal Conduction in Metal Inverse Opals.

Nano Lett **16**, 2754-2761, doi:10.1021/acs.nanolett.6b00468 (2016).
25 von Freymann, G., Kitaev, V., Lotsch, B. V. & Ozin, G. A. Bottom-up assembly of photonic crystals. *Chem Soc Rev* **42**, 2528-2554, doi:10.1039/c2cs35309a (2013).
26 Li, F., Josephson, D. P. & Stein, A. Colloidal assembly: the road from particles to colloidal molecules and crystals. *Angew Chem Int Ed Engl* **50**, 360-388, doi:10.1002/anie.201001451 (2011).
27 Curri, M. L., Comparelli, R., Striccoli, M. & Agostiano, A. Emerging methods for fabricating functional structures by patterning and assembling engineered nanocrystals. *Physical Chemistry Chemical Physics* **12**, 11197-11207, doi:10.1039/B926146J (2010).
28 Ozin, G. A. *et al.* Nanofabrication by self-assembly. *Materials Today* **12**, 12-23, doi:10.1016/s1369-7021(09)70156-7 (2009).
29 Moon, J. H. & Yang, S. Chemical aspects of three-dimensional photonic crystals. *Chem Rev* **110**, 547-574, doi:10.1021/cr900080v (2010).
30 Braun, P. V. Materials Chemistry in 3D Templates for Functional Photonics. *Chemistry of Materials* **26**, 277-286, doi:10.1021/cm4023437 (2013).
31 Xia, Y., Gates, B., Yin, Y. & Lu, Y. Monodispersed Colloidal Spheres: Old Materials with New Applications. *Advanced Materials* **12**, 693-713, doi:10.1002/(sici)1521-4095(200005)12:10<693::aid-adma693>3.0.co;2-j (2000).
32 Dhont, J. K. G., Smits, C. & Lekkerkerker, H. N. W. A time resolved static light scattering study on nucleation and crystallization in a colloidal system. *Journal of Colloid and Interface Science* **152**, 386-401, doi:https://doi.org/10.1016/0021-9797(92)90041-J (1992).
33 Kaplan, P. D., Rouke, J. L., Yodh, A. G. & Pine, D. J. Entropically Driven Surface Phase Separation in Binary Colloidal Mixtures. *Physical Review Letters* **72**, 582-585, doi:10.1103/PhysRevLett.72.582 (1994).
34 Anderson, V. J. & Lekkerkerker, H. N. W. Insights into phase transition kinetics from colloid science. *Nature* **416**, 811, doi:10.1038/416811a (2002).
35 Koh, Y. K., Yip, C. H., Chiang, Y. M. & Wong, C. C. Kinetic stages of single-component colloidal crystallization. *Langmuir* **24**, 5245-5248, doi:10.1021/la800702d (2008).
36 Gasser, U. Crystallization in three- and two-dimensional colloidal suspensions. *J Phys Condens Matter* **21**, 203101, doi:10.1088/0953-8984/21/20/203101 (2009).
37 Nguyen, D., Devlin, L., Koshy, P. & Sorrell, C. Impact of water-soluble cellulose ethers on polymer-modified mortars. *Journal of Materials Science* **39**, 923-951, doi:10.1007/s10853-013-7732-8 (2013).
38 Walker, D. A., Kowalczyk, B., de la Cruz, M. O. & Grzybowski, B. A. Electrostatics at the nanoscale. *Nanoscale* **3**, 1316-1344, doi:10.1039/c0nr00698j (2011).
39 M., B. K. J., E., W. C., Siowling, S. & A., G. B. Nanoscale Forces and Their Uses in Self-Assembly. *Small* **5**, 1600-1630, doi:doi:10.1002/smll.200900358 (2009).
40 Israelachvili, J. N. *Intermolecular and Surface Forces*. (Elsevier Science, 2011).
41 Cheng, Z. *et al.* Phase diagram of hard spheres. *Materials & Design* **22**, 529-534, doi:https://doi.org/10.1016/S0261-3069(01)00015-2 (2001).
42 Villeneuve, V. W. A. d. *et al.* Hard sphere crystal nucleation and growth near large spherical impurities. *Journal of Physics: Condensed Matter* **17**, S3371 (2005).
43 Iler, R. K. Formation of Precious Opal. *Nature* **207**, 472, doi:10.1038/207472a0 (1965).
44 Davis, K. E., Russel, W. B. & Glantschnig, W. J. Settling suspensions of colloidal silica: observations and X-ray measurements. *Journal of the Chemical Society, Faraday Transactions* **87**, 411-424, doi:10.1039/FT9918700411 (1991).

45 Míguez, H. *et al.* Evidence of FCC Crystallization of SiO2 Nanospheres. *Langmuir* **13**, 6009-6011, doi:10.1021/la970589o (1997).
46 M., M., R., Z., T., M., G., R. S. & M., S. T. C. Photonic Crystal Films with High Refractive Index Contrast. *Advanced Materials* **12**, 1499-1503, doi:doi:10.1002/1521-4095(200010)12:20<1499::AID-ADMA1499>3.0.CO;2-M (2000).
47 Yan, Q., Zhou, Z. & Zhao, X. S. Inward-Growing Self-Assembly of Colloidal Crystal Films on Horizontal Substrates. *Langmuir* **21**, 3158-3164, doi:10.1021/la047337p (2005).
48 Jiang, P., Bertone, J. F., Hwang, K. S. & Colvin, V. L. Single-Crystal Colloidal Multilayers of Controlled Thickness. *Chemistry of Materials* **11**, 2132-2140, doi:10.1021/cm990080+ (1999).
49 Prieve, D. C., Sides, P. J. & Wirth, C. L. 2-D assembly of colloidal particles on a planar electrode. *Current Opinion in Colloid & Interface Science* **15**, 160-174, doi:https://doi.org/10.1016/j.cocis.2010.01.005 (2010).
50 Rogach, A. L., Kotov, N. A., Koktysh, D. S., Ostrander, J. W. & Ragoisha, G. A. Electrophoretic Deposition of Latex-Based 3D Colloidal Photonic Crystals: A Technique for Rapid Production of High-Quality Opals. *Chemistry of Materials* **12**, 2721-2726, doi:10.1021/cm000274l (2000).
51 Holgado, M. *et al.* Electrophoretic Deposition To Control Artificial Opal Growth. *Langmuir* **15**, 4701-4704, doi:10.1021/la990161k (1999).
52 Soukoulis, C. *Photonic Crystals and Light Localization in the 21st Century*. (2001).
53 Bhatt, K. H. & Velev, O. D. Control and Modeling of the Dielectrophoretic Assembly of On-Chip Nanoparticle Wires. *Langmuir* **20**, 467-476, doi:10.1021/la0349976 (2004).
54 Hartgerink, J. D., Beniash, E. & Stupp, S. I. Self-Assembly and Mineralization of Peptide-Amphiphile Nanofibers. *Science* **294**, 1684-1688, doi:10.1126/science.1063187 (2001).
55 Zhang, K.-Q. & Liu, X. Y. In situ observation of colloidal monolayer nucleation driven by an alternating electric field. *Nature* **429**, 739, doi:10.1038/nature02630 (2004).
56 Jianping, G. & Yadong, Y. Responsive Photonic Crystals. *Angewandte Chemie International Edition* **50**, 1492-1522, doi:doi:10.1002/anie.200907091 (2011).
57 Ge, J. & Yin, Y. Magnetically responsive colloidal photonic crystals. *Journal of Materials Chemistry* **18**, 5041-5045, doi:10.1039/B809958H (2008).
58 Erb, R. M., Son, H. S., Samanta, B., Rotello, V. M. & Yellen, B. B. Magnetic assembly of colloidal superstructures with multipole symmetry. *Nature* **457**, 999, doi:10.1038/nature07766 (2009).
59 O., V., O., K. & E., K. Colloid Crystal Growth under Oscillatory Shear. *Advanced Materials* **12**, 110-112, doi:doi:10.1002/(SICI)1521-4095(200001)12:2<110::AID-ADMA110>3.0.CO;2-X (2000).
60 Wong, S., Kitaev, V. & Ozin, G. A. Colloidal Crystal Films: Advances in Universality and Perfection. *Journal of the American Chemical Society* **125**, 15589-15598, doi:10.1021/ja0379969 (2003).
61 Zhou, Z. & Zhao, X. S. Flow-Controlled Vertical Deposition Method for the Fabrication of Photonic Crystals. *Langmuir* **20**, 1524-1526, doi:10.1021/la035686y (2004).
62 Vlasov, Y. A., Bo, X.-Z., Sturm, J. C. & Norris, D. J. On-chip natural assembly of silicon photonic bandgap crystals. *Nature* **414**, 289, doi:10.1038/35104529 (2001).
63 Fustin, C.-A., Glasser, G., Spiess, H. W. & Jonas, U. Parameters Influencing the Templated Growth of Colloidal Crystals on Chemically Patterned Surfaces. *Langmuir* **20**, 9114-9123, doi:10.1021/la0489413 (2004).

64 Stein, A., Wilson, B. E. & Rudisill, S. G. Design and functionality of colloidal-crystal-templated materials-chemical applications of inverse opals. *Chemical Society Reviews* **42**, 2763-2803, doi:10.1039/C2CS35317B (2013).
65 Dumanli, A. G. & Savin, T. Recent advances in the biomimicry of structural colours. *Chemical Society Reviews* **45**, 6698-6724, doi:10.1039/C6CS00129G (2016).
66 Singh, B., Kumar Jena, B., Bhattacharjee, S. & Besra, L. Development of oxidation and corrosion resistance hydrophobic graphene oxide-polymer composite coating on copper. *Surface and Coatings Technology* **232**, 475–481, doi:10.1016/j.surfcoat.2013.06.004 (2013).
67 Braun, P. V. & Wiltzius, P. Electrochemically grown photonic crystals. *Nature* **402**, 603-604, doi:10.1038/45137 (1999).
68 Kim, J. *et al.* Epitaxial Growth of Three-Dimensionally Mesostructured Single-Crystalline Cu2O via Templated Electrodeposition. *Chemistry of Materials* **26**, 7051-7058, doi:10.1021/cm5034645 (2014).
69 H., M. *et al.* Photonic Bandgap Engineering in Germanium Inverse Opals by Chemical Vapor Deposition. *Advanced Materials* **13**, 1634-1637, doi:doi:10.1002/1521-4095(200111)13:21<1634::AID-ADMA1634>3.0.CO;2-9 (2001).
70 Pinna, N. & Knez, M. *Atomic Layer Deposition of Nanostructured Materials*. (Wiley, 2011).
71 Yeo, S. J., Choi, G. H. & Yoo, P. J. Multiscale-architectured functional membranes utilizing inverse opal structures. *Journal of Materials Chemistry A* **5**, 17111-17134, doi:10.1039/C7TA05033J (2017).
72 Imhof, A. & Pine, D. J. Ordered macroporous materials by emulsion templating. *Nature* **389**, 948, doi:10.1038/40105 (1997).
73 Holland, B. T., Blanford, C. F. & Stein, A. Synthesis of macroporous minerals with highly ordered three-dimensional arrays of spheroidal voids. *Science* **281**, 538-540, doi:10.1126/science.281.5376.538 (1998).
74 Holland, B. T., Blanford, C. F., Do, T. & Stein, A. Synthesis of Highly Ordered, Three-Dimensional, Macroporous Structures of Amorphous or Crystalline Inorganic Oxides, Phosphates, and Hybrid Composites. *Chemistry of Materials* **11**, 795-805, doi:10.1021/cm980666g (1999).
75 Lei, Z., Li, J., Zhang, Y. & Lu, S. Fabrication and characterization of highly-ordered periodic macroporous barium titanate by the sol-gel method. *Journal of Materials Chemistry* **10**, 2629-2631, doi:10.1039/B005555G (2000).
76 W., D., H., B., B., T. & F., M. Inverse Opals with a Skeleton Structure: Photonic Crystals with Two Complete Bandgaps. *Advanced Materials* **14**, 1457-1460, doi:doi:10.1002/1521-4095(20021016)14:20<1457::AID-ADMA1457>3.0.CO;2-P (2002).
77 A., V. Y., Nan, Y. & J., N. D. Synthesis of Photonic Crystals for Optical Wavelengths from Semiconductor Quantum Dots. *Advanced Materials* **11**, 165-169, doi:doi:10.1002/(SICI)1521-4095(199902)11:2<165::AID-ADMA165>3.0.CO;2-3 (1999).
78 Dong, W., Bongard, H. J. & Marlow, F. New Type of Inverse Opals: Titania With Skeleton Structure. *Chemistry of Materials* **15**, 568-574, doi:10.1021/cm021299i (2003).
79 J., N. D. & A., V. Y. Chemical Approaches to Three-Dimensional Semiconductor Photonic Crystals. *Advanced Materials* **13**, 371-376, doi:doi:10.1002/1521-4095(200103)13:6<371::AID-ADMA371>3.0.CO;2-K (2001).

80 Subramania, G., Biswas, R., Constant, K., Sigalas, M. M. & Ho, K. M. Structural characterization of thin film photonic crystals. *Physical Review B* **63**, doi:ARTN 235111 (2001).
81 Kim, J. *et al.* Template-Directed Directionally Solidified 3D Mesostructured AgCl-KCl Eutectic Photonic Crystals. *Adv Mater* **27**, 4551-4559, doi:10.1002/adma.201502265 (2015).
82 Kinoshita, S., Yoshioka, S. & Miyazaki, J. Physics of structural colors. *Reports on Progress in Physics* **71**, 076401 (2008).
83 Bar-Cohen, Y. *Biomimetics: Biologically Inspired Technologies*. (CRC Press, 2005).
84 S., S. *et al.* Bimaterial Microcantilevers as a Hybrid Sensing Platform. *Advanced Materials* **20**, 653-680, doi:doi:10.1002/adma.200701667 (2008).
85 Archibald, R. *et al.* Independent component analysis of nanomechanical responses of cantilever arrays. *Analytica Chimica Acta* **584**, 101-105, doi:https://doi.org/10.1016/j.aca.2006.11.007 (2007).
86 V., M. R. *et al.* Robotic Tentacles with Three-Dimensional Mobility Based on Flexible Elastomers. *Advanced Materials* **25**, 205-212, doi:doi:10.1002/adma.201203002 (2013).
87 Solomon, M. J. Tools and Functions of Reconfigurable Colloidal Assembly. *Langmuir*, doi:10.1021/acs.langmuir.7b03748 (2018).
88 Hoffman, A. S. Stimuli-responsive polymers: Biomedical applications and challenges for clinical translation. *Advanced Drug Delivery Reviews* **65**, 10-16, doi:https://doi.org/10.1016/j.addr.2012.11.004 (2013).
89 Meng, H. & Li, G. A review of stimuli-responsive shape memory polymer composites. *Polymer* **54**, 2199-2221, doi:https://doi.org/10.1016/j.polymer.2013.02.023 (2013).
90 Geryak, R. & Tsukruk, V. V. Reconfigurable and actuating structures from soft materials. *Soft Matter* **10**, 1246-1263, doi:10.1039/C3SM51768C (2014).
91 Ahn, S.-k., Kasi, R. M., Kim, S.-C., Sharma, N. & Zhou, Y. Stimuli-responsive polymer gels. *Soft Matter* **4**, 1151-1157, doi:10.1039/B714376A (2008).
92 R., H. G., H., S. M., B., S. A. & Andrew, L. L. Design of Multiresponsive Hydrogel Particles and Assemblies. *Advanced Functional Materials* **20**, 1697-1712, doi:doi:10.1002/adfm.200902429 (2010).
93 Lyon, L. A., Meng, Z., Singh, N., Sorrell, C. D. & St. John, A. Thermoresponsive microgel-based materials. *Chemical Society Reviews* **38**, 865-874, doi:10.1039/B715522K (2009).
94 Stuart, M. A. C. *et al.* Emerging applications of stimuli-responsive polymer materials. *Nature Materials* **9**, 101, doi:10.1038/nmat2614 (2010).
95 Eric, E., Jaewon, Y., Amit, M., Jimmy, H. K. & V., B. P. Colloidal Particles that Rapidly Change Shape via Elastic Instabilities. *Small* **11**, 6051-6057, doi:doi:10.1002/smll.201502198 (2015).
96 Holtz, J. H. & Asher, S. A. Polymerized colloidal crystal hydrogel films as intelligent chemical sensing materials. *Nature* **389**, 829, doi:10.1038/39834 (1997).
97 Asher, S. A., Holtz, J., Liu, L. & Wu, Z. Self-Assembly Motif for Creating Submicron Periodic Materials. Polymerized Crystalline Colloidal Arrays. *Journal of the American Chemical Society* **116**, 4997-4998, doi:10.1021/ja00090a059 (1994).
98 Zhang, J.-T., Wang, L., Chao, X. & Asher, S. A. Periodicity-Controlled Two-Dimensional Crystalline Colloidal Arrays. *Langmuir* **27**, 15230-15235, doi:10.1021/la203363e (2011).
99 Edwards, T. D., Yang, Y., Everett, W. N. & Bevan, M. A. Reconfigurable multi-scale colloidal assembly on excluded volume patterns. *Scientific Reports* **5**, 13612,

doi:10.1038/srep13612 (2015).
100 Rossi, L. *et al.* Shape-sensitive crystallization in colloidal superball fluids. *Proceedings of the National Academy of Sciences* **112**, 5286-5290, doi:10.1073/pnas.1415467112 (2015).
101 Gao, Y., Li, X. & Serpe, M. J. Stimuli-responsive microgel-based etalons for optical sensing. *RSC Advances* **5**, 44074-44087, doi:10.1039/C5RA02306H (2015).
102 Ganesan, M. & Solomon, M. J. High-density equilibrium phases of colloidal ellipsoids by application of optically enhanced, direct current electric fields. *Soft Matter* **13**, 3768-3776, doi:10.1039/C7SM00359E (2017).
103 Liu, B. *et al.* Switching plastic crystals of colloidal rods with electric fields. *Nature Communications* **5**, 3092, doi:10.1038/ncomms4092 (2014).
104 Smoukov, S. K., Gangwal, S., Marquez, M. & Velev, O. D. Reconfigurable responsive structures assembled from magnetic Janus particles. *Soft Matter* **5**, 1285-1292, doi:10.1039/b814304h (2009).
105 Kim, Y., Shah, A. A. & Solomon, M. J. Spatially and temporally reconfigurable assembly of colloidal crystals. *Nature Communications* **5**, 3676, doi:10.1038/ncomms4676 (2014).
106 Palacci, J., Sacanna, S., Steinberg, A. P., Pine, D. J. & Chaikin, P. M. Living Crystals of Light-Activated Colloidal Surfers. *Science* **339**, 936-940, doi:10.1126/science.1230020 (2013).
107 Margaret, R. & Annette, F. T. Colloidal dispersions. Edited by W. B. Russel, D. A. Saville & W. R. Schowalter, Cambridge University Press, Cambridge, UK, 1989, xvii + 506 pp., price: £60.00. ISBN 0 521 34188 4. *Journal of Chemical Technology & Biotechnology* **54**, 201-202, doi:doi:10.1002/jctb.280540216 (1992).
108 Xu, B. Gels as Functional Nanomaterials for Biology and Medicine. *Langmuir* **25**, 8375-8377, doi:10.1021/la900987r (2009).
109 Van Vlierberghe, S., Dubruel, P. & Schacht, E. Biopolymer-Based Hydrogels As Scaffolds for Tissue Engineering Applications: A Review. *Biomacromolecules* **12**, 1387-1408, doi:10.1021/bm200083n (2011).
110 Di Michele, L., Zaccone, A. & Eiser, E. Analytical theory of polymer-network-mediated interaction between colloidal particles. *Proceedings of the National Academy of Sciences* **109**, 10187-10192, doi:10.1073/pnas.1202171109 (2012).
111 Suzuki, T., Endo, H., Osaka, N. & Shibayama, M. Dynamics and Microstructure Analysis of N-Isopropylacrylamide/Silica Hybrid Gels. *Langmuir* **25**, 8824-8832, doi:10.1021/la900736y (2009).
112 Hall, L. M., Jayaraman, A. & Schweizer, K. S. Molecular theories of polymer nanocomposites. *Current Opinion in Solid State and Materials Science* **14**, 38-48, doi:https://doi.org/10.1016/j.cossms.2009.08.004 (2010).
113 Hall, L. M. & Schweizer, K. S. Many body effects on the phase separation and structure of dense polymer-particle melts. *The Journal of Chemical Physics* **128**, 234901, doi:10.1063/1.2938379 (2008).
114 Hooper, J. B. & Schweizer, K. S. Contact Aggregation, Bridging, and Steric Stabilization in Dense Polymer−Particle Mixtures. *Macromolecules* **38**, 8858-8869, doi:10.1021/ma051318k (2005).
115 Hall, L. M., Anderson, B. J., Zukoski, C. F. & Schweizer, K. S. Concentration Fluctuations, Local Order, and the Collective Structure of Polymer Nanocomposites. *Macromolecules* **42**, 8435-8442, doi:10.1021/ma901523w (2009).
116 Kim, S. Y., Hall, L. M., Schweizer, K. S. & Zukoski, C. F. Long Wavelength Concentration

Fluctuations and Cage Scale Ordering of Nanoparticles in Concentrated Polymer Solutions. *Macromolecules* **43**, 10123-10131, doi:10.1021/ma1021677 (2010).
117 Kim, S. Y., Schweizer, K. S. & Zukoski, C. F. Multiscale Structure, Interfacial Cohesion, Adsorbed Layers, and Thermodynamics in Dense Polymer-Nanoparticle Mixtures. *Physical Review Letters* **107**, 225504, doi:10.1103/PhysRevLett.107.225504 (2011).
118 Chen, H. *et al.* Blood-clotting-inspired reversible polymer–colloid composite assembly in flow. *Nature Communications* **4**, 1333, doi:10.1038/ncomms2326 (2013).

CHAPTER 2.

FABRICATION AND CHARACTERIZATION OF INORGANIC 3D EPITAXIAL MESO/NANOSTRUCTURES

2.1 Introduction

Development of a material possessing the low thermal conductivity and the high electrical conductivity at the same time has remained a huge challenge in a variety of fields including thermoelectric energy generation, thermal switching device, and power electronics because these two properties are highly interdependent with each other. To tackle this issue, reducing the dimensions of existing materials down to nanoscales in a controlled manner has been widely attempted to decouple these properties. This chapter explores previously reported nanostructuring approaches and then introduces our novel strategy based on the realization of inorganic single crystal 3D meso/nanostructures, which is distinctive from various earlier works. Then, we move onto the discussion of our experimental results on the fabrication and characterization of these structures made of three different inorganic materials.

2.1.1 Background

Exploiting renewable and eco-friendly energy sources has been the critical issue all around the world over the last decades[1]. This is due to the limited amount of the carbon-based fossil fuels such as coal, petroleum, and natural gas that are essential for our daily lives. In addition, they have detrimental effects on the environment by leaving a vast amount of CO_2, NO_2, and NO_x pollutants after combusting with oxygen. Among diverse approaches to figure this out, people have been paying attention to utilization of waste heat at very high temperature, for example, several hundred degrees Celsius, which is generally produced at gas exhaust and combustion engine in automobiles[2,3] or during general industrial processes[4]. In this regard, it is of importance to find an appropriate way to harvest this waste heat, and then covert it back to usable energy sources.

Thermoelectric energy harvesting is a promising technology for converting waste heat to usable energy[4]. The fundamental principle lying behind thermoelectric conversion is so called Seebeck effect, which is illustrated in **Figure 2.1a**[5]. If there is a temperature difference between

both ends of a material, the electric potential is generated between both. The Seebeck effect can be explained by following equation,

$$S = \frac{\Delta V}{\Delta T}$$

where S, ΔV, and ΔT denote the Seebeck coefficient, generated electric potential, and temperature difference between two ends. The larger ΔV under a given ΔT is, the higher the electricity generates. Utilizing the opposite mechanism, which is Peltier effect[5], the temperature of a side of a device could be cooled in a well-controlled manner (**Figure 2.1b**). Heat pumps for refrigerators and cooling modules in vehicles are the representative examples that could potentially compete with 1/3-hp compressor technology[6].

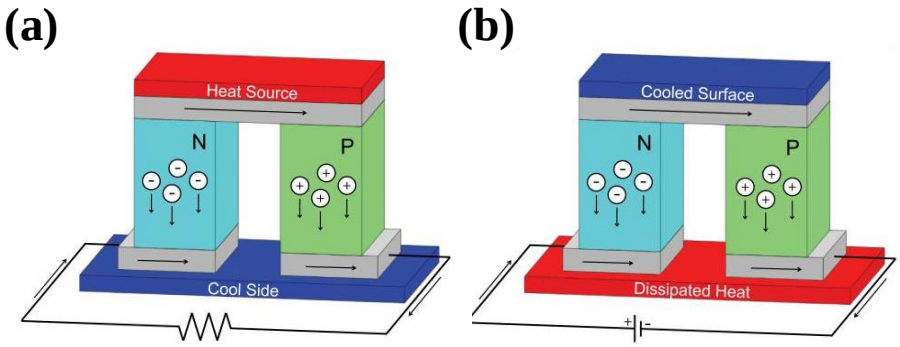

Figure 2.1 – Schematic diagrams of (a) thermoelectric power generator and (b) thermoelectric cooler. Adapted from ref. 5.

Status of the thermoelectric energy conversion are still far from the commercialization even with the state-of-art thermoelectric lab-scale advancement[1]. The main challenge is to exploit new materials with high thermoelectric performances[7], which emphasizes the importance of materials from a scientific point of view. Efficiency of a thermoelectric material is proportional to dimensionless thermoelectric figure of merit (zT):

$$zT = \frac{S^2 \sigma_{el}}{\Lambda_{el} + \Lambda_{ph}} T$$

where S is the Seebeck coefficient, σ_{el} is the electrical conductivity, Λ_{el} and Λ_{ph} are the electronic thermal conductivity and lattice thermal conductivity, respectively, and T is the absolute temperature. Thermoelectric zT has no upper limit. As the zT becomes infinity, the efficiency

converges to the Carnot efficiency. **Figure 2.2** represents plots of the efficiency of each zT (from 1 to infinity) against hot side temperature[8]. For comparison, those of other energy conversion systems utilizing geothermal, solar, coal, and nuclear powers are plotted.

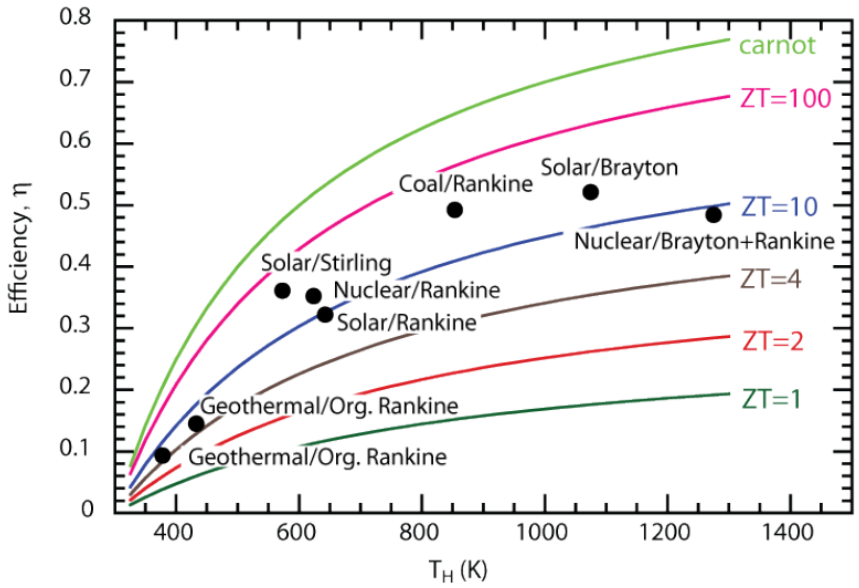

Figure 2.2 – Efficiency plots as a function of T_H, heat source temperature for different zT values. The efficiency of other energy sources and engine cycles are also included for comparison. Adapted from ref. 8.

To use thermoelectric generators in practice, it is reported that a zT of at least 3 is required to compete with the conventional power generation or cooling systems[1]. In spite of the numerous efforts to achieve this zT, the highest zT had remained ~1 before the nanostructures has been introduced to thermoelectric applications in the 1990s[9]. This stagnancy stems from the interdependency among three properties that consist of thermoelectric figure of merit: electrical conductivity, thermal conductivity, and Seebeck coefficient[4]. As evidenced in the equation above, the high zT can be achieved when the electrical conductivity and the Seebeck coefficient are high, still keeping the thermal conductivity as low as possible. However, for instance, if we intend to increase the electrical conductivity of a material, this leads to increasing thermal conductivity and decreasing Seebeck coefficient, resulting in few differences in the final zT. This interdependent relationship among three parameters are well depicted in **Figure 2.3**[4]. In principle, maximum zT can be achieved using semi-conductors or semi-metals who possess moderate charge carrier concentrations between 10^{19} and 10^{21} cm^{-3} depending on the material system. This falls in between typical metals and semi-conductors[4].

2.1.2 Nanostructuring strategy

To achieve a higher zT beyond 3, thermoelectric materials have been investigated in three different ways. The first one is to design new atomic composition solid-solutions which have the desired properties[4]. The key in this strategy is that these materials have very complex crystal structures enabled by adding substructures or disorders into Zintl compounds, skutterudites and clathrates, which can exhibit a low lattice thermal conductivity[4]. The second one is to employ anisotropic single crystals that exhibiting high electrical conductivity and ultralow thermal conductivity along specific crystallographic orientations[10,11]. Utilizing these materials, Zhao, et al. enhanced zT up to 2.6 ± 0.3 at 923 K. The last one is to modify the dimension of pre-existing thermoelectric candidates down to nanometer scales[1,7,9,12-15]. The nanostructure strategy could be divided into four branches: i) nanograined bulk composites, ii) epitaxial multilayered superlattices, iii) one-dimensional (1D) nanostructures, and iv) 2D or 3D porous structures. We discuss the fundamental principles lying behind the nanostructure strategy and then introduce some important works.

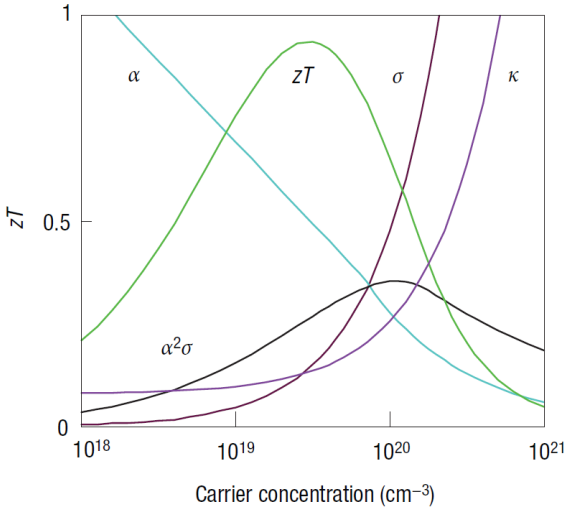

Figure 2.3 – Typical plots of thermoelectric properties and zT for insulators, semiconductors, and metals. The vertical axis indicates a thermal conductivity (κ) from 0 to 10 W m^{-1} K^{-1}, Seebeck coefficient (α) from 0 to 500 μV K^{-1}, and electrical conductivity (σ) from 0 to 5 x 10^5 S m^{-1}. The horizontal axis indicates the carrier concentration of (10^{18} ~ 10^{21} cm^{-3}). Adapted from ref. 4.

Underlying principle

L. D. Hicks and M. S. Dresselhaus reported the theoretical work on the effect of reduced dimensionality on thermoelectric performance of materials from the perspective of quantum

mechanics in the early 1990s[16,17]. Fundamental idea was that tailoring materials at the nanoscale could separate the thermal and electrical conductivities, resulting in a higher efficiency. Especially for semiconductors or semi-metals, thermal conductivity is governed by two primary heat transport carriers, electron (or hole) and phonon. It is possible to decouple the lattice thermal conductivity from the electronic thermal conductivity. The nanostructure approach stems from focusing this feature. Using nanostructures, numerous attempts have been made to reduce the lattice thermal conductivity as much as possible without affecting the electrical conductivity[7].

Phonon transport in the nanoscale materials is well described in the references[18,19]. The lattice thermal conductivity is determined by the phonon transport in solid states. In bulk materials, phonons are scattered by multiple processes that impede phonon movement and hence limit the lattice thermal conductivity, such as phonon-phonon Umklapp scattering, phonon-point defect scattering, and phonon-grain boundary scattering[18]. The scattering rate of each process can be expressed by Matthiessen's rule and Klemens's derivation as follows[18,20]:

$$\frac{1}{\tau} = \frac{1}{\tau_U} + \frac{1}{\tau_d} + \frac{1}{\tau_{gb}} + \cdots$$

$$\frac{1}{\tau_U} = A\omega^2 T^{\xi}\, exp\left(-\frac{B}{T}\right)$$

$$\frac{1}{\tau_d} = V_a C_i \left(\frac{m_i - m_{ave}}{m_{ave}}\right)^2 \frac{\omega^4}{4\pi v^3}$$

$$\frac{1}{\tau_{gb}} = \frac{v_s}{d}$$

where τ_U, τ_d, and τ_{gb} denote Umklapp scattering time, point defect scattering time, and grain boundary scattering time, respectively. d and v_s indicate grain size and phonon speed, respectively. Umklapp scattering originates from the anharmonicity after three phonons collisions, which is temperature dependent[18]. The other processes, which are temperature independent, are caused by defective microstructures inside the materials.

In nanoscale materials, one more scattering process take place: phonon-surface boundary scattering[18]. When the feature size of the material is reduced to the nanoscale dimension (film thickness and/or pitch of holes) which is comparable to or smaller than the phonon mean free path

(MFP), phonon transport is limited by the surface boundary scattering and intrinsic scattering processes. In other words, at a small enough feature size, the phonon transport mechanism would depend on the specific geometry of the structure and would not be the same as in the bulk[18,21]. Therefore, the total scattering rate can be rewritten as

$$\frac{1}{\tau} = \frac{1}{\tau_U} + \frac{1}{\tau_d} + \frac{1}{\tau_{gb}} + \frac{1}{\tau_{sb}}$$

$$\frac{1}{\tau_{sb}} = \frac{v_s}{d_{sb}}$$

where τ_{sb} and d_{sb} denote the surface boundary scattering time and the feature size of the surface boundary, respectively. If the boundary scattering effects become predominant, quasi-ballistic or ballistic phonon transports can be observed. This phenomenon is not explained by classical effective medium theory but by sub-continuum transport models[21].

Further reduction in the thermal conductivity which cannot be described by ballistic transport theory any more could result in adopting the wave-like phonon approaches[18]. In this theory, a reduction of phonon group velocity, a change in phonon dispersion curve, the coherent phonon scattering, and phononic band gap opening have been considered the main cause of the very low thermal conductivity.

Nanograined bulk composites

Nanograined bulk composites refer to a bulk heterostrutured material consisting of a host matrix uniformly surrounding nanoparticles inside[7]. Due to the embedded nanoparticles, so called nanograins, whose feature size is smaller than phonon MFP whereas bigger that the electron MFP, phonons are strongly scattered by the interfaces rather than electrons, we could expect a net increase in zT. The nanocomposite concept has been identified as a useful strategy in various systems such as p-type $Bi_xSb_{2-x}Te_3$[22,23], n-type $Si_{80}Ge_{20}$[24], and p-type $Si_{80}Ge_{20}$[25]. They are fabricated by a ball milling method in which raw component elements (Bi, Te, Sb, Si, and Ge) are pulverized into nanoparticles, followed by a hot-pressing method where the resulting nanopowder mixtures are hot pressed at specific temperature and pressure.

Another method to fabricate nanograined bulk composites is to utilize thermal processing techniques where a metastable solid solution of different elements can be made to undergo

spinodal decomposition or nucleation and growth mechanisms to create nanoscale precipitates[26]. Based on this methodology, in 2012, the high-performance bulk thermoelectrics with all-scale hierarchical micro/nanostructures were reported as shown in **Figure 2.4**[27]. They achieved a high zT of 2.2 in a Na-doped PbTe/SrTe system at 915 K fabricated by powder processing and spark plasma sintering methods. By combining i) atomic-scale lattice disorders from alloy doping, ii) nanoscale endotaxial precipitates, and iii) microscale grain boundaries, the reduction in the lattice thermal conductivity was maximized[26].

This concept has been applied to PbSe and PbS systems afterwards[15,28-33]. Incorporation of 12 % PbS nanograins into n-type PbSe matrix created additional phonon scattering that leads to overall ~ 35 % reduction of the lattice thermal conductivity[28]. They achieved zT values to the level of 1.3 ~ 1.5 at 900 K. In the case of PbS, the addition of nanocrystal Bi_2S_3 into n- or p-type PbS matrices induced additional scattering, resulting in ~ 30 % reduction of the lattice thermal conductivity[29]. The zT values were 1.2 and 1.1 for p- and n-type PbS, respectively.

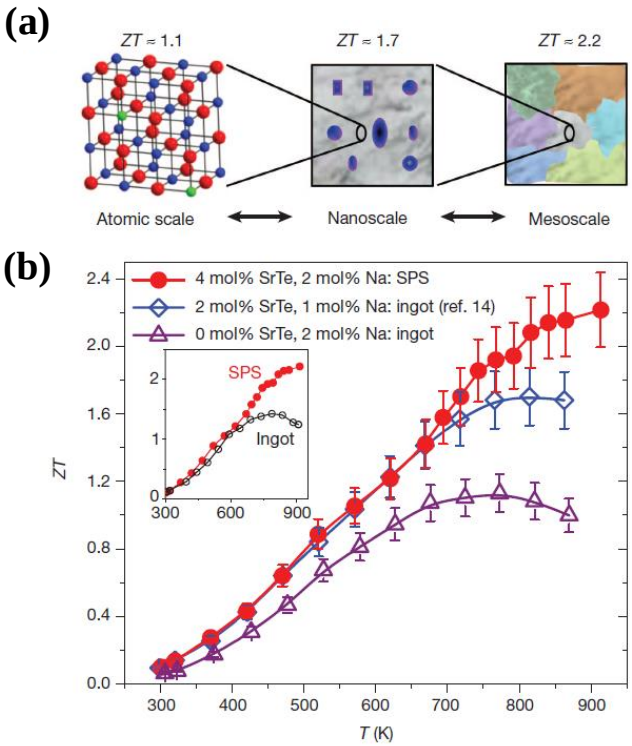

Figure 2.4 – All-length-scale hierarchy thermoelectric materials. (a) Schematic diagram of the atomic scale (dopants), the nanoscale (nanocrystals), and the mesoscale (grain boundaries) phonon scattering sites. (b) ZT as a function of temperature for ingots of Na-doped PbTe/SrTe system. They achieved a high-reported zT value of 2.2 at 915 K. Adapted from ref. 27.

Layered crystals and epitaxial superlattices

The formation of layered crystals or superlattices of alternating materials is one of the most widely investigated method of fabricating a controlled nanostructure for electrical and optical devices[12]. These structures have been also considered potential thermoelectric candidates, including layered WSe_2 crystals[34], $PbTe/PbSe_xTe_{1-x}$[35], Si/Ge[36], $GaAs/Al_xGa_{1-x}As$[37], and Bi_2Te_3/Sb_2Te_3[38]. The impacts of the superlattice structure on the reduction of the lattice thermal conductivity have been explained by diverse effects such as modification of the phonon dispersion and phonon localization (e.g. zone folding and band gap formation)[39-42], diffuse or specular scattering of phonons at interfaces due to acoustic mismatch[43] and scattering of phonons at defects[36]. In addition, the epitaxial superlattices and layered crystals were reported to conserve the electron transport along the interfaces between layers (**Figure 2.5a**)[14].

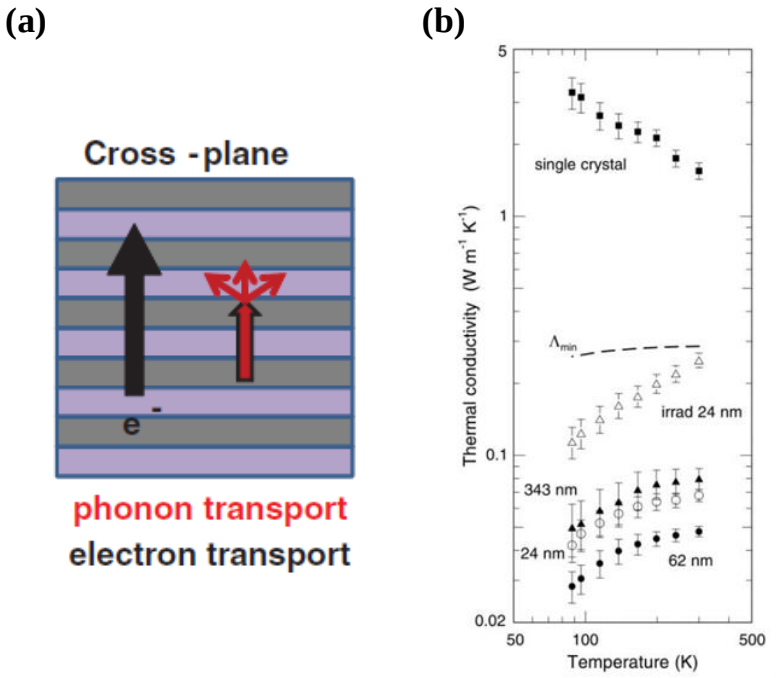

Figure 2.5 – (a) Phonon scattering is enhanced while electron conduction is preserved along the cross-plane direction in superlattices. Adapted from ref. 14. (b) Ultra-low thermal conductivity of WSe_2 layered crystals. The lowest thermal conductivity at 300 K is 0.048 W m^{-1} K^{-1}, 30 x smaller than the cross-plane thermal conductivity of a single-crystal WSe_2 and a factor of 6 smaller than the predicted minimum thermal conductivity. Adapted from ref. 34.

In 2007, an ultralow cross-plane lattice thermal conductivity, 0.05 W m^{-1} K^{-1} at room temperature was reported in the WSe_2 layered crystals, as depicted in **Figure 2.5b**[34]. This value is 30 times smaller than the c-axis thermal conductivity of single crystal of WSe_2 and a factor of 6

smaller than the predicted minimum value of this material. The ultralow thermal conductivity was ascribed to the localization of lattice vibrations induced by the random stacking of 2D crystalline WSe_2 sheets, where disordered structure was induced by ion bombardment.

Meanwhile, a significant reduction of lattice thermal conductivity has been also reported on superlattice system comprising $PbTe/PbTe_{0.75}Se_{0.25}$ layers[35]. The thermal conductivity was 0.5 W m^{-1} K^{-1} at 300 K, approximately half the alloy value. For a 3 nm period Si/Ge superlattice in the absence of dislocation, the thermal conductivity was reported to be 3 W m^{-1} K^{-1}, 40 % lower than that of $Si_{0.8}Ge_{0.2}$ alloy[36]. The AlAs/GaAs superlattice consisting of 3 monolayers by 3 monolayers, exhibited 3.1 W m^{-1} K^{-1}, which is as much as 4 times reduced value compared to thermal conductivity of a normal $Al_{0.5}Ga_{0.5}As$ alloy[37]. In p-type Bi_2Te_3/Sb_2Te_3 superlattice (1 nm/ 5 nm) grown by MOCVD, a reduction of the thermal conductivity by a factor of 2.2 in the cross-plane direction was achieved[44]. The electrical conductivity is hardly affected by the multilayered structures. **Table 2.1** summarizes thermoelectric properties of various superlattice systems[14].

Table 2.1 – Summary of the thermoelectric properties of epitaxial multilayers and superlattice structures measured along cross-plane direction in most cases[14].

Material system	**Λ (W m^{-1} K^{-1})**	**zT**
p-type Bi_2Te_3/Sb_2Te_3 MOCVD	0.22	2.4 (RT)
n-type Pb(Se,Te)/PbTe MBE	0.62 (RT) 3.3 (300 °C)	1.3 (RT) 3.4 (300 °C)
Ge/Si MBE	0.9	-
n-type $Bi_2Te_3/Bi_2(Te_xSe_{1-x})_3$ MBE	1.4	0.75 (RT)
(Zr,W)N/ScN sputtering	2.1	-
n-type (In,Ga,Al)As/ErAs MBE	5.9 (RT) 1.3 (530 °C)	0.07 (RT) 1.1 (530 °C)

One-dimensional (1D) nanostructures

Application of 1D nanowires was triggered by a theoretical prediction in which the electron confinement in a single moving direction and small electron effective masses would enhance the density of states, resulting in the increase of the Seebeck coefficient[16,17]. The lattice thermal conductivity could be reduced due to increased phonon scattering at the nanowire surface.

However, a dramatic enhancement of the power factor in nanowires has not been observed so far. **Figure 2.6** represents two representative reports on evaluating thermoelectric zT of Si nanowire systems[44,45]. For 1D nanowires, most studies have targeted Si in particular. Reduction of the lattice thermal conductivity in 1D nanowires was reported in several studies[44-52]. In 2008, zT of 1.2 at 350 K was reported using Si nanowire arrays with 20 nm in diameter and 7×10^{19} cm^{-3} of doping level[44]. Tuning diameter and doping concentration, Boukai, et al. reduced the lattice thermal conductivity dramatically and maintain the electrical conduction. Single crystal Si nanowires fabricated by vapor-liquid-solid (VLS) mechanism demonstrated a dramatic decrease of thermal conductivity as a function of diameter[48]. This is due to that in principle Si has larger phonon MFP and broader MFP spectra ranging from 10 nms ~ 100 μms[7,53]. Later, it was reported that lattice thermal conductivity of single crystal Si nanowires (50 nm in diameter) further decreased down to 1 W m^{-1} K^{-1}, close to the amorphous limit of Si, by roughening the nanowires surfaces[45,47]. Si/Ge alloy nanowires showed decreased thermal conductivity as well due to two kinds of scatterings: i) phonon-alloy scattering at high frequency and ii) phonon-surface scattering at low frequency[46,52].

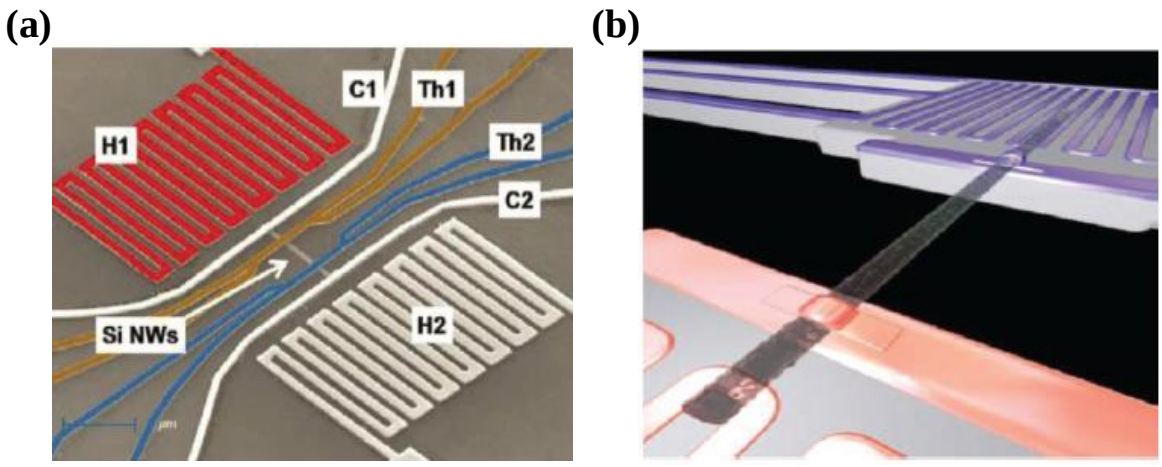

Figure 2.6 – (a) Si nanowire (20 nm in diameter) achieved a zT of 1.2 at 350 K. Adapted from ref. 44. (b) Rough-surface Si nanowire (50 nm in diameter) exhibited amorphous limit thermal conductivity of 1 W m^{-1} K^{-1} with a zT of 0.6 at 300 K. Adapted from ref. 45.

In the case of Bi_2Te_3, however, as diffusive phonon MFP is very small, any effects on the reduction of thermal conductivity in 50 nm nanowires have not been observed[49]. For PbTe nanowires having a diameter of ~ 180 nm, the thermal conductivity decreased to a half of the bulk value[51]. The polycrystalline Bi nanowires exhibited a reduced thermal conductivity which originated from the grain boundary scattering as well as the surface scattering[50].

2.1.3 2D and 3D porous structures

Utilization of 2D and 3D porous structures containing periodic features on thermal phonon length scale is another promising way to reduce lattice thermal conductivity. These structures have been utilized first as so-called phononic crystals that consist of periodic arrays of materials with dissimilar acoustic properties (density and sound speed) to control the propagation of sound waves in the crystals. Sound waves typically have frequencies ranging from kHz to GHz[54-58]. Since they have quite long wavelength scale (cm ~ sub-μm) compared to thermal phonon waves, it is relatively easy to fabricate periodic phononic crystals by diverse patterning processes[54]. Once phononic crystals meet the Bragg reflection along a certain orientation, sound waves cannot propagate anymore inside the crystals and hence transfer zero net energy, which happens similarly in photonic crystals[59]. In other words, multiple acoustic waves interfere destructively, thereby generating standing waves at the zone boundary.

Compared to sound waves, thermal phonons that deliver heat in the solids have much higher frequencies up to several THz[21,54]. As the corresponding wavelengths are also very short (10 ~ 20 nm), it is very hard to realize 3D porous structures containing the features on this scale. In almost meso/nanostructured materials with feature sizes of 50 ~ 500 nm, phonon transport is usually decribed by particle-like physics such as diffusive, quasi-ballistic and ballistic, which is incoherent[60-62]. At this regime, phonon dispersion remains the same as the bulk[63]. Once the feature size goes down further below 20 nm and becomes comparable to thermal phonon wavelength scales, phonons start to show wave-like behavior. In this regime, one could observe coherent phonon scattering and phononic band gap which are known to decrease lattice thermal conductively dramatically that cannot be explained by particle phonon transport theory. We focus on thermal phonon length scales, not acoustic ones.

Simulation works

In 2008, Grossman et al. reported lattice thermal conductivity of single crystal Si containing 3D periodic arrays of ~ 1 nm holes with inter-hole spacing of ~ 1 nm using molecular dynamics (MD) calculation[64]. Thermal conductivity was nearly the same as that of amorphous silicon. Electrical conductivity could decrease by a factor of 2 ~ 4, depending on doping levels due to quantum confinement effect. Seebeck coefficient yielded a 2-fold increase for carrier concentrations less than 2×10^{19} cm^{-3}. Another simulation work dealt with Si 3D porous crystals

containing spherical pores in 2014[65]. Using equilibrium MD, namely Green-Kubo method, they found that thermal conductivity decreases as porosity increases. They argued that when the porosity increased up to 90 %, the thermal conductivity decreased dramatically down to 0.022 W $m^{-1} K^{1}$, only 0.01% bulk Si. They attributed low thermal conductivity to localization of phonons. The strain effects on the thermal conductivity of graphene nanoribbons were studied using MD simulations[63,66]. Thermal conductivity of graphene was very sensitive to tensile strain. Some of strained graphene structures revealed a higher thermal conductivity than that in the graphene with no strain. They argued changing the strain field and edge roughness could engineer the phonon transport in the graphene. Recently, Puurtinen, et al. have calculated the dependence of thermal conductivity on the lattice period in SiN 2D porous crystals with hole-array[67]. They insisted that both density of states and average group velocity were strongly affected by the periodic structuring. Depending on the size of the period, they found that the density of states and average group velocity varied in a different manner.

Experimental works

Thermal transport investigation on 3D porous mesostructures was first reported in 2013[68]. They fabricated polycrystalline Si inverse opals, with periodicities and shell thicknesses of 420 ~ 900 and 18 ~ 38 nm respectively using chemical vapor deposition. The thermal conductivities of the Si inverse opals were measured using 3ω method. The thermal conductivities were relatively low, 0.6 ~ 1.4 W $m^{-1} K^{-1}$ at 300 K due to macroscopic bending of heat flow lines in the structure. They exhibit an anomalous $\sim T^{1.8}$ dependence at low temperatures, different from $\sim T^{3}$ behavior of bulk polycrystalline silicon, as depicted in **Figure 2.7**. Comparing it with modeling, they showed this anomaly originated from the coherent phonon reflections in the inter-grain region.

Recently, it has been reported that a metallic polycrystalline 3D mesostructures demonstrated quasi-ballistic transport at small feature scale as depicted in **Figure 2.8**[62]. The transition from diffusive to quasi-ballistic conduction took place when the feature size in Cu inverse opals was reduced from ~ 230 nm to ~23 nm. Thermal conductivity decreased by more than 57 % due to increased surface scattering. In contrast, Ni inverse opals exhibited diffusive-like behavior and a constant thermal conductivity over this size regime. Discrepancies between Cu and Ni were handled by a model considering the inverse opal geometry, surface scattering, and grain boundaries.

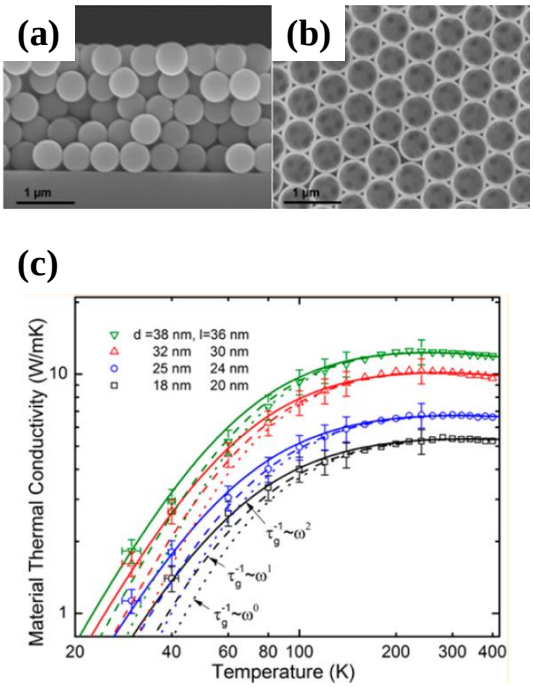

Figure 2.7 – Coherent phonon transport phenomena in polycrystalline Si 3D PnC. (a, b) SEM images of silica colloidal crystal and Si inverse opal respectively. (c) The material thermal conductivities vary as ~ $T^{1.8}$ at low temperatures. Quadratic frequency dependence in the phonon grain boundary scattering rate indicates coherent scattering in the inter-grain region. Adapted from ref. 68.

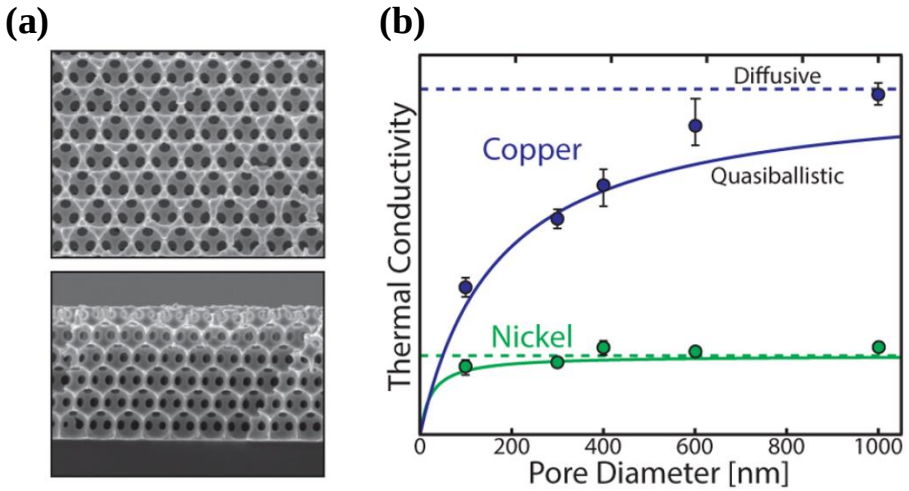

Figure 2.8 – Quasi-ballistic phonon transport study on Cu and Ni 3D inverse opals. (a) SEM images of Cu inverse opals. (b) Cu and Ni exhibit different phonon transport behavior with decreasing pore diameter: the former shows quasi-ballistic while the latter yet remains diffusive. At the same feature size, surface boundary scattering effect of Cu is much larger than that of Ni. Adapted from ref. 62.

Thermal transports of various 2D meso/nanostructured crystals were also reported. In 2010, Yu, et al. have investigated thermal conductivity of nanomesh made of a semiconductor[69]. The mesh structures were patterned with periodic spacing that are comparable to, or shorter than, the phonon MFP (~ 25 nm) using electron beam lithography, as shown in **Figure 2.9**. The nanomesh structure (1.9 W $m^{-1} K^{-1}$) exhibited lower thermal conductivity than nanowire arrays (2.9 W $m^{-1} K^{-1}$). They ascribed this to the change of phonon dispersion curves induced by coherent Bragg reflection of phonon waves. Bulk-like electrical conductivity was observed. Additionally, single crystal Si 2D porous structures with sub-micrometer geometries were fabricated by conventional micro-fabrication processes[70]. Thermal conductivity of 2D structures, 6.8 W $m^{-1} K^{-1}$, was an order of magnitude smaller than that of bulk Si, 148 W $m^{-1} K^{-1}$. This value is much smaller than that predicted by considering boundary scattering at the interfaces only. They revealed the significant reduction of thermal conductivity was attributed to the altered phonon dispersion in which phonon group velocities were greatly reduced.

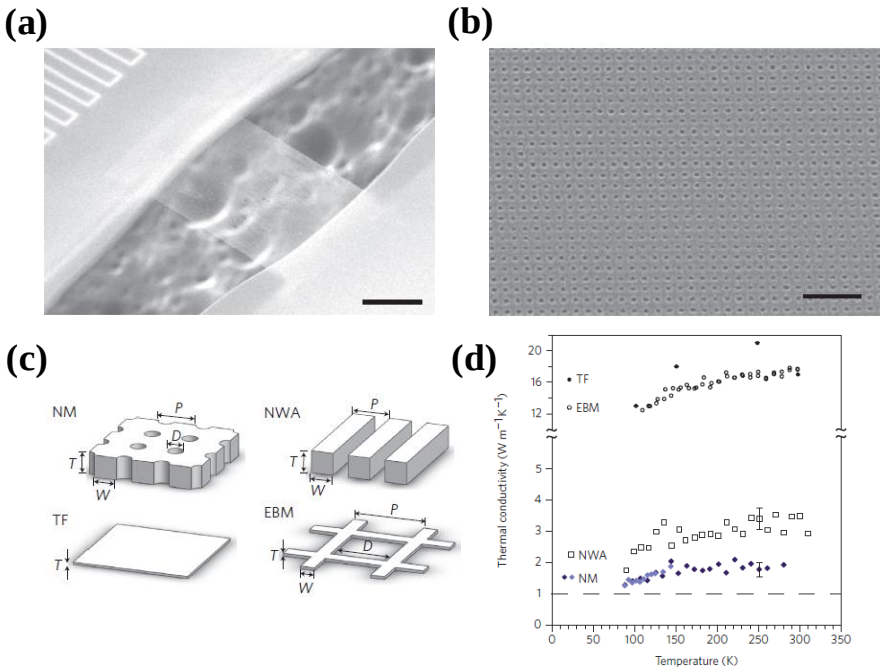

Figure 2.9 – 2D Si nanomesh (NM) phononic crystal. (a) SEM image of NM suspended between two membranes. Scale bar, 2 mm. (b) SEM image of NM with a uniform square-lattice matrix of cylindrical holes. Scale bar, 200 nm. (c) Geometry of NM film and three reference systems: dense thin film, larger feature-size mesh fabricated by e-beam lithography, and nanowire arrays. (d) NM shows thermal conductivity of 1.9 W $m^{-1} K^{-1}$ at 300 K, lower than nanowire array. Adapted from ref. 69.

2.1.4 Statement of objectives for Chapters 2, 3, and 4

As described previously, various approaches have been applied to achieve low thermal conductivity and high electrical conductivity simultaneously, but each has its own critical drawback. New solid solutions such as Zintl compounds, skutterudites and clathrates[4] are based on very complicated crystal structures and atomic compositions such as ternary, quaternary or even higher, which make it hard to control and fabricate. Although anisotropic single crystals made of SnSe or hole-doped SnS showed excellent performance[10,11], it costs too much to utilize them for practical purposes. Nanograined bulk composites are comprised of toxic and rare materials. Furthermore, fabrication is entirely based on the traditional bulk processes utilizing ball-milling, hot pressing, and thermal treatment, which require huge time and efforts. Fabrication of epitaxial superlattices is inefficient since molecular beam epitaxy and metal-organic chemical vapor deposition are costly and time-consuming. For 1D nanowires, it is very tricky to handle individual nanowires in a well-controlled manner.

In this context, we developed a novel strategy to achieve low thermal conductivity and high electrical conductivity at the same time in one material. Through simple, cost-effective, and time-saving processes comprised of colloidal templating, electrodeposition, and etching, we have successfully fabricated epitaxial 3D meso/nanostructures. Fundamental physics lying behind this approach is to reduce lattice thermal conductivity by surface boundary phonon scatterings and to maintain electrical conductivity through single crystalline microstructures. In the remainder of **Chapter 2**, we describe the fabrication and characterization of various kinds of materials, Bi_2Te_3, PbS and Fe_3O_4, which possess 3D architectures with high crystal quality. In following **Chapters 3** and **4**, we discuss thermal and electrical transport properties of these materials, especially for Fe_3O_4 case, respectively.

2.2 Experimental Methods

2.2.1 Synthesis of Bi_2Te_3 3D meso/nanostructures

For the fabrication of Bi_2Te_3 3D meso/nanostructures, surface of the electron-beam evaporated Au (100 nm)/Cr (3 nm)/glass substrate was cleaned with piranha solution and then functionalized with thiol molecules to give Au surface hydrophilicity. Using the vertical deposition

technique, where the convective colloidal self-assembly takes place, the sulfate-polystyrene spherical particles were assembled on the Au surface to form the colloidal crystals. The voids inside the colloidal crystals were filled with Bi_2Te_3 by pulsed electrochemical deposition in an acidic bath at room temperature. The bath was comprised of 7.5 mM $Bi(NO_3)_3 \cdot 5H_2O$, 10 mM TeO_2, 1 M nitric acid, 80 mg L^{-1} sodium lignosulfonate, and Type 1 water (18.2 MΩ cm). The pulsed electrodeposition was performed by alternately applying -0.058 V vs. Ag/AgCl for 0.1 s (on state) and 0.1 V for 5.0 s (off state) for multiple cycles. The polystyrene templates were removed by tetrahydrofuran (THF) at elevated temperatures (40 ~ 50°C) for 3 ~ 7 days depending on the polystyrene size.

2.2.2 Synthesis of epitaxial PbS systems

Other than Bi_2Te_3 which requires van der Waals epitaxy, it is relatively easy to grow a PbS epitaxy because the PbS is an ionic compound having a rock salt structure with a space group of $Fm\bar{3}m$[71,72]. To grow a PbS epitaxial film with electrodeposition, we needed a conductive and epitaxial seed layer whose lattice parameter was similar to that of PbS. We chose the PbS itself as the seed layer material. Prior to growing the seed layer, the surface of the GaAs (100) wafer was cleaned with $NH_4OH : H_2O$ (5 : 1 v/v) solution to remove native oxide layers that inhibit an epitaxy growth. A PbS epitaxial seed layer was grown on a heavily-doped GaAs (100) wafer using chemical bath deposition (CBD). The bath consisted of $SC(NH_2)_2$, $Pb(NO_3)_2$, NaOH and deionized water. Film growth was carried out at 30°C for various periods of time in order to reach the desired film thickness. On the PbS epitaxial seed layer, we have grown the colloidal crystals through the vertical deposition method.

2.2.3 Synthesis of epitaxial Fe_3O_4 3D meso/nanostructures

For the fabrication of epitaxial Fe_3O_4 3D meso/nanostructures, a 100 nm thick epitaxial Au (111) layer was deposited on a Ti (0002)/Al_2O_3 (0006) substrate using electron-beam evaporation method. Fe_3O_4 films were grown on the Au (111) layer with electrochemical deposition where freshly-made electrolytes comprising $Fe_2(SO_4)_3 \cdot xH_2O$, triethanolamine, NaOH, and Type 1 water were used. A platinum plate and an Ag/AgCl (4 M KCl saturated) electrode were employed as the counter electrode and the reference electrode, respectively. At 80°C of the bath temperature, a cathodic potential of -1.018 V vs. Ag/AgCl was imposed on the Au working electrode for several

minutes that varied according to the situations. To grow colloidal crystals on the Au film, we followed the same procedures as the ones used in Bi_2Te_3 synthesis. Depending on the diameter of colloidal particles, incubating condition was slightly modified. Overall procedures are well represented in **Figure 2.10**.

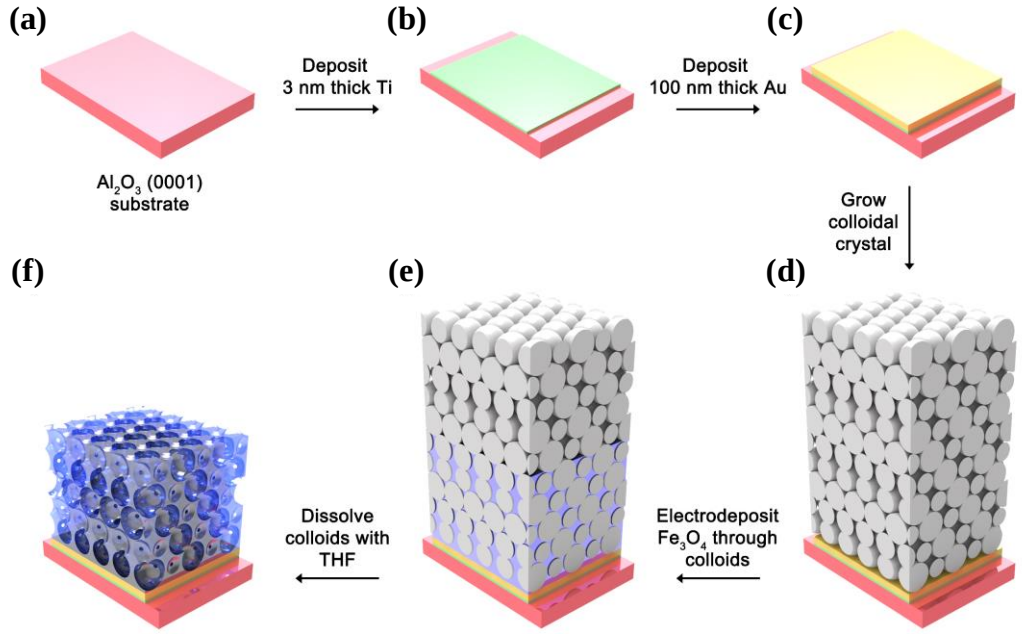

Figure 2.10 – Fabrication process of 3D epitaxial Fe_3O_4 porous structures. (a) Prepare Piranha-cleaned c-Al_2O_3 substrate. (b,c) Deposit 3 nm thick Ti layer followed by 100 nm thick Au layer using electron beam evaporator. Activate Au surface using thiol aqueous solution. (d) Grow polystyrene colloidal crystals through vertical deposition method. (e) Electrodeposit Fe_3O_4 film through the voids inside the colloidal crystals until the target thickness. (f) Dissolve polystyrene particles using THF.

2.2.4 Characterization

Scanning electron microscope (SEM)

We observed the morphologies of the sample by collecting top and cross-section images using field-emission SEM (FESEM; S-4800, Hitachi). Prior to imaging, we coated the sample using an Au-Pd sputter to enhance the imaging resolution.

X-ray diffraction (XRD)

Crystallographic characteristics of the sample were investigated using an XRD (Panalytical X'pert MRD, Phillips) system equipped with a Cu Kα (λ = 0.15418 nm) radiation source. We

performed the 2θ/ω scans over 2θ range of 10 ~ 80° to identify the phases and out-of-plane textures of the sample. Prior to every measurement, we corrected offsets of initial ω and ψ values by performing ω scan, ψ scan, and ω scan sequentially on the substrate peak as a reference. The rocking curves were obtained at fixed 2θ value that corresponds to an out-of-plane orientation of a synthesized film.

To study the in-plane epitaxial relationships, we performed the pole-figure measurements and the azimuthal scans. For the pole-figure measurements, the sample was tilted from ψ = 0° to 87°, and at each ψ, the sample was azimuthally rotated from φ = 0° to 360°. For both tilt and azimuthal movements, data were collected in the continuous mode with 3° intervals. Other than the pole-figure measurements, the azimuthal scans were performed at fixed ψ. Data were collected in the continuous mode during azimuthally rotating the sample from φ = 0° to 360° with 0.3° interval.

Confocal Raman spectroscopy

We acquired Raman spectra of the samples using a Horiba confocal Raman microscope (LabRAM HR 3D) equipped with a 532 nm laser. The laser beam passed through a filter with the optical density of 0.6 and then through a 20x objective lens. The final power of the laser beam reaching the sample was 3.5 mW according to a radiometer. Using 300 g mm^{-1} grating, we collected the data over Raman shift of 0 ~ 1000 cm^{-1} with an exposure time of 120 s. The small power and longer exposure time were selected to avoid excessive heating[73,74].

Energy dispersive spectroscopy (EDS)

Atomic composition of a material, especially for Bi_2Te_3, was determined using an EDS tool attached to the FESEM.

Rutherford backscattering spectrometry (RBS)

We employed RBS technique to obtain the densities of the dense film and porous films with different pore sizes. Using a tandem electrostatic accelerator system (Pelletron, NEC), we impinged 2 MeV $^4He^+$ ions onto the sample loaded in the vacuum chamber at the pressure below 5 x 10^{-5} Torr. The incident, exit and scattering angles were 15°, 15° and 150° respectively. The

beam size and the beam current were 2 mm in diameter and 100 ~ 200 nA. We collected the counts of the backscattered $^4He^+$ ions as a function of the energy distribution.

We used samples still including the polystyrene particles inside, for the sake of clarifying the boundary between Au and Fe spectra. Without the polystyrenes, the Au peak became too broad due to larger roughness, ending up with screening the Fe spectrum and hence making it hard to analyze the data. Prior to measuring Fe_3O_4 sample, we always collected the RBS spectrum of bare Au (100 nm)/Ti (3 nm)/c-sapphire substrate as a reference.

We measured the thickness of film using cross-section SEM images of mechanically-cleaved sample after the RBS measurement. The estimate of root-mean-square (RMS) roughness of the film surface was determined by scanning the surface with surface profilometry (Dektak3ST, Sloan) in which a diamond-tipped stylus is used to measure surface topography. We analyzed the data using a SIMNRA software (Version 7.0, Max-Planck-Institut).

X-ray fluorescence (XRF)

Using an energy dispersive X-ray fluorescence (EDX-7000, Shimadzu), the densities of samples were determined to cross-check the RBS results. A collimated X-ray beam with the diameter of 1 mm was accelerated at a voltage of 50 kV and impinged on samples surrounded in He atmospheres. We collected the intensity (cps μA^{-1}) of characteristic X-rays emitted from elements of each sample as a function of the energy of the emitted photons. The thicknesses of Fe_3O_4, Au, and Ti layers were deduced by quantitatively analyzing the intensity peaks corresponding to the electronic transitions of FeKα centered at 6.40 keV, AuLα at 9.72 keV, and TiKα at 4.50 keV, respectively. The density of Fe_3O_4 was calculated by dividing the thickness determined from the XRF measurement by the thickness determined from the SEM observation on the cross-section of a sample. For estimating the densities of porous samples, we used PS included ones for all cases.

Transmission electron microscopy (TEM)

(by Dr. Yang at Prof. Zuo group)

We prepared cross-sectional TEM samples using a FEI Helios 600i FIB/SEM. The 40 nm porous film was chosen for the TEM observation. Prior to the milling process, we first coated the

target area with carbon, and then a Pt/C protective layer with electron and ion beams sequentially. The Ga^+ ion beam was controlled from 2.3 nA at 30 kV to 7.7 pA at 5 kV for sample thinning, and 5 pA at 1 kV for final polishing. Final sample thickness was about 40 nm.

Bright-field TEM images, selected area electron diffraction (SAED) patterns and high-resolution TEM (HRTEM) images were collected using a JEOL 2100 Cryo TEM equipped with a LaB_6 gun. High-resolution scanning TEM (HRSTEM) images were obtained using an aberration-corrected JEOL 2200FS with a field emission gun. Both were operated at 200 kV.

The orientation and the rotation angle maps were constructed by the scanning electron nanobeam diffraction (SEND) technique and diffraction imaging. Using a convergent electron beam with 3.5 nm in full width half maximum and a slow scan CCD camera, we scanned over the area of 150 nm x 1.0 μm. We acquired diffraction patterns every 10 nm along both the horizontal and vertical directions with an exposure time of 0.3 s for each pattern, winding up with obtaining a total of 1500 points (15 x 100). In SEND experiment, we used 4 times binning (512 x 512 pixels). All patterns were recorded within 20 min. The obtained diffraction patterns were indexed and reconstructed into orientation and rotation angle maps. The rotation angle map was obtained by comparing the rotation angle of each diffraction pattern with a reference diffraction pattern and coloring the angles accordingly.

2.3 Meso/nanostructured Bi_2Te_3 and PbS Systems

2.3.1 Bi_2Te_3 3D meso/nanostructures

Figure 2.11 exhibits the plane-view images of Bi_2Te_3 dense film and 3D porous structures with different pore sizes. The dense film was smooth and dense, and the porous films were conformally grown. As shown in the cross-section images of **Figure 2.12**, the thickness of the dense film and the porous film could be controlled ranging 4 ~ 8 μm without forming any dendrites. The conformal morphology and large thickness are due to i) adding a small amount of a surfactant, sodium lignosulfonate, ii) using a pulsed electrodeposition instead of continuous deposition, and iii) high electrical conductivity of Bi_2Te_3 itself. The combined effects among three factors prevented crystallites from aggregating during film growth and induced uniform electric potential and current density over the entire area[75-77]. The 3D meso/nanostructures were identified as

polycrystalline Bi_2Te_3 (JCPDS 15-0863, tellurobismuthite) from XRD analysis (**Figure 2.13a**). The EDS proved that atomic ratio of Bi to Te was exactly 2:3, indicating that 3D structure is stoichiometric (**Figure 2.13b**).

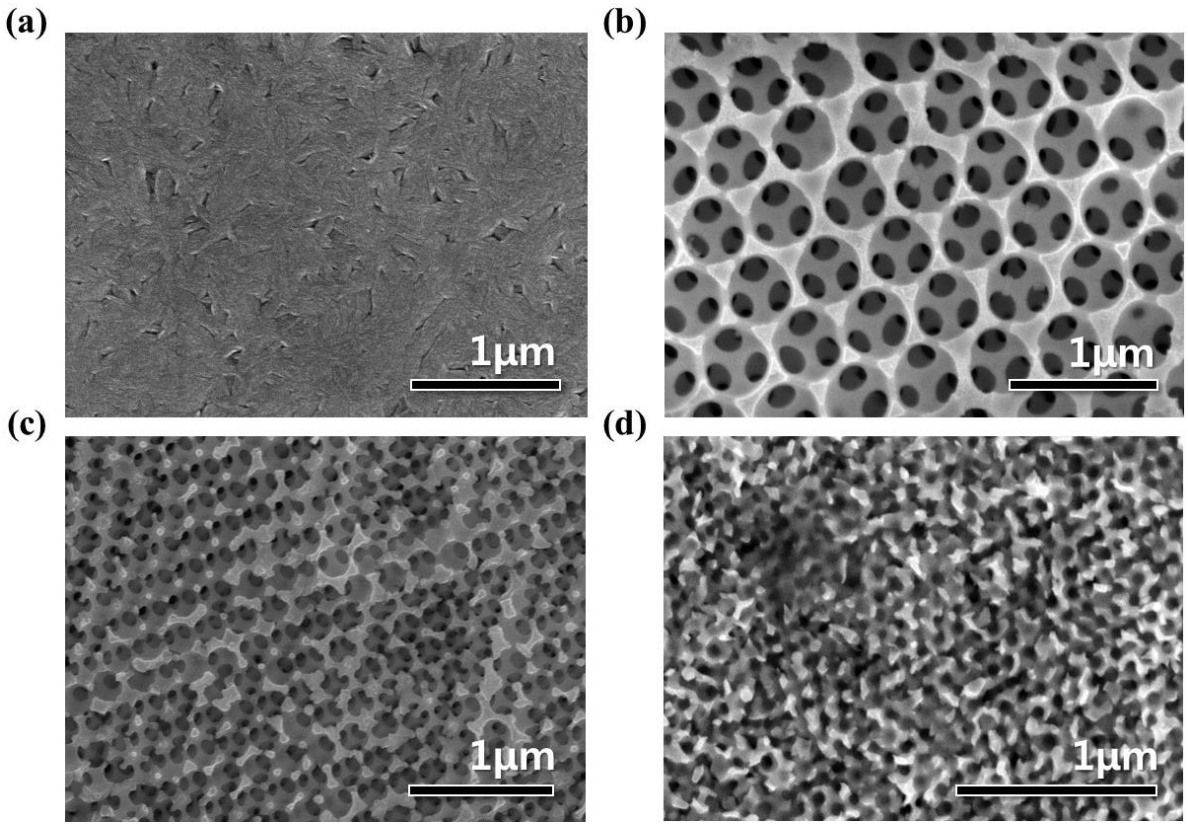

Figure 2.11 – Top-view SEM images of Bi_2Te_3 (a) dense film and 3D porous films with different pore sizes: (b) 500, (c) 200 and (d) 100 nm, respectively.

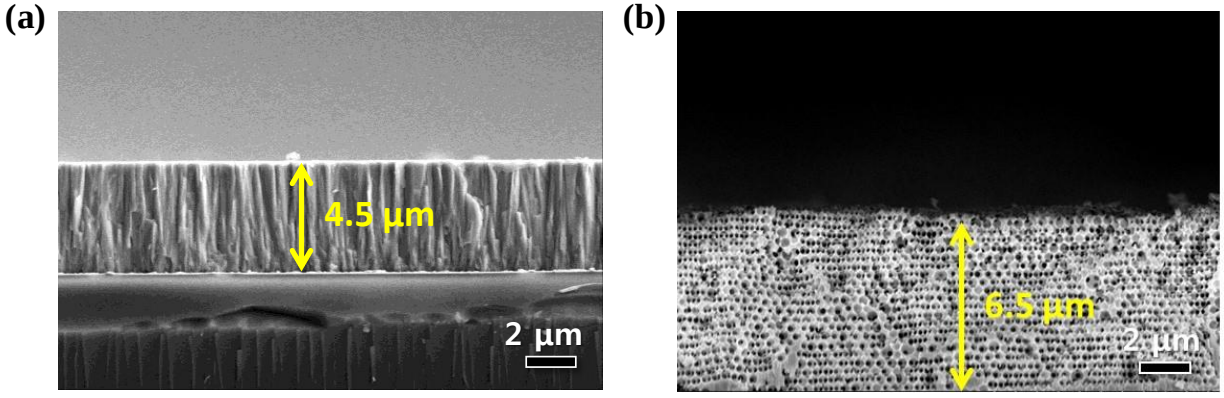

Figure 2.12 – Cross-section SEM images of Bi_2Te_3 (a) dense and (b) 500 nm porous films. Tuning the deposition condition, we could control the thickness, up to 7 µm or higher.

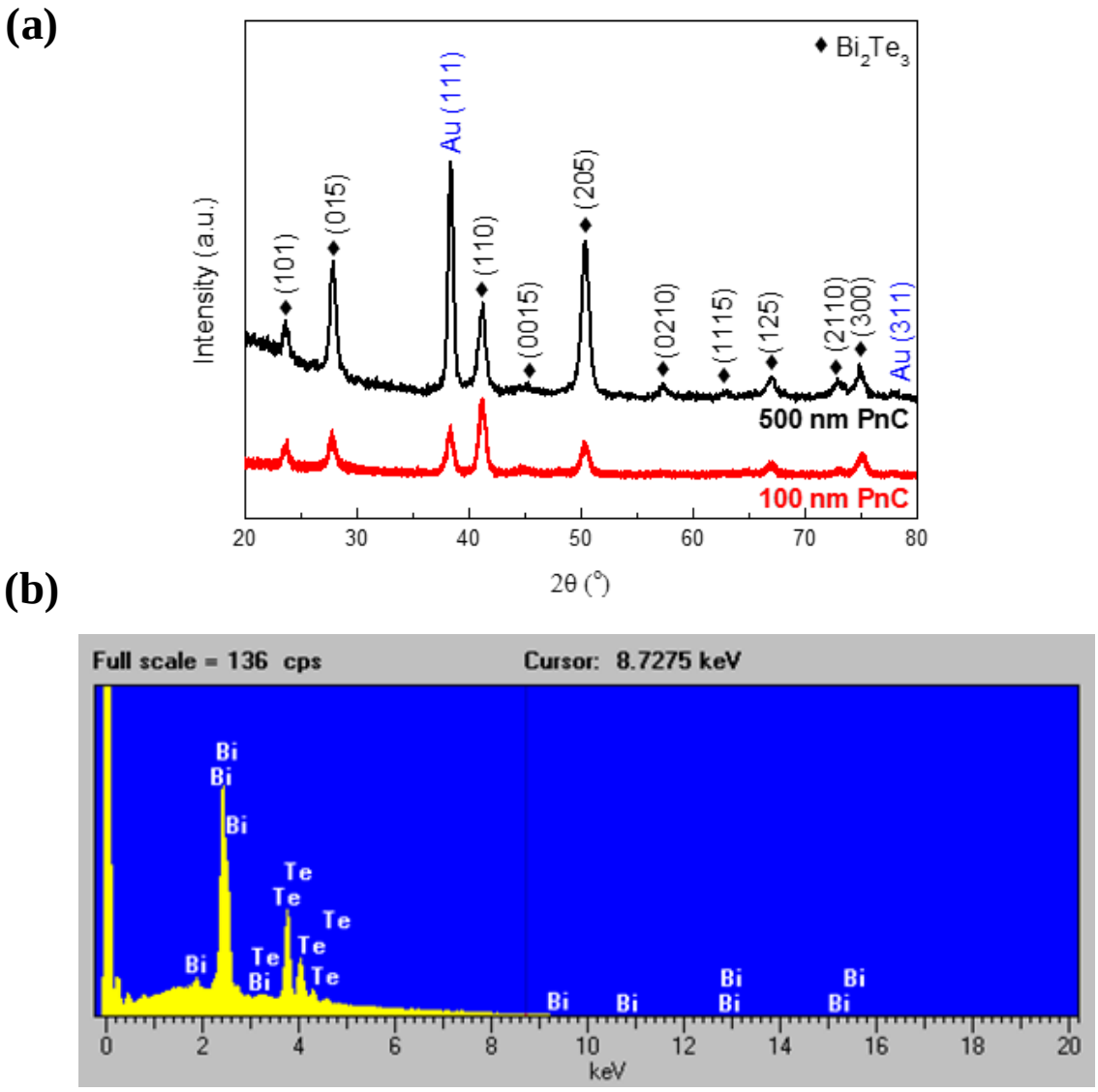

Figure 2.13 – (a) XRD patterns of 3D Bi_2Te_3 meso/nanostructures with 100 and 500 nm pores, respectively. Both are pure Bi_2Te_3 phase. (b) EDS spectrum of 100 nm sample indicates that ratio of Bi to Te is exactly stoichiometric, 2 : 3 within 1.1 % error.

Thermal conductivity of the polycrystalline Bi_2Te_3 dense film was measured by TDTR technique. As a transducer and a thermometer, ~ 80 nm thick Al film was deposited on top surface of the film using sputtering. We measured V_{in} and V_{out} signals as a function of time delay (picosecond ~ nanosecond). We estimated the Al film thickness from the acoustic signal appearing in the very initial stage of the measurement (**Figure 2.14a**). A plot of $-V_{in}/V_{out}$ over the entire range of time delay is demonstrated in **Figure 2.14b**. We fitted the measured data with a unidirectional heat flow model in multilayers film, which is well described in an early report[78], and deduce the

thermal conductivity of 1.49 W m^{-1} K^{-1}. This value is in accordance with previously reported ones[79-81].

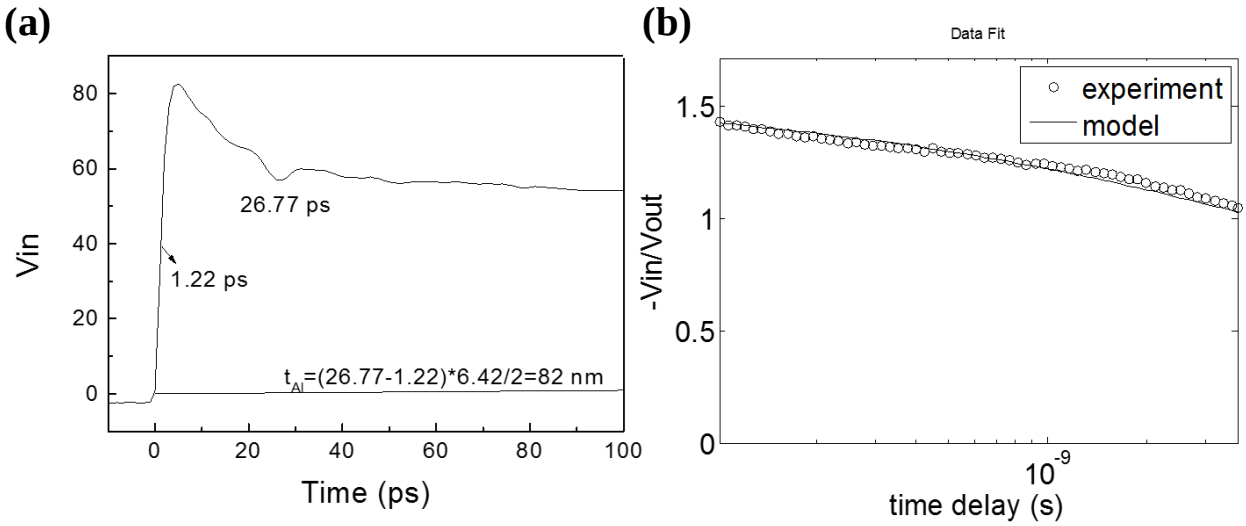

Figure 2.14 – TDTR measurement on the dense Bi_2Te_3 film. (a) Acoustic signal in V_{in} vs. time delay at the very initial time gives an estimate of Al transducer thickness. (b) Plot of $-V_{in}/V_{out}$ against entire range of time delay. 1D heat diffusion model and experimental data agree well.

Note that the epitaxial growth of Bi_2Te_3 with electrodeposition is very tricky. The Bi_2Te_3 has a rhombohedral crystal structure with a space group of $R\bar{3}m$[82,83]. It has a weak Van der Waals bonding along (111) direction, which makes it difficult to add additional atoms along this direction with a conventional electrodeposition technique. To do so, electrochemical atomic layer deposition could be employed to deposit each atomic layer one by one by changing the electrolyte for each layer[84-87], which is time consuming and costly. The maximum obtainable thickness through this way is only 50 ~ 100 nm. Furthermore, it does not guarantee the epitaxy all times. For this reason, the epitaxial growth of Bi_2Te_3 in the previous reports were enabled only by MBE process[83,88].

2.3.2 3D mesostructures on PbS epitaxial film

As shown in **Figure 2.15a**, the overall surface of the seed layer is smooth and dense after enough time of chemical reaction. It is ideal for colloidal crystal growth. When looking into the local region where highly textured pits are located due to insufficient time to be dense, it is observed in **Figure 2.15b** that PbS film exhibits a rectangular-faceted morphology characteristic to [110]-oriented films, with {100}-type facets exposed at 45° to the growth axis (to the surface normal).

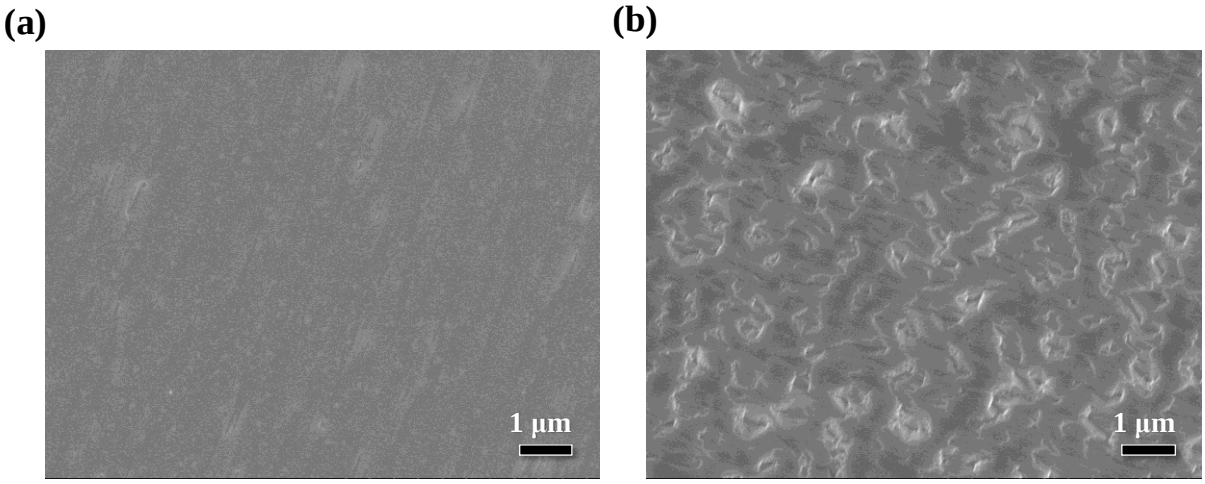

Figure 2.15 – Plane-view SEM images of epitaxially grown PbS seed layers with different surface morphologies on the GaAs substrate. (a) Smooth and dense film under enough time of reaction. (b) Rough film under insufficient time of reaction.

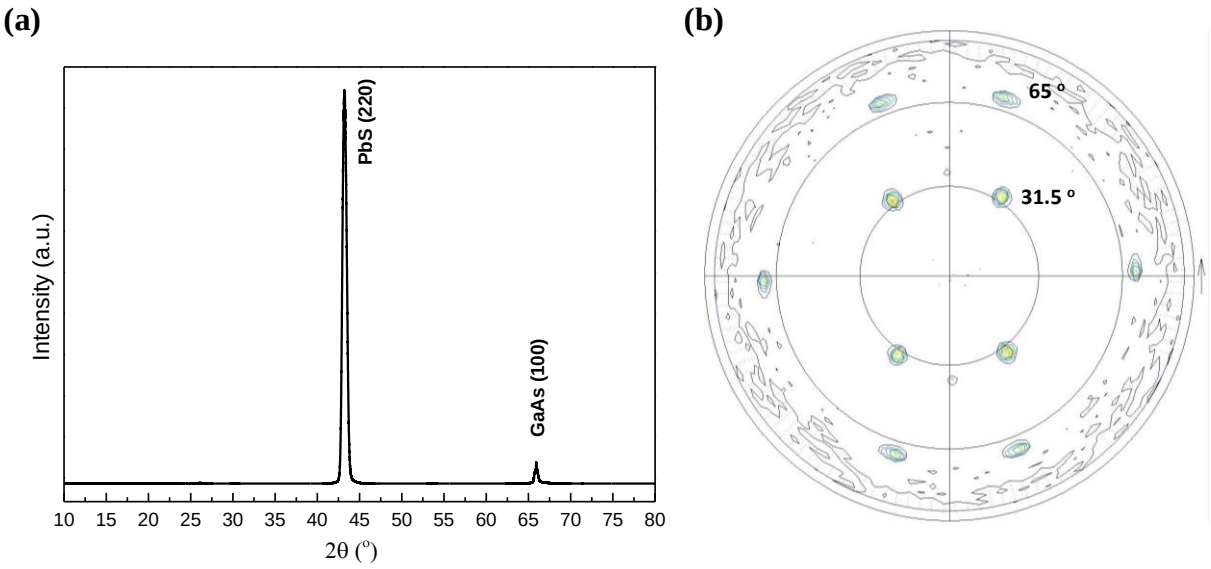

Figure 2.16 – XRD patterns of a PbS seed layer on the GaAs (100) substrate. (a) 2θ/ω curve indicates out-of-plane epitaxy along [110] direction. (b) PbS (311) pole-figure does in-plane epitaxy. The epitaxial relationship between PbS layer and GaAs wafer is expressed as PbS (110)[001]//GaAs (001)[110] and PbS (110)[$\bar{1}$10]//GaAs (001)[$\bar{1}$10].

This highly-textured characteristic is also verified in a 2θ/ω XRD patterns in **Figure 2.16a**. The out-of-orientation measurement indicates that a PbS seed layer was epitaxially grown along [110] direction of PbS (JCPDS 05-0592, galena) although the GaAs wafer had a (100) orientation.

This rather unusual orientation relationship could be favored due to a close lattice mismatch (less than 1 %) in the 3 : 2 superstructure formed between 3*d (110) GaAS and 2*d (100) PbS[71]. A pole-figure projected along PbS (311) in **Figure 2.16b** exhibits two sets of sharp peaks at 31.5° and 64.8°, which are possible inter-angles between {311} and {110} plane groups. This indicates that the PbS (110) seed layer had an in-plane epitaxial relationship as well. Therefore, epitaxial relationship between PbS seed layer and GaAs substrate can be expressed as PbS $(110)[001]$// GaAs $(001)[110]$ and PbS $(110)[\bar{1}10]$//GaAs $(001)[\bar{1}10]$.

The colloidal crystals were grown on the epitaxial PbS seed layer using the same technique used for the Bi_2Te_3 case. The negatively charged polystyrene particles were self-assembled on the seed layer surface in the form of face-centered cubic (FCC). **Figure 2.17** depicts that a 2.5 μm-thick colloidal crystal (200 nm in diameter) was grown on a 2 μm-thick PbS epitaxial layer in a highly ordered manner.

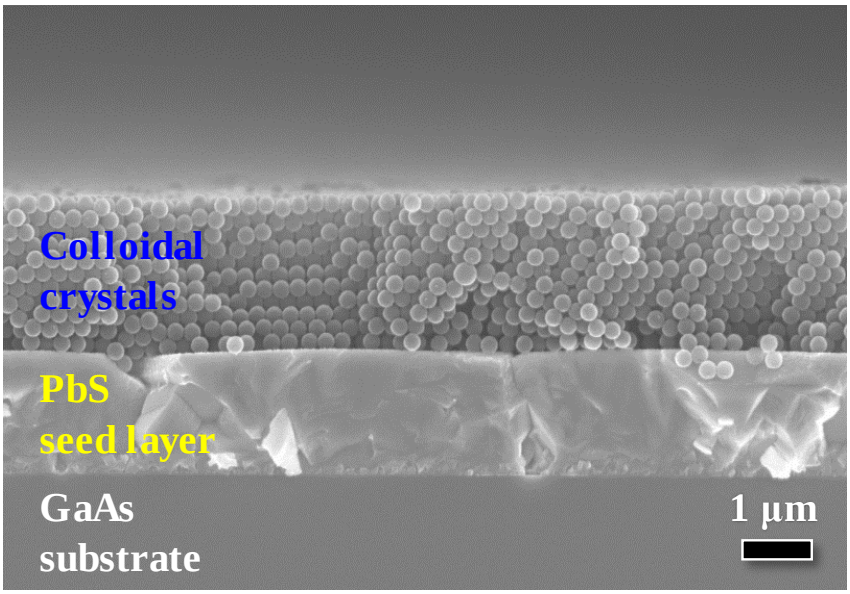

Figure 2.17 – Cross-section SEM image of colloidal crystals self-assembled on the PbS epitaxial seed layer grown on the GaAs (100) substrate.

2.4 Epitaxial Fe_3O_4 3D Meso/nanostructures

2.4.1 Multi-layered heteroepitaxial growth

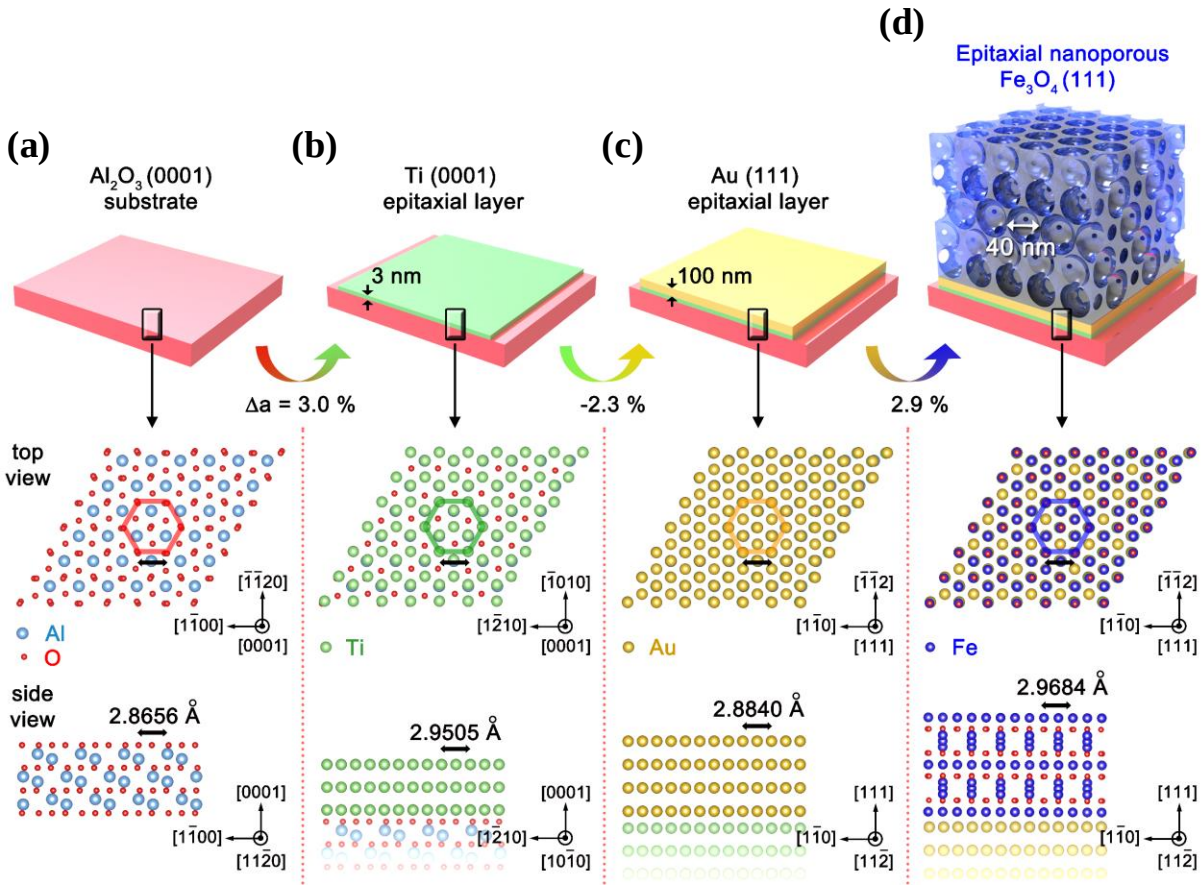

Figure 2.18 – Fabrication strategies of epitaxial 3D nanostructures. (a) Al_2O_3 (0001) substrate as a starting point for multilayer heteroepitaxies. Oxygen ions are exposed to top surface with interatomic distance (O - O) of 2.8656 Å. (b) Rotating Al_2O_3 (0001) substrate by 30°, Ti adhesion layer, in which interatomic distance is 2.9505 Å, is grown epitaxially along [0001] orientation on Al_2O_3 (0001) with coincidence lattice mismatch of 3.0 %. (c) Due to small coincidence lattice mismatch (-2.3 %), Au film is grown epitaxially along [111] orientation on Ti (0001) layer. The interatomic distance in Au (111) plane is 2.8840 Å. (d) Single crystalline Fe_3O_4 (111) 3D nanostructure is enabled on the Au (111) film by small coincidence lattice mismatch, 2.9 %, between two layers, and by the colloidal crystal growth and the electrodeposition. The interatomic distance (Fe - Fe) in Fe_3O_4 (111) plane is 2.9684 Å.

As a very bottom part of the epitaxial 3D nanostructures, the Al_2O_3 (0001) substrate (c-plane sapphire) was employed as shown in **Figure 2.18a**. Theoretically, rotating the sapphire by 30° with respect to the c-axis, we could grow a 3 nm thick epitaxial Ti adhesion layer on the oxygen atoms of the Al_2O_3 along [0001] direction followed by a 100 nm thick epitaxial Au film along

[111] direction (**Figure 2.18b** and **c**). These heteroepitaxial characteristics in both cases were enabled by a small coincidence lattice mismatch (3.0 %) between Ti layer and sapphire substrate and that (-2.3 %) between Au and Ti layers, where the lattice mismatch, Δa, is defined as

$$\Delta a\ (\%) = \frac{a_f - a_s}{a_s} \times 100$$

where a_f and a_s indicate the lattice parameters of film and substrate, respectively. Similarly, the Fe_3O_4 (111) has a small coincidence lattice mismatch of 2.9 % with the Au (111) film as illustrated in **Figure 2.18d**. The coincidence and original lattice mismatches of four layers are summarized in **Table 2.2**.

Table 2.2 – Summary of the coincidence and the original lattice mismatches among four layers. The lattice constants were taken from JCPDS cards (Al_2O_3: #46-1212, Ti: #44-1294, Au: #04-0784, Fe_3O_4: #19-0629).

Materials	**Coincidence**		Original	
	Lattice constant (Å)	**Lattice mismatch (%)**	Lattice constant (Å)	Lattice mismatch (%)
Al_2O_3 (0006)	**2.8656 (O - O)**		4.7587	
		3.0		-38.0
Ti (0002)	**2.9505 (Ti - Ti)**		2.9505	
		-2.3		38.0
Au (111)	**2.8840 (Au - Au)**		4.0786	
		2.9		105.9
Fe_3O_4 (111)	**2.9684 (Fe - Fe)**		8.3960	

To realize heteroepitaxial Au (111)/Ti (0002) layers is of great importance in two ways. It enables us to utilize the general colloidal crystal growth technique[89] as well as to grow the epitaxial Fe_3O_4 through one-step electrodeposition method[90]. The FCC metals such as Al, Ag, Cu, and Ni are known to epitaxially grow along [111] direction directly on the c-Al_2O_3 substrate[91-95]. Other than these metals, however, direct deposition of Au on sapphire usually accompanied poor

crystallinity[92,96-98] or required high-temperature deposition followed by post-annealing to enhance the crystallinity[97]. This problem has been partly resolved by inserting a Nb layer between Au and sapphire, in which there are still some limitations such as requiring the high temperature, 300ºC for Au deposition and limited thickness range of epitaxial Au, below 50 nm[99,100]. In the present study, instead of the Nb, we inserted a Ti layer between c-Al_2O_3 and Au film for achieving multiple purposes. First, it is easier to thermally evaporate Ti rather than Nb as Ti has a lower melting temperature (1660ºC for Ti and 2477ºC for Nb). Second, the lattice mismatches with sapphire and Au are only 3.0 % and -2.3 %, respectively, so that we can achieve high quality Au and Fe_3O_4 epitaxial layers. Finally, Ti is a well-known material as superior adhesion layer that promotes the bonding between Au and oxide substrate. These three features enabled us to fabricate high quality epitaxial 3D Fe_3O_4 porous films more easily without making any instability/delamination problems during Piranha clean, colloidal crystals growth, high-temperature electrodeposition, micro-fabrication steps, polishing, measurements, irradiations and so on. To the best of our knowledge, this strategy has not been reported elsewhere to date.

2.4.2 Morphology of epitaxial Fe_3O_4 3D meso/nanostructures

Using this strategy, we fabricated single crystalline meso/nanostructured Fe_3O_4 porous films through electrochemical deposition that Switzer and co-workers first demonstrated for making dense Fe_3O_4 film[90].

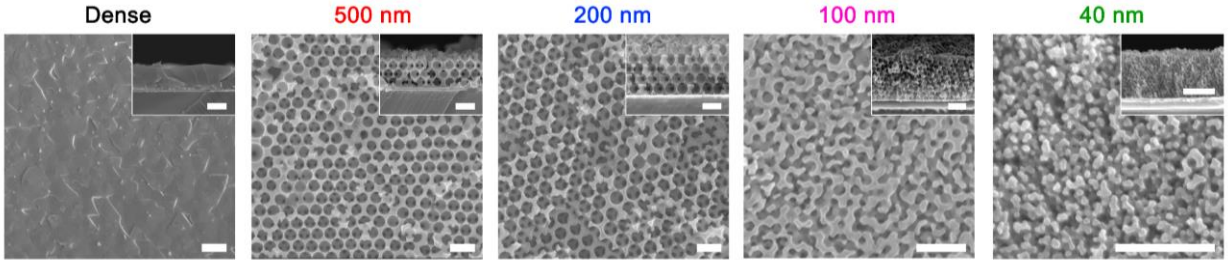

Figure 2.19 – Top and cross-section (inset) SEM images of the epitaxial Fe_3O_4 films such as dense film without any pore and porous films with different pore diameters of 500, 200, 100 and 40 nm that can be fabricated by the strategies above. Scale bars (including insets), 1 μm for the left two panels; and 400 nm for the right three panels.

Figure 2.19 shows SEM images of dense and porous Fe_3O_4 epitaxial films. The porous films have diameters from 500, 200, 100 and 40 nm, respectively. The dense film clearly reveals smooth and triangular large domains, indicative of the epitaxial nature. For the porous films, we

observed two distinct features. First, the smaller the pore size was, the smoother the surface was. Second, the orderliness of the pores become degraded as the pore size decreased, thereby leading to the higher volume fraction of Fe_3O_4 matrix at the smaller pore size. The cross-sectional images (insets of **Figure 2.19**) represent that regardless of the pore sizes the thickness of the epitaxial films was tunable from ~ 1 μm thick at least up to 4 ~ 5 μm at maximum.

2.5 Crystallographic Analysis on Epitaxial Fe_3O_4 3D Systems

2.5.1 Study on Au (111)/Ti (0002)/Al_2O_3 (0006) substrate

We first performed the 2θ/ω scan on the Au (100 nm)/Ti (3 nm)/c-Al_2O_3 substrate. In **Figure 2.20a**, a strong reflection is observed at 2θ corresponding to Au (111), which proves that the Au film has good out-of-plane epitaxies along [111] direction. It is hard to observe Ti (0002) peak because the 2θ of it is 38.422°, which is very similar with that of Au (111), 38.184°, and Ti layer is too thin to be detected. **Figure 2.20b** exhibits rocking curves of Au (111) film measured at fixed 2θ = 38.184°, whose mosaic spread, FWHM, is 0.565°.

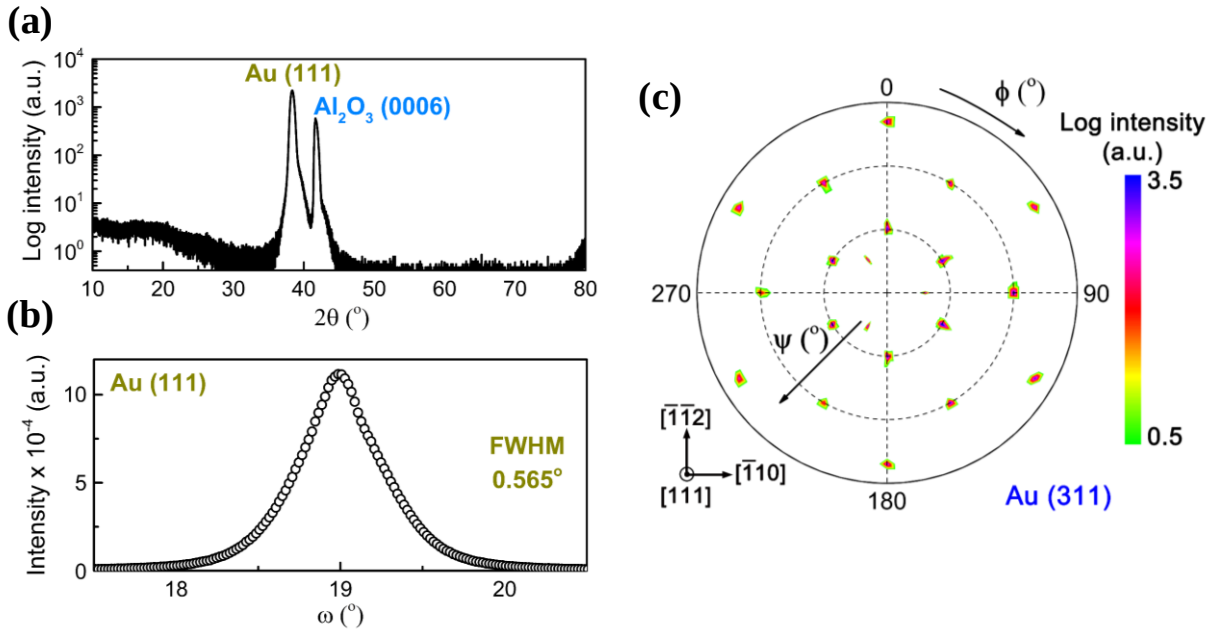

Figure 2.20 – Characterizations on Au layer. (a) 2θ/ω scan on Au (100 nm)/Ti (3 nm)/c-Al_2O_3 substrate. (b) Rocking curve of Au (111) layer, of which FWHM is 0.565°. (c) Au (311) pole-figure acquired at 2θ = 77.549°.

Pole-figure of Au (311) measured at the fixed 2θ = 77.549° in **Figure 2.20c** exhibits strong and discrete reflections at specific ψ and φ, without any continuous ring patterns. This is indicative of the Au (111) film having high-quality in-plane epitaxies too. We observe three sets of six strong reflections apart by φ = 60° at ψ = 30°, 58.5° and 81°, which are caused by Bragg reflections from Au {311} planes. In a cubic single crystal with single domain, there should be only three reflections at ψ = 30° and 81° respectively, based on the crystallographic calculations[101]. This means that our Au (111) film consists not of single domain but of two domains with [111] orientation rotated antiparallel to each other. Another one set of three reflections separated by φ = 120° at ψ = 17.5° is due to Al_2O_3 (1 0 $\bar{1}$ 10) plane, which has 2θ and interplanar angle with Al_2O_3 (0006) plane of 76.871° and 17.5°, respectively.

2.5.2 Out-of-plane epitaxy of Fe_3O_4 (111) film

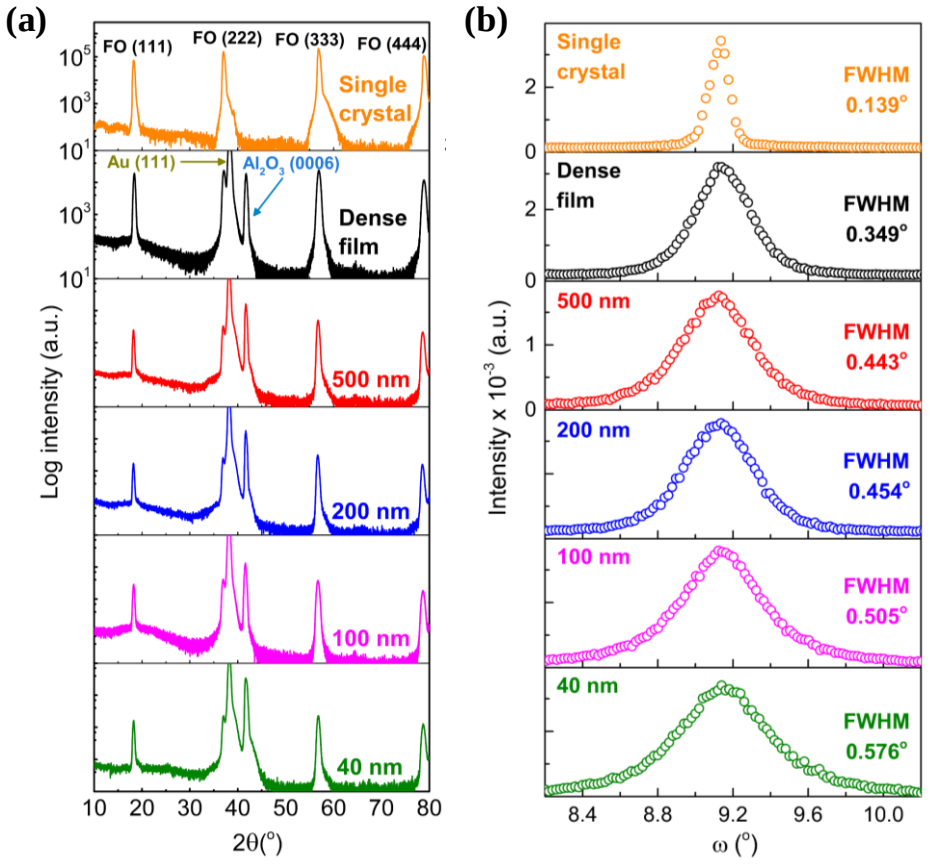

Figure 2.21 – Out-of-plane epitaxy. (a) 2θ/ω scans on the bulk single crystal, epitaxial dense and porous films, indicating all films are grown along [111] orientation. (b) Rocking curves of Fe_3O_4 (111) at 2θ = 18.290° where dense film has a broader peak than single crystal. As pore size decreases, out-of-plane mosaic spread increases.

Figure 2.21a shows the measured XRD data of the Fe_3O_4 dense and porous films using $2\theta/\omega$ scans. As a reference, we also examined bulk Fe_3O_4 (111) single crystal obtained from polishing Fe_3O_4 octahedron mineral along [111] direction. Clearly, all the films were perfectly grown along [111] out-of-plane orientation without containing any minor orientation or any secondary phase, in accordance with the pattern of the bulk single crystal. Rocking curves of Fe_3O_4 (111) plane at $2\theta = 18.290^o$ (**Figure 2.21b**) tell us the crystallinity of samples, so called mosaic spread. Larger full-width half-maximum (FWHM) means larger mosaic spread and lower crystallinity.

Two points are notable. First, the dense film has a broader mosaic spread than the bulk single crystal. Second, mosaicity increases as the pore size decreases. In an epitaxial growth through 3D colloidal template, the structural imperfections such as dislocations and stacking faults are known to be generated from the strain relaxation[102,103]. As smaller colloids have larger curvature and surface area, epitaxial film would undergo larger strain during the growth, resulting in larger mosaic spread.

2.5.3 In-plane epitaxy of Fe_3O_4 (111) film

To probe in-plane epitaxies, we collected Fe_3O_4 (311) pole-figures of the bulk single crystal, dense and 40 nm porous films as depicted in **Figure 2.22a**. Through simple mathematical calculations[101], we can deduce that in a (111)-oriented single crystal with a single domain, the stereographic projection of {311} planes is supposed to have three reflections apart by $\varphi = 120^o$ at $\psi = 30$ and 81^o respectively, and six reflections separated by $\varphi = 60^o$ at $\psi = 58.5^o$. At the same ψ angles, the dense and 40 nm porous films also showed periodic and strong {311} reflections from [111]-oriented samples without any ring pattern, indicating high-quality in-plane epitaxies. Three reflections at $\psi = 37.3^o$ came from $\{10\bar{1}4\}$ planes of Al_2O_3 (0006).

One difference from the bulk single crystal was that two films had six reflections apart by $\varphi = 60^o$ even at $\psi = 30$ and 81^o. This implies both synthesized films are comprised of two domains with [111] orientation rotated antiparallel to each other, not of single one. For the 40 nm porous film, we additionally observed six weak reflections separated by $\varphi = 60^o$ at $\psi = 9^o$ which were formed by reflections from {311} planes of [511]-oriented lattices[90], indicative of a small amount of mirror twins (six domains) created along [111] orientation by spinel law[104,105]. These reflections diminished with increasing pore diameters (**Figure 2.22b**) and then disappeared in the dense film.

We suspect that smaller surface area-to-volume ratio and curvature of larger colloids would have effects on the decreased twin formation. As (511) plane has the same d-spacing with (333) plane, we could not distinguish them in the 2θ/ω scans.

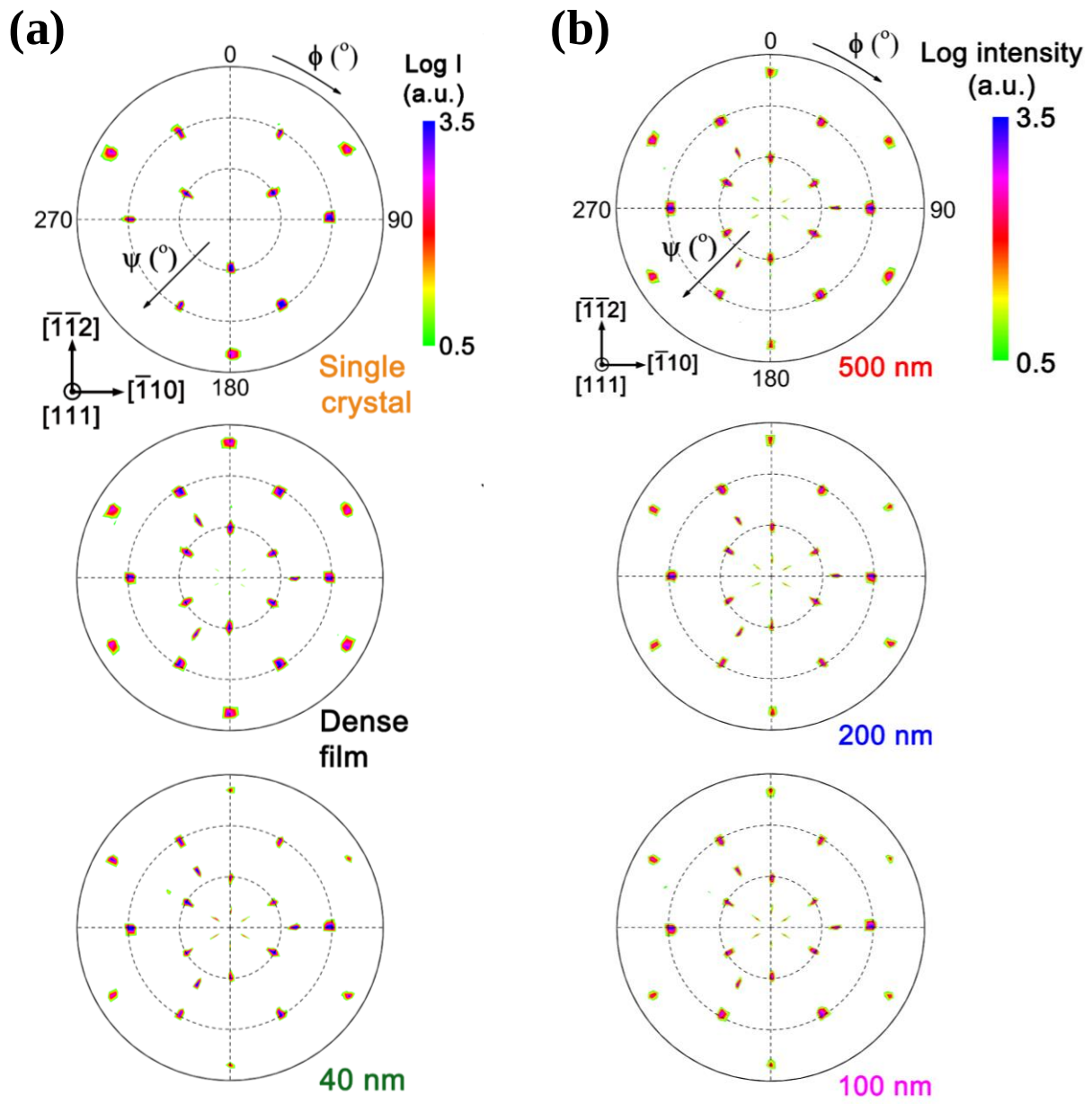

Figure 2.22 – In-plane epitaxy. (a) Fe_3O_4 (311) pole-figures of single crystal, dense and 40 nm porous films. Similar with single crystal and dense film, 40 nm sample also exhibits strong discrete reflections only at specific tilt (ψ) and azimuth (φ) angles, indicating high quality in-plane epitaxies conserved. (b) Fe_3O_4 (311) pole-figures of 500, 200 and 100 nm porous samples show that all have good in-plane epitaxies. Three reflections at $\psi = 37.3^o$ came from $\{10\bar{1}4\}$ planes of Al_2O_3 (0006).

2.5.4 In-plane epitaxial relationships among four layers

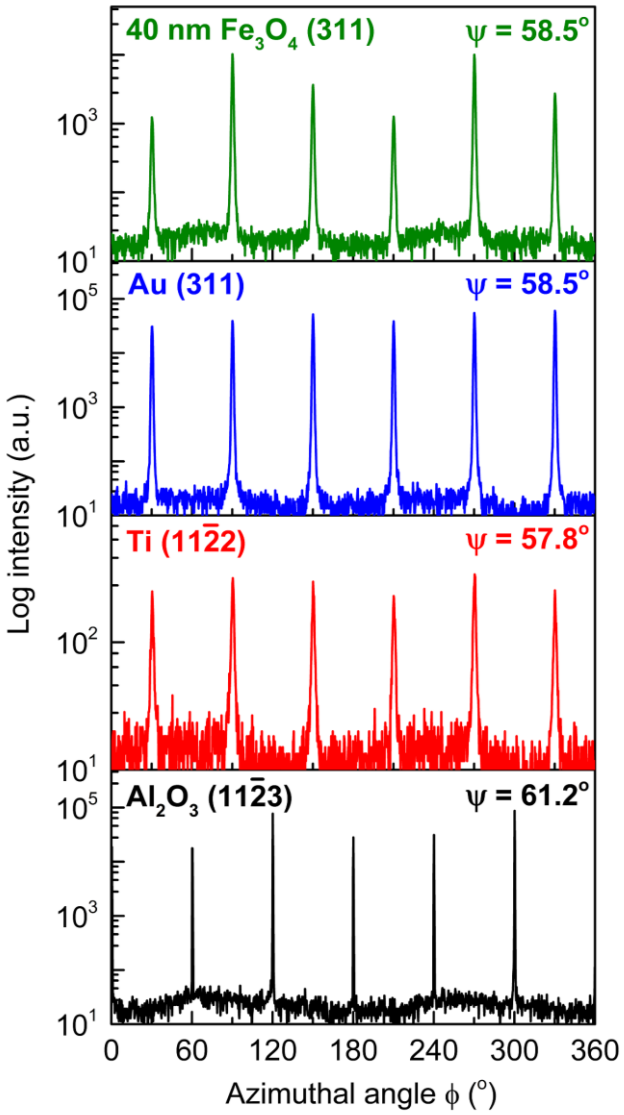

Figure 2.23 – Azimuthal scans on four layers along in-plane orientation where Fe_3O_4 (311), Au (311), Ti (11$\bar{2}$2) and Al_2O_3 (11$\bar{2}$3) atomic planes are aligned to each other.

To investigate in-plane epitaxial relationships of four layers in the 40 nm porous sample, we implemented azimuthal scans on Fe_3O_4 (311), Au (311), Ti (11$\bar{2}$2) and Al_2O_3 (11$\bar{2}$3) respectively at the similar ψ values, 58.5° for both Fe_3O_4 and Au layers, 57.8° for Ti layer and 61.2° for sapphire substrate, as shown in **Figure 2.23**. We observe that Fe_3O_4, Au and Ti layers show six strong reflections at the same azimuthal angles and so does the sapphire at the 30°-rotated angle, which tells us that the atomic lattices of four layers are highly coherent with neighbor layers along the in-plane direction. Although we know that they are highly aligned to each other, it is not

possible to determine the in-plane epitaxial relationships exactly only from this measurement because at this ψ angle the c-Al_2O_3 substrate is also supposed to have six reflections, the same as Fe_3O_4, Au and Ti, as shown in **Table 2.3.**

Table 2.3 – Comparison between ideal reflections by crystallographic calculations and real data of four layers at two different ψ angles.

Materials	**ψ = 57.8 ~ 61.2°**		**ψ = 32.4 ~ 37.3°**		**Number of domains**
	Ideal reflections	# of observed reflections	Ideal reflections	# of observed reflections	
Fe_3O_4 (111)	$(3\bar{1}1)(31\bar{1})$ $(13\bar{1})(\bar{1}31)$ $(1\bar{1}3)(\bar{1}13)$	6	(220) (202) (022)	6	2
Au (111)	$(3\bar{1}1)(31\bar{1})$ $(13\bar{1})(\bar{1}31)$ $(1\bar{1}3)(\bar{1}13)$	6	(220) (202) (022)	6	2
Ti (0001)	$(11\bar{2}2)(\bar{1}\bar{1}22)$ $(\bar{2}112)(2\bar{1}\bar{1}2)$ $(\bar{1}2\bar{1}2)(1\bar{2}12)$	6	$(10\bar{1}3)$ $(\bar{1}103)$ $(0\bar{1}13)$	6	2
Al_2O_3 (0001)	$(11\bar{2}3)(\bar{1}\bar{1}23)$ $(\bar{2}113)(2\bar{1}\bar{1}3)$ $(\bar{1}2\bar{1}3)(1\bar{2}13)$	6	$(10\bar{1}4)$ $(\bar{1}104)$ $(0\bar{1}14)$	3	1

Number of domains are extracted from this comparison. When calculating ideal reflections, we use two different equations, one for cubic structure and the other for hexagonal one, which define the interplanar angle (ψ**)** between two atomic planes, $(h_1k_1l_1)$ and $(h_2k_2l_2)$, as shown below[106]

$$\cos\psi = \frac{h_1h_2 + k_1k_2 + l_1l_2}{\sqrt{h_1^2 + k_1^2 + l_1^2}\sqrt{h_2^2 + k_2^2 + l_2^2}} \quad \text{for cubic,}$$

$$\cos\psi = d_{h_1k_1l_1}d_{h_2k_2l_2}\left[\left\{h_1h_2 + k_1k_2 + \frac{1}{2}(h_1k_2 + k_1h_2)\right\}a^{*^2} + l_1l_2c^{*^2}\right] \quad \text{for hexagonal,}$$

$$a^* = \frac{2}{a\sqrt{3}}, c^* = \frac{1}{c}$$

where $d_{h_1k_1l_1}$, $d_{h_2k_2l_2}$, a and c denote $(h_1k_1l_1)$, $(h_2k_2l_2)$ interplanar spacings, lattice constants along $[2\bar{1}\bar{1}0]$ and [0001] directions of hexagonal structure, respectively.

We therefore performed additional measurements on four layers that are aligned along another in-plane direction, different from above. **Figure 2.24a** shows the pole-figures of four layers, Fe_3O_4 (220), Au (220), Ti $(10\bar{1}3)$ and Al_2O_3 $(10\bar{1}4)$. The Fe_3O_4 and Au pole-figures have

six strong reflections respectively at ψ = 35.3° and Al_2O_3 one has three strong reflections at ψ = 37.3°. At this ψ range, both Fe_3O_4 (220) and Au (220) should exhibit only three reflections if they were comprised of the single domain according to the crystallographic calculations **(Table 2.3)**. We once again confirm that Fe_3O_4 and Au epitaxies have two domains, in good agreement with the (311) pole-figure results. Due to very small thickness, we were not able to collect any information on the Ti layer from the pole-figure measurement. It is essential to know the characteristic of the Ti layer to clearly reveal the overall in-plane epitaxial relationships.

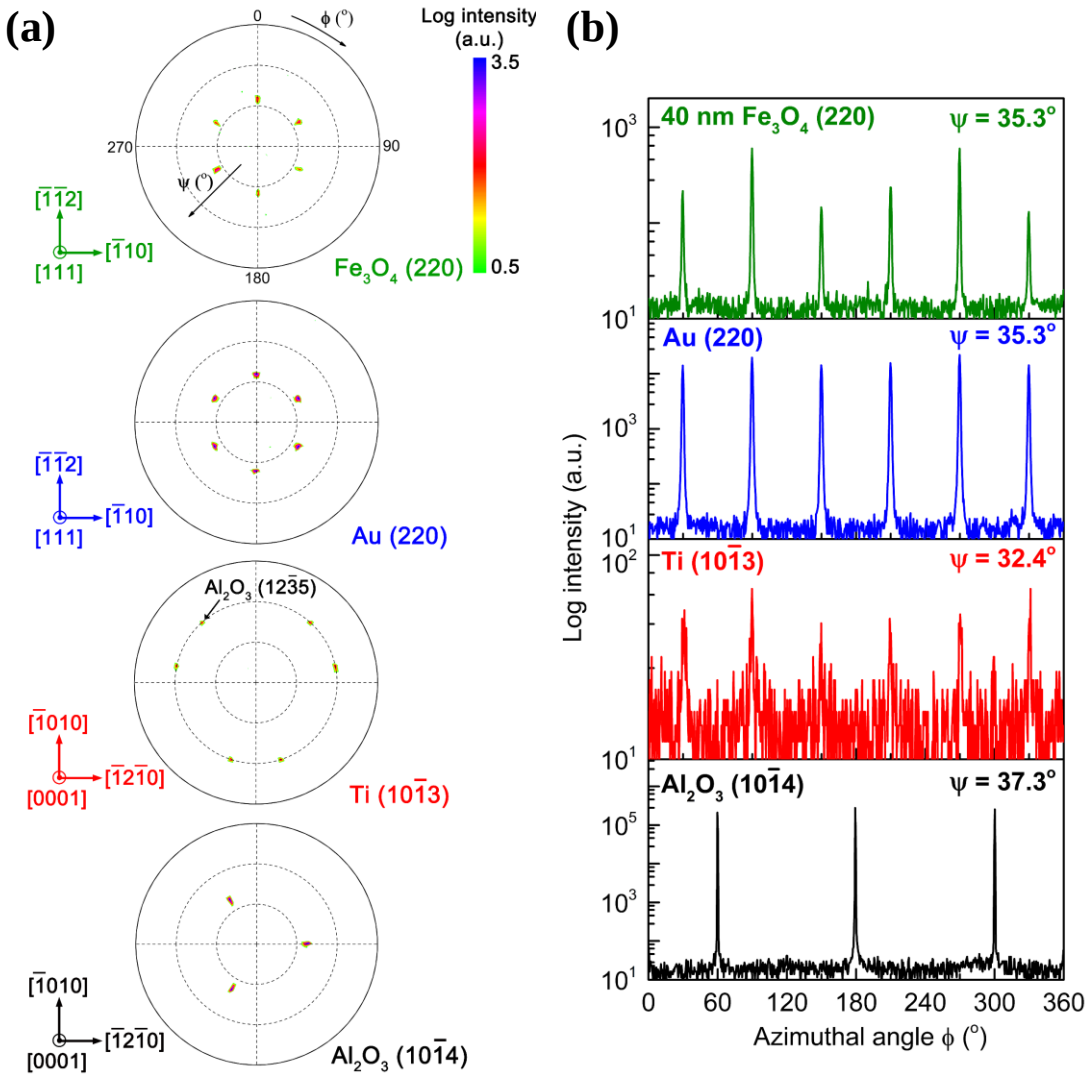

Figure 2.24 – Measurements along another in-plane orientation. **(**a) Pole-figures of Fe_3O_4 (220), Au (220), Ti (10$\bar{1}$3), and Al_2O_3 (10$\bar{1}$4). Six strong reflections in the Ti (10$\bar{1}$3) pole-figure are due to Al_2O_3 (12$\bar{3}$5). (b) Azimuthal scans on four layers along the in-plane orientation where Fe_3O_4 (220), Au (220), Ti (10$\bar{1}$3) and Al_2O_3 (10$\bar{1}$4) atomic planes are aligned to each other. The ψ values are 32.4 ~ 37.3°.

Using the same 2θ configurations as the pole-figure measurements, the azimuthal data were delicately collected at the ψ values of 35.3° for both Fe_3O_4 and Au layers, 32.4° for Ti layer and 37.3° for sapphire substrate respectively, as depicted in **Figure 2.24b**. We observe that six reflections from Ti layer are perfectly aligned with those of Au and Fe_3O_4 layers at the same azimuthal angles. Considering that Al_2O_3 has three reflections that are apart by 120° at the 30°-rotated angles, we can now deduce that the Ti layer has two domains with [0001] orientation rotated antiparallel to each other[107], which is the same case as the Au and Fe_3O_4 layers **(Table 2.3)**. The evolution of the 180°-rotated domain with respect to the original one has been reported to be due to the presence of two terraces of a stepped Al_2O_3 (0006) surface[108]. We finally conclude that there are two kinds of in-plane epitaxial relationships among four layers, the parallel and the antiparallel alignments with respect to the sapphire substrate, which can be expressed as Fe_3O_4 (111)$[1\bar{1}0]$//Au (111)$[1\bar{1}0]$//Ti (0002)$[1\bar{2}10]$//Al_2O_3 (0006)$[1\bar{1}00]$ and Fe_3O_4 (111)$[\bar{1}10]$//Au (111)$[\bar{1}10]$//Ti (0002)$[\bar{1}2\bar{1}0]$//Al_2O_3 (0006)$[1\bar{1}00]$, respectively.

2.6 Raman Spectroscopy on Epitaxial Fe_3O_4 3D Structures

One issue when analyzing Fe_3O_4 phase using XRD is that it is hard to distinguish between Fe_3O_4 (magnetite) and γ-Fe_2O_3 (maghemite; cation-deficient magnetite with a defective cubic structure) because the crystal structure and the lattice constants of Fe_3O_4 (cubic, Fd-3m, a = 8.396 Å) are very similar with those of γ-Fe_2O_3 (cubic, P 4_332, a = 8.342 Å)[109,110]. We performed Raman spectroscopy measurement on the dense and porous films to resolve this problem and to also study the chemical bonding characteristics and vibrational modes in our samples. **Figure 2.25** shows the measured 532 nm Raman laser spectra of the epitaxial dense and porous films. As a reference, we examined the bulk Fe_3O_4 (111) single crystal. In all cases, we observed three major peaks at the Raman shifts of 668 (A_{1g}), 538 ($T_{2g}(2)$) and 306 cm^{-1} (E_g) in order of decreasing intensity and one very weak peak at 194 cm^{-1} ($T_{2g}(1)$). All four peaks are Raman characteristics of pure single crystalline Fe_3O_4 phase[74]. The $T_{2g}(1)$ mode at 194 cm^{-1} is usually known to be barely observed or to be detected very weakly[111]. More specifically, four Raman shifts are related with the normal mode motions of the FeO_4 tetrahedrons[111]: symmetric stretch of O atoms along Fe-O bonds for A_{1g}, asymmetric stretch of Fe and O atoms for $T_{2g}(2)$, symmetric bends of O atom with respect to Fe for E_g and translatory movement of the whole FeO_4 unit ($T_{2g}(1)$). It is notable that for all

samples we did not observe any other Raman peaks from the γ-Fe_2O_3 phase with Raman shifts at 700 (A_{1g}), 491 (E_g) and 365 cm^{-1} (T_{2g})[74,109,110]. Raman characteristics of the films were in good agreement with that of bulk single crystal. Three peaks (A_{1g}, $T_{2g}(2)$, E_g) slightly broadened with decreasing pore size, which means increased mosaic spread. This behavior corresponds with the rocking curve results discussed above.

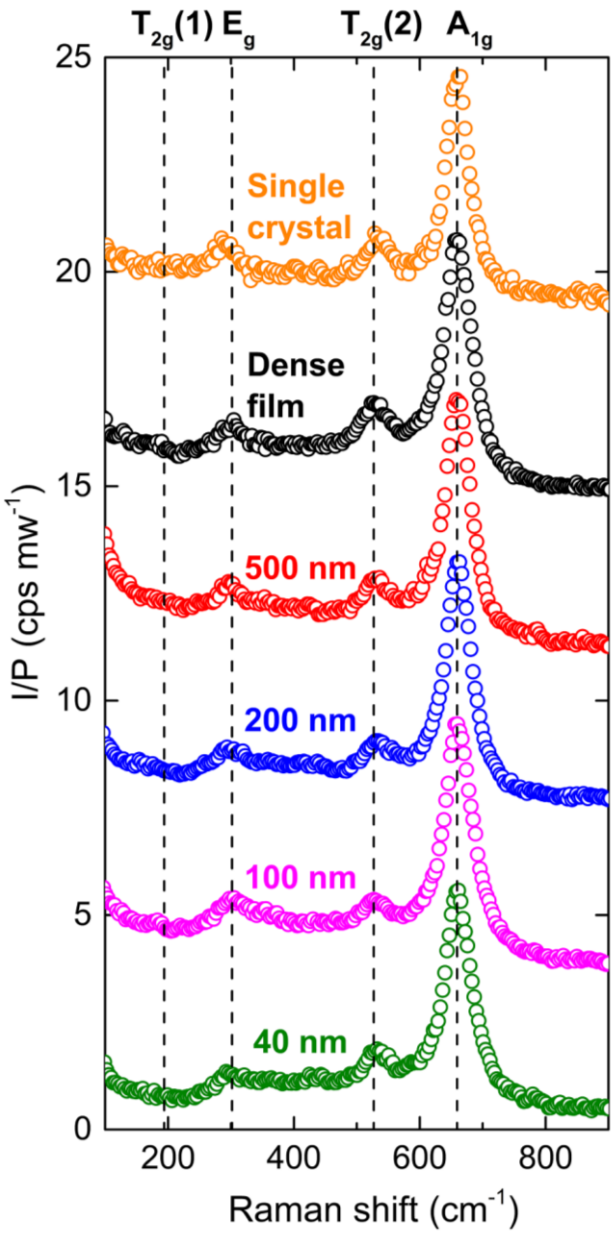

Figure 2.25 – Raman spectra (λ = 532 nm) of single crystal, dense and porous films with different pore sizes from 500, 200, 100 to 40 nm. Regardless of pore sizes, all porous films have the same Raman shift behaviors as the single crystal and the dense film have. No peaks from γ-Fe_2O_3 phase are observed, which strongly supports the XRD results.

2.7 Density Determination of Epitaxial Fe_3O_4 3D Structures

2.7.1 RBS data analysis

Every material has its characteristic thickness (nm) that corresponds to an areal number density of 1 x 10^{15} atoms cm^{-2}. It is reciprocal of its number density of atoms in the unit of 10^{22} atoms cm^{-3}. Number density of atoms is calculated by $\frac{number\ of\ atoms\ per\ unit\ formula}{V_m} \times N_A$, where V_m and N_A denote molar volume and Avogadro's number, respectively. Number of atoms per unit formula of Au and Fe_3O_4, for example, is 1 and 7, respectively. Characteristic thickness is typically used for analyzing the RBS data due to its convenience, as documented in **Table 2.4**. The density of Fe_3O_4 dense film (marked with *) fabricated in this study was determined by incorporating a characteristic thickness (0.1062 nm) calculated based on the reported Fe_3O_4 density (5.17 g cm^{-3}). The measured value is 95 ± 5 % of the reported one.

Table 2.4 – Summary of materials parameters used for RBS. Characteristic thickness of each material can be deduced from its inherent properties.

Unit formula	**Density (g cm^{-3})**	**M_W (g mol^{-1})**	**$\frac{1}{V_m}$ (mol cm^{-3})**	**# atoms per unit formula (atoms)**	**# density (10^{22} atoms cm^{-3})**	**Thickness corresponding to 10^{15} atoms cm^{-2} (nm)**
Au	19.3	197	0.0980	1	5.90	**0.1695**
Ti	4.51	47.9	0.0942	1	5.67	**0.1762**
Al_2O_3	3.98	102	0.0390	5	11.8	**0.0851**
Fe_3O_4	5.17	232	0.0223	7	9.41	**0.1062**
Fe_3O_4 DF	4.91 ± 0.26*	232	0.0212	7	8.92	**0.1121**
$(C_8H_8)_n$ (polystyrene)	1.06	$104n$	$\frac{0.0101}{n}$	$16n$	9.77	**0.1024**

Using these parameters and the RBS data of the Au/Ti/c-Al_2O_3 reference sample (**Figure 2.26a**), we first determined the thickness of Au and Ti layers through fitting. These values were directly used as fixed parameters for analyzing the spectrum of the Fe_3O_4 film. The Fe_3O_4 film, here, refers to either the dense film (**Figure 2.26b**) comprised of Fe_3O_4 matrix and pore, or the polystyrene-included film (**Figure 2.26c**) consisting of Fe_3O_4 matrix and polystyrene bead. In

Figures 2.26b and **c**, we observe that the Au peak is different from that in the reference sample data in terms of the shape and the position. The shape tells us the roughness of the Fe_3O_4 film. The broader it is, the rougher the film surface is.

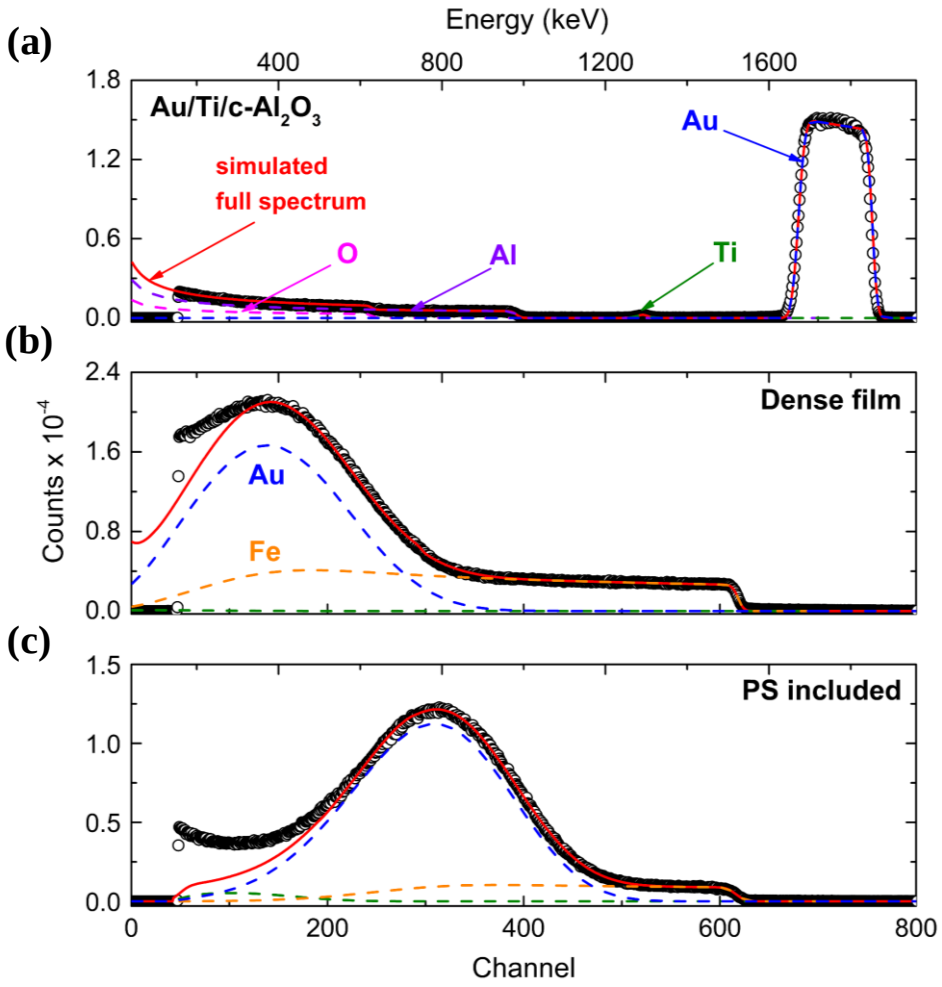

Figure 2.26 – RBS spectra of ion counts against channel (or energy). (a) Data (○) and simulated curve (–) of Au (100 nm)/Ti (3 nm)/c-Al_2O_3 substrate, as a reference. Fitting data with simulation, accurate thicknesses of Au and Ti layers were determined. (b, c) Spectra collected from Fe_3O_4 dense and Fe_3O_4/polystyrene films, respectively. Both are well fitted with calculated curves where we input Au and Ti parameters determined from reference sample analysis. Low energy tails of (b) and (c) are due to roughness of samples[112].

The position of the Au peak is significant in determining the Fe_3O_4 density of the film. The Au peak shifts toward lower energy as the film thickness increases or the density of Fe_3O_4 matrix in the film increases. As we know the thickness of the film from the SEM images (**Figure 2.27a**), we can narrow down the possible range of the Fe_3O_4 density through Au peak fitting processes. The measured RMS roughness of each sample, as shown in **Figure 2.27b**, was used as an initial

estimate for fitting. We can further narrow down the density range by fitting the Fe atom spectrum (orange dashed lines in **Figures 2.26b** and **c**) which tells us the actual counts of Fe atoms. The point where the experimental data including Au peak and Fe spectrum are best fitted to the simulation curve with the goodness of fit, χ^2, of ~ 10^{-2} typically (excluding low energy tails), gives the final Fe_3O_4 density with relative error of 10 ~ 13 %. The $\chi^2 = \sum_i \frac{(y_i - \hat{y}_i)^2}{\hat{y}_i}$, where y_i and $\hat{y}_i$ denote i^{th} real data and i^{th} simulated value, respectively.

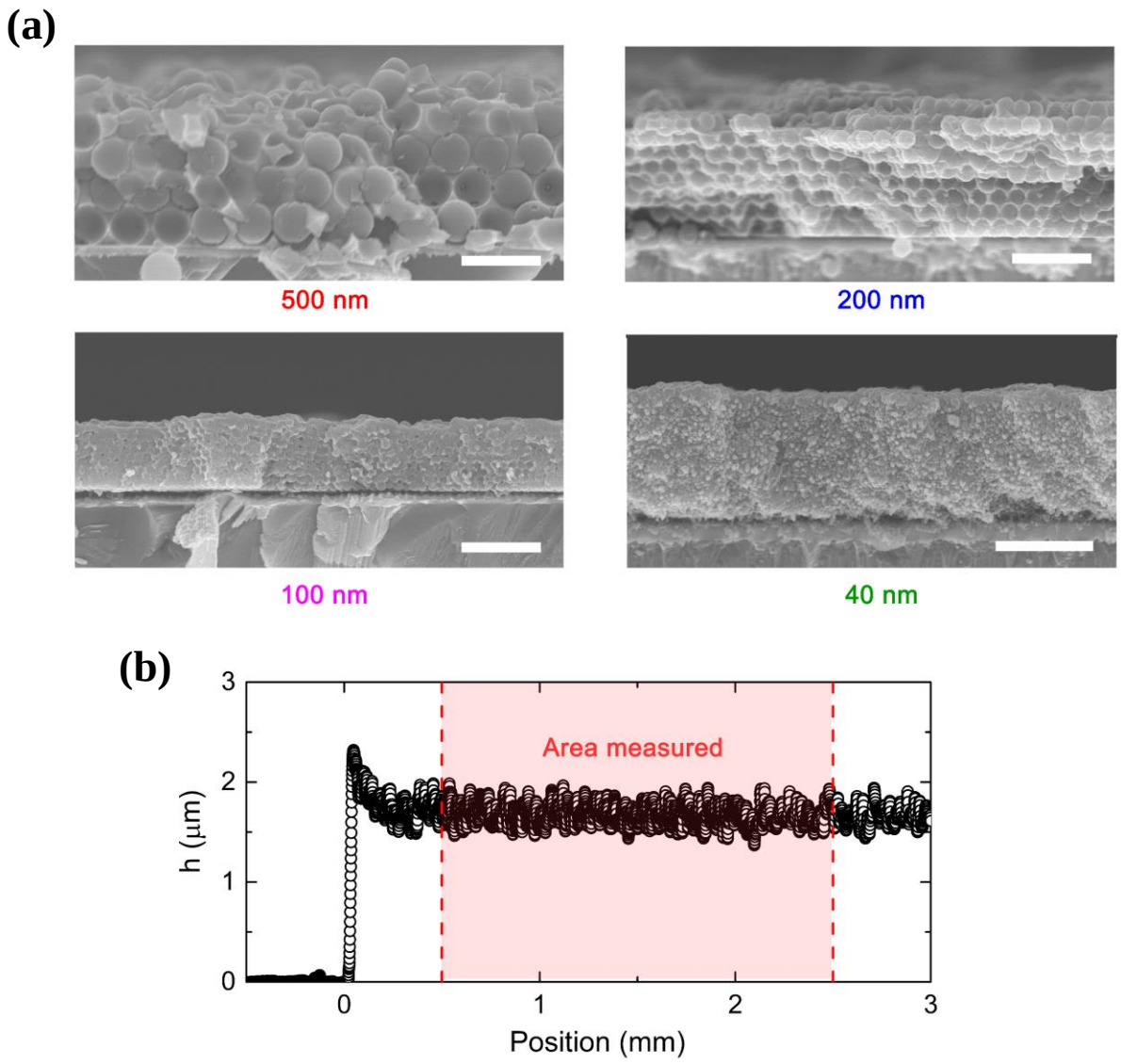

Figure 2.27 – Thickness and roughness measurements. (a) Cross-sectional SEM images of Fe_3O_4 samples yet containing polystyrene beads with different sizes. Scale bars, 1 μm. (b) Plot of sample height against position collected from surface profilometry. The root-mean-square roughness over 2 mm in length, where we irradiated beams with diameter of 2 mm, was used as an initial estimate.

2.7.2 XRF data analysis

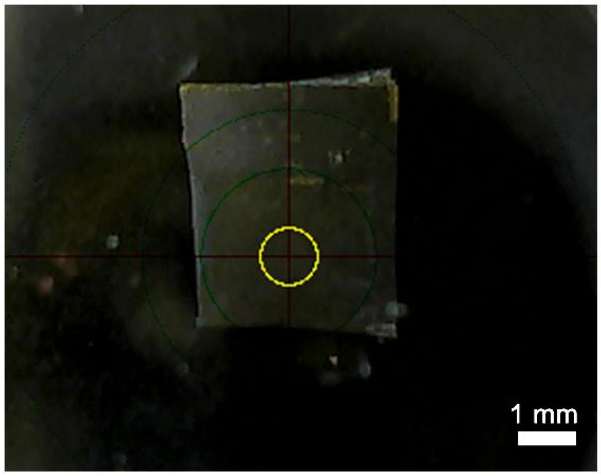

Figure 2.28 – Photograph of a Fe_3O_4 sample loaded into the XRF measurement chamber under He atmosphere. The yellow circle with 1 mm in diameter is where the X-ray beam is bombarded.

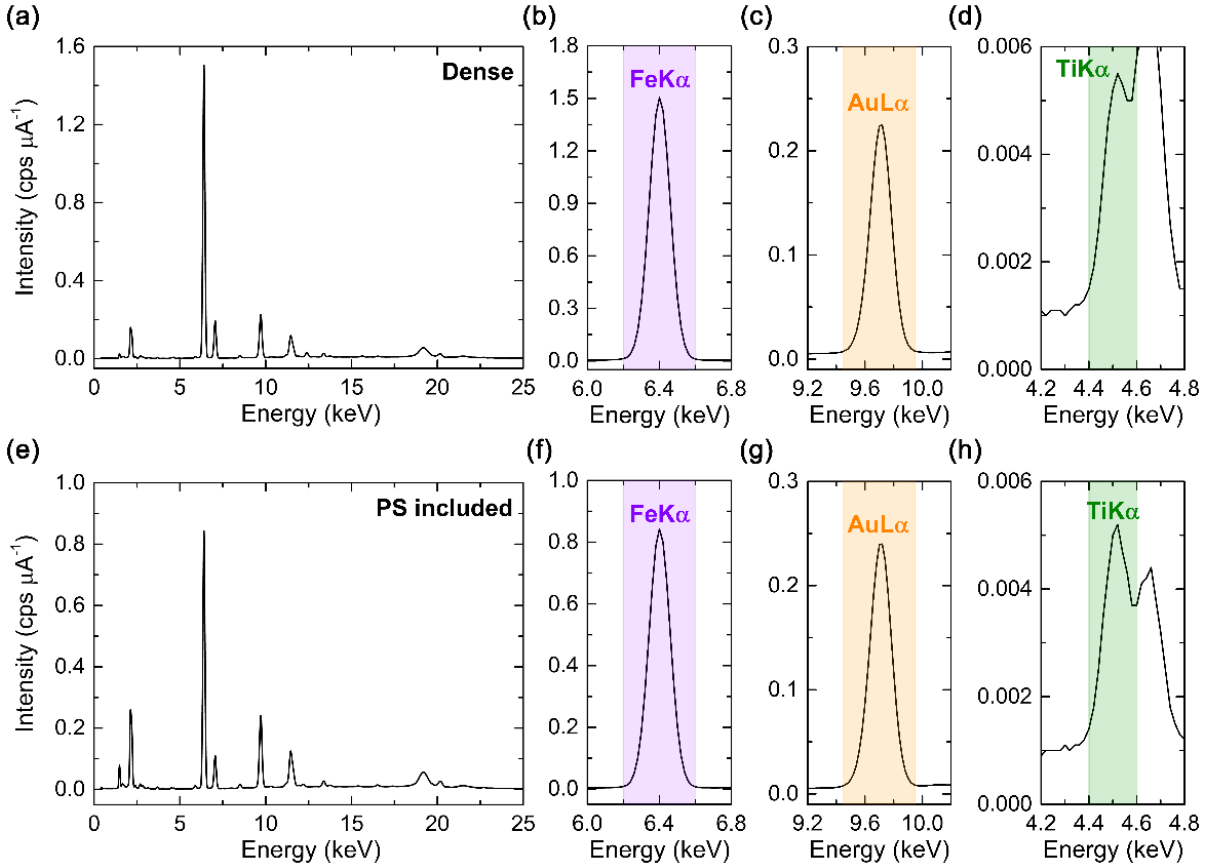

Figure 2.29 – Typical energy dispersive spectra collected from the XRF measurements on (a - d) dense and (e - h) PS included films. The thicknesses of Fe_3O_4, Au, and Ti layers were determined by the peak intensities of the characteristic X-rays emitted as a result of (b, f) FeKα, (c, g) AuLα, and (d, h) TiKα transitions.

Figure 2.28 shows the photograph of the Fe_3O_4 sample loaded into the XRF measurement instrument. The yellow spot with 1 mm in diameter indicates the area of the sample where the X-ray beam was irradiated. The representative energy dispersive spectra of a dense film and a PS included film are depicted in **Figure 2.29a** and **e**, respectively. Based on so-called film fundamental parameters (FP) method, the amounts of Fe_3O_4, Au, and Ti were deduced from analyzing the characteristic X-ray peaks corresponding to FeKα, AuLα, and TiKα transitions respectively, which are exhibited in **Figure 2.29b-d** for a dense film and **Figure 2.29f-h** for PS included films. More specifically, the intensities of the characteristic peaks in cps μA^{-1} were first converted to the areal densities of Fe, Au, and Ti in $\mu g\ cm^{-2}$ based on Sherman equation[113]. Then, the areal densities were converted to the thicknesses of Fe_3O_4, Au, and Ti layers by considering the mass densities of Fe_3O_4, Au, and Ti and the weight percent of the elements comprising the layers. Comparing the thickness obtained by XRF measurement with that by cross-section SEM image, we finally determined the Fe_3O_4 densities of PS included samples.

2.7.3 Relationship between density and colloidal packing fraction

Figure 2.30 presents the plots of the Fe_3O_4 densities of all porous samples determined by two independent methods, RBS and XRF. The results extracted from two types of measurements are in good agreement with each other.

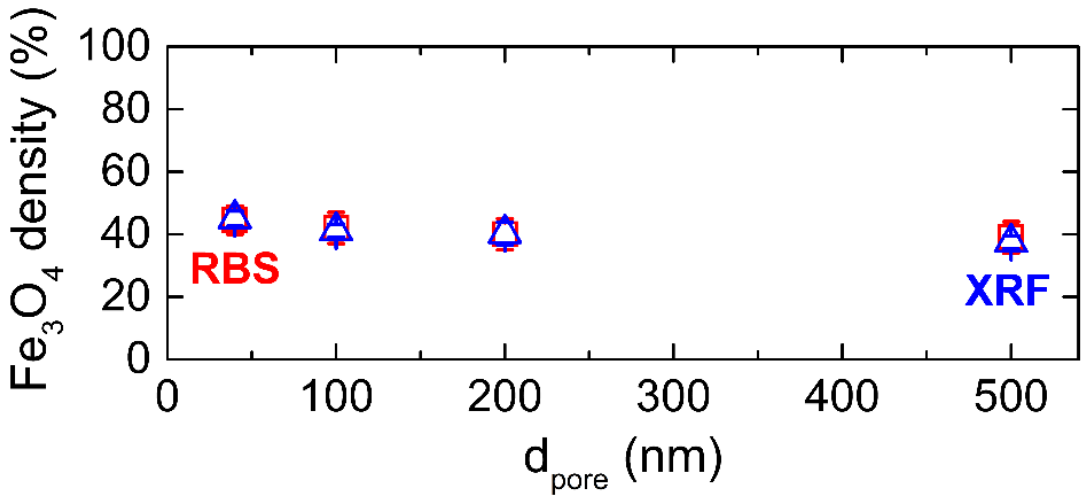

Figure 2.30 – Fe_3O_4 density of porous films as a function of pore diameter determined by RBS and XRF measurements, which increases with decreasing pore size.

It is notable that the density of the 40 nm nanoporous film even reached 44.5 ± 4.5 %, almost half-filled. The density (39.0 ± 5.0 %) of even 500 nm porous sample, was 1.5 times greater

than the theoretical density value, 26 %, of an inverse replica of a face-centered cubic (FCC) array of colloidal particles[62,114,115]. This tells us that during the self-assembly particles do not actually form close packed crystals but form crystals without close packing, according to the hard sphere assembly[116,117]. Close-packed FCC crystals, with the packing fraction of 74 %, could not be attained presumably due to the polydispersity of colloidal particles[118]. Another origin of high density could be the presence of dense Fe_3O_4 regions that were grown on the cracks inside colloidal crystals. These cracks are known to form by shrinkage of 1 ~ 10 nm thick solvation layers of charged colloidal surfaces during drying process[118].

Another interesting feature is observed in **Table 2.5** that summarizes the Fe_3O_4 densities and the corresponding packing fractions of colloidal crystals. The smaller the pore diameter is, the higher the Fe_3O_4 fraction is, implying that smaller particles were less packed and less ordered during colloidal crystallization. Packing fraction or quality of colloidal crystal is primarily determined by a polydispersity of colloidal particles, particle-particle repulsions/attractions in colloidal suspensions, and driving force for self-assembly[118-121]. We estimated the polydispersity of dried particles at each diameter utilizing the material information sheets of polystyrene beads supplied by vendor[122]. As shown in **Table 2.6,** the polydispersity of colloidal beads increases with decreasing particle diameter, which would be one major origin why colloidal crystals with smaller diameter have less compact and more disordered crystal arrays. Also, for smaller colloids, as there are larger numbers of solvation layers per unit volume resulting from larger surface area-to-volume ratio, more cracks could be generated in colloidal crystal upon drying and hence more Fe_3O_4 dense areas were formed in the porous sample.

Table 2.5 – Summary of measured Fe_3O_4 densities of porous films. Packing fraction of polystyrenes, 100 – (Fe_3O_4 density), %, is included to discuss the relation between crystallinity of colloidal crystals and hard sphere volume fraction. The Fe_3O_4 densities (%) of porous samples were determined using the dense film density (4.91 ± 0.26 g cm^{-3}) that was obtained from the RBS measurement above and its corresponding characteristic thickness (0.1121 nm).

Pore diameter (nm)	Fe_3O_4 density (%)	PS packing fraction (%)
500	39.0 ± 5.0	61.0 ± 5.0
200	40.0 ± 5.0	60.0 ± 5.0
100	42.0 ± 5.0	58.0 ± 5.0
40	44.5 ± 4.5	55.5 ± 4.5

Table 2.6 – Diameters of colloidal particles on their dried states characterized by TEM observation were obtained from supplier's material information sheets[122]. Polydispersity is defined as standard deviation divided by mean diameter of colloids[119,121].

Pore diameter (nm)	Dried	
	Diameter (nm)	Polydispersity (%)
500	530 ± 11	2.1
200	210 ± 6	2.9
100	100 ± 8	8.0
40	41 ± 6	15

2.8 TEM Analysis on 40 nm Porous Epitaxial Fe_3O_4 3D Structures

2.8.1 Characterization on Au (100 nm)/Ti (3 nm)/c-Al_2O_3 substrate

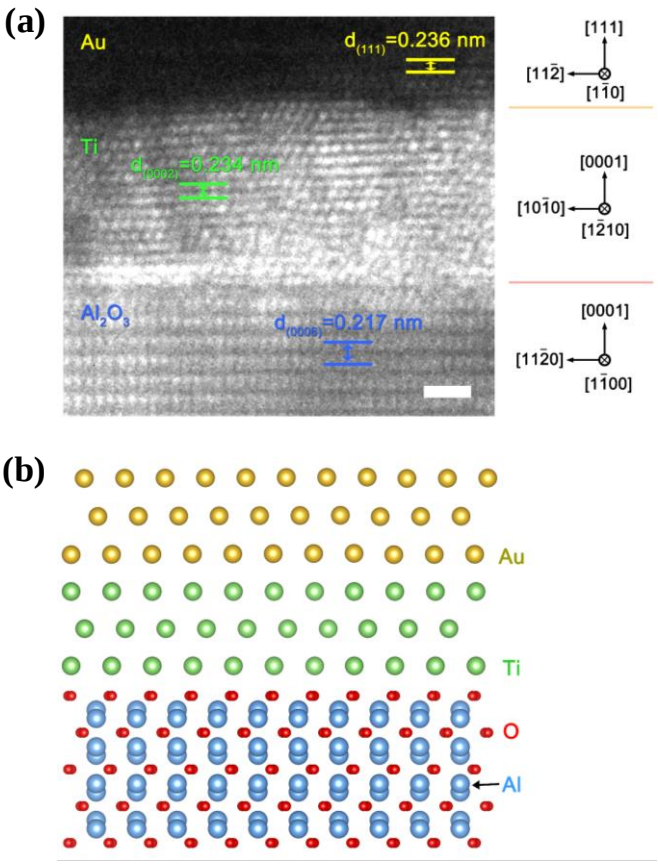

Figure 2.31 – Characterization on Au (100 nm)/Ti (3 nm)/c-Al_2O_3 substrate. (a) HRTEM image of three layers. Scale bar, 1 nm. (b) Fe_3O_4 [$1\bar{1}0$]-projected crystal structure models.

Figure 2.31a represents a high-resolution TEM (HRTEM) image of three layers taken along $[1\bar{1}0]$ orientation of Fe_3O_4 film. Each layer clearly reveals its atomic lattice fringes aligned along the crystal growth orientation, [111] for Au, [0002] for Ti, and [0006] for c-Al_2O_3 substrate, respectively. The interplanar distance of each layer is in good agreement with that of JCPDS card (Al_2O_3: #46-1212, Ti: #44-1294, Au: #04-0784). **Figure 2.31b** exhibits the crystal structure models of the layers projected into Fe_3O_4 $[1\bar{1}0]$ direction. Atomic distances at the interfaces match well with each other due to small lattice mismatches among three layers.

2.8.2 Microstructures of 40 nm porous epitaxial Fe_3O_4 film

We investigated the microstructures of the 40 nm porous film using TEM. **Figure 2.32a** shows a high-resolution STEM (HRSTEM) image acquired at the interface between Fe_3O_4 porous layer and Au film, located in a squared region (□) of low-magnification $[1\bar{1}0]$-projected image (**Figure 2.32b**). The measured distance between two parallel Fe_3O_4 atomic planes exactly matches with the reported d-spacing of Fe_3O_4 (111) plane (JCPDS # 19-0629). For the Au layer, the measured and reported values also correspond to each other (JCPDS # 04-0784). This implies again that the Fe_3O_4 was indeed grown along (111) orientation with good epitaxial relationship with the Au (111) layer, in good agreement with the XRD data.

In addition to analyzing the local area, we examined the overall crystallographic characteristics of 40 nm porous film by collecting the SAD pattern from the squared region (□ in **Figure 2.32b**) of 800 x 800 nm^2. As shown in **Figure 2.32c**, all the spots are indexed either to (111), (002) and $(\bar{1}\bar{1}1)$ atomic planes of the Fe_3O_4 matrix (red) with strong reflections or to those of the mirror-symmetric twin (blue) with weak reflections, indicating that 40 nm porous film is comprised mostly of the single crystalline domains containing small amounts of twins over the large area. The observation of the mirror twins along [111] direction is consistent with Fe_3O_4 (311) pole-figures in **Figure 2.22**.

Another important thing to note is that the reflections in the diffraction pattern look like elongated spots instead of circular ones (**Figure 2.32c**). To elucidate the origin of this, we constructed two kinds of maps that quantify the degree of misorientations between local crystallites and visualize their distributions. We performed the scanning electron nanobeam diffraction (SEND) technique using very small electron probe beam (3.5 nm in full width half maximum) over the rectangular area (□ in **Figure 2.32b**) of 150 x 1000 nm^2. **Figure 2.32d** presents the orientation

map (left), the rotation angle map (right) and the representative diffraction patterns (middle) that were used for constructing the two maps. A number in each pattern means that the corresponding pattern was collected from the location marked with that number in two maps.

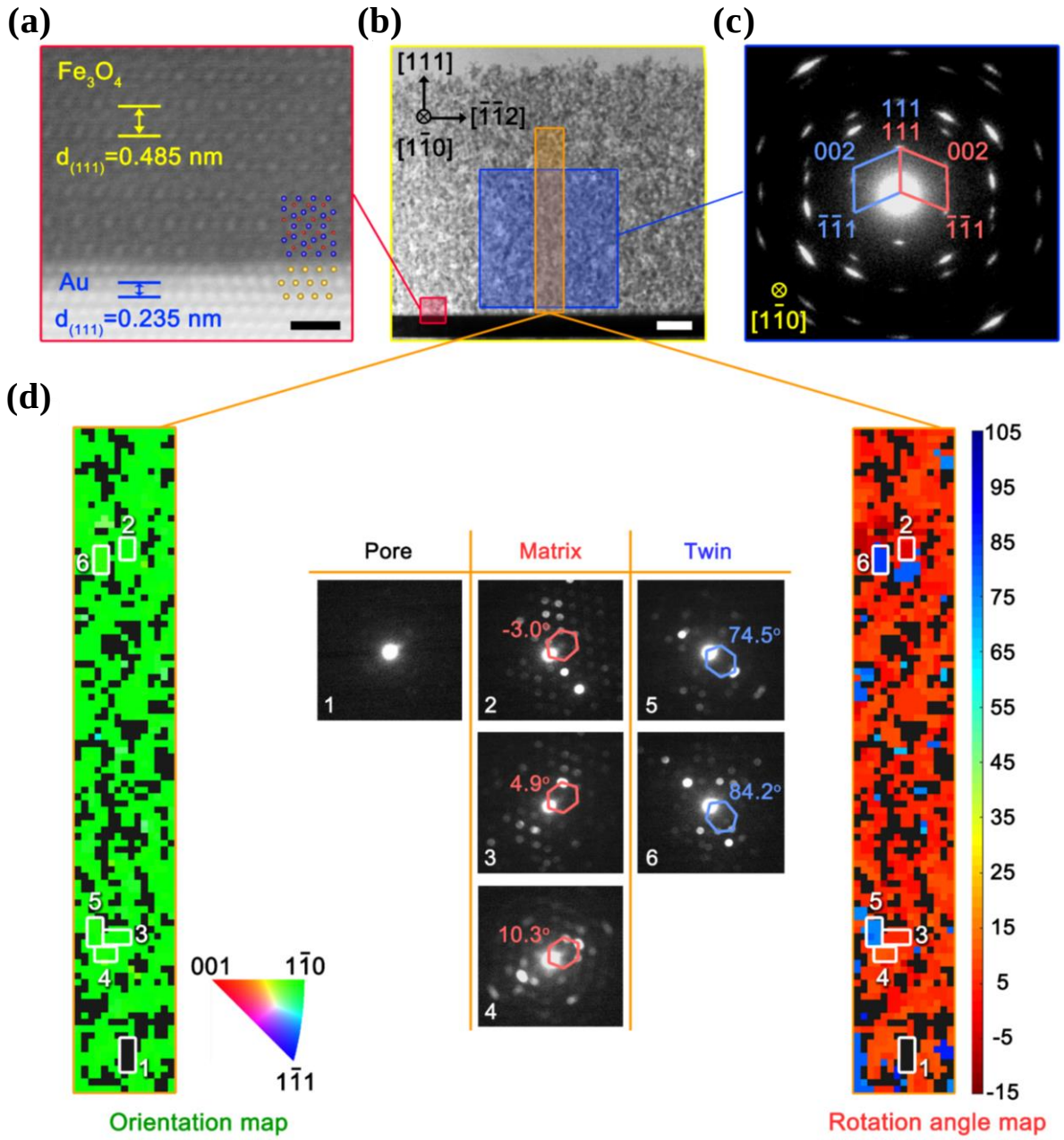

Figure 2.32 – Microstructural characterization of epitaxial 40 nm porous film. (a) [1$\bar{1}$0]-projected HRSTEM image taken at the interface between Au and Fe_3O_4 layers. Model atoms (inset; Fe: blue, Au: yellow) match with observed ones. Scale bar, 1 nm. (b) Bright-field low-magnification TEM image. Scale bar, 200 nm. (c) SAED pattern acquired over 800 x 800 nm^2. (d) Orientation (left), rotation angle (right) maps and SEND patterns (middle) used for constructing two maps. Red or blue number in diffraction pattern indicates rotation angle of matrix or twin, respectively.

The orientation map provides how much each crystal is deviated from a reference $[1\bar{1}0]$ direction. Except for the pores marked by black color, most regions seem to fall in with $[1\bar{1}0]$ direction when judging only from the color. However, our quantitative analysis revealed that the crystallites were tilted from a reference by 0.17 ~ 15.3^o with an average value of 3.3^o, implying that local crystalline domains are slightly misoriented to each other along $[1\bar{1}0]$ orientation keeping the epitaxy.

The rotation angle map visualizes 2D information on how much each domain is rotated from a reference [111] direction. Analyzing the direction of an elongated hexagon (marked with rotation angle) in each pattern of **Figure 2.32d**, which included an actual <111> direction of each crystallite, we figured out that the rotation angles of matrices ranged over -9.0 ~ 13.9^o with an average value of 3.3^o (reddish areas) and that those of twins were in the range of 68.3 ~ 87.4^o with an average value of 77.6^o (bluish areas). Other than the orientation mapping, the rotation map tells us the location of twins, which are usually observed nearby pores, as marked in **Figure 2.33**. Combining this result with the orientation map result, we can conclude that the 40 nm porous Fe_3O_4 film is comprised of the local crystal domains of ~ 3 nm size that are slightly misoriented each other three-dimensionally with the average misorientation angle of 3.3^o in all directions, keeping overall epitaxies along both in-plane and out-of-plane directions. To visualize the spatial distributions of orientations and rotation angles more clearly, two maps were reconstructed as the 3D histograms as exhibited in **Figure 2.34**. For the orientation map, tilt angles indicating deviation angles from the reference domain were used for clarification.

2.8.3 Principles of orientation and rotation angle mappings

A schematic in **Figure 2.35a** represents the way the orientation mapping was implemented. We measure how much each crystal is tilted (ψ) from an ideal $[1\bar{1}0]$-oriented crystal. Dark blue and light blue rectangular boxes indicate a reference (or ideal) crystal and a SEND-measured local crystal respectively. The reference one is defined to be perfectly orthogonal to the $[1\bar{1}0]$ orientation. In other words, diffraction pattern of the reference is supposed to be perfectly indexed to the $[1\bar{1}0]$-projected diffraction pattern of FCC single crystal[123], which lies in a greenest point of the stereographic projection triangle in the left part of **Figure 2.32d**. We compare each local crystal's diffraction pattern with the reference, and then decide if it is indexed to the ideal $(1\bar{1}0)$ pattern. If the film is a high-quality epitaxy, most local crystals will be $(1\bar{1}0)$ indexed. If the film

is polycrystalline, the local crystals will be indexed to diverse atomic planes such as (001) and $(1\bar{1}1)$ as well as $(1\bar{1}0)$. In our orientation mapping in **Figure 2.32d**, all areas, except for the pore regions, are green-colored, which tells us that the sample is highly epitaxial. **Table 2.7** exhibits the quantitative analysis results. The average tilt angle is 3.3°.

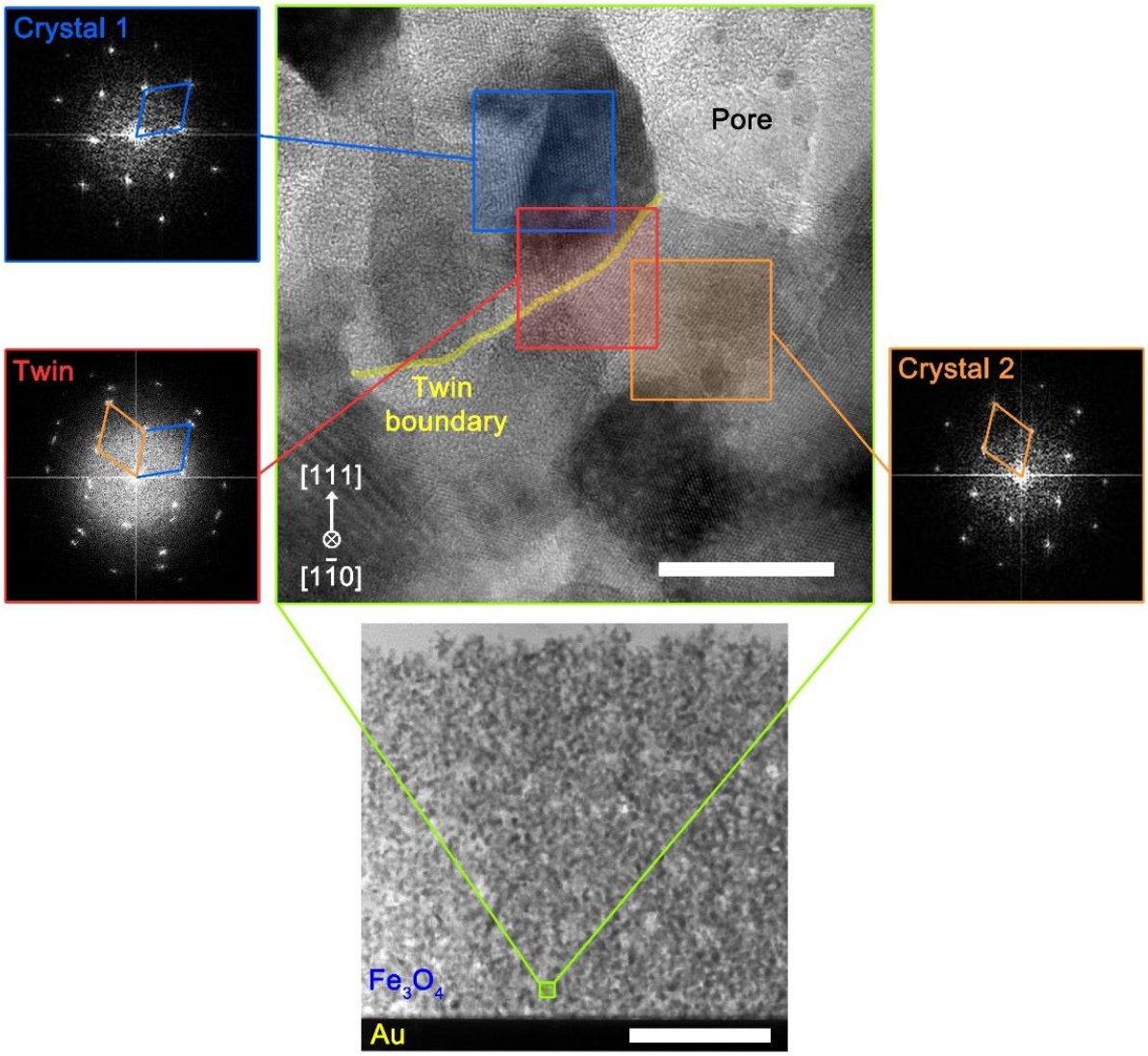

Figure 2.33 – Detailed look at twins formed around pores. HRTEM image and fast Fourier transform (FFT) patterns clearly show that mirror twins (□) comprised of two symmetric crystal regions (□ and □) are formed nearby the pore, especially for the boundary of colloids where two colloidal particles meet. This image is taken from a local region of the low-magnification TEM image below. Scale bars, 20 nm for the HRTEM image (top); and 500 nm for the low-magnification image (bottom).

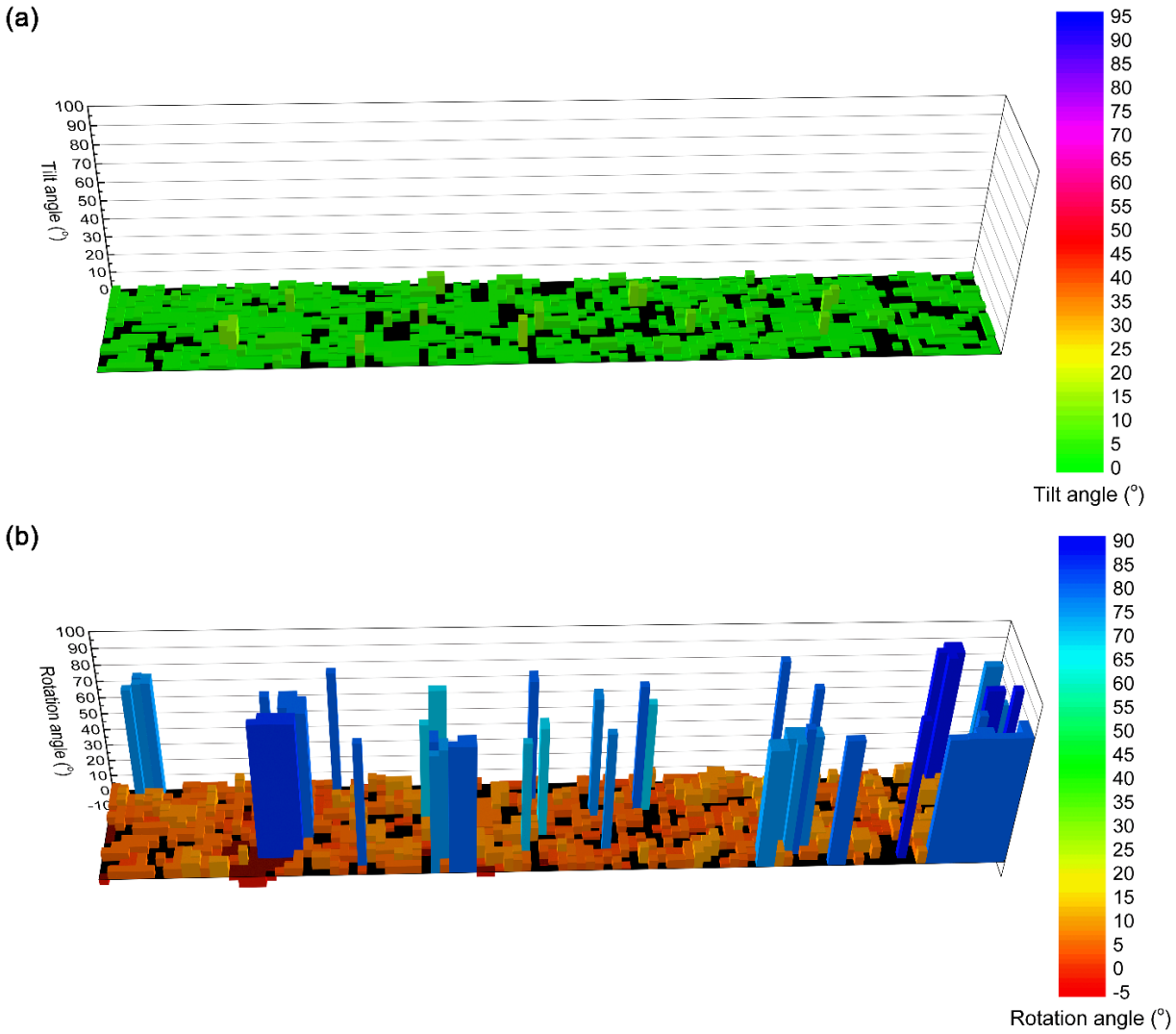

Figure 2.34 – 3D histograms reconstructed from the (a) orientation and the (b) rotation angle maps. Tilt angle in (a) implies how much the orientation of each domain is deviated from a reference one along plane normal direction. Histogram bars were colored so as to visualize the corresponding angles of domains more easily.

Similarly, **Figure 2.35b** illustrates the way the rotation angle mapping was conducted. We measure how much each crystal is rotated (φ) from an ideal [111]-oriented crystal (or reference crystal). The direction of (111) spot in the $[1\bar{1}0]$-projected reference pattern is supposed to be perfectly orthogonal to the sample surface, so that the rotation angle is zero degree (see a scale bar of the right part of **Figure 2.32d**). We compare each local crystal's diffraction pattern with the reference pattern to identify the rotation angle of each crystal. In the rotation angle map in **Figure 2.32d**, most areas are comprised of main matrices with small rotation angles (reddish), and a few areas are made of twins with larger rotation angles (bluish). The rotation angle mapping also

supports that our sample is highly epitaxial with the average rotation angle of 3.3°, as shown in **Table 2.7**.

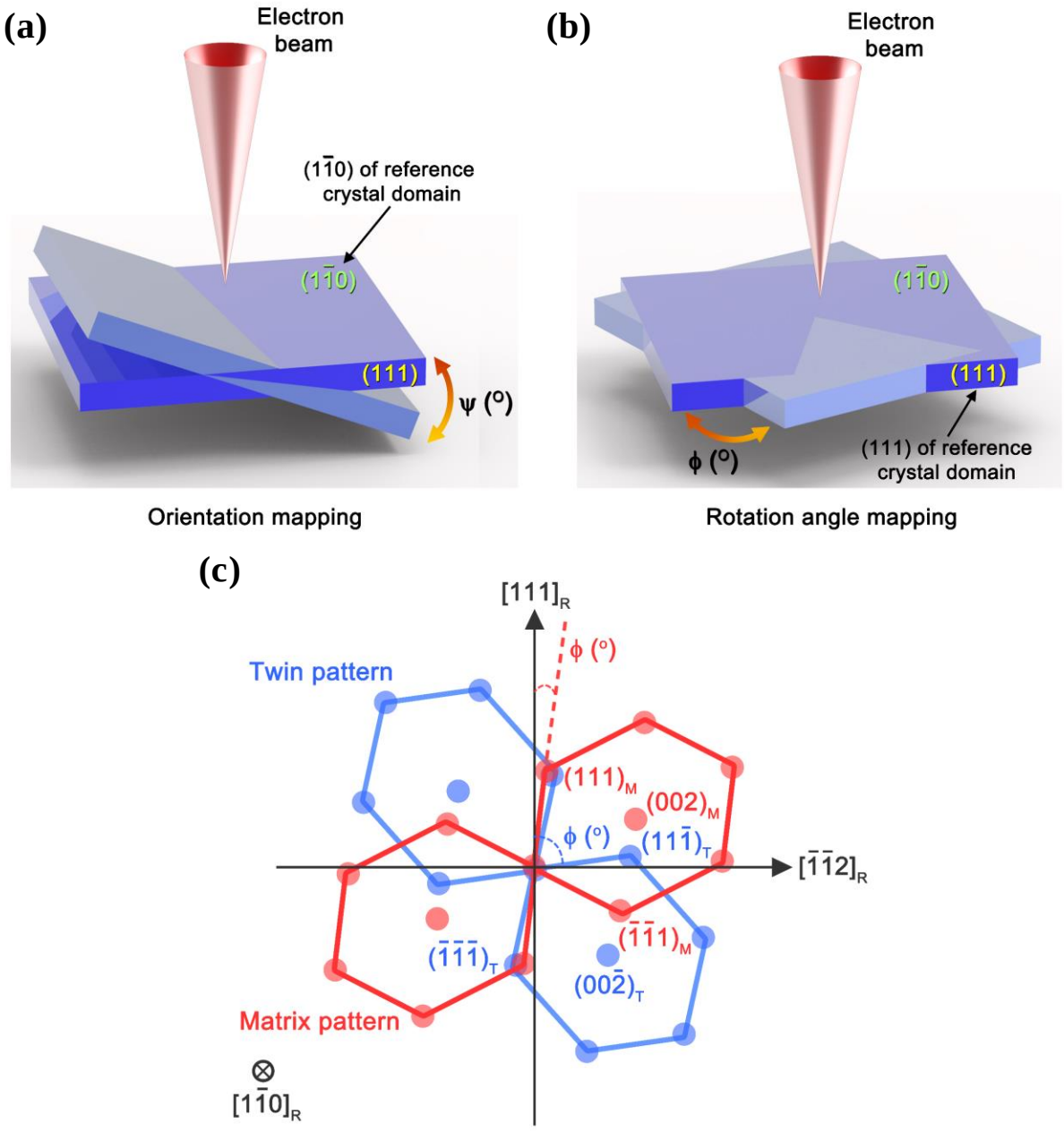

Figure 2.35 – Construction principles of two maps by scanning electron nanobeam diffraction (SEND) technique. (a, b) Schematics illustrating what information orientation and rotation maps contain, respectively. (c) Illustrations for the sake of explaining the meaning and the usage of the hexagons in the diffraction patterns in the middle part of **Figure 2.32d**.

Table 2.7 – Quantitative data of orientation and rotation angle maps. Average of both angles are 3.3°, indicative of the 40 nm porous Fe_3O_4 film is high-quality epitaxy consisting of three-dimensionally 3.3°-misoriented crystallites.

Diffraction pattern #	**Orientation index (hkl)**	**Rotation angle (°)**		**Component**
1	N.A.	N.A.		Pore
2	Close to $(1\bar{1}0)$	-3.0		Matrix
3		4.9		
4		10.3		
5		74.5		Twin
6		84.2		
	Tilt angle (°)	**Rotation angle (°)**		
	Matrix + Twin	Matrix	Twin	
Minimum	0.17	-9.0	68.3	
Maximum	15.3	13.9	87.4	
Average	**3.3**	**3.3**	77.6	

Figure 2.35c explains the meaning and the usage of the hexagons in the diffraction patterns in the middle part of **Figure 2.32d**. These hexagons are used for revealing the rotation angles of the local crystals. In a $[1\bar{1}0]$-projected diffraction pattern of the FCC single crystal[123], we can connect two sets of six spots that surrounds (002) and $(00\bar{2})$ spots respectively, and then we obtain two identical hexagons rotated by 180° to each other. By doing so, the <111> direction of each pattern can be easily identified. For the matrices, we measure how much the [111] direction of the pattern of the crystal (reddish) is rotated from the [111] direction of the reference pattern ($[111]_R$; grey colored in c). For the twins, we measure how much the $[11\bar{1}]$ direction of the pattern of the crystal (bluish) is rotated from the $[111]_R$. The reason we use different directions for the matrices and the twins, which are [111] and $[11\bar{1}]$ respectively, is that the matrix frame is set to be the same as the reference frame, but the twin frame is not.

2.9 Conclusions

We have successfully fabricated three different classes of materials, Bi_2Te_3, PbS, and Fe_3O_4 based on 3D meso/nanoarchitectures aiming at attaining low thermal conductivity and high electrical conductivity at the same time. Although Bi_2Te_3 is one of the best materials in terms of those two properties, fabrication of single crystalline 3D structure is very tricky due to its inherent crystallographic nature, van der Waal interactions along [111] directions. Instead, the conformal and polycrystalline 3D meso/nanostructures were synthesized *via* pulsed electrodeposition of precursors through colloidal crystal templates.

In contrast, another candidate, PbS has a rock-salt cubic structure, so we fabricated epitaxial PbS dense film on GaAs single crystal wafer using CBD method and then grew colloidal crystals on the top of the film. However, lower electrical conductivity of PbS compared to those of metals such as Au and Cu which serve conductive electrodes for conventional electrodeposition, limited the nucleation during electrochemical deposition of PbS through colloidal templates.

Ideal lattice mismatches among Fe_3O_4, Au, Ti, and sapphire substrate, enabled us to fabricate epitaxial Fe_3O_4 3D meso/nanostructures using colloidal crystal growth followed by electrodeposition. Keeping the single crystallin nature, we successfully reduced the pore sizes of 3D structures down to 40 nm where the feature sizes are similar with the MPFs of diffusive thermal phonons induced by Umklapp phonon-phonon scatterings at room temperature. Thermal and electrical transport properties of single crystalline Fe_3O_4 3D structures are discussed in following chapters.

2.10 References

1 Liu, W., Yan, X., Chen, G. & Ren, Z. Recent advances in thermoelectric nanocomposites. *Nano Energy* **1**, 42-56, doi:10.1016/j.nanoen.2011.10.001 (2012).

2 Hsiao, Y. Y., Chang, W. C. & Chen, S. L. A mathematic model of thermoelectric module with applications on waste heat recovery from automobile engine. *Energy* **35**, 1447-1454, doi:https://doi.org/10.1016/j.energy.2009.11.030 (2010).

3 Orr, B., Akbarzadeh, A., Mochizuki, M. & Singh, R. A review of car waste heat recovery systems utilising thermoelectric generators and heat pipes. *Applied Thermal Engineering* **101**, 490-495, doi:https://doi.org/10.1016/j.applthermaleng.2015.10.081 (2016).

4 Snyder, G. J. & Toberer, E. S. Complex thermoelectric materials. *Nat Mater* **7**, 105-114, doi:10.1038/nmat2090 (2008).

5 Ihab El-Kady, R. H. O. I., Patrick E. Hopkins, Zayd C. Leseman, Drew F. Goettler, Bongsang Kim, Charles M. Reinke, and Mehmet F. Su. Phonon Manipulation with Phononic Crystals. *SANDIA REPORT* **SAND2012-0127** (2012).
6 Takabatake, T., Suekuni, K., Nakayama, T. & Kaneshita, E. Phonon-glass electron-crystal thermoelectric clathrates: Experiments and theory. *Reviews of Modern Physics* **86**, 669-716, doi:10.1103/RevModPhys.86.669 (2014).
7 A. J. Minnich, a. M. S. D., b Z. F. Ren*c and G. Chen*a. Bulk nanostructured thermoelectric materials: current research and future prospects. *Energy & Environmental Science* **2**, doi:10.1039/b822664b (2009).
8 Vining, C. B. An inconvenient truth about thermoelectrics. *Nat Mater* **8**, 83-85, doi:10.1038/nmat2361 (2009).
9 Heremans, J. P., Dresselhaus, M. S., Bell, L. E. & Morelli, D. T. When thermoelectrics reached the nanoscale. *Nat Nanotechnol* **8**, 471-473, doi:10.1038/nnano.2013.129 (2013).
10 Zhao, L. D. *et al.* Ultralow thermal conductivity and high thermoelectric figure of merit in SnSe crystals. *Nature* **508**, 373-377, doi:10.1038/nature13184 (2014).
11 Zhao, L. D. *et al.* Ultrahigh power factor and thermoelectric performance in hole-doped single-crystal SnSe. *Science* **351**, 141-144, doi:10.1126/science.aad3749 (2016).
12 Vineis, C. J., Shakouri, A., Majumdar, A. & Kanatzidis, M. G. Nanostructured thermoelectrics: big efficiency gains from small features. *Adv Mater* **22**, 3970-3980, doi:10.1002/adma.201000839 (2010).
13 Zebarjadi, M., Esfarjani, K., Dresselhaus, M. S., Ren, Z. F. & Chen, G. Perspectives on thermoelectrics: from fundamentals to device applications. *Energy Environ. Sci.* **5**, 5147-5162, doi:10.1039/c1ee02497c (2012).
14 Nielsch, K., Bachmann, J., Kimling, J. & Böttner, H. Thermoelectric Nanostructures: From Physical Model Systems towards Nanograined Composites. *Advanced Energy Materials* **1**, 713-731, doi:10.1002/aenm.201100207 (2011).
15 Zhao, L.-D., Dravid, V. P. & Kanatzidis, M. G. The panoscopic approach to high performance thermoelectrics. *Energy Environ. Sci.* **7**, 251-268, doi:10.1039/c3ee43099e (2014).
16 Hicks, L. D. & Dresselhaus, M. S. Effect of quantum-well structures on the thermoelectric figure of merit. *Physical Review B* **47**, 12727-12731, doi:10.1103/PhysRevB.47.12727 (1993).
17 Hicks, L. D. & Dresselhaus, M. S. Thermoelectric figure of merit of a one-dimensional conductor. *Physical Review B* **47**, 16631-16634, doi:10.1103/PhysRevB.47.16631 (1993).
18 Cahill, D. G. *et al.* Nanoscale thermal transport. II. 2003–2012. *Applied Physics Reviews* **1**, 011305, doi:10.1063/1.4832615 (2014).
19 Cahill, D. G. *et al.* Nanoscale thermal transport. *Journal of Applied Physics* **93**, 793, doi:10.1063/1.1524305 (2003).
20 Klemens, P. G. Thermal Conductivity and Lattice Vibrational Modes. **7**, 1-98, doi:10.1016/s0081-1947(08)60551-2 (1958).
21 Ma, J., Sadhu, J. S., Ganta, D., Tian, H. & Sinha, S. Thermal transport in 2- and 3-dimensional periodic "holey" nanostructures. *AIP Advances* **4**, 124502, doi:10.1063/1.4904073 (2014).
22 Poudel, B. *et al.* High-thermoelectric performance of nanostructured bismuth antimony telluride bulk alloys. *Science* **320**, 634-638, doi:10.1126/science.1156446 (2008).
23 Ma, Y. *et al.* Enhanced thermoelectric figure-of-merit in p-type nanostructured bismuth

antimony tellurium alloys made from elemental chunks. *Nano Lett* **8**, 2580-2584, doi:10.1021/nl8009928 (2008).
24 Wang, X. W. *et al.* Enhanced thermoelectric figure of merit in nanostructured n-type silicon germanium bulk alloy. *Applied Physics Letters* **93**, 193121, doi:10.1063/1.3027060 (2008).
25 Joshi, G. *et al.* Enhanced thermoelectric figure-of-merit in nanostructured p-type silicon germanium bulk alloys. *Nano Lett* **8**, 4670-4674, doi:10.1021/nl8026795 (2008).
26 Androulakis, J. *et al.* Spinodal decomposition and nucleation and growth as a means to bulk nanostructured thermoelectrics: enhanced performance in Pb(1-x)Sn(x)Te-PbS. *J Am Chem Soc* **129**, 9780-9788, doi:10.1021/ja071875h (2007).
27 Biswas, K. *et al.* High-performance bulk thermoelectrics with all-scale hierarchical architectures. *Nature* **489**, 414-418, doi:10.1038/nature11439 (2012).
28 Androulakis, J. *et al.* Thermoelectrics from abundant chemical elements: high-performance nanostructured PbSe-PbS. *J Am Chem Soc* **133**, 10920-10927, doi:10.1021/ja203022c (2011).
29 Zhao, L. D. *et al.* High performance thermoelectrics from earth-abundant materials: enhanced figure of merit in PbS by second phase nanostructures. *J Am Chem Soc* **133**, 20476-20487, doi:10.1021/ja208658w (2011).
30 Wang, H., Pei, Y., LaLonde, A. D. & Snyder, G. J. Weak electron-phonon coupling contributing to high thermoelectric performance in n-type PbSe. *Proc Natl Acad Sci U S A* **109**, 9705-9709, doi:10.1073/pnas.1111419109 (2012).
31 Wang, H., Pei, Y., LaLonde, A. D. & Snyder, G. J. Heavily doped p-type PbSe with high thermoelectric performance: an alternative for PbTe. *Adv Mater* **23**, 1366-1370, doi:10.1002/adma.201004200 (2011).
32 Peng, H., Song, J.-H., Kanatzidis, M. G. & Freeman, A. J. Electronic structure and transport properties of doped PbSe. *Physical Review B* **84**, doi:10.1103/PhysRevB.84.125207 (2011).
33 Androulakis, J. *et al.* High-temperature charge and thermal transport properties of then-type thermoelectric material PbSe. *Physical Review B* **84**, doi:10.1103/PhysRevB.84.155207 (2011).
34 Chiritescu, C. *et al.* Ultralow thermal conductivity in disordered, layered WSe2 crystals. *Science* **315**, 351-353, doi:10.1126/science.1136494 (2007).
35 Caylor, J. C., Coonley, K., Stuart, J., Colpitts, T. & Venkatasubramanian, R. Enhanced thermoelectric performance in PbTe-based superlattice structures from reduction of lattice thermal conductivity. *Applied Physics Letters* **87**, 023105, doi:10.1063/1.1992662 (2005).
36 Lee, S. M., Cahill, D. G. & Venkatasubramanian, R. Thermal conductivity of Si–Ge superlattices. *Applied Physics Letters* **70**, 2957, doi:10.1063/1.118755 (1997).
37 Capinski, W. S. & Maris, H. J. Thermal conductivity of GaAs/AlAs superlattices. *Physica B: Condensed Matter* **219-220**, 699-701, doi:10.1016/0921-4526(95)00858-6 (1996).
38 Venkatasubramanian, R., Siivola, E., Colpitts, T. & O'Quinn, B. Thin-film thermoelectric devices with high room-temperature figures of merit. *Nature* **413**, 597-602, doi:10.1038/35098012 (2001).
39 Hyldgaard, P. & Mahan, G. D. Phonon superlattice transport. *Physical Review B* **56**, 10754-10757, doi:10.1103/PhysRevB.56.10754 (1997).
40 Narayanamurti, V., Störmer, H. L., Chin, M. A., Gossard, A. C. & Wiegmann, W. Selective Transmission of High-Frequency Phonons by a Superlattice: The "Dielectric" Phonon Filter. *Physical Review Letters* **43**, 2012-2016, doi:10.1103/PhysRevLett.43.2012 (1979).
41 Simkin, M. V. & Mahan, G. D. Minimum thermal conductivity of superlattices. *Phys Rev*

Lett **84**, 927-930, doi:10.1103/PhysRevLett.84.927 (2000).
42 Venkatasubramanian, R. Lattice thermal conductivity reduction and phonon localizationlike behavior in superlattice structures. *Physical Review B* **61**, 3091-3097, doi:10.1103/PhysRevB.61.3091 (2000).
43 Chen, G. Thermal conductivity and ballistic-phonon transport in the cross-plane direction of superlattices. *Physical Review B* **57**, 14958-14973, doi:10.1103/PhysRevB.57.14958 (1998).
44 Boukai, A. I. *et al.* Silicon nanowires as efficient thermoelectric materials. *Nature* **451**, 168-171, doi:10.1038/nature06458 (2008).
45 Hochbaum, A. I. *et al.* Enhanced thermoelectric performance of rough silicon nanowires. *Nature* **451**, 163-167, doi:10.1038/nature06381 (2008).
46 Kim, H., Kim, I., Choi, H.-j. & Kim, W. Thermal conductivities of Si[sub 1−x]Ge[sub x] nanowires with different germanium concentrations and diameters. *Applied Physics Letters* **96**, 233106, doi:10.1063/1.3443707 (2010).
47 Kittel, C. Interpretation of the Thermal Conductivity of Glasses. *Physical Review* **75**, 972-974, doi:10.1103/PhysRev.75.972 (1949).
48 Li, D. *et al.* Thermal conductivity of individual silicon nanowires. *Applied Physics Letters* **83**, 2934, doi:10.1063/1.1616981 (2003).
49 Mavrokefalos, A. *et al.* Thermoelectric and structural characterizations of individual electrodeposited bismuth telluride nanowires. *Journal of Applied Physics* **105**, 104318, doi:10.1063/1.3133145 (2009).
50 Moore, A. L., Pettes, M. T., Zhou, F. & Shi, L. Thermal conductivity suppression in bismuth nanowires. *Journal of Applied Physics* **106**, 034310, doi:10.1063/1.3191657 (2009).
51 Roh, J. W. *et al.* Size-dependent thermal conductivity of individual single-crystalline PbTe nanowires. *Applied Physics Letters* **96**, 103101, doi:10.1063/1.3352049 (2010).
52 Wang, Z. & Mingo, N. Diameter dependence of SiGe nanowire thermal conductivity. *Applied Physics Letters* **97**, 101903, doi:10.1063/1.3486171 (2010).
53 Zeng, L. *et al.* Measuring Phonon Mean Free Path Distributions by Probing Quasiballistic Phonon Transport in Grating Nanostructures. *Sci Rep* **5**, 17131, doi:10.1038/srep17131 (2015).
54 Gorishnyy, T., Ullal, C. K., Maldovan, M. & Thomas, E. L. Sound ideas. *Physics World* **18** (2005).
55 Thomas, J. Phononic crystals: Sound barrier. *Nature Nanotechnology*, doi:10.1038/nnano.2006.65 (2006).
56 Kushwaha, M. S. Classical Band Structure of Periodic Elastic Composites. *International Journal of Modern Physics B* **10**, 977-1094, doi:10.1142/s0217979296000398 (1996).
57 Gorishnyy, T., Ullal, C. K., Maldovan, M., Fytas, G. & Thomas, E. L. Hypersonic phononic crystals. *Phys Rev Lett* **94**, 115501, doi:10.1103/PhysRevLett.94.115501 (2005).
58 Balandin, A. A. Nanophononics: phonon engineering in nanostructures and nanodevices. *J Nanosci Nanotechnol* **5**, 1015-1022, doi:10.1166/jnn.2005.175 (2005).
59 Joannopoulos, J. D., Villeneuve, P. R. & Fan, S. Photonic crystals: putting a new twist on light. *Nature* **386**, 143-149, doi:10.1038/386143a0 (1997).
60 Hoogeboom-Pot, K. M. *et al.* A new regime of nanoscale thermal transport: Collective diffusion increases dissipation efficiency. *Proc Natl Acad Sci U S A* **112**, 4846-4851, doi:10.1073/pnas.1503449112 (2015).

61 Hu, Y., Zeng, L., Minnich, A. J., Dresselhaus, M. S. & Chen, G. Spectral mapping of thermal conductivity through nanoscale ballistic transport. *Nat Nanotechnol* **10**, 701-706, doi:10.1038/nnano.2015.109 (2015).
62 Barako, M. T. *et al.* Quasi-ballistic Electronic Thermal Conduction in Metal Inverse Opals. *Nano Lett* **16**, 2754-2761, doi:10.1021/acs.nanolett.6b00468 (2016).
63 Balandin, A. A. & Nika, D. L. Phononics in low-dimensional materials. *Materials Today* **15**, 266-275, doi:10.1016/s1369-7021(12)70117-7 (2012).
64 Lee, J. H., Galli, G. A. & Grossman, J. C. Nanoporous Si as an efficient thermoelectric material. *Nano Lett* **8**, 3750-3754, doi:10.1021/nl802045f (2008).
65 Yang, L., Yang, N. & Li, B. Extreme low thermal conductivity in nanoscale 3D Si phononic crystal with spherical pores. *Nano Lett* **14**, 1734-1738, doi:10.1021/nl403750s (2014).
66 Wei, N., Xu, L., Wang, H. Q. & Zheng, J. C. Strain engineering of thermal conductivity in graphene sheets and nanoribbons: a demonstration of magic flexibility. *Nanotechnology* **22**, 105705, doi:10.1088/0957-4484/22/10/105705 (2011).
67 Puurtinen, T. & Maasilta, I. Low-Temperature Coherent Thermal Conduction in Thin Phononic Crystal Membranes. *Crystals* **6**, 72, doi:10.3390/cryst6060072 (2016).
68 Ma, J. *et al.* Coherent phonon-grain boundary scattering in silicon inverse opals. *Nano Lett* **13**, 618-624, doi:10.1021/nl304190s (2013).
69 Yu, J. K., Mitrovic, S., Tham, D., Varghese, J. & Heath, J. R. Reduction of thermal conductivity in phononic nanomesh structures. *Nat Nanotechnol* **5**, 718-721, doi:10.1038/nnano.2010.149 (2010).
70 Hopkins, P. E. *et al.* Reduction in the thermal conductivity of single crystalline silicon by phononic crystal patterning. *Nano Lett* **11**, 107-112, doi:10.1021/nl102918q (2011).
71 Osherov, A., Shandalov, M., Ezersky, V. & Golan, Y. EPITAXY and orientation control in chemical solution deposited PbS and PbSe monocrystalline films. *Journal of Crystal Growth* **304**, 169-178, doi:10.1016/j.jcrysgro.2007.02.021 (2007).
72 Osherov, A., Ezersky, V. & Golan, Y. The role of solution composition in chemical bath deposition of epitaxial thin films of PbS on GaAs(100). *Journal of Crystal Growth* **308**, 334-339, doi:10.1016/j.jcrysgro.2007.07.046 (2007).
73 Shebanova, O. N. & Lazor, P. Raman spectroscopic study of magnetite (FeFe2O4): a new assignment for the vibrational spectrum. *Journal of Solid State Chemistry* **174**, 424-430, doi:https://doi.org/10.1016/S0022-4596(03)00294-9 (2003).
74 Shebanova, O. N. & Lazor, P. Raman study of magnetite (Fe3O4): laser-induced thermal effects and oxidation. *Journal of Raman Spectroscopy* **34**, 845-852, doi:10.1002/jrs.1056 (2003).
75 Naylor, A. J., Koukharenko, E., Nandhakumar, I. S. & White, N. M. Surfactant-mediated electrodeposition of bismuth telluride films and its effect on microstructural properties. *Langmuir* **28**, 8296-8299, doi:10.1021/la301367m (2012).
76 Zou, Z. G., Cai, K. F., Chen, S. & Qin, Z. Pulsed electrodeposition and characterization of Bi2Te3−ySey films. *Materials Research Bulletin* **47**, 3292-3295, doi:10.1016/j.materresbull.2012.07.036 (2012).
77 Li, L., Yang, Y., Huang, X., Li, G. & Zhang, L. Pulsed electrodeposition of single-crystalline Bi2Te3 nanowire arrays. *Nanotechnology* **17**, 1706-1712, doi:10.1088/0957-4484/17/6/027 (2006).
78 Cahill, D. G. Analysis of heat flow in layered structures for time-domain thermoreflectance. *Review of Scientific Instruments* **75**, 5119-5122, doi:10.1063/1.1819431 (2004).

79 Soni, A. *et al.* Enhanced thermoelectric properties of solution grown Bi2Te(3-x)Se(x) nanoplatelet composites. *Nano Lett* **12**, 1203-1209, doi:10.1021/nl2034859 (2012).
80 Yan, X. *et al.* Experimental studies on anisotropic thermoelectric properties and structures of n-type Bi2Te2.7Se0.3. *Nano Lett* **10**, 3373-3378, doi:10.1021/nl101156v (2010).
81 Goldsmid, H. Bismuth Telluride and Its Alloys as Materials for Thermoelectric Generation. *Materials* **7**, 2577-2592, doi:10.3390/ma7042577 (2014).
82 Teweldebrhan, D., Goyal, V. & Balandin, A. A. Exfoliation and characterization of bismuth telluride atomic quintuples and quasi-two-dimensional crystals. *Nano Lett* **10**, 1209-1218, doi:10.1021/nl903590b (2010).
83 Zeng, Z. *et al.* Molecular beam epitaxial growth of Bi2Te3 and Sb2Te3 topological insulators on GaAs (111) substrates: a potential route to fabricate topological insulator p-n junction. *AIP Advances* **3**, 072112, doi:10.1063/1.4815972 (2013).
84 Switzer, J. A. Chemistry. Atomic layer electrodeposition. *Science* **338**, 1300-1301, doi:10.1126/science.1231853 (2012).
85 Zhu, W. *et al.* Optimization of the formation of bismuth telluride thin film by using ECALE. *Journal of Electroanalytical Chemistry* **585**, 83-88, doi:10.1016/j.jelechem.2005.07.016 (2005).
86 Zhu, W. *et al.* Effect of potential on bismuth telluride thin film growth by electrochemical atomic layer epitaxy. *Electrochimica Acta* **50**, 4041-4047, doi:10.1016/j.electacta.2005.01.003 (2005).
87 Yang, J., Zhu, W., Gao, X., Bao, S. & Fan, X. Electrochemical aspects of the formation of Bi2Te3 thin film via the route of ECALE. *Journal of Electroanalytical Chemistry* **577**, 117-123, doi:10.1016/j.jelechem.2004.11.023 (2005).
88 Roy, A. *et al.* Two-dimensional weak anti-localization in Bi2Te3 thin film grown on Si(111)-(7 × 7) surface by molecular beam epitaxy. *Applied Physics Letters* **102**, 163118, doi:10.1063/1.4803018 (2013).
89 Zhang, H., Yu, X. & Braun, P. V. Three-dimensional bicontinuous ultrafast-charge and -discharge bulk battery electrodes. *Nat Nanotechnol* **6**, 277-281, doi:10.1038/nnano.2011.38 (2011).
90 Kulp, E. A. *et al.* Electrodeposition of Epitaxial Magnetite Films and Ferrihydrite Nanoribbons on Single-Crystal Gold. *Chemistry of Materials* **21**, 5022-5031, doi:10.1021/cm9013514 (2009).
91 Dehm, G. Growth and microstructural stability of epitaxial Al films on (0001) α-Al2O3 substrates. *Acta Materialia* **50**, 5021-5032, doi:10.1016/s1359-6454(02)00347-6 (2002).
92 Bialas, H. & Heneka, K. Epitaxy of fcc metals on dielectric substrates. *Vacuum* **45**, 79-87, doi:https://doi.org/10.1016/0042-207X(94)90346-8 (1994).
93 Batyrev, I. G. & Kleinman, L. In-plane relaxation of Cu(111) andAl(111)/α−Al2O3(0001) interfaces. *Physical Review B* **64**, doi:10.1103/PhysRevB.64.033410 (2001).
94 Dehm, G., Rühle, M., Ding, G. & Raj, R. Growth and structure of copper thin films deposited on (0001) sapphire by molecular beam epitaxy. *Philosophical Magazine B* **71**, 1111-1124, doi:10.1080/01418639508241899 (1995).
95 Fogarassy, Z., Dobrik, G., Varga, L. K., Biró, L. P. & Lábár, J. L. Growth of Ni layers on single crystal sapphire substrates. *Thin Solid Films* **539**, 96-101, doi:https://doi.org/10.1016/j.tsf.2013.05.077 (2013).
96 Muslimov, A. E., Butashin, A. V., Kolymagin, A. B., Vlasov, V. P. & Kanevsky, V. M. Epitaxy of gold films on the structured (0001) sapphire surface. *Crystallography Reports*

60, 942-945, doi:10.1134/s1063774515060218 (2015).
97 Heinemann, K., Kim, H. K. & Poppa, H. Nucleation, growth, and postdeposition thermally induced epitaxy of gold on sapphire. *Journal of Vacuum Science and Technology* **16**, 622-624, doi:10.1116/1.570014 (1979).
98 Pilliar, R. M. & Nutting, J. Solid-solid interfacial energy determinations in metal-ceramic systems. *The Philosophical Magazine: A Journal of Theoretical Experimental and Applied Physics* **16**, 181-188, doi:10.1080/14786436708229267 (1967).
99 Kästle, G., Boyen, H. G., Schröder, A., Plettl, A. & Ziemann, P. Size effect of the resistivity of thin epitaxial gold films. *Physical Review B* **70**, 165414, doi:10.1103/PhysRevB.70.165414 (2004).
100 Kästle, G. *et al.* Growth of thin, flat, epitaxial (111) oriented gold films on c-cut sapphire. *Surface Science* **498**, 168-174, doi:https://doi.org/10.1016/S0039-6028(01)01685-5 (2002).
101 Sorenson, T. A., Morton, S. A., Waddill, G. D. & Switzer, J. A. Epitaxial Electrodeposition of Fe3O4Thin Films on the Low-Index Planes of Gold. *Journal of the American Chemical Society* **124**, 7604-7609, doi:10.1021/ja0201101 (2002).
102 Zheng, Q. *et al.* Epitaxial growth of three dimensionally structured III-V photonic crystal via hydride vapor phase epitaxy. *Journal of Applied Physics* **118**, 224303, doi:10.1063/1.4937273 (2015).
103 Pereira, S. *et al.* Strain and composition distributions in wurtzite InGaN/GaN layers extracted from x-ray reciprocal space mapping. *Applied Physics Letters* **80**, 3913-3915, doi:10.1063/1.1481786 (2002).
104 Magnetite from magnetotactic bacteria; size distributions and twinning. *Am Mineral* **83**, 1387-1398, doi:10.2138/am-1998-11-1228 (1998).
105 DANA, J. D. & Hurlbut, C. S. *Dana's Manual of Mineralogy. Revised by Cornelius S. Hurlbut. (17th Edition.)*. (New York; Chapman & Hall: London, 1959).
106 Kelly, A. & Groves, G. W. *Crystallography and crystal defects, Appendix 3*. (Addison-Wesley, 1970).
107 Thelander, E., Gerlach, J. W., Ross, U., Lotnyk, A. & Rauschenbach, B. Low temperature epitaxy of Ge-Sb-Te films on BaF2 (111) by pulsed laser deposition. *Applied Physics Letters* **105**, 221908, doi:10.1063/1.4903489 (2014).
108 Guo, J., Chang, H. L. M. & Lam, D. J. Substrate surface step effects on microstructure of epitaxial films. *Applied Physics Letters* **61**, 3116-3117, doi:10.1063/1.107978 (1992).
109 Dar, M. I. & Shivashankar, S. A. Single crystalline magnetite, maghemite, and hematite nanoparticles with rich coercivity. *RSC Advances* **4**, 4105-4113, doi:10.1039/C3RA45457F (2014).
110 Jubb, A. M. & Allen, H. C. Vibrational Spectroscopic Characterization of Hematite, Maghemite, and Magnetite Thin Films Produced by Vapor Deposition. *ACS Applied Materials & Interfaces* **2**, 2804-2812, doi:10.1021/am1004943 (2010).
111 Shebanova, O. N. & Lazor, P. Vibrational modeling of the thermodynamic properties of magnetite (Fe3O4) at high pressure from Raman spectroscopic study. *The Journal of Chemical Physics* **119**, 6100-6110, doi:10.1063/1.1602072 (2003).
112 Mayer, M. Ion beam analysis of rough thin films. *Nuclear Instruments and Methods in Physics Research Section B: Beam Interactions with Materials and Atoms* **194**, 177-186, doi:https://doi.org/10.1016/S0168-583X(02)00689-4 (2002).
113 Sitko, R. & Zawisza, B. *Quantification in X-Ray Fluorescence Spectrometry*. (2012).
114 Ma, J. & Sinha, S. Thermoelectric properties of highly doped n-type polysilicon inverse

opals. *Journal of Applied Physics* **112**, 073719, doi:10.1063/1.4758382 (2012).
115 Mahan, G. D., Poilvert, N. & Crespi, V. H. Thermoelectric properties of inverse opals. *Journal of Applied Physics* **119**, 075101, doi:10.1063/1.4941784 (2016).
116 Villeneuve, V. W. A. d. *et al.* Hard sphere crystal nucleation and growth near large spherical impurities. *Journal of Physics: Condensed Matter* **17**, S3371 (2005).
117 Cheng, Z. *et al.* Phase diagram of hard spheres. *Materials & Design* **22**, 529-534, doi:https://doi.org/10.1016/S0261-3069(01)00015-2 (2001).
118 von Freymann, G., Kitaev, V., Lotsch, B. V. & Ozin, G. A. Bottom-up assembly of photonic crystals. *Chem Soc Rev* **42**, 2528-2554, doi:10.1039/c2cs35309a (2013).
119 Vargas, M. C. & Pérez-Ángel, G. Crystallization time scales for polydisperse hard-sphere fluids. *Physical Review E* **87**, 042313, doi:10.1103/PhysRevE.87.042313 (2013).
120 Dickinson, E., Parker, R. & Lal, M. Polydispersity and the colloidal order-disorder transition. *Chemical Physics Letters* **79**, 578-582, doi:https://doi.org/10.1016/0009-2614(81)85039-7 (1981).
121 Pusey, P. N. The effect of polydispersity on the crystallization of hard spherical colloids. *Journal de Physique* **48**, 709-712, doi:10.1051/jphys:01987004805070900 (1987).
122 We used 8 % w/v sulfate latex beads suspensions from ThermoFisher Scientific, of which lot numbers are 727433, 638478, 1229744, and 1189918 for 500, 200, 100, and 40 nm, respectively.
123 Williams, D. B. & Carter, C. B. *Transmission Electron Microscopy: A Textbook for Materials Science. Diffraction. II*. 300, (Springer, 1996).

CHAPTER 3.

THERMAL TRANSPORT PROPERTIES OF EPITAXIAL Fe_3O_4 3D MESO/NANOSTRUCTURES

3.1 Introduction

Bi_2Te_3[1-4] and PbS[5,6] have been considered promising thermoelectric candidates at low and high temperatures respectively due to their ideal thermal and electrical properties. Thermal and electrical conductivities of bulk Bi_2Te_3 are 1.4 W m^{-1} K^{-1} and 10^5 S m^{-1} respectively[1-4], and those of bulk PbS are 2.5 W m^{-1} K^{-1} and 3 x 10^4 S m^{-1} respectively[5,6]. However, both have critical drawbacks. Tellurium is costly, and lead is toxic. Besides, it is very challenging to grow those materials as epitaxies around complex 3D geometry of colloidal crystals using the electrochemical deposition as discussed above.

In contrast, Fe_3O_4, which we successfully fabricated into epitaxial 3D meso/nanostructures, possesses diverse advantageous aspects including non-toxicity, abundant iron source, thermal stability, and easiness to synthesize[7]. The thermal conductivity of Fe_3O_4[8,9] is quite low, 6 ~ 7 W m^{-1} K^{-1}, but still has enough room to decrease. Also, it has the moderately high electrical conductivity[10-13], ~ 10^4 S m^{-1}. The electrical properties of Fe_3O_4 is very distinct from other transition binary oxides such as ZnO, TiO_2, CuO, CoO, and Fe_2O_3 which are known to demonstrate typical semi-conducting behaviors. In this chapter, we focus on studying the thermal transport of Fe_3O_4 epitaxial 3D meso/nanostructures. The electron transport will be discussed in **Chapter 4**.

3.1.1 Crystal structure of Fe_3O_4

Fe_3O_4, namely magnetite, is a ferrimagnetic n-type half-metallic material with an inverse spinel structure (space group Fd3m) with a lattice constant of 0.8397 nm[14-16]. The inverse spinel structure consists of a face centered cubic oxygen lattice, with Fe^{3+} ions filling 1/8 of the available tetrahedral sites (so called A sites) and equal amounts of Fe^{2+} and Fe^{3+} ions filling half of the available octahedral sites (called B sites) as depicted in **Figure 3.1**[17]. This is denoted by $Fe^{3+}(Fe^{2+},Fe^{3+})O_4$. The ferrimagnetism is observed below Curie temperature of 860 K, where the Fermi level electrons are 100 % spin-polarized[14,18].

3.1.2 Thermal conductivity of Fe_3O_4

Slack et al. measured the thermal conductivity of single crystal Fe_3O_4 bulk as a function of temperature, as shown in **Figure 3.2**[8]. As the temperature decreases from 120 K, the Verwey transition temperature[10-13], the thermal conductivity increases up to maximum point mainly due to decrease in Umklapp scatting. Below the maximum point, it reduces with decreasing temperature as the phonon-boundary and phonon-defect scatterings becomes predominant at this regime. This behavior is typical for the most of diamagnetic crystals[8].

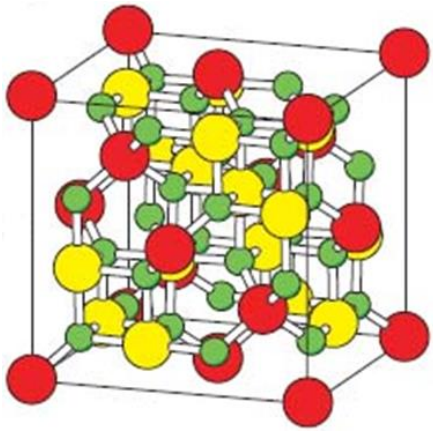

Figure 3.1 – The inverse spinel structure of Fe_3O_4, is composed of an FCC-packed oxygen lattice (green sphere), Fe^{3+} ions occupying 1/8 of the tetrahedral sites (red sphere), and equal amount of Fe^{3+} and Fe^{2+} ions occupying half of the octahedral sites (yellow sphere). Adapted from ref. 17.

One interesting feature of the temperature dependence of Fe_3O_4 thermal conductivity is that the thermal conductivity hardly changes from 120 ~ 300 K. Above 120 K, the Fe^{2+} and Fe^{3+} ions in the octahedral become disordered[19-22]. The disordered states could be rearranged to the ordered ones by an acoustic phonon-induced ordering (or stress-induced ordering) process in Fe_3O_4[23]. During this process, phonons would be absorbed to induce the ions to order and then be incoherently reradiated, i.e., scattered. The authors suggested that this might be a core origin of the abnormal thermal conductivity behavior at this temperature regimes[8]. Beyond 590 K, the Debye temperature, the phonon scatterings by this magnetic ordering processes may still take places, but their effects may be screened by the Umklapp scatterings. This well explains the gradual degradation of the thermal conductivity from the Debye temperature[8].

From the thermal conductivity behaviors of Fe_3O_4, we could deduce that the majorities of the heat are transported by phonons. The phonons would be scattered by the typical processes

found in the diamagnetic crystals including Umklapp, isotopes, vacancies, chemical impurities, and boundaries. One additional mechanism to be considered is the scattering from the magnetically disordered states of paramagnetic ions in the octahedral sites. This same model was found sufficient to explain the results for antiferromagnetic MnF_2 and CoF_2[24].

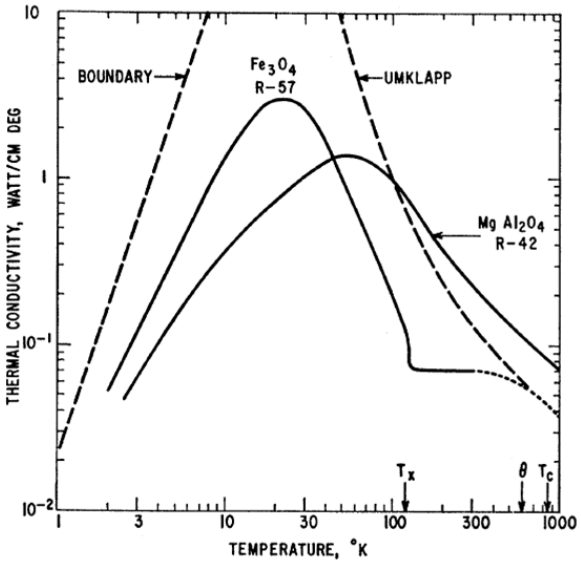

Figure 3.2 – Thermal conductivity of single crystal Fe_3O_4 (R-57) vs. temperature. Dashed curves give theoretical limits for Fe_3O_4 imposed by boundary and Umklapp scattering. T_x, θ, and, T_c are the Verwey transition, Debye, and Curie temperatures, respectively. Adapted from ref. 8.

3.1.3 Phonon dispersion curves of Fe_3O_4

The phonon dispersion relations of Fe_3O_4 are especially important when it comes to elucidating the origin of the Verwey transition[25-27]. To obtain the phonon dispersion curves, Piekarz, et al. have carried out inelastic neutron scattering experiment[27] as well as the ab-initio simulation[25,26]. Here, we briefly introduce the dispersion curves collected from neutron scattering experiment on single crystal Fe_3O_4 in 1974[27]. The first Brillouin zone for an FCC lattice with a space group of Fd3m is depicted in **Figure 3.3**[27]. This figure has been widely accepted as one of standards for the notation of points and directions in the reciprocal space. The Bouckaert-Smoluchowski-Wigner (BSW) notation was used, in accordance with Warren's paper[28].

Figure 3.4 represents the observed phonon dispersion relations in Fe_3O_4 below 28 meV at room temperature for three principal symmetry directions, [111] (Λ), [100] (Δ), and [110] (Σ)[27]. The longitudinal modes and the transverse modes are represented by the square and the circle

symbols, respectively. The solid lines denote branches where the identification is certain, while the dotted and dashed ones are only tentative.

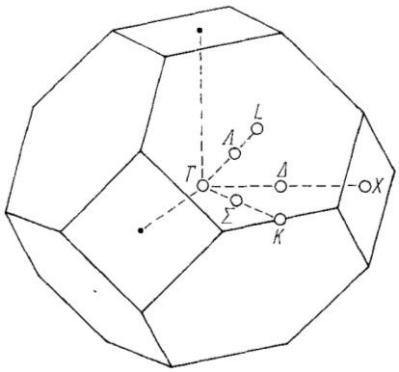

Figure 3.3 – The first Brillouin zone for an FCC structure, with the labelling of points along three principal orientations. [111] (Λ), [100] (Δ), and [110] (Σ). Adapted from ref. 27.

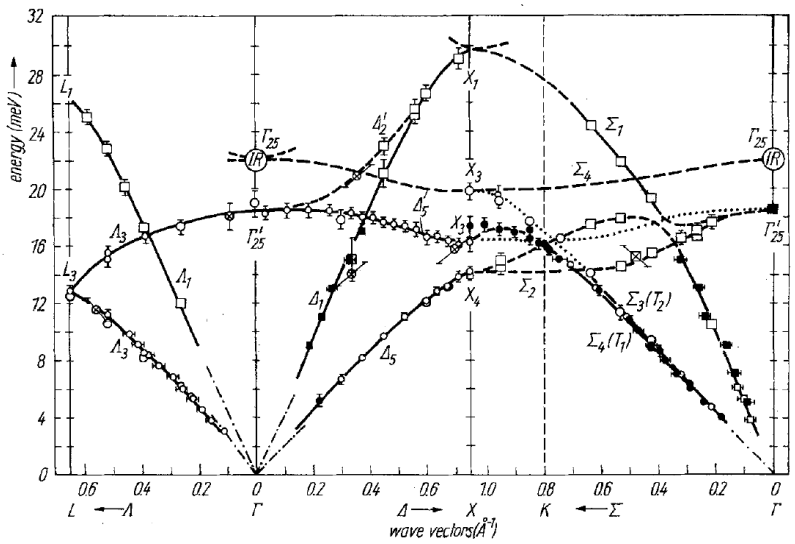

Figure 3.4 – Phonon dispersion curves of Fe_3O_4 at room temperature obtained from inelastic neutron scattering experiment. Three principal directions are included. Square and circle symbols denote the longitudinal and transverse modes, respectively. Adapted from ref. 27.

For the optical phonons, infrared active mode at 22 meV and Raman active modes at 18.5 meV are marked with Γ_{25} and Γ'_{25}, respectively. From the initial slopes of the acoustic branches, the longitudinal and transverse sound velocities along each crystal direction were estimated, which differed from the values given by the ultrasonic method. This discrepancy was ascribed to the fact that the neutron scattering and the ultrasonic methods give the dissimilar sound information. The sound waves in the former are zero sound (i.e. adiabatic) whereas those in the latter are first sound

(i.e. isothermal)[29]. The authors also revealed there could be some anharmonicities at room temperature because the data showed a slight deviation from the elastic relations of typical cubic.

3.2 Experimental Methods

3.2.1 3ω technique

Sample preparation

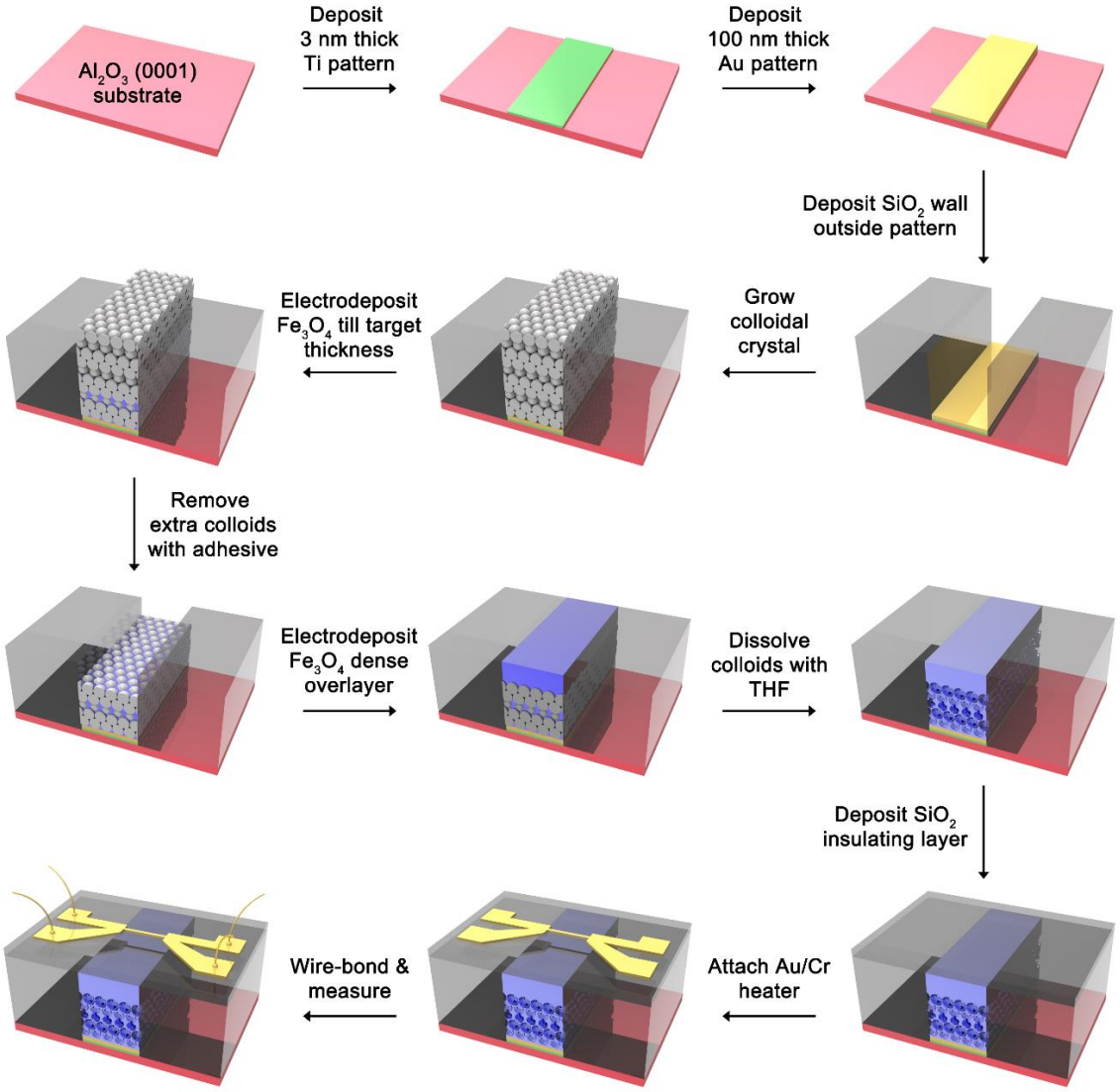

Figure 3.5 – Schematics of microfabrication process of making samples for 3ω measurement. Key idea is to locate ball-bonding contact pads outside the porous regime and to grow pinhole-free dense layer on the porous film to prevent the formation of defective SiO_2 layer on top.

To measure the thermal conductivity of the sample, we used the 3ω technique based on the previous report[30]. The sample was fabricated by the micro-fabrication process combined with electrodeposition, as depicted in **Figure 3.5**. First, we deposited a 5 mm wide patterned 3 nm thick Ti layer followed by 100 nm thick Au layer on the Piranha-cleaned sapphire substrate by the electron beam evaporation. Using a plasma enhanced chemical vapor deposition (PECVD; Minilock - Orion, Trion), the 3.0 ~ 3.5 μm thick SiO_2 walls were grown only on the sapphire areas. The SiO_2 walls were necessary because the wire-bonding required a solid base. We grew the polystyrene (PS) colloidal crystals on the Au surface and then filled the voids with the Fe_3O_4 through electrodeposition at -1.018 V vs. Ag/AgCl for 7 ~ 8 mins, resulting in 1.5 ~ 2.0 μm thickness typically. The extra polystyrene layers on top were detached by any kind of adhesive and the adhesive residue was thoroughly rinsed away by isopropyl alcohol.

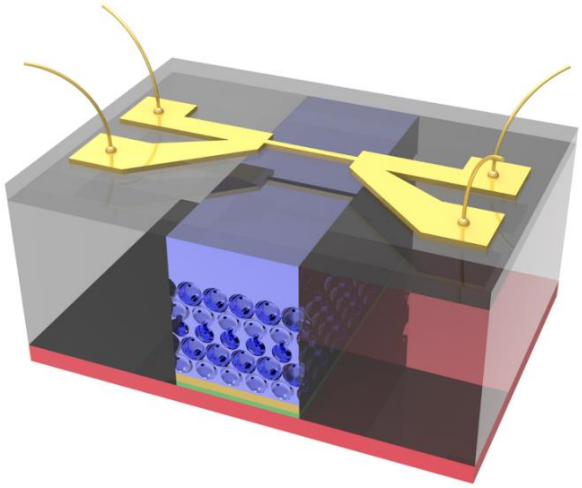

Figure 3.6 – Schematic of final porous sample structure for 3ω measurement.

We masked the sample surface with a water-proof and alkaline-resistant Teflon adhesive (ASF-110FR, Chukoh) except for the 5 x 5 mm^2 area. On this unmasked area, we grew the Fe_3O_4 dense overlayer (OL) by electrodeposition at -1.090 V vs. Ag/AgCl for 3 mins, which ensured pinhole-free OL with the thickness of 1.2 ~ 1.5 μm, and then removed the Teflon adhesive to expose the Fe_3O_4/polystyrenes region without OL on top. The sample was left in THF at 40 ~ 45°C for 2 ~ 5 days to remove the polystyrene particles. Having the Fe_3O_4/polystyrenes area without OL on top, we could facilitate the etch rate of the polystyrenes below the OL. We deposited 400 ~ 500 nm thick PECVD SiO_2 electrically-insulating layers on the OL and at the same time on the bare sapphire substrate for figuring out the thermal conductivity of the PECVD SiO_2 layer. The Au (300 nm)/Cr (10 nm) heaters were deposited on them through the mask containing a configuration of

60 μm x 2 mm heater line connected to four-probe pads. We finally packaged the samples to a chip holder through 25 μm thick Au wire-bonding (4524A Ball Bonder, K&S) and loaded it to the cryostat for measurement. For the dense film, we skipped colloidal crystals growth, overlayer deposition, and polystyrene etch steps. The schematic of final sample structure is represented in **Figure 3.6**.

Measurement

All measurements were performed in a temperature-controlled (Lake Shore) vacuum environment. The metal heater was calibrated every time by measuring the resistance of the metal line as a function of temperature over 300 ~ 400 K with increments of 20 K. At each stabilized temperature, we carried an AC current of ~ 250 nA to the metal line and measured the voltage drop using lock-in amplifiers (SR830, Stanford Research Systems). The temperature coefficient of resistance of the metal, dR/dT was obtained using a linear regression.

The 3ω method is a frequency-domain measurement that utilizes a metallic heater to simultaneously generate Joule heating and detect the corresponding temperature rise[30,31]. Over the frequency (ω) range of 10 ~ 2000 Hz, we obtained a plot of temperature rise at 2ω ($\Delta T_{2\omega}$) vs. frequency by applying a sinusoidal current at 1ω to the sample and then detecting the voltages at 1ω and 3ω ($V_{1\omega}$ and $V_{3\omega}$, respectively) using a lock-in amplifier. The data were collected in the temperature range of 300 ~ 400 K with 20 K intervals. Any noise cancelling element such as nulling bridge circuit was not used[32] because SR830 lock-in amplifier has a sufficient dynamic reserve (> 100 dB) and can detect the $V_{3\omega}$ with a high signal-to-noise ratio[33]. Since we used a voltage source of the lock-in amplifier instead of a current source to supply the sinusoidal current, we converted the measured $V_{3\omega}$ to the true $V_{3\omega}$ by considering the ballast resistance that includes the leads and the output impedance of the voltage source based on the previous reports[33,34].

The thermal conductivity of the layer of interest was extracted by fitting the experimental in-phase and out-of-phase signals with a thermal model which is a full solution of the multi-layered heat-diffusion equation[35]. As the input parameters for the analysis, we used the measured thermal conductivities for the PECVD SiO_2 layer and the OL on the porous film. From a separate 3ω measurement on the SiO_2/sapphire sample, we found that typical thermal conductivity of the PECVD-grown SiO_2 was 1.35 ± 0.06 W m^{-1} K^{-1}. From a separate TDTR measurement on the

polished OL on the porous film, thermal conductivity was determined to be 2.0 ± 0.2 W m^{-1} K^{-1} (see **Figure 3.13**). The sapphire thermal conductivity was obtained from a slope method[36].

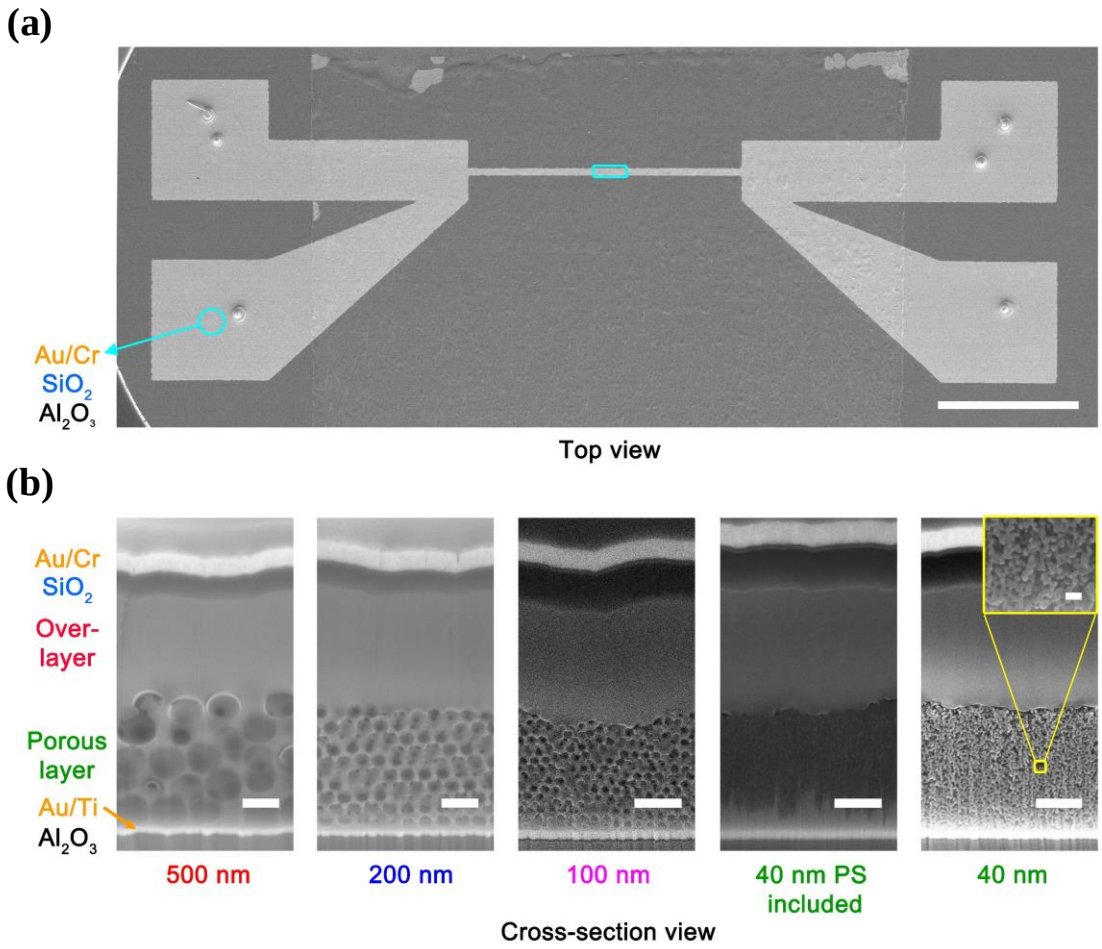

Figure 3.7 – SEM images of the sample for 3ω measurement. (a) Top view image showing the metal heater on the center, and four contact pads outside the center where SiO_2/Al_2O_3 solid ground exists (marked with cyan circle). Scale bar, 1 mm. (b) FIB cross-sectioned SEM images of porous samples and a sample having 40 nm PS inside. The images are taken from a rectangular region of (a). Scale bars, 500 nm for five main images; and 100 nm for an inset.

All the heat capacities below indicate the volumetric heat capacities. The heat capacity of SiO_2 was taken from the literature[37]. In the case of the dense Fe_3O_4 film, the heat capacity value of the literature[38] was multiplied by the measured density of Fe_3O_4 by RBS (95 ± 5 %). For the porous samples, we calculated the heat capacity using $C_{Fe_3O_4}\phi_{Fe_3O_4} + C_{vac}(1-\phi_{Fe_3O_4})$, where $C_{Fe_3O_4}$, C_{vac} and $\phi_{Fe_3O_4}$ denote the heat capacities of Fe_3O_4[38], vacuum and the density of Fe_3O_4 determined by RBS respectively. For the 40 nm polystyrene included film, the heat capacity was calculated by $C_{Fe_3O_4}\phi_{Fe_3O_4} + C_{PS}(1-\phi_{Fe_3O_4})$, where C_{PS} indicates the heat capacity of PS[39].

After 3ω measurement, we characterized the width and length of the heater from plane-view SEM image (**Figure 3.7a**). We cross-sectioned the sample using a FEI Helios 600i FIB/SEM and measured the thickness of each layer (**Figure 3.7b**). The measured thickness was divided by sin 52^{o} to correct the 52^{o}-tilted projection of the FIB/SEM cross-section image[40,41]. The uncertainty of thermal conductivity was calculated using the sensitivity calculation.

3.2.2 Time-domain thermo-reflectance (TDTR) technique

Sample preparation

We polished the surfaces of the dense film and the PS included films at different diameters (500, 200, 100, and 40 nm) using an Ar-ion polisher (PECS II, Gatan). The ion-polisher had two ion guns 100^{o} apart along the rotational axis of the sample. The ion beams at 8 kV were introduced to the sample surface with a 3^{o} tilt angle. The low tilt angle helped to keep the sample milling at an even pace, even if there were materials with different milling rates.

The bulk single crystal and the overlayer on the porous film were polished using a mechanical polisher (Multiprep, Allied) and the diamond lapping films (8" disc, Allied) consisting of precision graded diamond particles with the sizes of 6, 3, 1 and 0.1 μm respectively. For 6, 3 and 1 μm cases, water was supplied, and for 0.1 μm case, the GreenLube (Allied) was used during the polishing. We polished the surfaces of the amorphized dense films using a Ga-ion source of the Helios 600i FIB/SEM.

Measurement

TDTR technique we used in the present study is well described elsewhere with more details[42,43]. Prior to the measurement, the polished surface of the sample was deposited with 70 nm thick NbV thin film or Al thin film as an optical transducer using magnetron sputter. We employed a mode-locked Ti:sapphire laser to produce periodic optical pulses with the wavelength of 785 ± 10 nm. The laser beam was split into the pump and the probe beams through a polarizing beam splitter. The pump beam modulated at a frequency, f, by an electro-optic modulator heated the sample surface. The arrival of the probe beam was controlled to be delayed from 0 to 3600 ps by varying the length of the pump beam path with a delay stage. At each time delay, temperature-induced change in the intensity of a reflected probe beam that was synchronous with the pump modulation was detected by a photodiode connected to a RF lock-in amplifier. In this study, we

performed the experiment at the modulation frequency either at 11.0 or 1.12 MHz depending on the thermal penetration depth of the material. Either a 20x or a 10x objective lens was used to focus the laser beams to 2.7 μm or 5.3 μm in $1/e^2$ radius, respectively. In the case of measuring 40 nm PS included samples which necessitate the 20x objective lens owing to the limited size of an optically specular region, NbV layer was sputtered on samples as a transducer instead of Al layer because at such small beam size the lateral heat spreading in the Al layer introduced larger uncertainties.

The measured data was compared with a thermal model that describes the heat diffusion in the multilayered system to extract the thermal conductivity of the layer of interest[42]. The thermal conductivity of the transducer film was determined by measuring the electrical conductivity of the transducer on 300 nm thick SiO_2 layer on Si (100) wafer with four-point probes and then converting it to the thermal conductivity using the Wiedemann - Franz law.

We used the literature volumetric heat capacities of NbV[44] and Al[45]. To determine those of the dense film and PS included films, we employed the same heat capacity values and the same equations as the ones we used in the 3ω method above. The thickness of the transducer was determined by picking up a picosecond acoustic peak created by the acoustic impedance mismatch between two dissimilar layers and then converting it to the distance using the speed of sound in the transducer. A Fe_3O_4 layer below the transducer was designed to be much thicker than the thermal penetration depth at modulation frequency so that the thickness of the Fe_3O_4 layer has negligible effects on the measured signal.

3.2.3 Picosecond acoustics

Sample preparation

We determined the longitudinal sound velocities of epitaxial dense film and 40 nm polystyrenes included film using TDTR technique which required a smooth surface. Since thin sample with 50 ~ 100 nm in thickness is better to be measured, we polished using Ga-ion beams of Helios 600i FIB/SEM, which enabled us to keep monitoring thickness in real-time through high-resolution SEM. The procedure is shown in **Figure 3.8**. We cleaved the sample and then loaded it into FIB chamber such that the cross-sectioned area could face toward the electron beams. The sample was tilted by 52° to have the target surface to be in parallel with the ion beams. We

deposited a Pt protective layer on the cross-sectioned area. The ion beams with high currents of ~ 2 nA at 30 kV were irradiated on the sample surface in parallel to polish very roughly. Once the thickness of target layer reached 100 ~ 200 nm, we fine-polished the surface with low currents of 300 ~ 400 pA at 30 kV until the target thickness was attained.

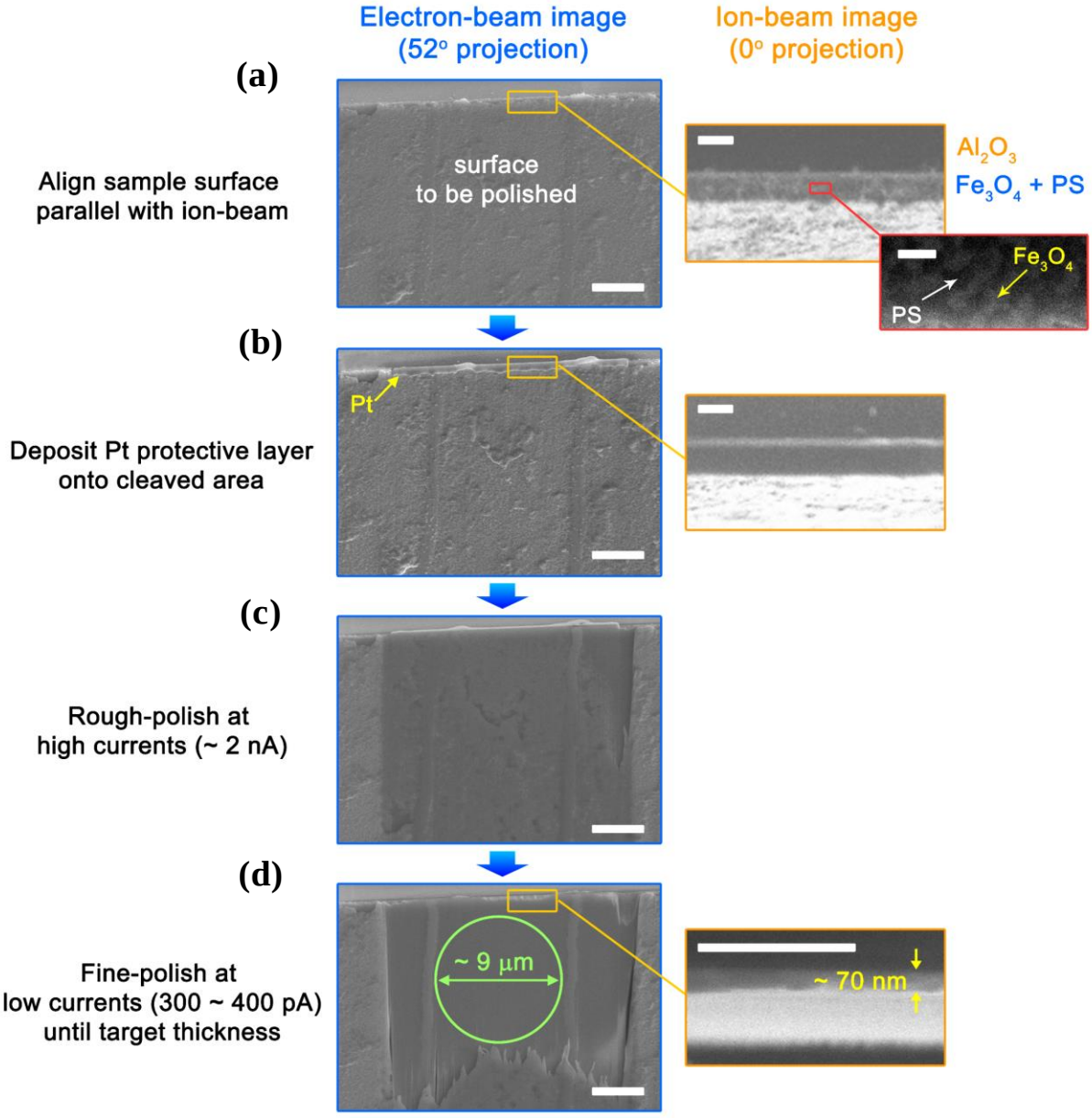

Figure 3.8 – FIB-mediated local polishing process on 40 nm PS included Fe_3O_4 sample. (a) Align the surface we want to polish in parallel with Ga ion-beam direction. Initial thickness is ~ 500 nm. (b) Deposit Pt layer onto cleaved region to protect the region during ion-beam milling process. (c) Rough-polish the surface at high ion-beam currents, ~ 2 nA. (d) Fine-polish at low currents, 300 ~ 400 pA until reaching the target thickness of ~ 70 nm. Scale bars, 3 μm for the electron-beam images; 500 nm for the ion-beam images; and 50 nm for an inset of the ion-beam image of (a).

Measurement

Ahead of the measurement, the sample was coated with a thicker NbV thin film (~ 110 nm) than before to augment the periodicity of the acoustic signals from the NbV/Fe_3O_4 interface. The same TDTR technique as above was employed, but we focused more on the in-phase signal here. We linear-scanned the data over the time delay of 0 ~ 140 ps to observe the acoustic peaks arising from the acoustic impedance mismatches at the interfaces.

In the V_{in} vs. time delay curves, the travel time ($t_{Fe_3O_4}$) required for the acoustic waves to make a round trip in the Fe_3O_4 layer was obtained from the time gap between two different kinds of acoustic peaks, one from the NbV/Fe_3O_4 interface and the other from the Fe_3O_4/Au interface. The thickness (h) of the layer was determined from observing the cross-sectioned sample with FIB/SEM or SEM. The speed of sound in the Fe_3O_4 layer could be therefore calculated by $2h/t_{Fe_3O_4}$. The longitudinal effective elastic constant of the layer, C_{eff}^{L}, was calculated by $\rho v_{L,[111]}{}^2$, where ρ is the mass density of the layer.

3.2.4 Heavy-ion irradiations

(by Dr. Hattar at Sandia National Laboratory)

20 MeV Au^{4+} ion irradiations were completed on 1 μm thick Fe_3O_4 epitaxial dense films with 6 MV HVE (High Voltage Engineering Europa) Tandem Accelerator. The irradiations were done at nominal room temperature at ion fluences over 10^{11} ~ 1.64 x 10^{17} ions cm^{-2} at an average ion flux over 2.47 x 10^{11} ~ 2.47 x 10^{12} ions cm^{-2} s^{-1}. The irradiated samples were characterized by SEM, XRD, and Raman spectroscopy. We polished the surface of sample with FIB-polishing technique described above and then measured the thermal conductivity using TDTR technique.

3.3 Amorphous Minimum Thermal Conductivity

3.3.1 Cahill-Pohl model

We calculated the amorphous minimum thermal conductivity of Fe_3O_4 material using Cahill-Pohl model[46]. They predicted that thermal conductivity of a material reached amorphous limit when the phonon MFP approaches inter-atomic spacing, which is expressed by

$$\Lambda_{min} = \left(\frac{\pi}{6}\right)^{\frac{1}{3}} k_B n^{\frac{2}{3}} \sum_i v_i \left(\frac{T}{\theta_i}\right)^2 \int_0^{\frac{\theta_i}{T}} \frac{x^3 e^x}{(e^x - 1)^2} dx$$

$$\theta_i = \frac{v_i h}{2\pi k_B} (6\pi^2 n)^{1/3}$$

where k_B, v_i, θ_i and n denote the Boltzmann constant, the speed of sound for each polarization (two transverse and one longitudinal), the cutoff frequency for each polarization and the number density of atoms, respectively. The parameters used for calculating the minimum thermal conductivity of Fe_3O_4 are listed in the **Table 3.1**. At 300 K, the calculated thermal conductivity of amorphous Fe_3O_4 is 1.29 W m^{-1} K^{-1} as shown in **Figure 3.9**. It asymptotically approaches 1.63 W m^{-1} K^{-1} at high temperatures.

Table 3.1 – Fe_3O_4 parameters used for Cahill-Pohl model calculation.

N, number of atoms in unit cell (atoms)	56
Ω_0, unit cell volume (m^3)	0.592 x 10^{-27}
n , number density of atoms (# m^{-3})	0.946 x 10^{29}
$v_{L,s}$, longitudinal sound velocity (m s^{-1})[47]	7214
$v_{T,s}$, transverse sound velocity (m s^{-1})[47]	3496

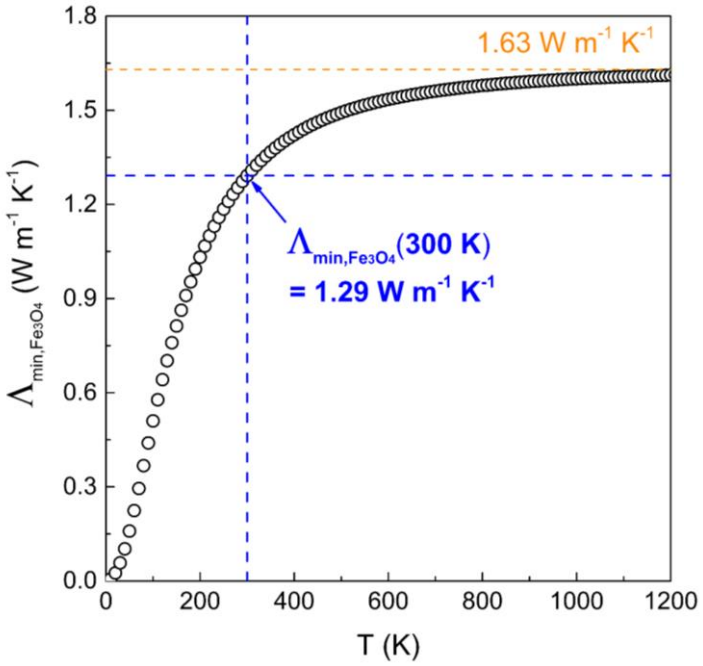

Figure 3.9 – Calculated plot of minimum thermal conductivity of Fe_3O_4 against temperature.

3.3.2 Differential-effective-medium (DEM) theory

Using the Fe_3O_4 minimum thermal conductivity calculated above, we predict that of porous films using DEM theory[48],

$$\frac{\Lambda_{min,porous}}{\Lambda_{Cahill-Pohl}} = \left(\phi_{Fe_3O_4}\right)^{3/2}$$

where $\Lambda_{min,porous}$, $\Lambda_{Cahill-Pohl}$ and $\phi_{Fe_3O_4}$ denote the minimum thermal conductivity limit of porous Fe_3O_4 film, the minimum thermal conductivity limit of dense Fe_3O_4 material calculated by Cahill-Pohl mode and the density (dimensionless fraction) of Fe_3O_4 in the porous film. DEM theory has proven to show good estimation in material systems when two phases have the large contrast in the properties[48].

The DEM theory is also used for calculating the diffusive limit of thermal conductivity of porous film. The diffusive limit is a minimal boundary of thermal conductivity where phonon transport inside a porous medium can be still described by classical continuum theories[49]. To be above this limit, feature size of the surface boundary in porous structure should be larger than or comparable to the diffusive MFP of Umklapp phonons. When the feature size goes below the MFP, the quasi-ballistic or ballistic transport of phonon particles takes place, where the sub-continuum approach needs to be considered[50]. As our porous materials are mesostructured or nanostructured, it is meaningful to figure out where each porous film lies in. We calculate this limit using DEM theory as follows,

$$\frac{\Lambda_{diff,porous}}{\Lambda_{dense}} = \left(\phi_{Fe_3O_4}\right)^{3/2}$$

where $\Lambda_{diff,porous}$ and Λ_{dense} indicate the diffusive thermal conductivity limit of porous film and the measured thermal conductivity value of the Fe_3O_4 dense film.

3.4 Thermal Conductivity Measurement by 3ω Technique

3.4.1 Data acquisition and analysis

In the 3ω method[30], a sinusoidal current at a modulation frequency ω through a metallic heater induces an oscillatory temperature rise, $\Delta T_{2\omega}$ at the harmonic frequency 2ω. The linear

relationship between the temperature and resistance of a metallic heater causes resistance fluctuations at frequency 2ω. This results in a voltage drop, $V_{3\omega}$, across the heater oscillating at frequency 3ω. Picking up $V_{3\omega}$ through a lock-in amplifier gives the measured $\Delta T_{2\omega}$, which is expressed by[30]

$$\Delta T_{2\omega} = 2\frac{V_{3\omega}}{V_{1\omega}} R_0 \left(\frac{dR}{dT}\right)^{-1}$$

where $V_{1\omega}$, R_0, and $\frac{dR}{dT}$ denote the 1ω voltage across the heater, the average resistance of the heater, and the temperature coefficient of the heater resistance (TCR; α_m). The α_m is deduced by linear fitting of a plot of the resistance versus the temperature **(Figure 3.10a)**.

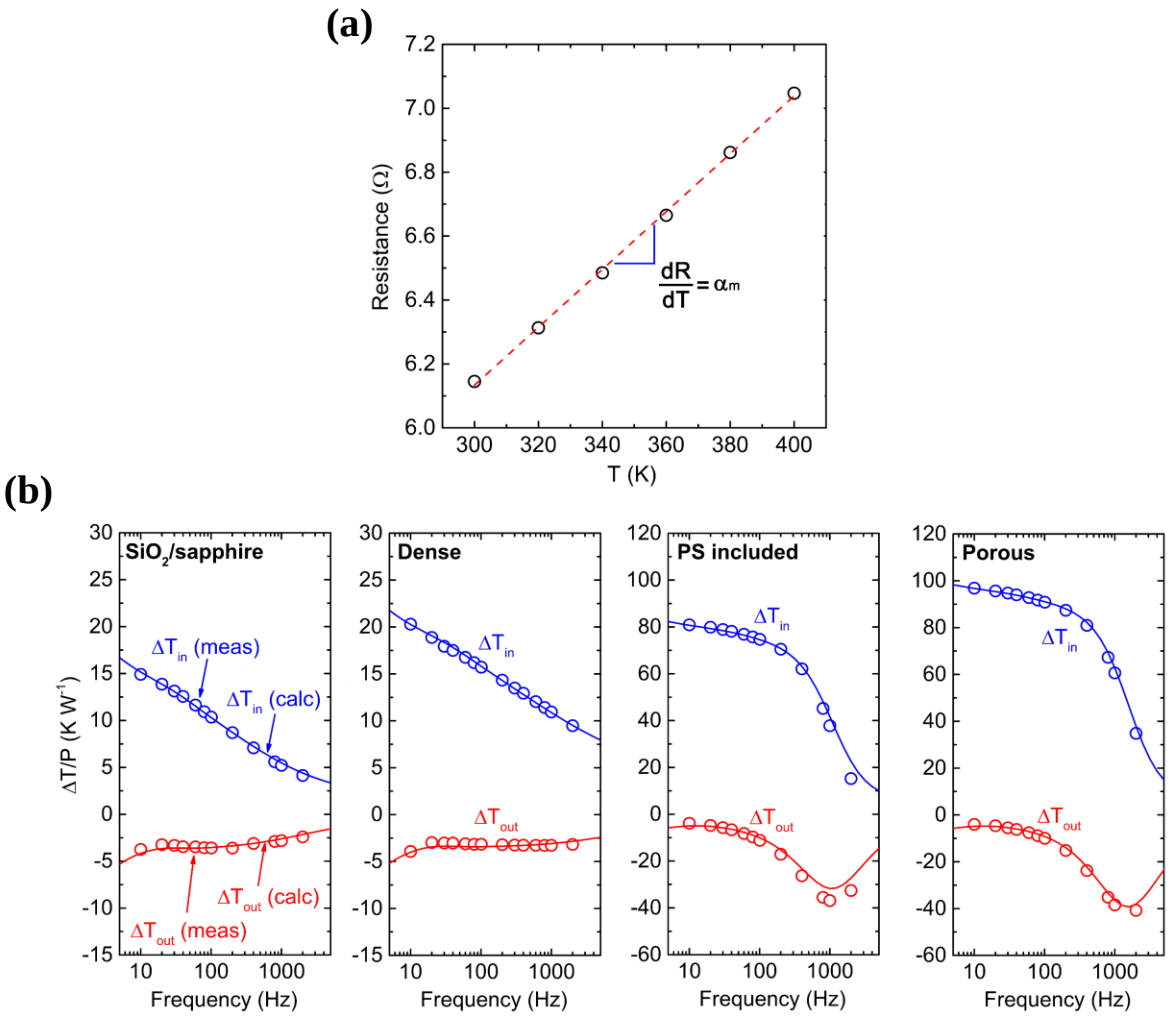

Figure 3.10 – (a) Calibration plot of heater resistance vs. temperature over 300 ~ 400 K. Dashed red line and open black circles denote linear fitted result and experimental data, respectively (b)

Figure 3.10 (cont.) – Typical plots of $\Delta T/P$ vs. frequency over 10 ~ 2000 Hz. In-phase and out-of-phase data are represented with blue and red open circles respectively and the corresponding fitted curves are with blue and red solid lines respectively. Drastic drops of $\Delta T/P$ at high frequencies in right two plots would come from the combination effect of large thermal resistance of porous (or PS-included) layer with large volumetric heat capacity of dense overlayer.

As shown in **Figure 3.10b**, the thermal conductivity of the sample is extracted by fitting the measured $\Delta T_{2\omega}$ with a full solution of multilayer heat diffusion equation[35],

$$\Delta T = \frac{P}{2\pi l b^2}\int_0^\infty \frac{B^+(m)+B^-(m)}{A^+(m)B^-(m)-A^-(m)B^+(m)}\frac{sin^2(mb)}{\gamma_j m^2}dm$$

$$\gamma_j = \Lambda_j\sqrt{m^2 - i\frac{\omega}{D_j}};\ D_j = \frac{\Lambda_j}{C_j}$$

where P, l and $2b$ denote the Joule heating power, heater length and heater width, respectively. The parameters Λ_j, D_j and C_j indicate the thermal conductivity, thermal diffusivity and volumetric heat capacity of layer j, respectively; m is the variable of integration; and $B^+(m)$, $B^-(m)$, $A^+(m)$ and $A^-(m)$ are dimensionless parameters determined by a recursive matrix method[51,52]. We use an effective heater width, $b' = b + 0.38h_t$, where h_t is total film thickness, to consider the lateral heat flow in an isotropic thin film[31]. Note that the heater width (60 um) is chosen to be much larger than the sample thickness, typically 2 ~ 4 μm so that heat flow can be one-dimensional[53].

3.4.2 Uncertainty calculation

In the 3ω technique, one source of the uncertainty is the input parameter, α, of the thermal model that we use for the data analysis. The uncertainty also comes from the inaccuracy of the calibration measurement, where the α_m usually has ~ 5 % relative error in our 3ω measurement[34]. The sensitivity is a quantitative measure of how sensitive the temperature rise, ΔT, is to a small amount of change in an error source such as α in the thermal model, or such as α_m in the measurement. Thus, the sensitivities, S_α and S_{α_m} are defined as[54,55]

$$S_\alpha = \frac{\partial\, ln(\Delta T)}{\partial\, ln\,\alpha},$$

$$S_{\alpha_m} = \frac{\partial\, ln(\Delta T_{2\omega})}{\partial\, ln\,\alpha_m}$$

where α indicates the input parameters such Λ_j, C_j, l, b and the thickness of layer j, h_j. **Figure 3.11** displays the S_α to various input parameters of each sample. Note that S_{α_m} is equal to 1. Assuming all the error sources mentioned above are random and independent, the uncertainty of the thermal conductivity of sample, Λ_f, is estimated in the form of the quadratic sums[56]

$$\left(\frac{\delta\Lambda_f}{\Lambda_f}\right)^2 = \sum_\alpha \left(\frac{S_\alpha}{S_{\Lambda_f}}\frac{\delta\alpha}{\alpha}\right)^2 + \left(\frac{S_{\alpha_m}}{S_{\Lambda_f}}\frac{\delta\alpha_m}{\alpha_m}\right)^2$$

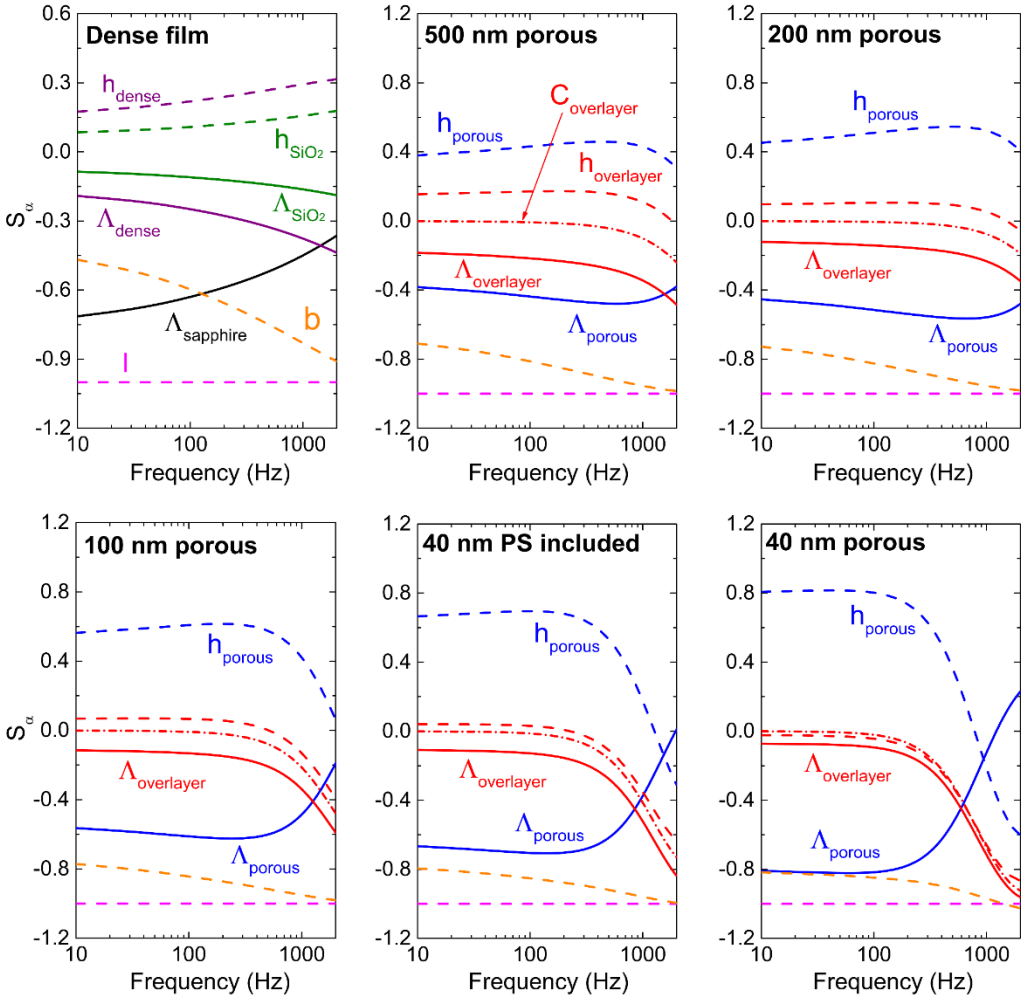

Figure 3.11 – Sensitivity plots for 3ω measurement on epitaxial Fe_3O_4 films at 300 K. In all porous samples, thermal conductivity and thickness of porous layer have the largest sensitivities, resulting in high accuracy of the measurement. Volumetric heat capacities have negligible sensitivities.

The sensitivity plot of the dense film represents that not only the sensitivity to Λ_{dense} but also those to $\Lambda_{\text{sapphire}}$, Λ_{SiO_2} and h_{SiO_2} are pretty large, which means that it is essential to

accurately determine $\Lambda_{\text{sapphire}}$, Λ_{SiO_2} and h_{SiO_2}. To do so, we separately measured the thermal conductivity of PECVD SiO_2 layer (1.35 ± 0.06 W m^{-1} K^{-1}) directly grown on the sapphire substrate before we measured the main samples. We determined the sapphire thermal conductivity using the slope method[36]. Thickness was measured using FIB-cut SEM image.

In the case of porous films, we observe that sensitivities to Λ_{porous} and h_{porous} increase significantly with decreasing pore size. Those to $\Lambda_{\text{sapphire}}$, Λ_{SiO_2} and h_{SiO_2} are negligible. Instead, we need to consider the sensitivities to $\Lambda_{overlayer}$ and $h_{overlayer}$, especially for samples with large pore diameters. Therefore, the thermal conductivity of the overlayer was determined to be 2.0 ± 0.2 W m^{-1} K^{-1} by separate TDTR measurement (see **Figure 3.13**). Same as the dense film case, thickness of porous layer and overlayer were accurately measured by FIB-sectioned SEM images. Again, it is of importance to consider 52°-tilted projection of FIB image in order not to underestimate the thickness. **Table 3.2** summarizes the measured thermal conductivities of the Fe_3O_4 films by 3ω technique at 300 K.

Table 3.2 – Summary of thermal conductivities measured by 3ω method at 300 K.

d_{pore} (nm)	Dense film	500	200	100	40 PS	40
Λ (W m^{-1} K^{-1})	5.0 ± 0.9	0.95 ± 0.16	0.63 ± 0.09	0.32 ± 0.03	0.21 ± 0.02	0.10 ± 0.01

3.4.3 Overlayer characterization

High-quality overlayer is essential for successful 3ω measurement. It needs to be pinhole free and thick enough so that complete passivation can be achieved by electrically insulating SiO_2 layer on top. **Figure 3.12a** shows top view SEM images, one (left) with pinholes and the other (right) without pinholes. We found that the overlayer started to be pinhole free when it became thicker than ~ 1 μm. The thickness we usually used was ~ 1.5 μm which could be enabled by potentiostatic electrodeposition at -1.090 V vs. Ag/AgCl for 3 min in the same electrolyte.

Figure 3.12b exhibits a 2θ/ω scan result on the sample consisting of dense Fe_3O_4 overlayer grown on porous Fe_3O_4 layer. We clearly see that the overlayer is also the Fe_3O_4 phase aligned along the [111] out-of-plane orientation without including any secondary phases or any crystallites grown along other orientations. The Fe_3O_4 (311) pole-figure in **Figure 3.12c** indicates the

overlayer has a lot of mirror twins, comprised of six domains apart by 60° azimuthally, aligned along [511] orientation[15]. The amounts of twins are much larger than those in the normal dense film because the overlayer was electrodeposited by applying larger electric potential (-1.090 V vs. Ag/AgCl) than normal dense film (-1.018 V vs. Ag/AgCl). This led the overlayer to grow much faster and hence have columnar morphology instead of triangular one.

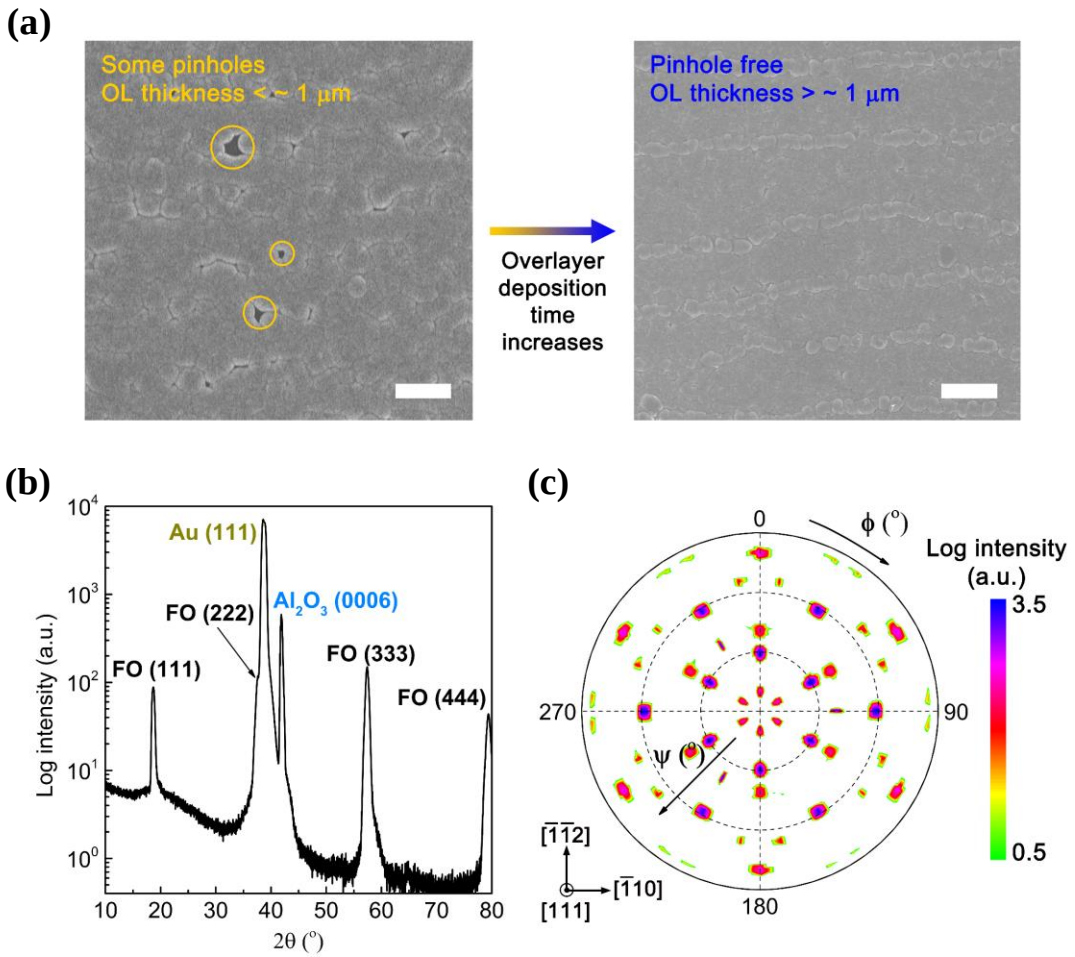

Figure 3.12 – Characterization of dense Fe_3O_4 overlayer. (a) Top view SEM images of the overlayers with pinholes (left) and without pinholes (right). Over thickness of ~ 1 μm, the overlayer becomes completely pinhole-free. Scale bars, 10 μm. (b) 2θ/ω scan on the film consisting of Fe_3O_4 dense overlayer grown on the Fe_3O_4 porous layer. (c) Fe_3O_4 (311) pole-figure acquired from the same sample.

Thermal conductivity of the overlayer was evaluated by TDTR technique. Figure **3.13a** shows the cross-sectional SEM images of Fe_3O_4 sample containing 200 nm colloidal crystals inside, of which the top surface is smoothened by mechanical polishing processes. At a modulation frequency of 11.0 MHz, we collected the TDTR data and then extracted the thermal conductivity

value by fitting the data with a thermal model (**Figure 3.13b**). Error was evaluated from the sensitivity calculation as depicted in **Figure 3.13c**. The obtained thermal conductivity was 2.0 ± 0.2 W m^{-1} K^{-1}. More details on the TDTR data processing are well described in the following chapter.

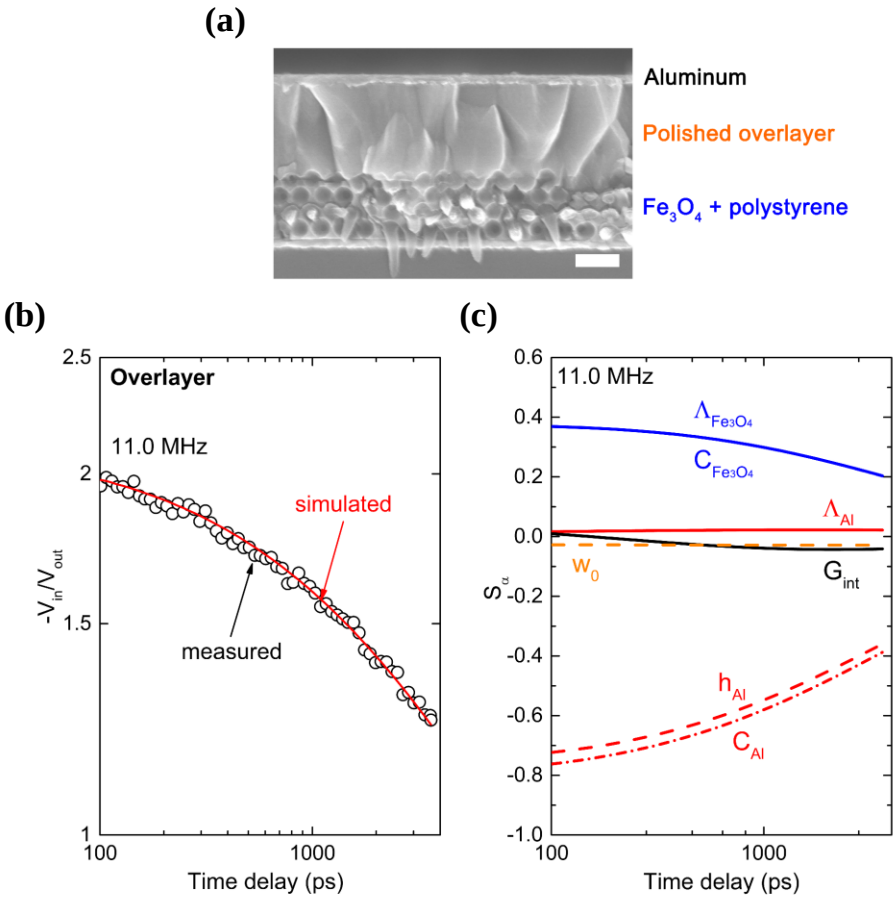

Figure 3.13 – TDTR measurement at a frequency of 11.0 MHz on dense Fe_3O_4 overlayer grown on 200 nm PS included Fe_3O_4 film. (a) Cross-section SEM image of the mechanically polished Fe_3O_4 dense overlayer with the Al transducer on top. To prevent the structure collapse, we polished the sample including polystyrene beads inside. Scale bar, 500 nm. (b) Plot of V_r vs. time delay collected and fitted curve. (c) Sensitivity plots of the sample.

3.5 Thermal Conductivity Measurement by TDTR Technique

3.5.1 Data acquisition and analysis

We polished all kinds of Fe_3O_4 samples using an Ar-ion polisher. As shown in **Figures 3.14a** and **3.15a**, the surfaces of a PS included film and a dense film were specular enough to be

measured with TDTR technique. **Figures 3.14b** and **3.15b** exhibit that the measured data are well-fitted with the unidirectional heat diffusion model explained in a previous report[42]. In multiple references, more details on the experimental setup, data collection and analysis are well described[42,43,57].

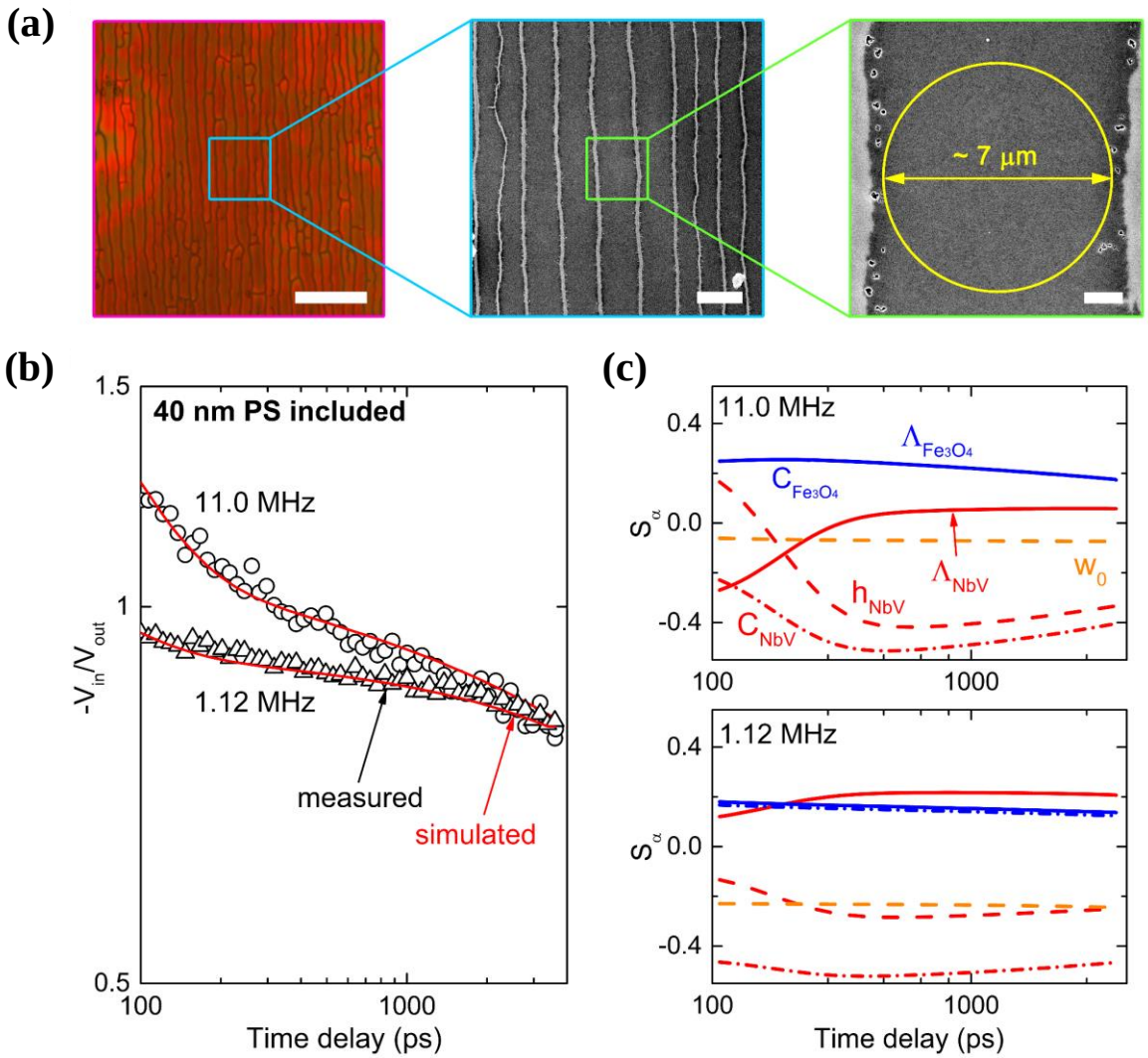

Figure 3.14 – TDTR measurements on 40 nm PS included epitaxial Fe_3O_4 film. (a) Top view optical microscope (OM, left) and SEM (middle and right) images of Ar-ion polished sample surface. In OM image, we see that the surface could be smoothened over 150 x 150 μm^2. SEM images indicate that smooth Fe_3O_4/PS areas, technically measurable with TDTR, are usually 7 ~ 8 µm in diameter. Scale bars, 50 µm for the left panel; 10 µm for the middle panel; and 1 µm for the right panel. (b) Plots of V_r vs. time delay acquired at 11.0 and 1.12 MHz respectively. Measured data are displayed with black open symbols and fitted curves are with red solid lines. (c) Sensitivity plots calculated at 11.0 and 1.12 MHz respectively.

3.5.2 Uncertainty calculation

We estimated the uncertainty of the measured thermal conductivity of our sample based on the sensitivity analysis describe elsewhere[31]. Similar with 3ω method above, the sensitivity of detected TDTR signal to an input parameter of the thermal model, S_α, is defined as

$$S_\alpha = \frac{\partial \ln V_r}{\partial \ln \alpha}$$

where V_r indicates the negative ratio between the in-phase and the out-of-phase signals, $-\frac{V_{in}}{V_{out}}$, and α denotes the input variables such as the thermal conductivity of layer j (Λ_j), the volumetric heat capacity of layer j (C_j), the thickness of layer j (h_j), the interfacial thermal conductance between transducer and Fe_3O_4 film (G_{int}) and $1/e^2$ radius of the laser beam (w_0).

In addition, the absolute value of the phase, ϕ, of the reference channel of the lock-in amplifier is another source of uncertainty in TDTR measurement[31]. This needs to be adjusted properly so that the out-of-phase signal can remain constant across zero time delay. Otherwise, the temperature rise in the transducer will not only be included in the in-phase signal but also in the out-of-phase signal, resulting in deterring the accuracy of the measurement. The sensitivity of TDTR signal to the absolute value of the phase, S_ϕ, is defined as[31]

$$S_\phi = \frac{\partial \ln V_r}{\partial \phi} = V_r + \frac{1}{V_r}$$

The uncertainty of the phase, $\delta\phi$, is expressed as[31]

$$\delta\phi = \frac{\delta V_{out}}{\Delta V_{in}}$$

where δV_{out} and ΔV_{in} are the uncertainty of the out-of-phase signal and the jump in the in-phase signal at zero time delay, respectively. Again, under the assumption that all uncertainty sources described above are random and independent, the uncertainty of the thermal conductivity of the film of interest (Λ_f) can be estimated as[56]

$$\left(\frac{\delta\Lambda_f}{\Lambda_f}\right)^2 = \sum_\alpha \left(\frac{S_\alpha}{S_{\Lambda_f}}\frac{\delta\alpha}{\alpha}\right)^2 + \left(\frac{S_\phi}{S_{\Lambda_f}}\delta\phi\right)^2$$

Figures 3.14c and **3.15c** below exhibit the sensitivity plots that we employed to estimate the uncertainty of the thermal conductivity of the samples measured by TDTR technique.

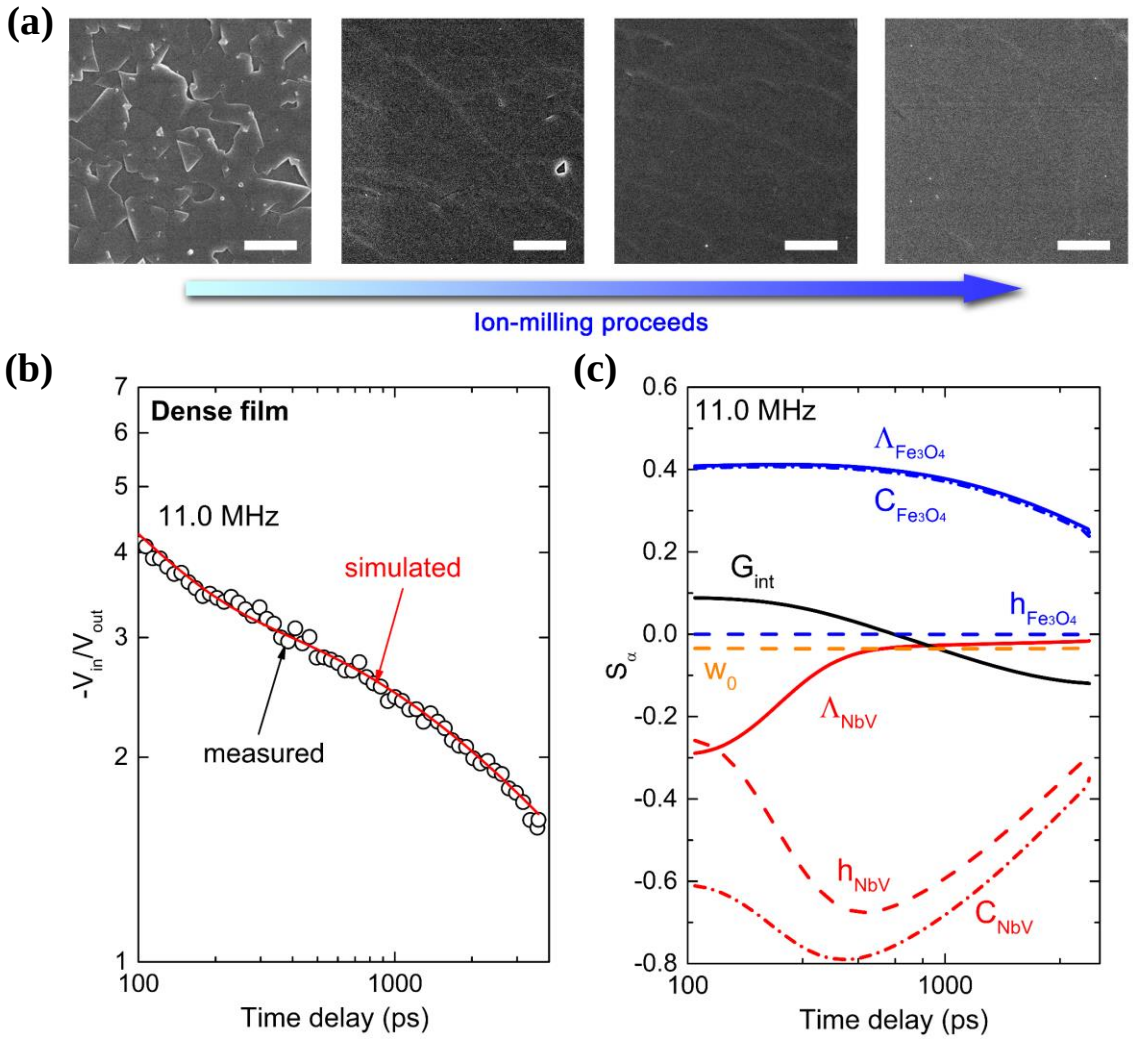

Figure 3.15 – TDTR measurement on epitaxial Fe_3O_4 dense film. (a) SEM images of dense film surface being smoother as ion-milling proceeds. We obtained smooth surface measurable with TDTR (the rightmost image) using an Ar-ion polisher at 8 kV for 8 min. Scale bars, 3 μm for the left three panels; and 5 μm for a right panel. (b) Plot of V_r versus time delay collected at 11.0 MHz and the fitted curve. (c) Sensitivity plots calculated at 11.0 MHz.

3.5.3 Thermal penetration depth

The thermal penetration depth informs us how far the generated heat pulse in the metal transducer can travel through the sample below for a given time length scale, $1/f$, where f is a modulation frequency in the TDTR measurement. It is a good indicator of selecting the appropriate

modulation frequency when measuring the thermal conductivity of a material system with TDTR. For 1D heat diffusion along semi-infinite film j, the thermal penetration depth, d_p is defined as[58]

$$d_p = \sqrt{\frac{D_j}{\pi f}}$$

where D_j is the thermal diffusivity of film j; $D_j = \Lambda_j / C_j$. The temperature at d_p is equal to 1/e of the surface temperature.

For the epitaxial Fe_3O_4 sample containing 40 nm polystyrene beads, the thermal diffusivity is calculated to be ~ 10^{-7} m^2 s^{-1} based on the thermal conductivity and the volumetric heat capacity used above. At a modulation frequency of 11.0 MHz, the thermal penetration depth is ~ 50 nm, which means that our measurement at this frequency probes the thermal conductivity of the first one or two Fe_3O_4/polystyrene layers at most. To gain the thermal conductivity that reflects the collective phonon scatterings generated by the 3D nanoarchitecture of our sample, we changed the modulation frequency down to 1.12 MHz, where the thermal penetration depth is about 160 nm. According to the cross-section SEM image, this length scale corresponds to 5 ~ 6 layers of the Fe_3O_4/polystyrene, which would include sufficient number of 3D distributed surface boundaries in nanoscale that are able to induce the multiple and the back scatterings of phonons. For the samples containing PS beads with the diameters of 100, 200, and 500 nm, the thermal penetration depths are about 230 (3 ~ 4 layers), 300 (1 ~ 2 layers), and 380 nm (< 1 layer) respectively.

3.6 Picosecond Acoustics Measurement by TDTR Technique

3.6.1 Principle

Using the TDTR technique, we pick up the picosecond acoustic signals from our sample. At the early stage of the measurement, the laser beam hitting on the sample surface generates the acoustic waves, which then travel through the sample. Once they meet any barrier such as the interface between two dissimilar materials with different acoustic impedances, they are reflected and come back to the sample surface again, generating the upward or downward peaks in the in-phase signal. The acoustic impedance, Z, is defined as the product of the mass density and longitudinal speed of sound of a material. The magnitude of the peak depends on the difference in

the Z between two materials and the direction of the peak depends on whether the Z increases or decreases when the acoustic waves cross the interface along the forward direction. For example, in a sample with AB structure where the laser beam hits the A, the upward peak is created if the Z of B is larger than that of A, and vice versa.

3.6.2 Sound velocity and elastic constant

From this measurement, we can deduce two important properties of our epitaxial Fe_3O_4 films: the longitudinal speed of sound and the longitudinal effective elastic constant. To do so, as demonstrated in **Figure 3.8**, we polished the local region of sample, approximately 8 ~ 9 μm in diameter, to be thinner and smoother using Ga-ion FIB, and then deposited ~ 110 nm thick NbV film on the surface using magnetron sputtering. This region was exposed to pump-probe beams (**Figure 3.16a**) to obtain pico-second acoustic signals. **Figures 3.16b** and **3.17a** represent the picosecond acoustic data of the PS 40 nm included film and the dense Fe_3O_4 film, respectively.

The time difference between the 1st upward peak and the 1st downward one corresponds to the round-trip travel time of the acoustic waves, $t_{Fe_3O_4}$, in the Fe_3O_4 layer. The thickness of the Fe_3O_4 layer, h, is determined by cross-section SEM images of the sample (**Figures 3.16c** and **3.17b**). Then, the longitudinal speed of sound along [111] direction of the Fe_3O_4 layer, $v_{L,[111]}$, is calculated by

$$v_{L,[111]} = \frac{2h}{t_{Fe_3O_4}}$$

Using the sound velocity, we determine the longitudinal effective elastic constant of the Fe_3O_4 layer, C_{eff}^{L}, by [47,59]

$$\rho {v_{L,[111]}}^2 = C_{eff}^{L}$$

where ρ is the mass density of Fe_3O_4 layer, obtained by the RBS measurement. **Table 3.3** summarizes the experimental results of a dense and a 40 nm PS included epitaxial films. **Table 3.4** summarizes the acoustic impedance of each layer used for indexing acoustic peaks.

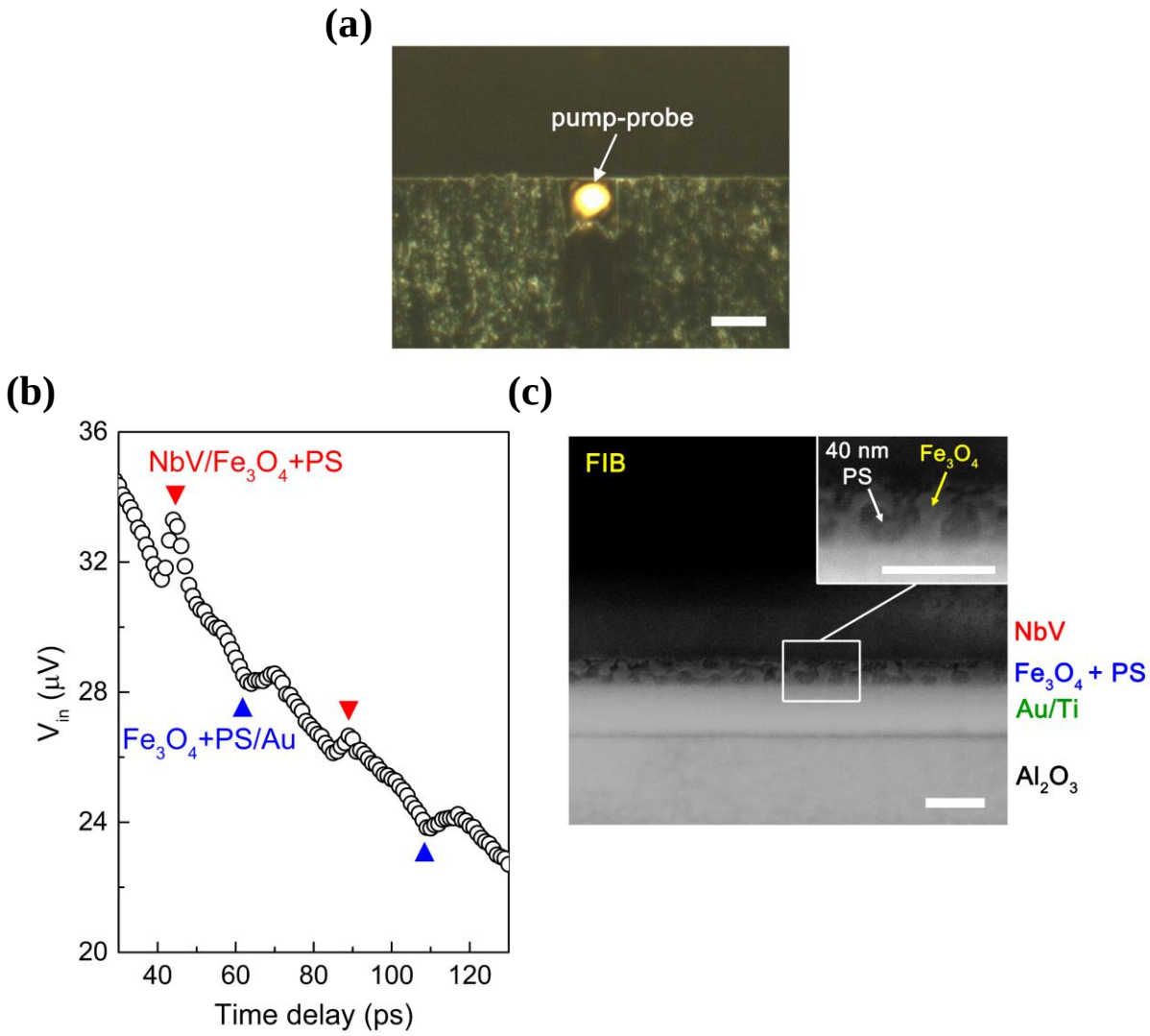

Figure 3.16 – Picosecond acoustic measurement on PS 40 nm included Fe_3O_4 film. (a) CCD camera image of pump and probe beams illuminating a Ga-ion polished area. Scale bar, 10 μm. (b) Picosecond acoustic plot of V_{in} versus time delay of 30 ~ 130 ps. Upward (▼) and downward peaks (▲) are caused by acoustic impedance mismatches at the interfaces between NbV and Fe_3O_4/PS layers and between Fe_3O_4/PS and Au layers, respectively. The time difference between the 1st upward and the 1st downward peaks, 19 ps, corresponds to the time required for acoustic waves to make a round trip inside the Fe_3O_4/PS layer. (c) Cross-section SEM image of the FIB-cut area that we exactly measured. The thickness of Fe_3O_4/PS layer is 65 ± 3 nm. Scale bars, 100 nm for both main and inset images.

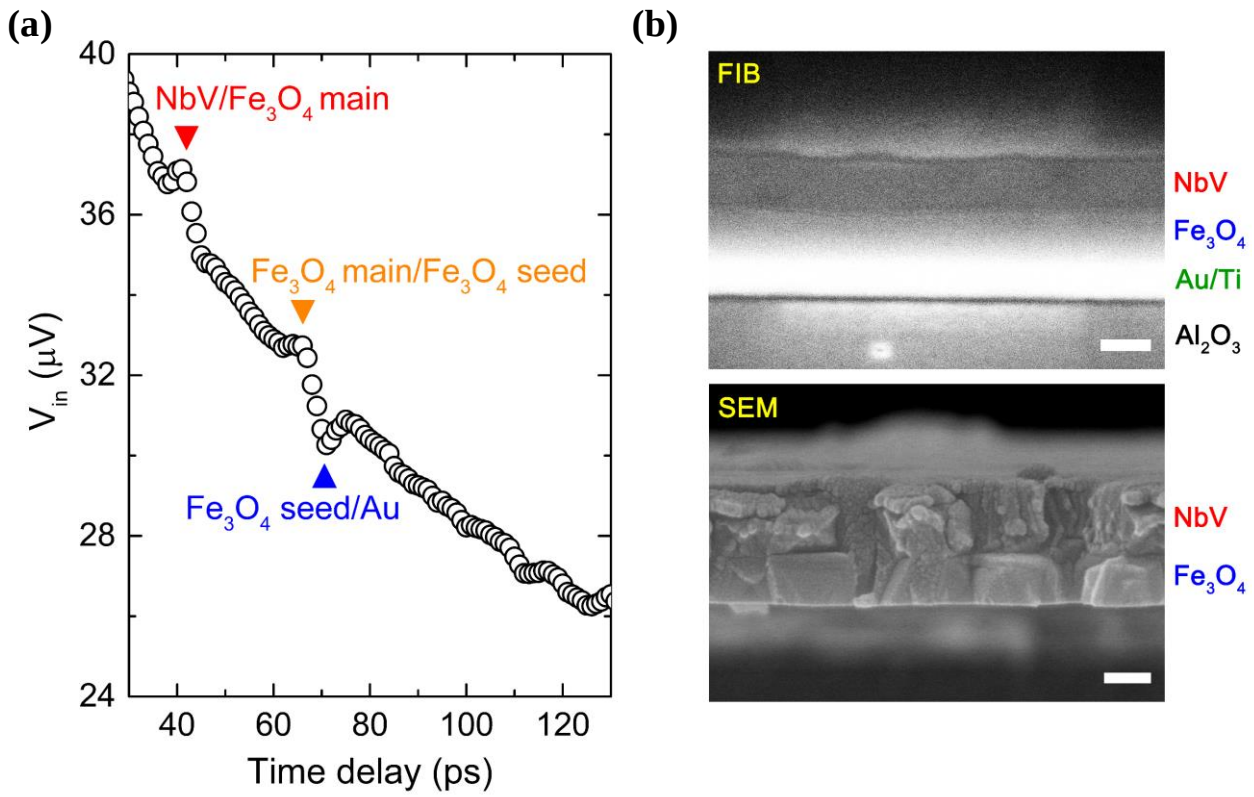

Figure 3.17 – Picosecond acoustic measurement on dense Fe_3O_4 film. (a) Picosecond acoustic plot of the V_{in} vs time delay of 30 ~ 130 ps. Upward (▼) and downward peaks (▲) are induced by the acoustic impedance mismatches at the interfaces between the NbV and the Fe_3O_4 layers and between the Fe_3O_4 and the Au layers, respectively. (b) Cross-section SEM images of FIB-cut area (top) and mechanically-cleaved area (bottom) that we exactly measured. Both images indicate that the thickness of Fe_3O_4 layer is 103 ± 6 nm. Scale bars, 100 nm for both images.

Table 3.3 – Sound velocities and elastic constants of two samples.

	h (nm)*	$t_{Fe_3O_4}$ (ps)†	ρ (g cm^{-3})‡	$v_{L,[111]}$ (nm ps^{-1})	C^L_{eff} (GPa)
40 nm PS + Fe_3O_4	65 ± 3	19.0	2.77 ± 0.30	6.85 ± 0.31	130 ± 20
Dense Fe_3O_4	103 ± 6	29.0	4.91 ± 0.26	7.12 ± 0.40	250 ± 20

h: thickness, $t_{Fe_3O_4}$: travel time, ρ: mass density, $v_{L,[111]}$: longitudinal sound velocity along [111] direction ($= \frac{2h}{t_{Fe_3O_4}}$), C^L_{eff}: longitudinal effective elastic constant ($= \rho v_{L,[111]}{}^2$)

* Converted value by dividing thickness in FIB image by sin 52° to correct the tilted projection

† From picosecond acoustic measurement

‡ From RBS measurement for the Fe_3O_4 density and from vendor (Thermofisher Scientific, USA) for the polystyrene density

Table 3.4 – Summary of acoustic impedances of materials in this study. Z denotes acoustic impedance ($= \rho v_L$).

	ρ (g cm^{-3})	**v_L (nm ps^{-1})**	**Z (Pa s m^{-1})**
NbV	7.40	5.40	40
Fe_3O_4 dense film	4.91 ± 0.26	7.12 ± 0.40	35 ± 3
Fe_3O_4 (44.5%) + 40 nm PS (55.5%)	2.77 ± 0.30	6.85 ± 0.31	19 ± 2
Polystyrene	1.06	1.77	2
Au	19.3	3.24	63
Ti	4.50	6.10	27
Sapphire	3.98	9.80	39

3.6.3 Discussions

In **Figure 3.17a**, the time difference between an upward (▼) peak and a downward peak (▲), 29 ps, corresponds to the time required for the acoustic waves to make a round trip inside the whole Fe_3O_4 dense layer that consists of the main and the seed parts. We got to know the presence of Fe_3O_4 seed layer formed at the very bottom of the film from observing a small upward peak (▼) appearing ahead of the downward peak (▲). After simple mathematical calculations, we identified that the seed layer had thickness of 18 nm and the density of 4.76 g cm^{-3}, which is 2.9 % smaller than the main layer (4.91 g cm^{-3}).

The longitudinal sound velocity of the dense Fe_3O_4 epitaxial film, 7.12 ± 0.40 nm ps^{-1}, is in good agreement with those of the Fe_3O_4 (111) single crystals, 7.05 ~ 7.21 nm ps^{-1}, reported in

the literatures[47,60,61]. More importantly, the 40 nm PS included Fe_3O_4 film also shows the similar value, 6.85 ± 0.31 nm ps^{-1}, to the single crystal values within the error boundary, only 3.8 % reduction of the dense film value. This small decrease implies that both the mass density and the effective elastic constant decreased by approximately the same amount in our periodic structure with isotropic medium.

In a cubic (111) single crystal, the effective elastic constant along the longitudinal direction of acoustic waves, C_{eff}^{L}, was derived in the form of a linear combination of three independent elastic constants[47,59],

$$C_{eff}^{L} = \frac{1}{3}(C_{11} + 4\,C_{44} + 2C_{12})$$

where C_{11}, C_{44} and C_{12} are the elastic constants of the material. For the natural Fe_3O_4 (111) single crystal, Reichmann and co-worker have experimentally obtained[47]: C_{11} = 260.5 GPa, C_{44} = 63.3 GPa and C_{12} = 148.3 GPa, which gives C_{eff}^{L} = 270.1 GPa. This value well matches with the C_{eff}^{L} of our dense epitaxial film, 250 ± 20 GPa. According to the DEM theory to the elastic constants[48], the elastic constant of 40 nm PS included Fe_3O_4 film is supposed to be 51 ± 11 GPa, calculated by using 3.3 GPa and 55.5 % for the elastic modulus and density of polystyrene. In our experiment, the C_{eff}^{L} was estimated to be 130 ± 20 GPa, which is ~ 2.5 times larger than the value predicted by the DEM theory.

3.7 Heavy Ion Irradiations on Fe_3O_4 Dense Films

3.7.1 Amorphization

There have been some reports on the heavy ion irradiations on Fe_3O_4 bulks and thin films to study the effects of the irradiations on the magnetic properties[62-65]. Owing to the low fluences ranging from 10^{11} ~ 10^{13} ions cm^{-2}, none of them could obtain the fully amorphized phase. Only partial amorphization, discontinuous latent tracks, or spherical extended defects were observed[64,65]. Also, the irradiation effects on the thermal conductivity of Fe_3O_4 have not been investigated so far.

Based on the Stopping and Range of Ions in Matters (SRIM) simulations of irradiation damage cascades[66,67], and the Fe_3O_4 dense sample parameters such as the mass density and the geometric dimension, we used 20 MeV Au^{4+} as a heavy ion source and irradiated samples at different levels of fluences in the range of 10^{11} ~ 1.64 x 10^{17} ions cm^{-2}, as summarized in **Table 3.5**. From the XRD measurements, we found that the low fluence levels of 10^{11} ~ 10^{14} ions cm^{-2}, had few effects on the macroscopic crystallinity of dense film. Starting from 10^{15} ions cm^{-2}, decrease of XRD peaks was discernably observed.

Table 3.5 – Experimental parameters of irradiations performed on dense films. Charge state of an ion, +4, and elementary charge of an electron, 1.6 x 10^{-19} C, were used.

Current (nA)	**Area (cm^2)**	**Flux (10^{11} ions cm^{-2} s^{-1})**	**Fluence (10^{16} ions cm^{-2})**	**Time (10^4 s)**	**Count (10^7)**
35	0.221	2.47	0.00001	0.00004	0.000142
35	0.221	2.47	0.0001	0.0004	0.00142
40	0.221	2.83	0.001	0.0035	0.0142
55	0.221	3.89	0.01	0.0257	0.142
70	0.221	**4.95**	**0.1**	0.202	1.42
80	0.221	**5.66**	**1.5**	2.65	21.2
300	0.190	**24.7**	**16.4**	6.65	20

Figure 3.18a represents the top view SEM images of an unirradiated sample and the irradiated ones at three different fluences, 1 x 10^{15}, 1.50 x 10^{16}, and 1.64 x 10^{17} ions cm^{-2}, respectively. As the ion dose increases, the film gets to lose the distinctive triangular textures. Instead, the morphology becomes more irregular and agglomerated, indicative of the destruction of local periodicity and the evolution of disordered regions. **Figure 3.18b** shows that crystalline nature completely faded away beyond 10^{15} ions cm^{-2}, consistent with the morphology changes in the SEM images. Similar trend is also observed in the Raman spectra of **Figure 3.18c**. The sample damaged at 10^{15} ions cm^{-2} still reveals three major peaks with weak intensities. The other two samples differ from each other. The sample irradiated at 1.50 x 10^{16} ions cm^{-2} still has a peak corresponding to A_{1g} mode whereas the other irradiated at 1.64 x 10^{17} ions cm^{-2} does not have any. Combining two results (Raman and XRD), we deduced the former still possessed a small degree of local periodicity while the latter became completely amorphized with no local spatial order.

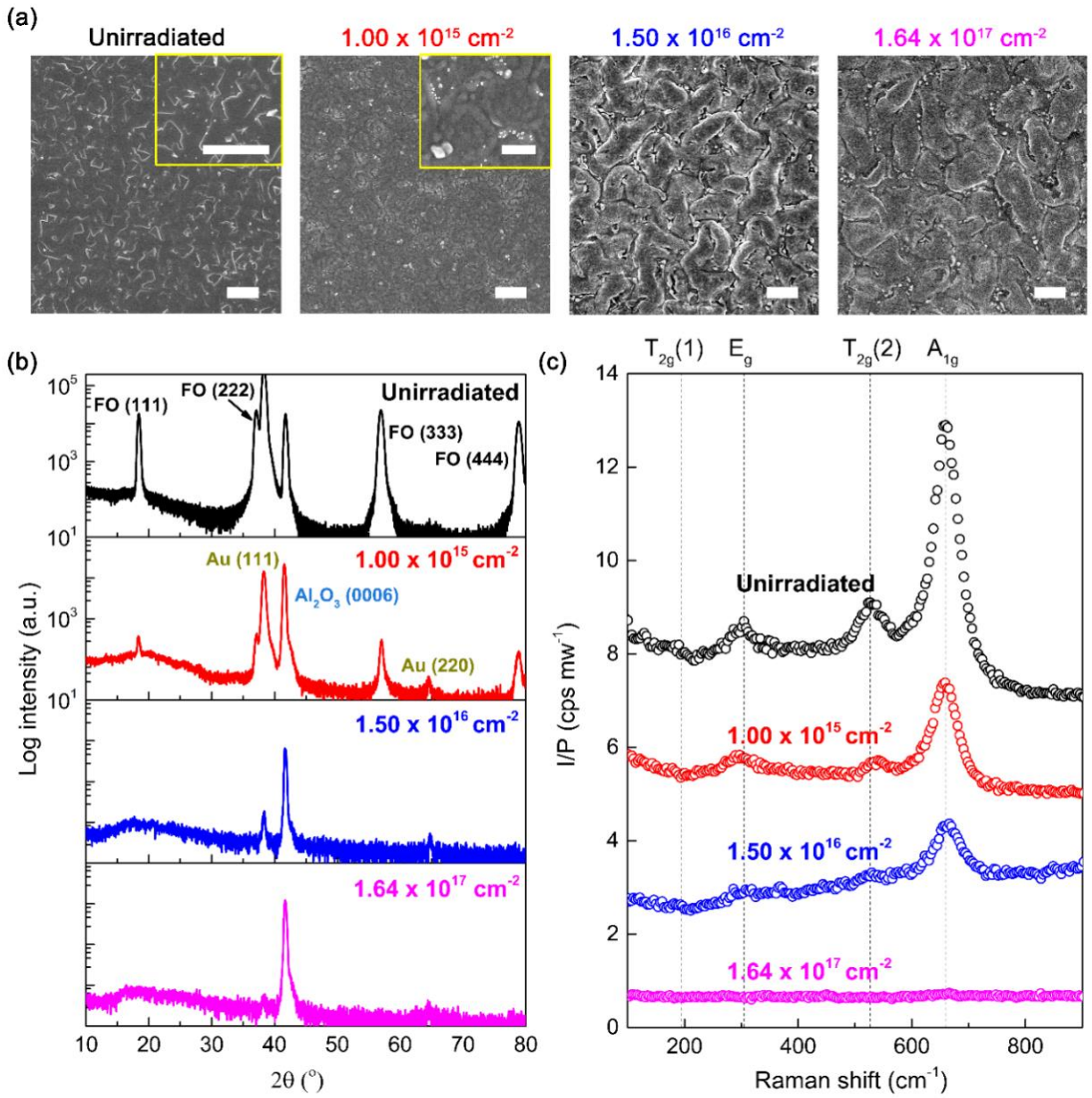

Figure 3.18 – Characterizations on irradiated dense films at different ion fluences. (a) Top view SEM images. Scale bars, 5 µm for the main images; and 2 µm for the insets. (b) 2θ/ω scans. (c) Confocal Raman spectra.

3.7.2 Thermal conductivity of amorphized samples

Local regions, typically ~ 13 µm in diameter, of these two samples were ion-polished with FIB and then thermal conductivities of which were measured by TDTR technique (**Figure 3.19)**. The measured thermal conductivities are summarized with the XRD and Raman results in **Table 3.6**. It is evident that the thermal conductivities of two irradiated samples are more than three times

smaller than that of unirradiated one, implying that phonon transport was significantly deterred due to the macroscopic evolution of amorphized regions by the high-dose ion damages. More importantly, the one irradiated at the highest dose, 1.64 x 10^{17} ions cm^{-2}, shows the measured thermal conductivity of 1.29 ± 0.11 W m^{-1} K^{-1}, which is the same as the one predicted by Cahill-Pohl model[46], 1.29 W m^{-1} K^{-1}. This is consistent with XRD and Raman data which proved complete amorphization of Fe_3O_4 film by irradiation damage cascades[67].

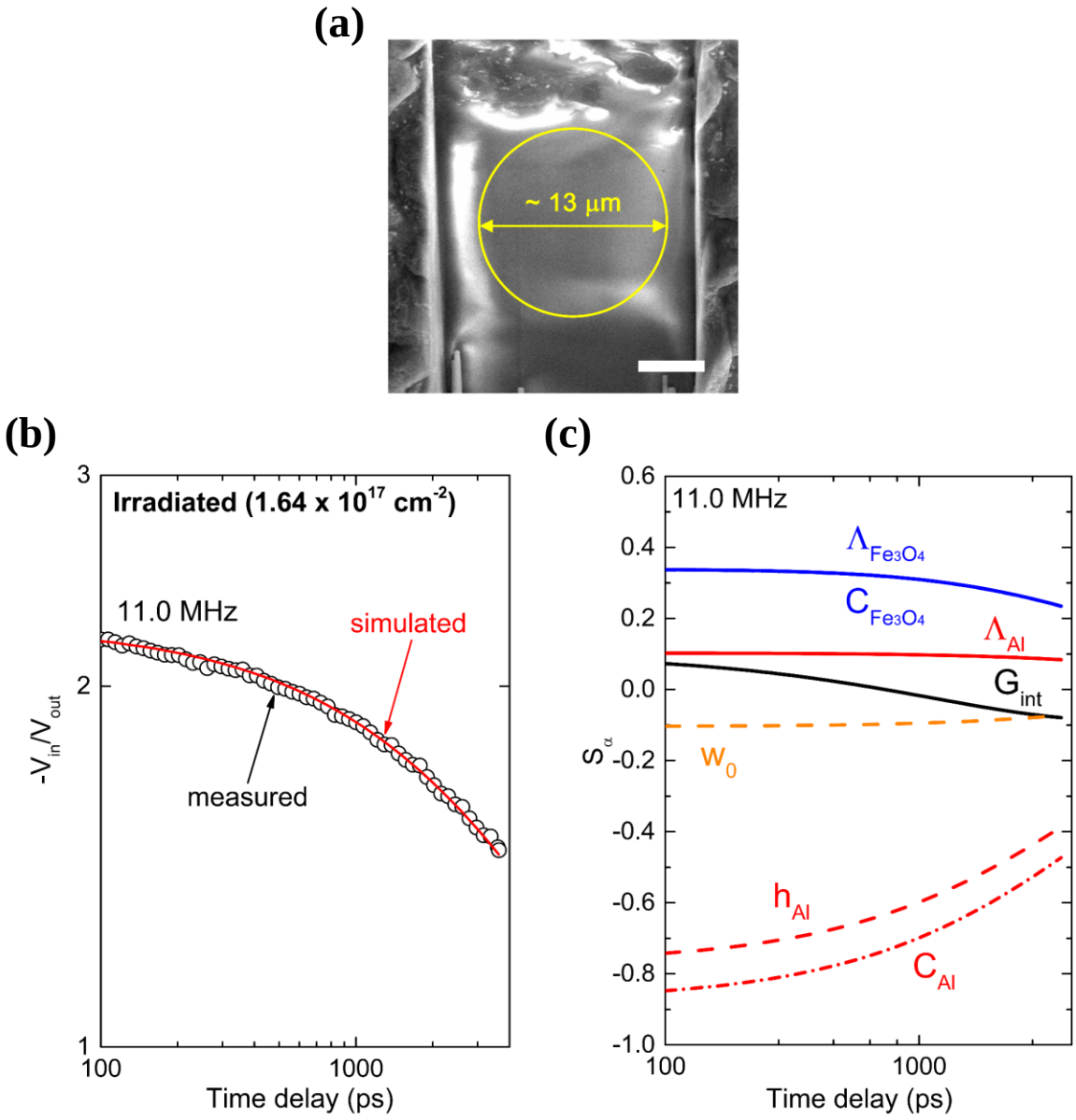

Figure 3.19 – TDTR measurement on dense film irradiated at 1.64 x 10^{17} ions cm^{-2}. (a) SEM image of a local area polished by Ga-ion milling. Scale bar, 5 μm. (b) Plot of V_r vs. time delay at collected at 11.0 MHz and fitted curve. (c) Sensitivity plots calculated at 11.0 MHz.

Table 3.6 – Summary of thermal conductivities, XRD, and Raman results of unirradiated and irradiated dense films. The theoretical amorphous minimum thermal conductivity calculated by Cahill-Pohl model is also included for the comparison.

Materials	**Λ (W m^{-1} K^{-1})**	**XRD & Raman**
Unirradiated	5.0 ± 0.9 (3ω)	Almost same as bulk single crystal, except for number of domains
	4.3 ± 0.4	
Irradiated (1.50 x 10^{16} ions cm^{-2})	1.36 ± 0.12	No XRD peaks Very weak Raman peaks
Irradiated (1.64 x 10^{17} ions cm^{-2})	1.29 ± 0.11	No XRD peaks No Raman peaks
Cahill-Pohl model	1.29 (calculated)	N.A.

3.8 Discussions on Thermal Conductivity Results

3.8.1 Comparison between 3ω and TDTR results

We compare the thermal conductivities of epitaxial dense film and 40 nm PS included Fe_3O_4 film measured by TDTR method with those by 3ω method, as summarized in **Table 3.7**.

Table 3.7 – Comparison of thermal conductivities measured by 3ω and TDTR.

	Thermal conductivity (W m^{-1} K^{-1})		
	3ω	**TDTR @ 11.0 MHz**	**TDTR @ 1.12 MHz**
Dense	5.0 ± 0.9	4.3 ± 0.4	N.A.
40 nm PS + Fe_3O_4	0.21 ± 0.02	0.18 ± 0.02	0.20 ± 0.03

We first notice that the thermal conductivity of the 40 nm PS included Fe_3O_4 film measured by TDTR at a frequency of 1.12 MHz is in excellent agreement with that measured by 3ω technique. This indicates that even in 5 ~ 6 layers of porous media we can expect the same phonon scattering effects as we observe in the 3ω sample with larger number (> 10) of porous layers. From this, we suspect that our hypothesis that 5 ~ 6 layers would have enough number of surface boundaries for the phonons to undergo 3D multiple and back scatterings, is quite reasonable. Also, by cross-checking the data acquired from two independent techniques, we could ensure the

reliabilities of both data. Another noticeable thing is that the thermal conductivity measured by TDTR at 11.0 MHz is ~ 10 % smaller than those by 3ω method and TDTR technique at 1.12 MHz frequency. This behavior would be explained by the frequency dependent thermal conductivity which was previously handled in the semiconductor alloys[58]. They revealed that phonons with MFPs larger than the thermal penetration depth do not contribute to the thermal conductivity measured in the experiments.

We also see that the thermal conductivities of the dense film obtained by TDTR and 3ω measurements slightly differ from each other within the error boundaries. This is due to that the sensitivity of $\Delta T_{2\omega}$ to the $\Lambda_{Fe_3O_4}$ is not high enough in the 3ω measurement because of the presence of the SiO_2 layer whose thermal conductivity is 3 ~ 4 times smaller than that of dense Fe_3O_4 material. Note that we used the sample consisting of 150 nm thick SiO_2 layer on 2 μm thick dense Fe_3O_4 film for 3ω measurement to increase the accuracy as high as possible.

3.8.2 Single crystal vs. epitaxial dense film

Through the overall process consisting of mechanical polishing, TDTR measurement, and error analysis (**Figure 3.20**), we obtained the thermal conductivity of bulk Fe_3O_4 (111) single crystal, 5.9 ± 0.6 W m^{-1} K^{-1}, in accordance with a previously reported value, 5.8 W m^{-1} K^{-1} in 1975[9]. Slack et al[8] reported the Czochralski-grown Fe_3O_4 single crystal showed 6.9 W m^{-1} K^{-1}, which is 1.2 times larger than our data. We suspect this dissimilarity would originate from the difference in crystal quality between samples.

One thing to note here is the difference in the thermal conductivity between the single crystal, 5.9 ± 0.6 W m^{-1} K^{-1}, and the epitaxial dense film, 4.3 ± 0.4 W m^{-1} K^{-1}. As revealed in the Fe_3O_4 (311) pole-figures of both samples, the natural single crystal consists of single domain whereas the synthesized dense film is comprised of two domains that are antiparallel to each other. The boundaries between the domains are technically defects that can scatter the phonons. Thus, although it is hard to describe in a quantitative manner, we suspect the more domains and their interfacial boundaries would be one feasible reason for the smaller thermal conductivity of the epitaxial film than the natural single crystal.

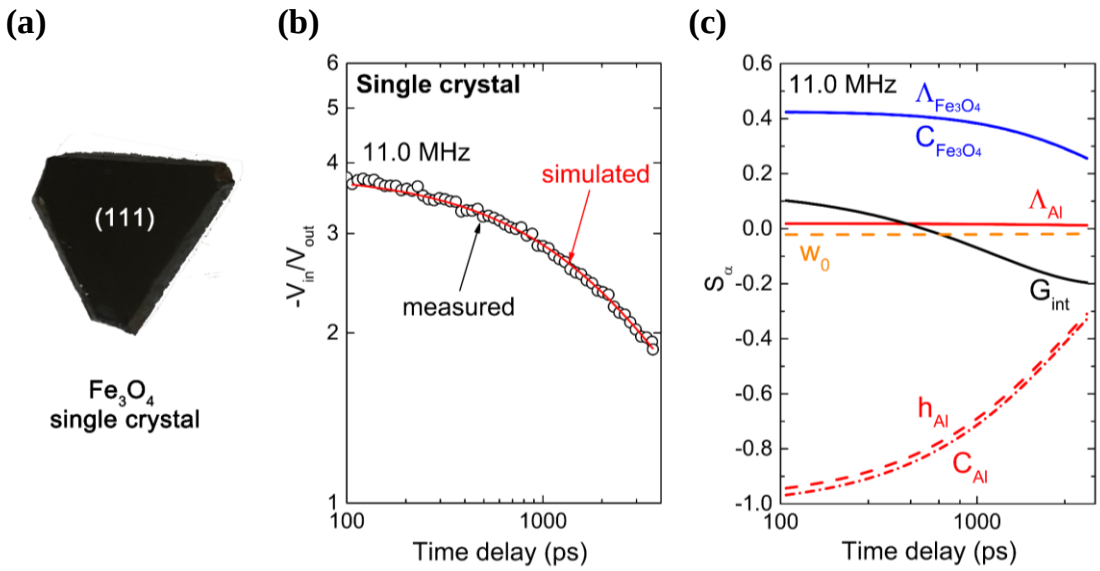

Figure 3.20 – TDTR measurement on natural Fe_3O_4 (111) single crystal. (a) A photograph of a single crystal mechanically polished along [111] direction. (b) Plot of V_r vs. time delay acquired at 11.0 MHz and fitted curve. (c) Sensitivity plots calculated at 11.0 MHz.

3.8.3 Pore diameter dependence of thermal conductivity

Using the measured densities by RBS, we calculated two kinds of thermal conductivity boundaries for the porous samples. First is the amorphous minimum limit (○ in **Figure 3.21a**) of the dense and porous films with different pore diameters. To estimate the value of the dense Fe_3O_4 material, we employed Cahill-Pohl model that predicted that thermal conductivity of a material reached the amorphous limit when the phonon MFP approaches inter-atomic spacing[46]. The calculated value was 1.29 W m^{-1} K^{-1} at room temperature and further utilized for obtaining the amorphous limit of the porous Fe_3O_4 films by combining with DEM theory[48]. Second is the diffusive limit (Δ in **Figure 3.21a**) of the porous films at the corresponding porosities. Above this limit, phonon transport inside the porous medium can be still explained by the classical continuum approaches that consider only the diffusive motions of phonons[49,68]. We used the DEM theory and measured thermal conductivity of the dense Fe_3O_4 film to obtain this limit of porous films.

Figure 3.21b summarizes the thermal conductivities of all kinds of Fe_3O_4 samples investigated in this study. This plot encompasses four distinctive features to be discussed. First, the thermal conductivity of the epitaxial dense film (4.3 ± 0.4 W m^{-1} K^{-1}) was smaller than that of the single crystal (5.9 ± 0.6 W m^{-1} K^{-1}) by a factor of 1.4. This seems to originate from the fact that the dense film contains two domains and hence more defects whereas the bulk single crystal does only one domain, as discussed in **Chapter 2**.

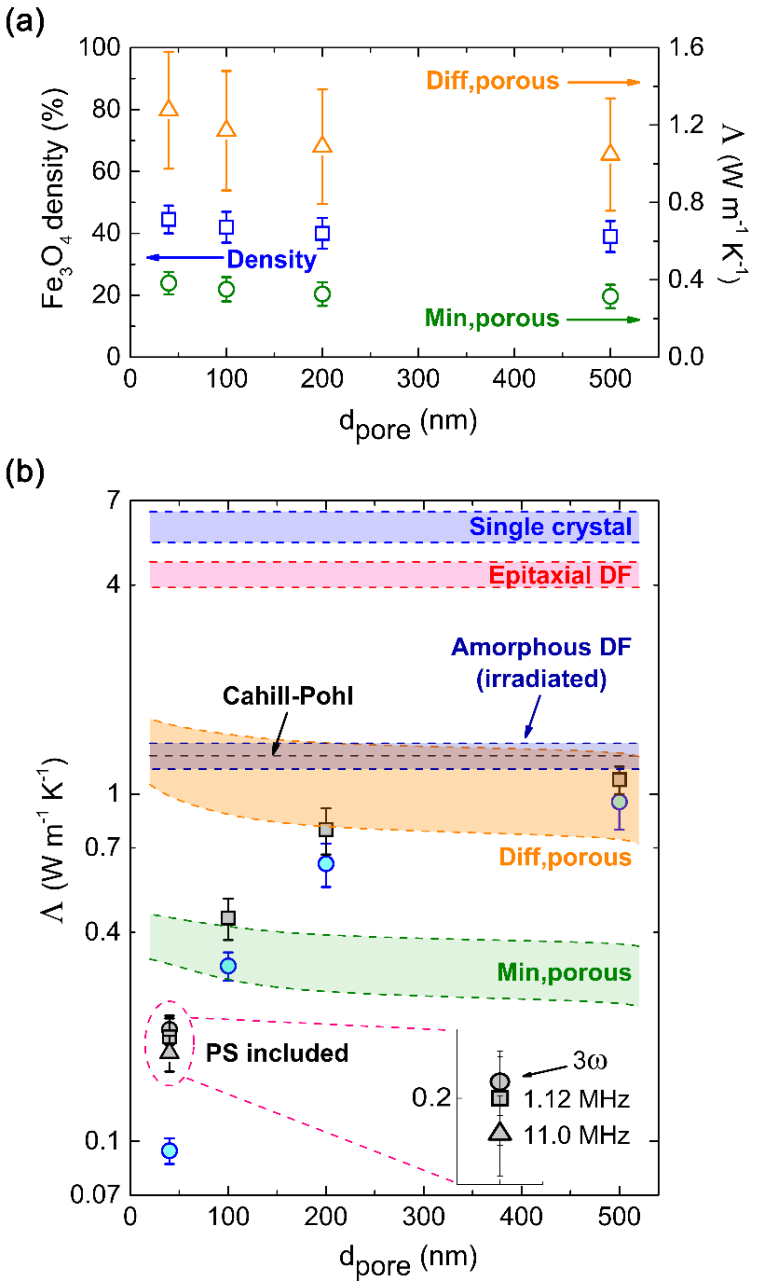

Figure 3.21 – Measured densities and thermal conductivities of epitaxial 3D porous structures. (a) Fe_3O_4 density determined by RBS measurement (□; left axis), diffusive limit (Δ; right axis) and amorphous limit (○; right axis) predicted by DEM approximation, against pore diameter. (b) Measured thermal conductivities of the porous films (blue circle), the PS included films (black symbols), the single crystal, the epitaxial dense film and the amorphized dense film. Cahill-Pohl denotes the amorphous minimum thermal conductivity calculated by Cahill-Pohl model (1.29 W m^{-1} K^{-1}). At pore diameter of 100 nm, the thermal conductivity falls in the range of the amorphous limit. Going further down to 40 nm, we observe the ultralow thermal conductivity of ~ 0.1 W m^{-1} K^{-1}, far below the amorphous limit.

Second, the porous films containing pores with the diameters of 200, 100 and 40 nm had lower thermal conductivities than their corresponding diffusive limits, with the gaps getting larger with decreasing pore size. At this regime, we would expect the quasi-ballistic or ballistic phonon transport to be predominant, which was similarly observed in the metallic inverse opals[69]. This conclusion is also supported by **Figure 3.22** where the thermal conductivity becomes less dependent on the temperature as the pore diameter decreases. Third, the calculated thermal conductivity of the dense Fe_3O_4 material using Cahill-Pohl model perfectly matched with the measured one of the amorphized dense film enabled by heavy ion irradiation experiment. This good match ensures the accuracy and reliability of the amorphous limits of porous media we deduced.

Finally, we observed the 40 nm porous film showed unexpectedly low thermal conductivity of ~ 0.1 W m^{-1} K^{-1}. This value is similar with or smaller than thermal conductivities of some typical polymers[70-72]. More importantly, it is far below the theoretical minimum thermal conductivity that amorphous porous material with the Fe_3O_4 density of 44.5 ± 4.5 % should have. It is significant considering that the porous film is comprised of the single crystals, not the randomly oriented nor the amorphous phases, and that the porosity is only ~ 56 %. To make sure that the measured value was true, we measured the thermal conductivity of the samples containing 40 nm polystyrenes inside using both 3ω and TDTR techniques. As can be seen in inset of **Figure 3.21b**, all measurements gave similar thermal conductivities of ~ 0.2 W m^{-1} K^{-1}, which could be the upper bound for the 40 nm porous film. Through this result, we are convinced of the ultra-low thermal conductivity of the 40 nm porous epitaxial film.

3.8.4 Temperature dependence of thermal conductivity

In **Figure 3.22**, as the temperature increases from 300 to 400 K, the thermal conductivities of the dense film and 500 nm porous film decrease about 17 ~ 18 % because in these samples the scattering of the diffusive phonons, whose mean free paths are highly dependent on temperature, predominates over other phonon scatterings such as surface boundary scattering. For the 200 nm porous film, the thermal conductivity becomes less dependent on the temperature, which means that surface boundary scattering of phonons starts to dominate over the diffusive scattering and hence quasi-ballistic phonon transport is likely to appear. Below this pore diameter, 100 and 40 nm, we barely observe any change in the thermal conductivity upon temperature, indicating that

boundary phonon scattering is highly predominant. In the 40 nm polystyrene-included Fe_3O_4 film, there is no change in the thermal conductivity over the temperature of 300 ~ 360 K, but a sudden decrease is observed around 380 K, probably due to glass transition of the polystyrene[73].

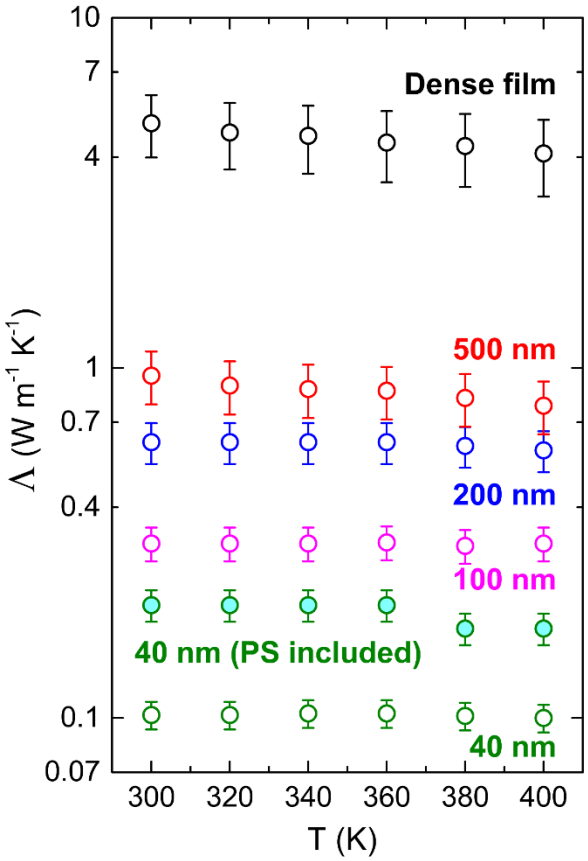

Figure 3.22 – Temperature dependence of thermal conductivity of the epitaxial Fe_3O_4 dense film, porous Fe_3O_4 films having different pore diameters, and 40 nm PS included Fe_3O_4 film.

3.9 Conclusions

We measured the thermal conductivities of Fe_3O_4 epitaxial 3D meso/nansotructures with different pore sizes from 500, 200, 100 to 40 nm using two independent methods, 3ω and TDTR techniques. The most intriguing observation is the ultra-low thermal conductivity of 40 nm porous films, ~ 0.1 W m^{-1} K^{-1}. This is far below the theoretical minimum limit of a porous Fe_3O_4 material having the same density as our 40 nm sample, 44.5 ± 4.5 %. This is a surprising result because our sample is epitaxial, as verified by multiple characterizations in **Chapter 2**. We are not sure of the exact reason of this behavior, but we suspect two possible scenarios that could significantly deter

the propagation of phonon waves. In a porous medium made from the inversion of an FCC-based colloidal templates, the feature size of the structure could be estimated to be 1/4 of the pore diameter. SEM images also support that the characteristic length scale of the feature of 40 nm porous Fe_3O_4 film is ~ 10 nm, where wave behaviors of phonons could appear. From this point of view, the ultra-low thermal conductivity of the 40 nm porous sample might be attributed to i) the modification of the dispersion relationship (or group velocity) or ii) the localization of optical phonons. However, it seems not easy at this moment to quantitatively elucidate the origin of this anomaly.

3.10 References

1 Snyder, G. J. & Toberer, E. S. Complex thermoelectric materials. *Nat Mater* **7**, 105-114, doi:10.1038/nmat2090 (2008).

2 Yan, X. *et al.* Experimental studies on anisotropic thermoelectric properties and structures of n-type Bi2Te2.7Se0.3. *Nano Lett* **10**, 3373-3378, doi:10.1021/nl101156v (2010).

3 Soni, A. *et al.* Enhanced thermoelectric properties of solution grown Bi2Te(3-x)Se(x) nanoplatelet composites. *Nano Lett* **12**, 1203-1209, doi:10.1021/nl2034859 (2012).

4 Goldsmid, H. Bismuth Telluride and Its Alloys as Materials for Thermoelectric Generation. *Materials* **7**, 2577-2592, doi:10.3390/ma7042577 (2014).

5 Androulakis, J. *et al.* Thermoelectrics from abundant chemical elements: high-performance nanostructured PbSe-PbS. *J Am Chem Soc* **133**, 10920-10927, doi:10.1021/ja203022c (2011).

6 Zhao, L. D. *et al.* High performance thermoelectrics from earth-abundant materials: enhanced figure of merit in PbS by second phase nanostructures. *J Am Chem Soc* **133**, 20476-20487, doi:10.1021/ja208658w (2011).

7 Sparks, T. D. Ph. D Disseration: Oxide Thermoelectrics: The Role of Crystal Structure on Thermopower in Strongly Correlated Spinels. *Harvard University* (2012).

8 Slack, G. A. Thermal Conductivity of MgO, Al2O3, MgAl2O4, and Fe3O4 Crystals from 3° to 300°K. *Physical Review* **126**, 427-441, doi:10.1103/PhysRev.126.427 (1962).

9 I. K. Kamilov, G. M. S., Kh. K. Aliev, G. G. Musaev, and M. M. & Khamidov. Some features of the behavior of the thermal conductivity of ferrites in the vicinity of magnetic phase transitions. *Zh. Eksp. Teor. Fiz* **68** (1975).

10 Verwey, E. J. W. Electronic Conduction of Magnetite (Fe3O4) and its Transition Point at Low Temperatures. *Nature* **144**, 327-328, doi:10.1038/144327b0 (1939).

11 Kuipers, A. J. M. & Brabers, V. A. M. Thermoelectric properties of magnetite at the Verwey transition. *Physical Review B* **14**, 1401-1405, doi:10.1103/PhysRevB.14.1401 (1976).

12 Walz, F. The Verwey transition - a topical review. *Journal of Physics: Condensed Matter* **14**, R285-R340, doi:10.1088/0953-8984/14/12/203 (2002).

13 García, J. & Subías, G. The Verwey transition—a new perspective. *Journal of Physics: Condensed Matter* **16**, R145-R178, doi:10.1088/0953-8984/16/7/r01 (2004).

14 Sorenson, T. A., Morton, S. A., Waddill, G. D. & Switzer, J. A. Epitaxial Electrodeposition of Fe3O4Thin Films on the Low-Index Planes of Gold. *Journal of the American Chemical Society* **124**, 7604-7609, doi:10.1021/ja0201101 (2002).
15 Kulp, E. A. *et al.* Electrodeposition of Epitaxial Magnetite Films and Ferrihydrite Nanoribbons on Single-Crystal Gold. *Chemistry of Materials* **21**, 5022-5031, doi:10.1021/cm9013514 (2009).
16 Gudavarthy, R. V. *et al.* Epitaxial Electrodeposition of Fe3O4 on Single-Crystal Ni(111). *Chemistry of Materials* **23**, 2017-2019, doi:10.1021/cm2002176 (2011).
17 Friák, M., Schindlmayr, A. & Scheffler, M. Ab initio study of the half-metal to metal transition in strained magnetite. *New Journal of Physics* **9**, 5-5, doi:10.1088/1367-2630/9/1/005 (2007).
18 He, Z. *et al.* Electrodeposition of CoxFe3–xO4 Epitaxial Films and Superlattices. *Chemistry of Materials* **25**, 223-232, doi:10.1021/cm303289t (2013).
19 Calhoun, B. A. Magnetic and Electric Properties of Magnetite at Low Temperatures. *Physical Review* **94**, 1577-1585, doi:10.1103/PhysRev.94.1577 (1954).
20 Verwey, E. J. W. & Haayman, P. W. Electronic conductivity and transition point of magnetite ("Fe3O4"). *Physica* **8**, 979-987, doi:https://doi.org/10.1016/S0031-8914(41)80005-6 (1941).
21 Hamilton, W. C. Neutron Diffraction Investigation of the 119°K Transition in Magnetite. *Physical Review* **110**, 1050-1057, doi:10.1103/PhysRev.110.1050 (1958).
22 Bauminger, R., Cohen, S. G., Marinov, A., Ofer, S. & Segal, E. Study of the Low-Temperature Transition in Magnetite and the Internal Fields Acting on Iron Nuclei in Some Spinel Ferrites, Using Mossbauer Absorption. *Physical Review* **122**, 1447-1450, doi:10.1103/PhysRev.122.1447 (1961).
23 Mason, W. P. Physical Acoustics and the Properties of Solids. *The Journal of the Acoustical Society of America* **28**, 1197-1206, doi:10.1121/1.1908593 (1956).
24 Slack, G. A. Thermal Conductivity of CaF2, MnF2, CoF2, and ZnF2 Crystals. *Physical Review* **122**, 1451-1464, doi:10.1103/PhysRev.122.1451 (1961).
25 Piekarz, P., Parlinski, K. & Oleś, A. M. Origin of the Verwey transition in magnetite: Group theory, electronic structure, and lattice dynamics study. *Physical Review B* **76**, 165124, doi:10.1103/PhysRevB.76.165124 (2007).
26 Piekarz, P., Parlinski, K. & Oleś, A. M. Mechanism of the Verwey Transition in Magnetite. *Physical Review Letters* **97**, 156402, doi:10.1103/PhysRevLett.97.156402 (2006).
27 J., S. E. & O., S. Low-Energy Phonons in Magnetite. *physica status solidi (b)* **61**, 615-620, doi:doi:10.1002/pssb.2220610227 (1974).
28 Warren, J. L. Further Considerations on the Symmetry Properties of the Normal Vibrations of a Crystal. *Reviews of Modern Physics* **40**, 38-76, doi:10.1103/RevModPhys.40.38 (1968).
29 Cowley, R. A. Zero sound, first sound and second sound of solids. *Proceedings of the Physical Society* **90**, 1127 (1967).
30 Cahill, D. G. Thermal conductivity measurement from 30 to 750 K: the 3ω method. *Review of Scientific Instruments* **61**, 802, doi:10.1063/1.1141498 (1990).
31 Koh, Y. K. *et al.* Comparison of the 3ω method and time-domain thermoreflectance for measurements of the cross-plane thermal conductivity of epitaxial semiconductors. *Journal of Applied Physics* **105**, 054303, doi:10.1063/1.3078808 (2009).
32 Hu, X. J., Padilla, A. A., Xu, J., Fisher, T. S. & Goodson, K. E. 3-Omega Measurements

of Vertically Oriented Carbon Nanotubes on Silicon. *Journal of Heat Transfer* **128**, 1109-1113, doi:10.1115/1.2352778 (2005).

33 Dames, C. & Chen, G. 1ω,2ω, and 3ω methods for measurements of thermal properties. *Review of Scientific Instruments* **76**, 124902, doi:10.1063/1.2130718 (2005).

34 Feser, J. P. *Scalable routes to efficient thermoelectric materials* Ph.D thesis, University of California, Berkeley, (2010).

35 Kim, J. H., Feldman, A. & Novotny, D. Application of the three omega thermal conductivity measurement method to a film on a substrate of finite thickness. *Journal of Applied Physics* **86**, 3959-3963, doi:10.1063/1.371314 (1999).

36 Lee, S.-M. & Cahill, D. G. Heat transport in thin dielectric films. *Journal of Applied Physics* **81**, 2590-2595, doi:10.1063/1.363923 (1997).

37 Kimling, J., Philippi-Kobs, A., Jacobsohn, J., Oepen, H. P. & Cahill, D. G. Thermal conductance of interfaces with amorphous SiO2 measured by time-resolved magneto-optic Kerr-effect thermometry. *Physical Review B* **95**, 184305, doi:10.1103/PhysRevB.95.184305 (2017).

38 Bartel, J. J. & Westrum, E. F. Heat capacities of Fe3O4 and ZnFe2O4 from 300 to 500 K. *The Journal of Chemical Thermodynamics* **7**, 706-708, doi:https://doi.org/10.1016/0021-9614(75)90012-9 (1975).

39 Gaur, U. & Wunderlich, B. Heat Capacity and Other Thermodynamic Properties of Linear Macromolecules. V. Polystyrene. *Journal of Physical and Chemical Reference Data* **11**, 313-325, doi:10.1063/1.555663 (1982).

40 S., C., W., T., W., V. D. B. & D., S. Optimization of a FIB/SEM slice-and-view study of the 3D distribution of Ni4Ti3 precipitates in Ni–Ti. *Journal of Microscopy* **233**, 61-68, doi:doi:10.1111/j.1365-2818.2008.03095.x (2009).

41 Wico, C. L. H. *et al.* Focused ion beam scan routine, dwell time and dose optimizations for submicrometre period planar photonic crystal components and stamps in silicon. *Nanotechnology* **18**, 195305 (2007).

42 Cahill, D. G. Analysis of heat flow in layered structures for time-domain thermoreflectance. *Review of Scientific Instruments* **75**, 5119-5122, doi:10.1063/1.1819431 (2004).

43 Wilson, R. B., Apgar, B. A., Martin, L. W. & Cahill, D. G. Thermoreflectance of metal transducers for optical pump-probe studies of thermal properties. *Opt. Express* **20**, 28829-28838, doi:10.1364/OE.20.028829 (2012).

44 Feser, J. P., Liu, J. & Cahill, D. G. Pump-probe measurements of the thermal conductivity tensor for materials lacking in-plane symmetry. *Review of Scientific Instruments* **85**, 104903, doi:10.1063/1.4897622 (2014).

45 Center, P. U. T. P. R. & Touloukian, Y. S. *Thermophysical Properties of Matter: The TPRC Data Series; a Comprehensive Compilation of Data*. (IFI/Plenum, 1979).

46 Cahill, D. G., Watson, S. K. & Pohl, R. O. Lower limit to the thermal conductivity of disordered crystals. *Phys Rev B Condens Matter* **46**, 6131-6140, doi:https://doi.org/10.1103/PhysRevB.46.6131 (1992).

47 Reichmann, H. J. & Jacobsen, S. D. High-pressure elasticity of a natural magnetite crystal. *Am Mineral* **89**, 1061-1066 (2004).

48 Costescu, R. M., Bullen, A. J., Matamis, G., O'Hara, K. E. & Cahill, D. G. Thermal conductivity and sound velocities of hydrogen-silsesquioxane low-k dielectrics. *Physical Review B* **65**, doi:ARTN 094205 s10.1103/PhysRevB.65.094205 (2002).

49 Cahill, D. G. *et al.* Nanoscale thermal transport. *Journal of Applied Physics* **93**, 793,

doi:10.1063/1.1524305 (2003).
50 Ma, J., Sadhu, J. S., Ganta, D., Tian, H. & Sinha, S. Thermal transport in 2- and 3-dimensional periodic "holey" nanostructures. *AIP Advances* **4**, 124502, doi:10.1063/1.4904073 (2014).
51 Feldman, A. *Algorithm for solutions of the thermal diffusion equation in a stratified medium with a modulated heating source*. Vol. 31 (1999).
52 Carslaw, H. S. & Jaeger, J. C. *Conduction of Heat in Solids*. (Clarendon Press, 1986).
53 Cahill, D. G., Katiyar, M. & Abelson, J. R. Thermal conductivity of a-Si:H thin films. *Physical Review B* **50**, 6077-6081, doi:10.1103/PhysRevB.50.6077 (1994).
54 Bauer, M. L. & Norris, P. M. General bidirectional thermal characterization via the 3ω technique. *Review of Scientific Instruments* **85**, 064903, doi:10.1063/1.4884638 (2014).
55 Wei, C., Zheng, X., Cahill, D. G. & Zhao, J.-C. Invited Article: Micron resolution spatially resolved measurement of heat capacity using dual-frequency time-domain thermoreflectance. *Review of Scientific Instruments* **84**, 071301, doi:10.1063/1.4815867 (2013).
56 Jiang, P., Huang, B. & Koh, Y. K. Accurate measurements of cross-plane thermal conductivity of thin films by dual-frequency time-domain thermoreflectance (TDTR). *Review of Scientific Instruments* **87**, 075101, doi:10.1063/1.4954969 (2016).
57 Wang, Y., Park, J. Y., Koh, Y. K. & Cahill, D. G. Thermoreflectance of metal transducers for time-domain thermoreflectance. *Journal of Applied Physics* **108**, 043507, doi:10.1063/1.3457151 (2010).
58 Koh, Y. K. & Cahill, D. G. Frequency dependence of the thermal conductivity of semiconductor alloys. *Physical Review B* **76**, 075207, doi:10.1103/PhysRevB.76.075207 (2007).
59 Brugger, K. Pure Modes for Elastic Waves in Crystals. *Journal of Applied Physics* **36**, 759-768, doi:10.1063/1.1714215 (1965).
60 Isida, S., Suzuki, M., Todo, S., Moˆri, N. & Siratori, K. Pressure effect on the elastic constants of magnetite. *Physica B: Condensed Matter* **219-220**, 638-640, doi:https://doi.org/10.1016/0921-4526(95)00837-3 (1996).
61 Siratori, K. & Kino, Y. A note on the magnetic anisotropy of Fe3O4. *Journal of Magnetism and Magnetic Materials* **20**, 87-90, doi:https://doi.org/10.1016/0304-8853(80)90530-2 (1980).
62 Khan, W. *et al. 1/ f noise studies of swift heavy ion irradiated magnetite thin films*. Vol. 266 (2008).
63 Sun, J. *et al.* Study of the magnetic modifications of Fe3O4 ferrite thin films induced by 2.03GeV Kr ions irradiation. *Nuclear Instruments and Methods in Physics Research Section B: Beam Interactions with Materials and Atoms* **269**, 873-875, doi:https://doi.org/10.1016/j.nimb.2010.11.073 (2011).
64 Houpert, C., Hervieu, M., Groult, D., Studer, F. & Toulemonde, M. HREM investigation of GeV heavy ion latent tracks in ferrites. *Nuclear Instruments and Methods in Physics Research Section B: Beam Interactions with Materials and Atoms* **32**, 393-396, doi:https://doi.org/10.1016/0168-583X(88)90243-1 (1988).
65 Meillon, S., Studer, F., Hervieu, M. & Pascard, H. Changes in magnetic properties of magnetite Fe3O4 ceramics induced by high energy heavy ion irradiation. *Nuclear Instruments and Methods in Physics Research Section B: Beam Interactions with Materials and Atoms* **107**, 363-367, doi:https://doi.org/10.1016/0168-583X(95)00843-8 (1996).

66 Ziegler, J. F., Ziegler, M. D. & Biersack, J. P. SRIM – The stopping and range of ions in matter (2010). *Nuclear Instruments and Methods in Physics Research Section B: Beam Interactions with Materials and Atoms* **268**, 1818-1823, doi:https://doi.org/10.1016/j.nimb.2010.02.091 (2010).
67 Ziegler, J. F. & Biersack, J. P. in *Treatise on Heavy-Ion Science: Volume 6: Astrophysics, Chemistry, and Condensed Matter* (ed D. Allan Bromley) 93-129 (Springer US, 1985).
68 Cahill, D. G. *et al.* Nanoscale thermal transport. II. 2003–2012. *Applied Physics Reviews* **1**, 011305, doi:10.1063/1.4832615 (2014).
69 Barako, M. T. *et al.* Quasi-ballistic Electronic Thermal Conduction in Metal Inverse Opals. *Nano Lett* **16**, 2754-2761, doi:10.1021/acs.nanolett.6b00468 (2016).
70 Choy, C. L. Thermal conductivity of polymers. *Polymer* **18**, 984-1004, doi:https://doi.org/10.1016/0032-3861(77)90002-7 (1977).
71 Xie, X. *et al.* High and low thermal conductivity of amorphous macromolecules. *Physical Review B* **95**, 035406, doi:10.1103/PhysRevB.95.035406 (2017).
72 Anderson, D. R. Thermal Conductivity of Polymers. *Chemical Reviews* **66**, 677-690, doi:10.1021/cr60244a004 (1966).
73 Rieger, J. The glass transition temperature of polystyrene. *Journal of thermal analysis* **46**, 965-972, doi:10.1007/bf01983614 (1996).

CHAPTER 4.

ELECTRICAL TRANSPORT PROPERTIES OF EPITAXIAL Fe_3O_4 3D MESO/NANOSTRUCTURES

4.1 Introduction

4.1.1 Motivation

In **Chapter 2**, we emphasized the importance of the development of a material demonstrating thermally insulating and electrically conducting properties simultaneously for diverse applications such as thermoelectrics and power electronics. It is also a very intriguing subject from the scientific perspectives because breaking of the coupling between the thermal conductivity and the electrical conductivity in one material is hard to achieve owing to their strong interdependencies[1]. In this regard, we proposed the single crystalline 3D nanostructures where the feature size go below the sub-100 nm, which is comparable with the Umklapp scattering limited phonon MFP of typical semiconductor (e.g. Si)[2], as a novel approach to tackle this issue.

We have successfully fabricated the epitaxial Fe_3O_4 3D nanostructures with the pores 40 nm in diameter. The 40 nm porous epitaxial sample exhibited the ultra-low thermal conductivity of ~ 0.1 W m^{-1} K^{-1} at room temperature, comparable to some polymer materials[3,4]. This result is worthy of notice when we the consider the two unique aspects of this porous material. First, it is single crystalline with small degrees of mosaic spread. Second, the matrix is comprised of the Fe_3O_4 whose bulk electrical property is half-metallic[5-10]. These features spontaneously led us to investigate the electrical conductivities of the epitaxial Fe_3O_4 nanoporous structure.

In this chapter, we will discuss the cross-plane electrical conductivity results of the epitaxial dense and the epitaxial PS included films. The electrical conductivity was determined by measuring the cross-plane electrical resistances of three identical samples with different thickness using a 4-point probe technique[11-13]. Those of the dense film and the PS included films were explained by magnetic properties and the optical constants, respectively. The 'true' effective medium approximation derived from the electrical conductivity results was applied to explain two types of lower bounds of the thermal conductivities of the porous films.

4.1.2 Electron transport mechanism

The Fe_3O_4 is a mixed-valence ferrimagnetic material with the inverse spinel structure. The unit cell is composed of 32 close-packed FCC O^{2-} lattices in which 8 Fe^{3+} are distributed over the tetrahedral sites (A) and the remaining 8 Fe^{3+} and 8 Fe^{2+} are distributed over the octahedral sites (B)[8,9]. Considering this distribution, the Fe_3O_4 can be denoted as the $[Fe^{3+}]_A[Fe^{2+}, Fe^{3+}]_BO_4$. The electrical conductivity of the Fe_3O_4 in the range of $10^3 \sim 2 \times 10^4$ S m^{-1}, which is much higher than the conductivities of the normal spinel-type materials such as Co_3O_4 and Mn_3O_4 (~10^{-5} S m^{-1}), is closely related to the crystal structure of the Fe_3O_4[9]. The rapid electron exchange through the electron hopping between Fe^{3+} and Fe^{2+} located at the octahedral sites, has been accepted as a main origin of the high electrical conductivity of the Fe_3O_4 at room temperature[5,14].

4.1.3 Verwey transition

When the temperature drops below 120 K, the Fe_3O_4 exhibits a metal-to-insulator transition, which was first discovered by Verwey in 1939[15]. The transition temperature is called the Verwey transition temperature, T_v. **Figure 4.1** represents that below the Verwey transition temperature, the electrical conductivity of the Fe_3O_4 abruptly decreases by two orders of magnitude[16]. To explain this, Verwey proposed an ionic model where he attributed this drastic change in the electrical conductivity to a charge order-disorder transition in the octahedral sites[10,15,17,18].

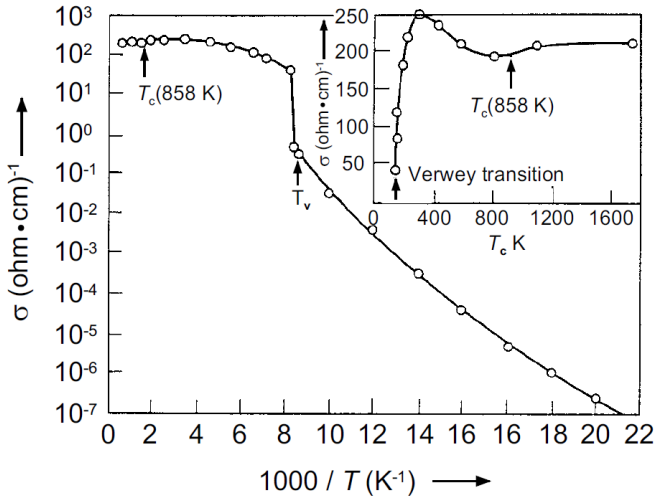

Figure 4.1 – Typical temperature dependence of the electrical conductivity of the Fe_3O_4 single crystal, clearly showing the drastic change in the electrical conductivity around the Verwey transition temperature. Adapted from 16.

According to the model, above T_V, Fe^{3+} and Fe^{2+} are dynamically randomized in the lattice, so that the electron can rapidly hop between Fe^{2+} and Fe^{3+} ions. Below T_V, however, the Fe^{2+} and Fe^{3+} ions form a long-range spatial ordering arrays. This periodic order localizes the electron, deterring the motion of the electron. Although this ionic model has been widely used to understand the various macroscopic behaviors such as electrical conductivity, heat capacity, magnetic response, and thermal conductivity to date[8,9,16,19], it still remains controversial in the field[8,9].

4.1.4 Electronic thermal conductivity

Despite some discrepancies among literature values, the electrical conductivity of the bulk Fe_3O_4 single crystal at room temperature is 2 x 10^4 S m^{-1} in typical[10,16,20]. Using the Wiedemann – Franz law[1],

$$\Lambda_{el} = \sigma L T$$

where Λ_{el}, σ, and L are the electronic thermal conductivity, the electrical conductivity, and the Lorenz constant (2.44 x 10^{-8} W Ω K^{-2}), respectively, the electronic thermal conductivity of the bulk Fe_3O_4 single crystal, Λ_{el,Fe_3O_4}, can be computed as

$$\Lambda_{el,Fe_3O_4} \approx 0.146\ W\ m^{-1}\ K^{-1}\ .$$

If we adopt 6.9 W m^{-1} K^{-1} as a thermal conductivity of the bulk single crystal, measured by Slack at el.[19], the electronic contribution to the total thermal conductivity, $\Lambda_{Fe_3O_4}$, is calculated as

$$\frac{\Lambda_{el,Fe_3O_4}}{\Lambda_{Fe_3O_4}} = \frac{0.146}{6.9} \approx 0.02$$

which indicates that 98 % of the heat are carried by the phonons in the Fe_3O_4 single crystal.

4.2 Experimental Methods

4.2.1 Cross-plane electrical conductivity measurement

Sample preparation

We deposited a 120 μm wide patterned 10 nm thick Ti layer followed by 500 nm thick Au layer on the Piranha-cleaned Al_2O_3 (0001) wafer using the electron beam evaporation. Employing

the same recipes described in **Chapters 2** and **3**, we fabricated the colloidal crystals on the Au surface followed by infilled the pores with the Fe_3O_4 through the electrochemical deposition. Three identical samples with three different thicknesses were fabricated by controlling the electrodeposition durations. The extra colloidal crystals on top were removed by the adhesives. Note that prior to the electrodeposition, the bare Au area where the colloidal crystals were not grown, needed to be masked by an alkaline-resistant Teflon adhesive (ASF-110FR, Chukoh), so that we could later use this bare Au region as the tip contact points for the electrical conductivity measurement. For the fabrication of dense samples, the Piranha-cleaned Au/Ti/sapphire substrates were directly used for the electrodeposition and all the colloid-related processes were skipped.

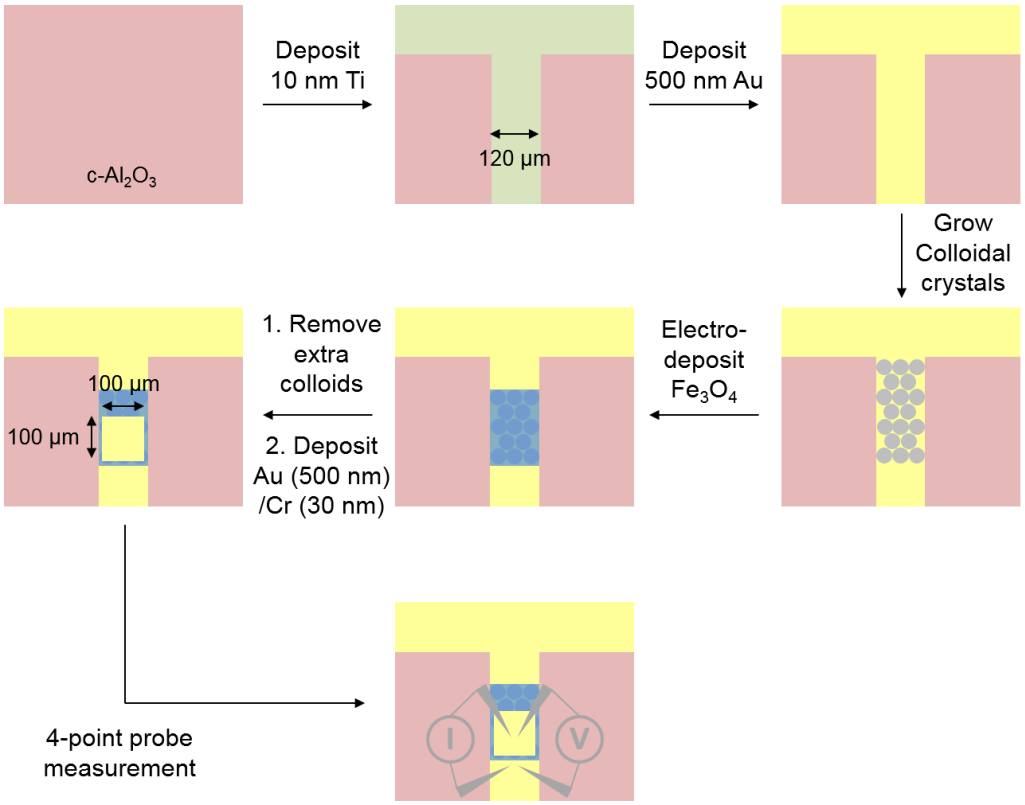

Figure 4.2 – Schematic illustration of the overall fabrication processes for measuring the cross-plane electrical conductivity of a Fe_3O_4 film by 4-point probe method.

Under an optical microscope with long working distance, we aligned a brass hard mask having the 100 x 100 μm^2 square patterns on top of Fe_3O_4 layers. The location of the square pattern was delicately adjusted so that the distance with the bottom Au layer can be as small as possible to minimize the error. Through these patterns, we deposited a 30 nm thick Cr layer followed by a 500 nm thick Au layer using the ebeam evaporation. Two probe tips were located on the top Au

electrode and the other two were on the bottom Au electrode for the through-plane electrical measurement *via* 4-point probe method. The overall processes are depicted in **Figure 4.2**.

Data acquisition

The cross-plane electrical conductivity was measured by a 4-point probe technique combined with the differential thickness method[11-13] at room temperature. We used a customized benchtop probe station connected with a semiconductor parameter analyzer (4155c, Agilent). Through an optical microscope, the four tungsten probe tips, 5.0 μm in diameter (SE-T, Signatone) were located on the samples in such a way that two tips had contacts with the top Au layer and the other two tips contacted with the bottom Au layer. Note that the distance between the top tips and the bottom tips was always *kept constant* during the whole measurements in order to minimize the variations in the sheet resistance of the bottom Au layer. The current-voltage characteristics were obtained by sweeping the current over -100 ~ 100 μA multiple times per each sample. **Figure 4.3** exhibits the overall measurement setup (**a**) and the magnified actual image showing the configuration of four tips and a sample during measurement (**b**).

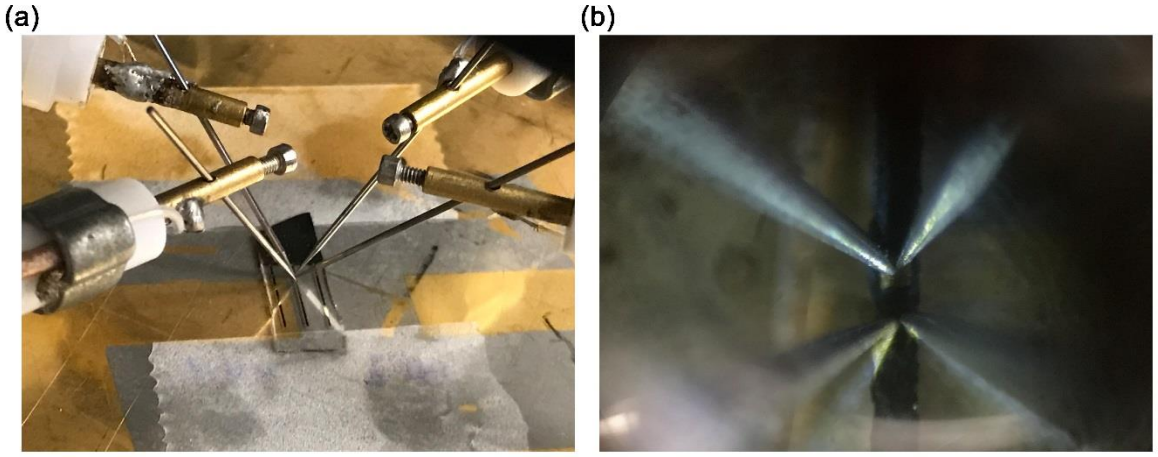

Figure 4.3 – Experimental setup used to measure the cross-plane electrical conductivity of our samples. (a) Photograph exhibiting the four probes tips located on the sample. (b) Magnified photograph of (a). We can clearly see that two tips are on the top electrode and the other two tips are on the bottom electrode.

Spreading resistance

Since the areas of the top and the bottom Au electrodes in our samples differ from each other, the spreading resistance needs to be considered. The spreading resistance has been a main issue for those working on the electrical measurement on the semiconductor devices[21-23]. Cox and

Strack[23] first proposed an analytical solution that considered the electric spreading effects occurring in a sample sandwiched between two asymmetric electrodes, as shown in **Figure 4.4**[22,23]. According to them, the total resistance, R_T, can be written as

$$R_T = R_S + \frac{4\rho_c}{\pi d^2} + R_0$$

where R_S, ρ_c, d, and R_0 denote the spreading resistance (Ω), the specific contact resistivity (Ω m^2) between the top electrode and the sample, the top electrode diameter, and the contact resistance (Ω) between the sample and the bottom electrode, respectively. The spreading resistance, R_S, is expressed as

$$R_S = \frac{\rho}{d\pi} arctan \frac{4}{d/h}$$

where ρ and h denote the sample resistivity (Ω m) and the sample thickness, respectively. They proved that when the diameter of the electrode becomes much larger than the thickness of the sample, the spreading effect becomes negligible. The spreading resistance can then be simplified as

$$R_S \approx \frac{\rho h}{\pi (d/2)^2}$$

which is the same form as the case when the areas of both electrodes are identical (or symmetric)[21]. Cox and Strack experimentally proved that this approximation is valid when the d/h becomes larger than 10, as demonstrated in **Figure 4.5**[23]. In our samples, the ratio between the width ($A^{1/2}$; instead of diameter) of the top square Au electrode and the thickness of the Fe_3O_4 layer (h) is typically in the range of 15 ~ 100, where the above approximation is valid. Therefore, we used the following simple relation to extract the electrical resistivity for our samples.

$$R_S \approx \frac{\rho h}{A}$$

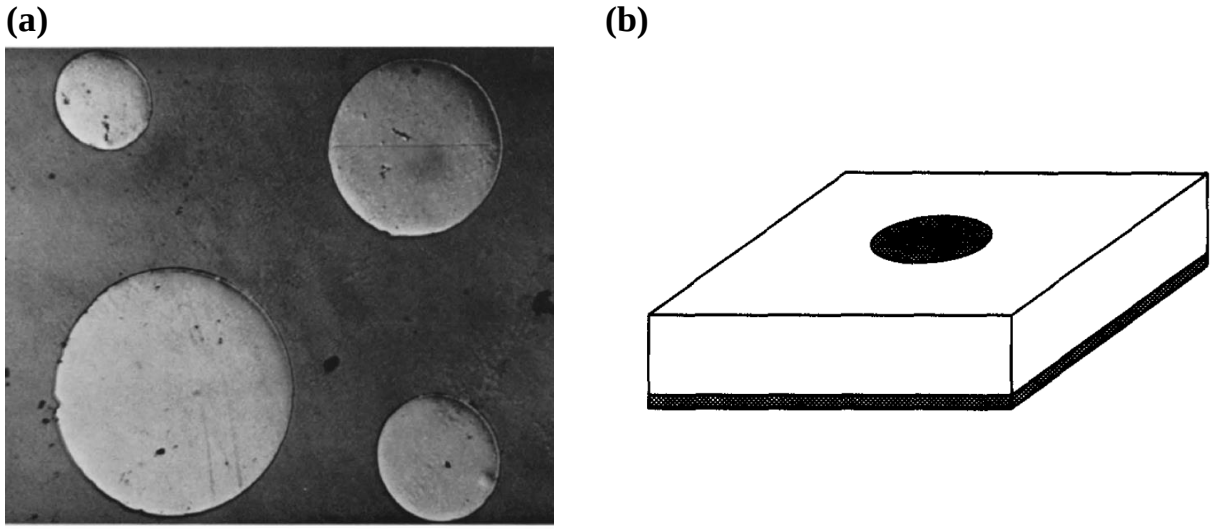

Figure 4.4 – The sample structures having the asymmetric electrodes for the electrical conductivity measurement. (a) Top-view image of the sample measured by Cox and Strack. Four circular electrodes with different diameters were used for extracting the contact resistivity. Adapted from ref. 25. (b) Schematic of the sample geometry that shows the large bottom electrode and the circular small top electrode. Adapted from ref. 24.

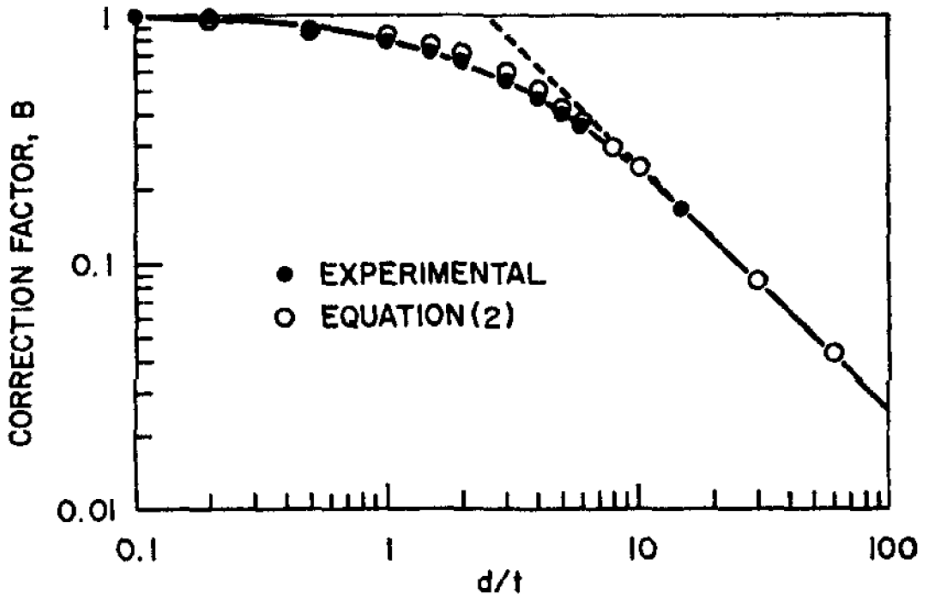

Figure 4.5 – Above the *d/t* (ratio of electrode diameter to layer thickness) of 10, the spreading resistance effect becomes negligible. Adapted from ref. 25.

Data analysis

The thickness of each sample was determined by observing the cross-section exposed by the Ga-ion milling (Helios 600i FIB/SEM, FEI), as described in **Chapter 3**. The measured

thickness was divided by sin 52° to correct the 52°-tilted projection of the FIB/SEM cross-section image[24,25]. The area of the top Au electrode was 10^4 μm^2 with a 5 % error, in typical.

Three measured resistances (R) were plotted against the geometry factor composed of the film thickness (h) divided by the top electrode area (A). The electrical resistivity of the Fe_3O_4 layer was extracted from the slope of a linear regression of the plot. The y-intercept of the regression comprises the sheet resistance of the bottom Au layer and the overall contact resistance of the interfaces between the Fe_3O_4 layer and the Au electrodes.

Figure 4.6 is a collection of the acquired data to measure the electrical conductivity of the dense epitaxial Fe_3O_4 film: (a) plane-view SEM image showing that the Fe_3O_4 layer is sandwiched between two Au electrodes, (b) voltage vs. current characteristics of three samples with different thickness, (c) FIB-cut cross-section SEM images of those three samples, and (d) linear regression of a plot of R vs. h/A. **Figures 4.7 ~ 4.10** correspond to those of the PS included samples at the diameters of 500, 200, 100, and 40 nm, respectively.

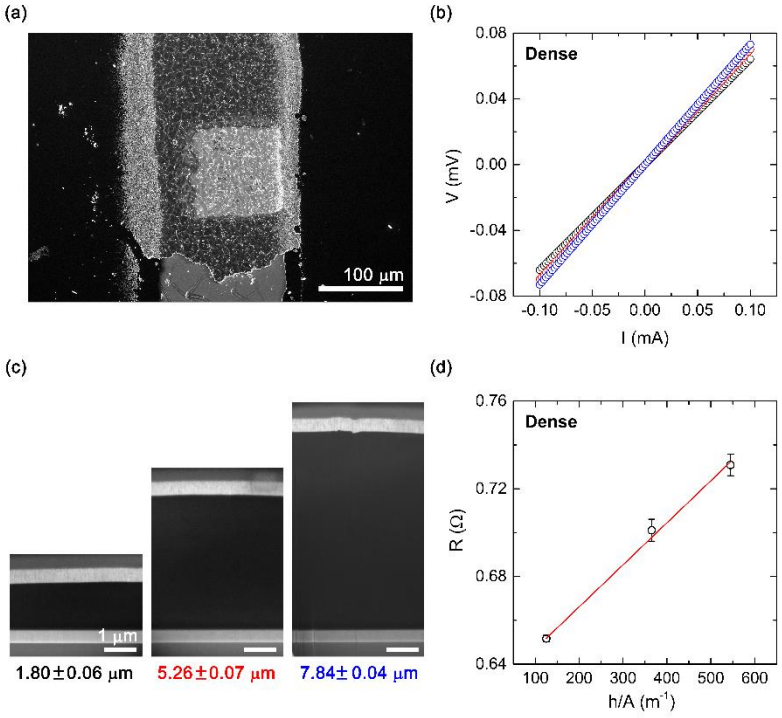

Figure 4.6 – Data collection used to extract the through-plane electrical conductivity of epitaxial Fe_3O_4 dense film *via* 4-point probe technique in combination with differential thickness method. (a) Plane-view SEM image, (b) I-V characteristics, (c) FIB-cross-sectioned SEM images with the thicknesses of Fe_3O_4 layers indicated below, and (d) R vs. h/A plot.

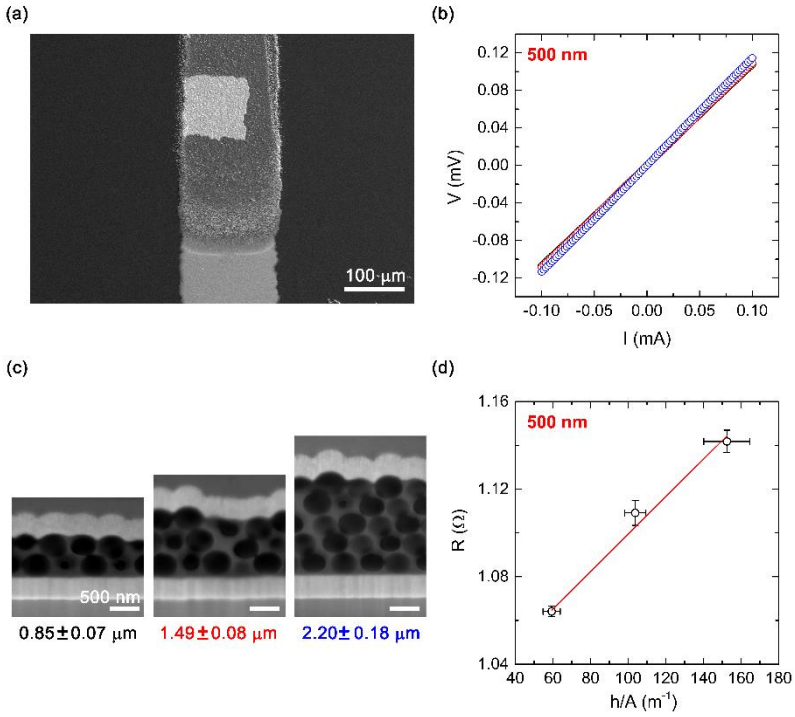

Figure 4.7 – Data collection used to extract the through-plane electrical conductivity of 500 nm PS included film *via* 4-point probe technique in combination with differential thickness method.

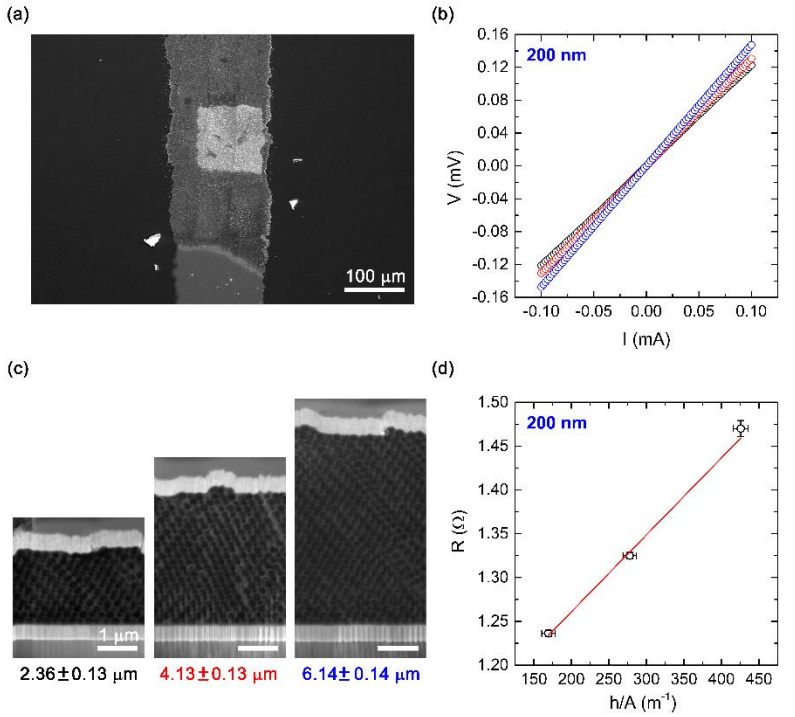

Figure 4.8 – Data collection used to extract the through-plane electrical conductivity of 200 nm PS included film *via* 4-point probe technique in combination with differential thickness method.

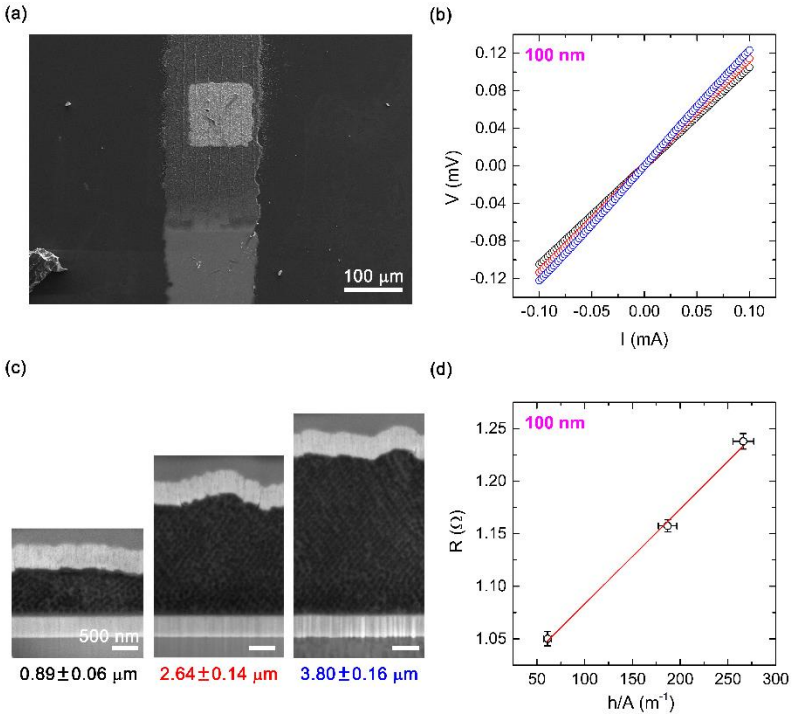

Figure 4.9 – Data collection used to extract the through-plane electrical conductivity of 100 nm PS included film *via* 4-point probe technique in combination with differential thickness method.

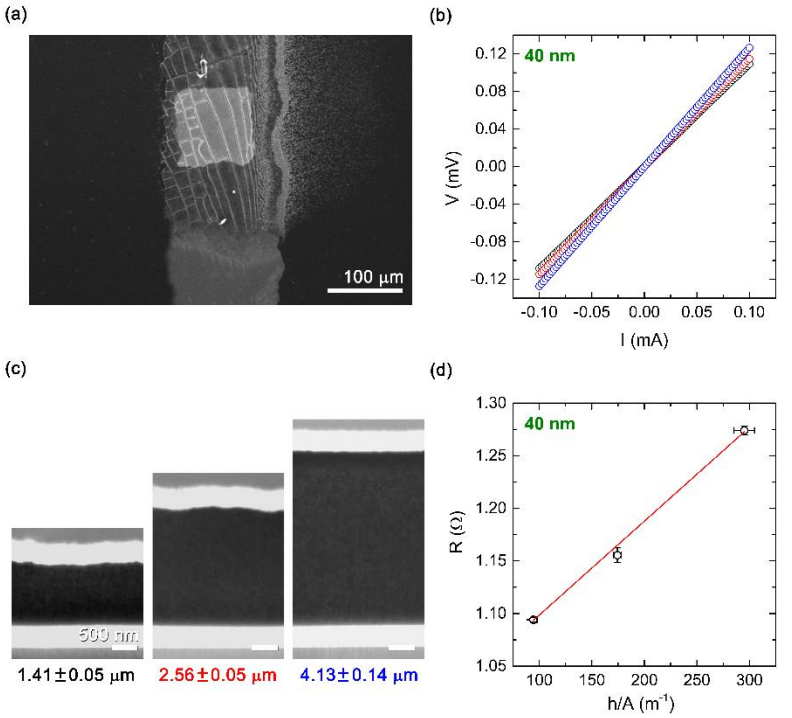

Figure 4.10 – Data collection used to extract the through-plane electrical conductivity of 40 nm PS included film *via* 4-point probe technique in combination with differential thickness method.

4.2.2 Optical constant measurement

FT-IR

Over the wavelengths of Near-IR ~ Mid-IR, the reflectance spectrum from the sample was measured using Vertex-70 FT-IR and a Bruker Hyperion microscope. A globar source, KBr beam-splitter, and 15x cassegrain objective (N.A. 0.4) were used to irradiate an unpolarized light on a spot size of 70 um in diameter, and its reflectance was measured using a liquid nitrogen cooled HgCdTe detector. The bare Au/Ti/sapphire substrate where Fe_3O_4 layers were grown was directly used as the reference. To collect the refractive indices over the wider range of wavelength, multiple samples with various thickness for each case were fabricated and measured. The thickness of the Fe_3O_4 layer was characterized by the SEM image.

Figure 4.11 presents the reflectance spectra as a function of the wavelength of (a) dense films with various thickness and (b) PS included samples with the different diameter of PS beads. Using the spacing between adjacent maxima (or minima) of the oscillations in the reflectance spectrum, which resulted from the thin-film interference[26,27], refractive index information of Fe_3O_4 layer was obtained. More specifically, the phase condition for constructive interference order m is expressed by

$$\frac{2\pi}{\lambda_m} n\Delta L = 2\pi m$$

where λ_m is the wavelength, n is the refractive index of the Fe_3O_4 film, and ΔL is the difference in path length traveled by waves that reflect at the air/film interface and film/substrate interface, respectively. Using the difference between the m and $m+1$ orders and rearranging, the following relationship can be obtained.

$$n = \frac{1}{\Delta L\left(\frac{1}{\lambda_m} - \frac{1}{\lambda_{m+1}}\right)}$$

Here, n is considered to be constant over the region between two oscillations. From the relationship among the path length difference, the film geometry, and the angles of the rays in combination with Snell's law, the path length difference can be expressed by

$$\Delta L = \frac{2h}{cos\left(sin^{-1}\left(\frac{sin(\theta_{inc})}{n}\right)\right)}$$

where h and θ_{inc} are the film thickness and the angle of incident light, respectively. Therefore, the final form of the equation to extract the refractive indices of the Fe_3O_4 films is

$$n = \frac{cos\left(sin^{-1}\left(\frac{sin(\theta_{inc})}{n}\right)\right)}{2h\left(\frac{1}{\lambda_m} - \frac{1}{\lambda_{m+1}}\right)}.$$

We solved this transcendental equation through a numerical method using the MATLAB code.

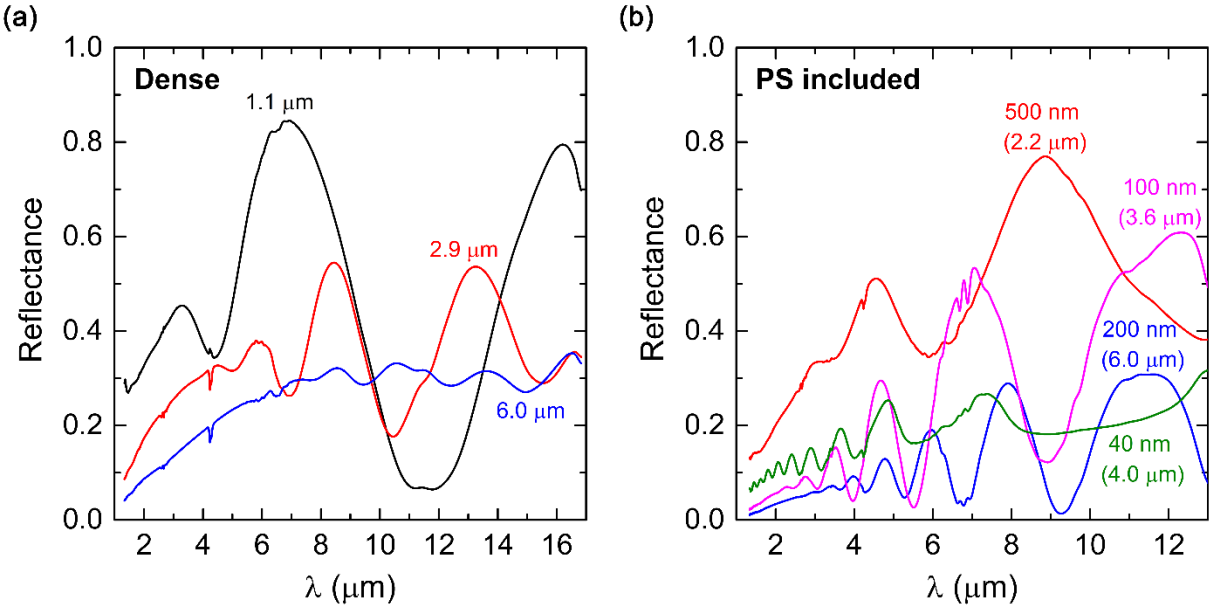

Figure 4.11 – Oscillating reflectance spectra collected over the wavelength of NIR ~ MIR on the (a) dense films and (b) PS included films at the diameters of 500, 200, 100, and 40 nm, respectively. The number in (a) denote the thickness of a dense film. Those outside and inside the parenthesis in (b) indicate the diameter of PS beads and the thickness of the corresponding Fe_3O_4 layer, respectively.

Ellipsometry

The refractive indices of the Fe_3O_4 dense film and the porous film including the pores with 40 nm in diameter were measured using a variable angle spectroscopic ellipsometer (VASE, J.A. Woollam Co. Inc.) over the spectral range of 1.0 ~ 1.2 μm. We measured at three different angles of ψ = 45, 60, and 75° and performed a global fitting to extract the refractive index of a layer.

4.2.3 Magnetic property measurement

The magnetic properties of samples were measured in a superconducting quantum interference device (SQUID) magnetometer (MPMS3, Quantum Design Inc.) in the vibrating sample magnetometry mode. The measurement was carried out with the sample in low vacuum of about 20 Torr under He atmosphere. We acquired the magnetization against external magnetic field over -2 ~ 2 T at the temperatures of 4, 90, 150, 200, 250, and 300 K. Under the magnetic field of 150 mT, the magnetization against the temperature over 4 ~ 300 K were collected.

4.3 Electrical conductivity of Dense Film

Figure 4.12 exhibits a plot of the measured electrical conductivity of our samples as a function of pore diameter. The electrical conductivity of the dense epitaxial Fe_3O_4 film is (5.22 ± 0.17) x 10^3 Ω^{-1} m^{-1} and those of the PS included films are (1.17 ± 0.10) x 10^3 Ω^{-1} m^{-1} for 500 nm case, (1.14 ± 0.08) x 10^3 Ω^{-1} m^{-1} for 200 nm, (1.10 ± 0.09) x 10^3 Ω^{-1} m^{-1} for 100 nm, and (1.12 ± 0.04) x 10^3 Ω^{-1} m^{-1} for 40 nm, respectively.

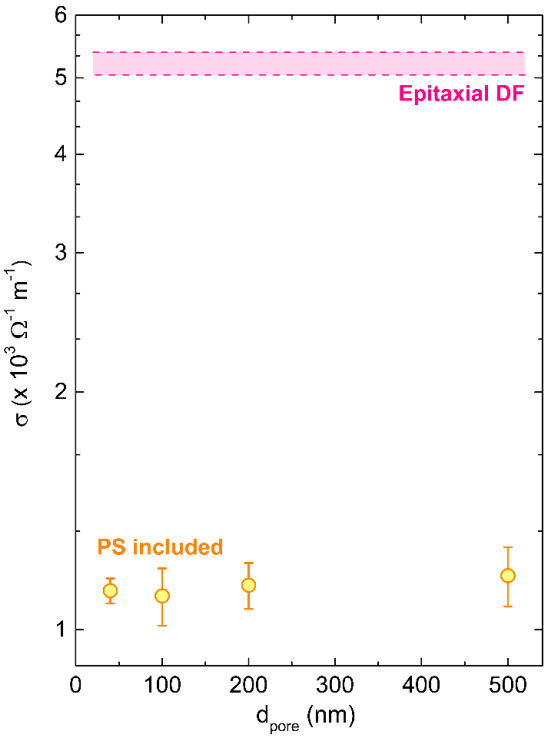

Figure 4.12 – Measured electrical conductivities of the Fe_3O_4 epitaxial dense film and the PS included films at different PS bead diameters of 500, 200, 100, and 40 nm, respectively.

Typically, a bulk Fe_3O_4 single crystal is known to have the electrical conductivity of 2 x 10^4 Ω^{-1} m^{-1} at room temperature[8,9,16,18,20]. The electrical conductivity of the epitaxial Fe_3O_4 dense film in this work is 3.8 times smaller than that of the bulk single crystal. This might be first related to the difference in the crystallinity between two. As mentioned in **Chapter 2**, our dense film is comprised of dual domains oriented along [111] direction that are antiparallel to each other, so called rotational twins. Also, the dense film has 2.5 times larger FWHM of the rocking curves than the bulk single crystal. These collectively indicate that the epitaxial dense film contains more domain boundaries than the single crystal consisting only of single domain. The adverse effects of the degraded crystallinity induced by domain boundaries on the electron transport properties of Fe_3O_4 epitaxial films are widely investigated[28-32].

Along with this effect, the non-stoichiometry, δ, of the Fe_3O_4 film could be another possible origin of the degraded electrical conductivity of our dense film. It has been widely investigated that the ratio between the amounts of Fe^{2+} and Fe^{3+} ions, which is closely related with the oxidation state, could change the electron transport properties of the Fe_3O_4 dramatically[9,15,17,33-35]. The balance between the Fe^{3+} and the Fe^{2+} ions in the octahedral sites is essential to facilitate the electron exchange and hence to enable electron hopping conduction between these two ions[6,9,10,16,18].

For a non-stoichiometric Fe_3O_4, the structure is generally expressed as $Fe_{3-\delta}O_4$, where δ can vary from zero (stoichiometric Fe_3O_4) to 1/3 (completely oxidized). The non-stoichiometry can be described in the form of

$$x = \frac{[Fe^{2+}]}{[Fe^{3+}]} = \frac{1-3\delta}{2+2\delta}$$

where $[Fe^{2+}]$ and $[Fe^{3+}]$ are the number concentrations of Fe^{2+} and Fe^{3+} ions in the Fe_3O_4 lattice, respectively. The ratio of the concentrations between two species is tightly coupled to the non-stoichiometry of a Fe_3O_4.

In this context, we performed the magnetic measurements on the dense and the 100 nm porous films to gain qualitative insights into the oxidation states of our system. **Figures 4.13a** and **b** represent that the saturation magnetization of both films is 78 emu/g (383000 A m^{-1}), which is slightly smaller than the reported values of a stoichiometric single crystal, 83 ~ 91 emu/g[36-39].

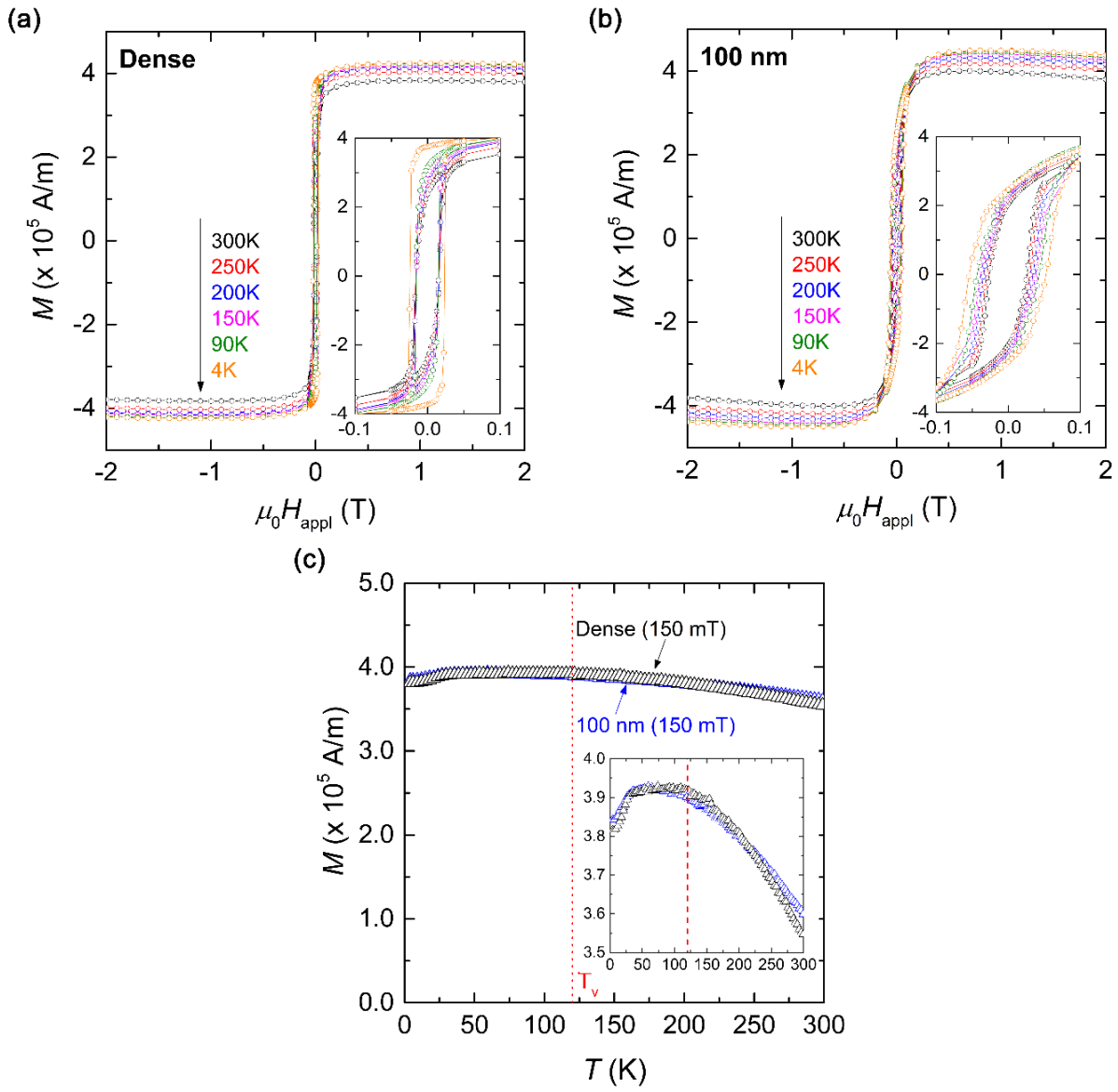

Figure 4.13 – Magnetic properties of the epitaxial Fe_3O_4 dense film and the 100 nm porous film. (a, b) Magnetization curves acquired by applying the magnetic field ranging over -2 to 2 T at five different temperatures on the dense and 100 nm porous films, respectively. Insets are the magnified views of the center regions over the magnetic field of -0.1 ~ 0.1 T. (c) Magnetization curves of both films collected by sweeping the temperature over 4 ~ 300 K under 150 mT. T_v denotes the Verwey transition temperature. Inset is the magnified view.

The effects of the non-stoichiometry of the Fe_3O_4 on its magnetic properties have been studied[40-43]. Especially, Ozdemir and Dunlop[42] have reported that the saturation magnetization was very sensitive to the oxidation state of a Fe_3O_4 material. They revealed that as the oxidation state increased, the saturation magnetization degraded. Based on their result, we can conclude that the

stoichiometry of our films is not perfect but a little bit off. This argument is also fortified by the characteristic of the magnetization curves measured over the temperature range of 4 to 300 K under the applied magnetic field of 150 mT as shown in **Figure 4.13c**. In the inset of **Figure 4.13c**, both films demonstrate the monotonous decrease in the magnetization with increasing temperature without showing any sudden drop at the Verwey transition temperature (~ 120 K). It is well known that the non-stoichiometric nature of a Fe_3O_4 phase usually deters the Verwey transition characteristic or shifts the transition temperature itself[9,15,17].

When we grow the epitaxial Fe_3O_4 film by the electrodeposition, we apply a cathodic potential with very small magnitude (-1.018 V vs. Ag/AgCl) to the working electrode, where the charge-transfer kinetics dominates the diffusion kinetics[44-46] and therefore very small current flows. This is essential to improve the crystalline quality of the films. However, the insufficient amounts of Fe^{3+} precursors in the electrolyte are reduced to Fe^{2+} ions incorporated into the Fe_3O_4 lattice during the film growth, resulting in the non-stoichiometry. Indeed, the Fe_3O_4 dense film grown at this potential regime has been previously identified to be the Fe^{2+}-deficit phase by Mossbauer spectroscopy[44].

For both dense and 100 nm porous films, the magnetization decreases with increasing temperature from 4 to 300 K, a typical characteristic of ferrimagnetic materials. Also, both films show the hysteresis loops, a signature of the spontaneous magnetization. As well exhibited in the insets of **Figures 4.13a** and **b**, the hysteresis of the porous film is wider and smoother than that of the dense film. The 3D nature of the porous film seemed to lead to an enhanced coercivity, probably due to domain wall pinning and internal stress[47,48].

4.4 Electrical conductivities of PS included films

Another interesting feature observed in **Figure 4.12** is that the electrical conductivity is independent on the size of the PS beads inside. In all cases, the electrical conductivity falls within the range of 22 % of that of the dense film. Since the electron mean free path is much smaller than the feature size of the PS included film with the smallest PS beads (40 nm in diameter), the electrical conductivity result can be handled with an effective medium approximation regardless of the PS bead size. If we incorporate the electrical conductivity ratio between the dense film and

a PS included film, 22 %, into the differential effective medium (DEM) theory[49], which was introduced in **Chapter 3**, the volume density of Fe_3O_4 in the PS included film is calculated to be 36.4 %. This value is deviated from those obtained by the RBS and XRF measurements in **Chapter 2**. Assuming that the densities experimentally measured by two independent techniques, we could deduce that the DEM approximation needs to be slightly modified depending on the diameter of the PS beads inside the samples. Two factors should be considered: the degree of isotropy and the degree of percolation. We know that as the PS beads get smaller, a PS included sample has less isotropic (or more disordered) structure and higher degree of percolation. All the values and arguments described above should be the same for the porous Fe_3O_4 films because the electrical conductivity of air is also nearly zero.

The electrical conductivity results are supplemented by the optical constants measured on the dense and the PS included films using FT-IR and ellipsometer. **Figure 4.14a** represents the refractive indices of the Fe_3O_4 samples over the wavelength of 1 ~ 13 μm extracted from the oscillating FT-IR reflectance spectra in **Figure 4.11**. The index of refraction of the dense film is about 90 % of that of the bulk single crystal reported elsewhere[50]. As the wavelengths of the IR waves are larger or much larger than the diameters of the PS beads inside, similar to the electrical conductivity case, we can also apply an effective medium approximation to analyze the optical constant data[51,52]. The equation of the DEM theory here is more complex than the electrical conductivity case because the refractive indices of the PS and air are not zero whereas the electrical conductivities of them are almost zero. Therefore, the density of the Fe_3O_4, $\phi_{Fe_3O_4}$, in the PS include film can be expressed by

$$\phi_{Fe_3O_4} = \left(\frac{n_{PS-incl} - n_{PS}}{n_{Fe_3O_4} - n_{PS}}\right)\left(\frac{n_{Fe_3O_4}}{n_{PS-incl}}\right)^{1/3}$$

where $n_{PS-incl}$, n_{PS}, and $n_{Fe_3O_4}$ are the refractive indices of a PS-included film, the polystyrene bead (~ 1.57)[53], and the epitaxial dense Fe_3O_4 film, respectively. As evidently shown in **Figure 4.14a**, the refractive indices of PS included films are perfectly fitted with the DEM curve calculated based on the Fe_3O_4 density of 37 % regardless of the PS particle diameter, in good agreement with the electrical conductivity result (36.4 %). This result is also supported by the refractive indices of a 40 nm porous film measured by an ellipsometer in the range of 1 ~ 1.2 μm, as shown in **Figure 4.14b**.

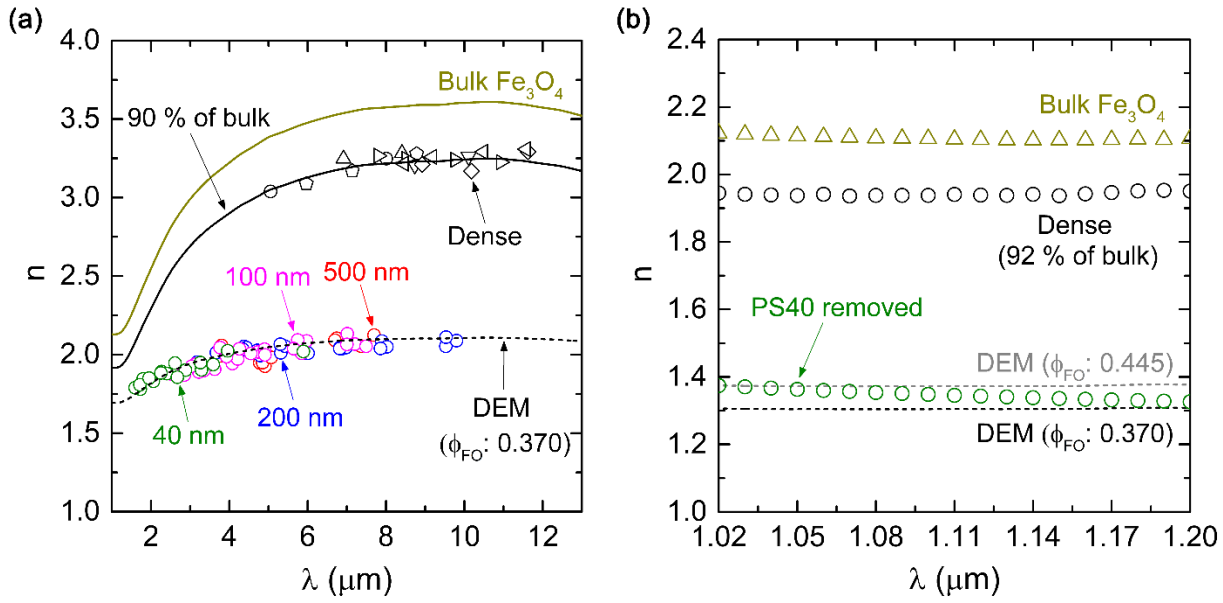

Figure 4.14 – Refractive indices of the Fe_3O_4 films measured with (a) FT-IR and (b) ellipsometer. They follow the same effective medium approximation as the electrical conductivities do.

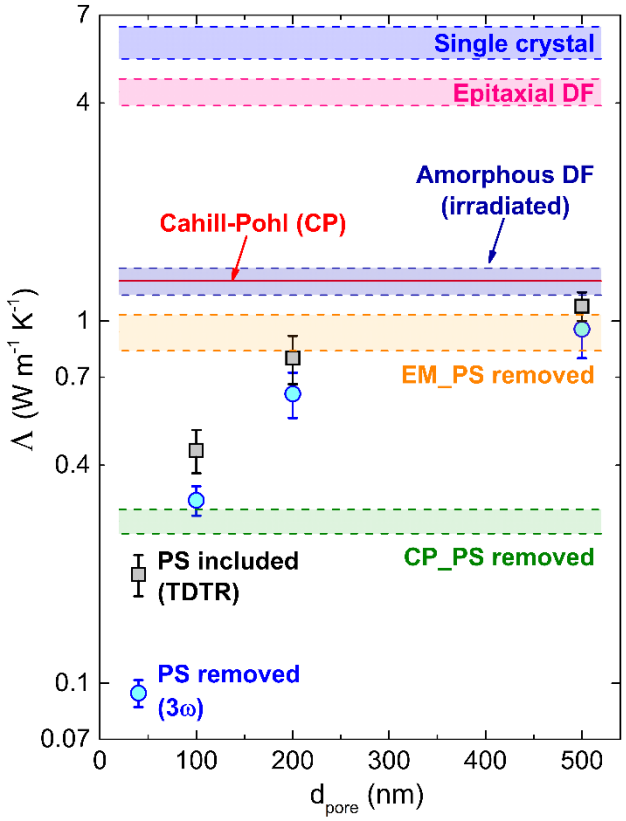

Figure 4.15 – Revised plot of thermal conductivity as a function of pore diameter using the 'true' effective medium approximation to predict the lower limits of the thermal conductivity for the porous epitaxial Fe_3O_4 film and the porous amorphous film, respectively.

Therefore, the electrical conductivity ratio of the dense film to a PS included film, 22 %, is the 'true' effective medium approximation that can describe various properties of our PS included Fe_3O_4 films best. This effective medium approximation can be directly utilized to predict the thermal conductivity limit of a porous medium consisting either of the epitaxial or the amorphous Fe_3O_4 phase because the thermal conductivity of air is almost zero, in analogous to the case where the electrical conductivity of the PS bead is negligible. **Figure 4.15** is the modified version of **Figure 3.21b** by replacing the DEM theory with the true EM approximation for estimating the lower bounds of the thermal conductivity for the epitaxial and the amorphous porous films, respectively.

4.5 Decoupled Phonon and Electron Transports

Figure 4.16 represents the ratio of the electrical conductivity to the thermal conductivity of the porous Fe_3O_4 films as a function of pore diameter. Since the electrical conductivity is independent on the pore size of the porous Fe_3O_4 film whereas the thermal conductivity is highly dependent on the pore size, the ratio between two properties becomes larger as the pore diameter gets smaller. This implies that the phonon and the electron transports can be effectively decoupled on smaller length scales. Especially for the 40 nm case, the ratio exceeds far beyond the bulk single crystal value.

One thing to note here is that the PS removed samples and the PS included samples contain the domain walls made of the epitaxial dense film. The formation of these walls is inevitable because the colloidal self-assembly driven by solvent evaporation always leaves certain amounts of defective cracks between colloidal crystal domains after complete drying of the solvent. However, as exhibited in **Figure 4.17**, the areal densities of the walls are only 2.9, 3.5, 4.1, and 5.5 % for the PS included samples with the diameters of 500, 200, 100, and 40 nm, respectively. As the relative errors of thermal and electrical conductivities measured in this study are usually 8 ~ 11 %, the effects of the domain walls on the conductivities can be ignored.

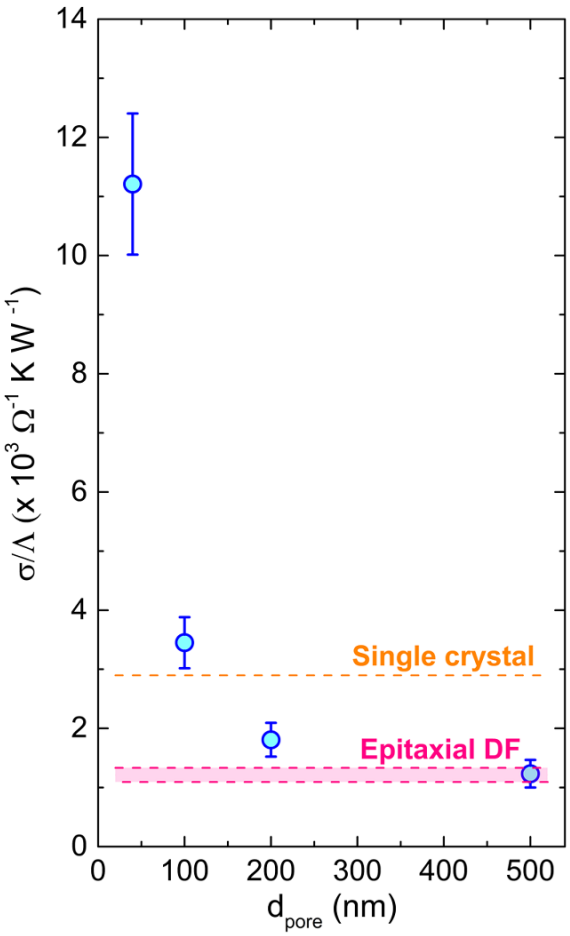

Figure 4.16 – Plot of the electrical conductivity divided by the thermal conductivity of the Fe_3O_4 films of this study as a function of pore diameter. As the pore diameter decreases, decoupling between the phonon and electron transports becomes pronounced.

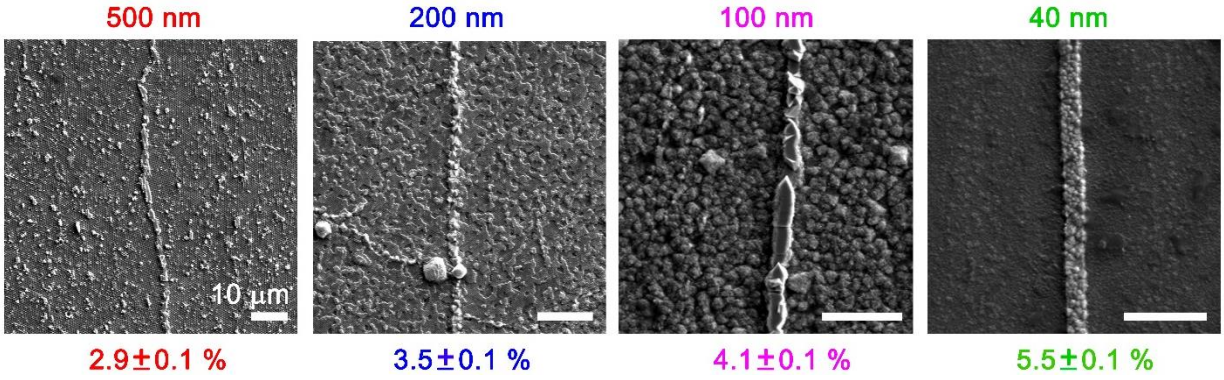

Figure 4.17 – Plane-view SEM images of the PS included samples at the pore diameters of 500, 200, 100, and 40 nm, respectively, revealing the domain walls in the center. The areal density was calculated by dividing the area of the wall by the total area.

4.6 Conclusions

In this chapter, we discussed the techniques for the cross-plane electrical conductivity measurement on the conductive thin films grown on the conducting electrode. Utilizing 4-point probe method combined with the differential thickness method, we could successfully rule out the contributions of the overall contact resistances to the total measured resistance. As the area of the Au top electrode was much larger than the film thickness in our study, the spreading resistance was negligible based on the Cox and Strack method.

The electrical conductivity results were discussed using the magnetic and the optical properties. From the electrical conductivity ratio between the PS included and dense films, we could obtain the true effective medium approximation which was applicable to analyzing the thermal conductivity. At the smallest pore diameter, decoupling between the phonon and the electron transports was maximized, winding up with the excellent performance being far beyond the bulk single crystal. The epitaxial 3D nanoporous structure realized in this thesis study was proven to be very effective for tailoring the thermal and the electrical properties independently.

4.7 References

1 Snyder, G. J. & Toberer, E. S. Complex thermoelectric materials. *Nat Mater* **7**, 105-114, doi:10.1038/nmat2090 (2008).

2 Cahill, D. G. *et al.* Nanoscale thermal transport. *Journal of Applied Physics* **93**, 793, doi:10.1063/1.1524305 (2003).

3 Choy, C. L. Thermal conductivity of polymers. *Polymer* **18**, 984-1004, doi:https://doi.org/10.1016/0032-3861(77)90002-7 (1977).

4 Xie, X. *et al.* High and low thermal conductivity of amorphous macromolecules. *Physical Review B* **95**, 035406, doi:10.1103/PhysRevB.95.035406 (2017).

5 Yanase, A. & Siratori, K. Band Structure in the High Temperature Phase of Fe3O4. *Journal of the Physical Society of Japan* **53**, 312-317, doi:10.1143/jpsj.53.312 (1984).

6 Zhang, Z. & Satpathy, S. Electron states, magnetism, and the Verwey transition in magnetite. *Physical Review B* **44**, 13319-13331, doi:10.1103/PhysRevB.44.13319 (1991).

7 Jain, S., Adeyeye, A. O. & Boothroyd, C. B. Electronic properties of half metallic Fe3O4 films. *Journal of Applied Physics* **97**, doi:Artn 093713 10.1063/1.1889247 (2005).

8 García, J. & Subías, G. The Verwey transition—a new perspective. *Journal of Physics: Condensed Matter* **16**, R145-R178, doi:10.1088/0953-8984/16/7/r01 (2004).

9 Walz, F. The Verwey transition - a topical review. *Journal of Physics: Condensed Matter* **14**, R285-R340, doi:10.1088/0953-8984/14/12/203 (2002).

10 Leonov, I., Yaresko, A. N., Antonov, V. N., Korotin, M. A. & Anisimov, V. I. Charge and

orbital order in Fe3O4. *Phys Rev Lett* **93**, 146404, doi:10.1103/PhysRevLett.93.146404 (2004).
11 Venkatasubramanian, R., Siivola, E., Colpitts, T. & O'Quinn, B. Thin-film thermoelectric devices with high room-temperature figures of merit. *Nature* **413**, 597-602, doi:10.1038/35098012 (2001).
12 Rojo, M. M. *et al.* High electrical conductivity in out of plane direction of electrodeposited Bi2Te3 films. *AIP Advances* **5**, 087142, doi:10.1063/1.4928863 (2015).
13 Bahk, J.-H., Favaloro, T. & Shakouri, A. *THIN FILM THERMOELECTRIC CHARACTERIZATION TECHNIQUES*. Vol. 16 (2013).
14 Anisimov, V. I., Elfimov, I. S., Hamada, N. & Terakura, K. Charge-ordered insulating state of Fe3O4 from first-principles electronic structure calculations. *Physical Review B* **54**, 4387-4390, doi:10.1103/PhysRevB.54.4387 (1996).
15 Verwey, E. J. W. Electronic Conduction of Magnetite (Fe3O4) and its Transition Point at Low Temperatures. *Nature* **144**, 327-328, doi:10.1038/144327b0 (1939).
16 Miles, P. A., Westphal, W. B. & Von Hippel, A. Dielectric Spectroscopy of Ferromagnetic Semiconductors. *Reviews of Modern Physics* **29**, 279-307, doi:10.1103/RevModPhys.29.279 (1957).
17 Verwey, E. J. W. & Haayman, P. W. Electronic conductivity and transition point of magnetite ("Fe3O4"). *Physica* **8**, 979-987, doi:https://doi.org/10.1016/S0031-8914(41)80005-6 (1941).
18 Verwey, E. J., Haayman, P. W. & Romeijn, F. C. Physical Properties and Cation Arrangement of Oxides with Spinel Structures II. Electronic Conductivity. *The Journal of Chemical Physics* **15**, 181-187, doi:10.1063/1.1746466 (1947).
19 Slack, G. A. Thermal Conductivity of MgO, Al2O3, MgAl2O4, and Fe3O4 Crystals from 3° to 300°K. *Physical Review* **126**, 427-441, doi:10.1103/PhysRev.126.427 (1962).
20 Kuipers, A. J. M. & Brabers, V. A. M. Thermoelectric properties of magnetite at the Verwey transition. *Physical Review B* **14**, 1401-1405, doi:10.1103/PhysRevB.14.1401 (1976).
21 Cohen, S. S. Contact resistance and methods for its determination. *Thin Solid Films* **104**, 361-379, doi:https://doi.org/10.1016/0040-6090(83)90577-1 (1983).
22 Gelmont, B. & Shur, M. Spreading resistance of a round ohmic contact. *Solid-State Electronics* **36**, 143-146, doi:https://doi.org/10.1016/0038-1101(93)90132-A (1993).
23 Cox, R. H. & Strack, H. Ohmic contacts for GaAs devices. *Solid-State Electronics* **10**, 1213-1218, doi:https://doi.org/10.1016/0038-1101(67)90063-9 (1967).
24 S., C., W., T., W., V. D. B. & D., S. Optimization of a FIB/SEM slice-and-view study of the 3D distribution of Ni4Ti3 precipitates in Ni–Ti. *Journal of Microscopy* **233**, 61-68, doi:doi:10.1111/j.1365-2818.2008.03095.x (2009).
25 Wico, C. L. H. *et al.* Focused ion beam scan routine, dwell time and dose optimizations for submicrometre period planar photonic crystal components and stamps in silicon. *Nanotechnology* **18**, 195305 (2007).
26 Manifacier, J. C., Gasiot, J. & Fillard, J. P. A simple method for the determination of the optical constants n, k and the thickness of a weakly absorbing thin film. *Journal of Physics E: Scientific Instruments* **9**, 1002 (1976).
27 Krueger, N. A. *et al.* Porous Silicon Gradient Refractive Index Micro-Optics. *Nano Letters* **16**, 7402-7407, doi:10.1021/acs.nanolett.6b02939 (2016).
28 Li, X. W., Gupta, A., Xiao, G. & Gong, G. Q. Transport and magnetic properties of

epitaxial and polycrystalline magnetite thin films. *Journal of Applied Physics* **83**, 7049-7051, doi:10.1063/1.367547 (1998).

29 Eerenstein, W., Palstra, T. T. M., Hibma, T. & Celotto, S. Origin of the increased resistivity in epitaxial ${\mathrm{Fe}}_{3}{\mathrm{O}}_{4}$ films. *Physical Review B* **66**, 201101, doi:10.1103/PhysRevB.66.201101 (2002).

30 Arora, S. K., Sofin, R. G. S. & Shvets, I. V. Magnetoresistance enhancement in epitaxial magnetite films grown on vicinal substrates. *Physical Review B* **72**, 134404, doi:10.1103/PhysRevB.72.134404 (2005).

31 Ramos, A. V. *et al.* Magnetotransport properties of Fe3O4 epitaxial thin films: Thickness effects driven by antiphase boundaries. *Journal of Applied Physics* **100**, 103902, doi:10.1063/1.2386927 (2006).

32 Gilks, D. *et al.* Structural study of Fe3O4(111) thin films with bulk like magnetic and magnetotransport behaviour. *Journal of Applied Physics* **115**, 17C107, doi:10.1063/1.4862524 (2014).

33 Itai, R., Shibuya, M., Matsumura, T. & Ishi, G. Electrical Resistivity of Magnetite Anodes. *Journal of The Electrochemical Society* **118**, 1709-1711, doi:10.1149/1.2407817 (1971).

34 Mi, W. B., Jiang, E. Y. & Bai, H. L. Fe 3+ /Fe 2+ ratio controlled magnetic and electrical transport properties of polycrystalline Fe 3(1−δ) O 4 films. *Journal of Physics D: Applied Physics* **42**, 105007 (2009).

35 Gorski, C. A. & Scherer, M. M. Determination of nanoparticulate magnetite stoichiometry by Mössbauer spectroscopy, acidic dissolution, and powder X-ray diffraction: A critical review. *Am Mineral* **95**, 1017-1026, doi:10.2138/am.2010.3435 (2010).

36 Goodenough, J. B. *et al. Magnetic and Other Properties of Oxides and Related Compounds*. (Springer Berlin Heidelberg, 1970).

37 Kale, S. *et al.* Film thickness and temperature dependence of the magnetic properties of pulsed-laser-deposited ${\mathrm{Fe}}_{3}{\mathrm{O}}_{4}$ films on different substrates. *Physical Review B* **64**, 205413, doi:10.1103/PhysRevB.64.205413 (2001).

38 Margulies, D. T. *et al.* Anomalous moment and anisotropy behavior in Fe3O4 films. *Physical Review B* **53**, 9175-9187, doi:10.1103/PhysRevB.53.9175 (1996).

39 Bickford, L. R. Ferromagnetic Resonance Absorption in Magnetite Single Crystals. *Physical Review* **78**, 449-457, doi:10.1103/PhysRev.78.449 (1950).

40 Mi, W. B., Jiang, E. Y. & Bai, H. L. Fe 3+/Fe 2+ ratio controlled magnetic and electrical transport properties of polycrystalline Fe3(1−δ)O4 films. *Journal of Physics D: Applied Physics* **42**, 105007 (2009).

41 Schedin, F., Hill, E. W., Laan, G. v. d. & Thornton, G. Magnetic properties of stoichiometric and nonstoichiometric ultrathin Fe3O4(111) films on Al2O3(0001). *Journal of Applied Physics* **96**, 1165-1169, doi:10.1063/1.1762715 (2004).

42 Özdemir, Ö., Dunlop, D. J. & Moskowitz, B. M. The effect of oxidation on the Verwey transition in magnetite. *Geophysical Research Letters* **20**, 1671-1674, doi:doi:10.1029/93GL01483 (1993).

43 Readman, P. W. & O'Reilly, W. Magnetic Properties of Oxidized (Cation-Deficient) Titanomagnetites *Journal of geomagnetism and geoelectricity* **24**, 69-90, doi:10.5636/jgg.24.69 (1972).

44 Kulp, E. A. *et al.* Electrodeposition of Epitaxial Magnetite Films and Ferrihydrite Nanoribbons on Single-Crystal Gold. *Chemistry of Materials* **21**, 5022-5031, doi:10.1021/cm9013514 (2009).

45 Switzer, J. A. *et al.* Resistance Switching in Electrodeposited Magnetite Superlattices. *Journal of the American Chemical Society* **132**, 1258-1260, doi:10.1021/ja909295y (2010).
46 Bard, A. J. & Faulkner, L. R. *Electrochemical Methods: Fundamentals and Applications*. (Wiley, 2000).
47 Hodych, J. P. Magnetic hysteresis as a function of low temperature in rocks: evidence for internal stress control of remanence in multi-domain and pseudo-single-domain magnetite. *Physics of the Earth and Planetary Interiors* **64**, 21-36, doi:https://doi.org/10.1016/0031-9201(90)90003-G (1990).
48 Özdemir, Ö. Coercive force of single crystals of magnetite at low temperatures. *Geophysical Journal International* **141**, 351-356, doi:10.1046/j.1365-246x.2000.00081.x (2000).
49 Landauer, R. Electrical conductivity in inhomogeneous media. *AIP Conference Proceedings* **40**, 2-45, doi:10.1063/1.31150 (1978).
50 Querry, M. R. *Optical constants*. (1985).
51 Niklasson, G. A., Granqvist, C. G. & Hunderi, O. Effective medium models for the optical properties of inhomogeneous materials. *Appl. Opt.* **20**, 26-30, doi:10.1364/AO.20.000026 (1981).
52 Gehr, R. J. & Boyd, R. W. Optical Properties of Nanostructured Optical Materials. *Chemistry of Materials* **8**, 1807-1819, doi:10.1021/cm9600788 (1996).
53 Sultanova, N., Kasarova, S. & Nikolov, I. Dispersion Properties of Optical Polymers. *Acta Physica Polonica A* **116**, 585, doi:10.12693/aphyspola.116.585 (2009).

CHAPTER 5.

INTEGRATION OF COLLOIDS INTO A SEMI-FLEXIBLE NETWORK OF FIBRIN[‡]

5.1 Introduction

The field of colloid assembly developed based on particles dispersed in liquids without dynamic memory nor viscoelastic time-dependent responses[1]. Yet, complex systems of "particles" in viscoelastic polymer gels are ubiquitous in functional biological assemblies. For example, in the dynamically reconfigurable cytoskeleton, compact proteins, organelles and/or extended cross-linkers permeate a large mesh gel composed of rod-like filaments (e.g. F-actin, microtubules)[2,3]. A fundamental understanding of colloid-polymer gel systems could allow novel material functionality to be realized via, for example, employing deformable networks as passive or active "internal fields" to control particle spatial organization and dynamics[1,4]. To achieve these visions, the standard highly extensible entangled gels composed of synthetic flexible chain polymers[5] are inadequate since their meshes are small compared to colloid size and networks are relatively stiff.

This motivates using large mesh fibrillar physical gels composed of assembled strands of high persistence length with a relatively small cross section[2,6]. A network with semi-flexible filaments i.e. with persistence length comparable to their contour length, exhibits strong strain-stiffening in shear[7]. Within eukaryotic cells, active myosin II motors interact with a strain-stiffening network of actin to cause strong contractile prestress that stiffen the cell[8,9]. Retaining such strain-stiffening properties of the composite is therefore desirable to allow the possibility of this type of functionality.

Crosslinked biopolymer networks possess semi-flexible components and show strain-stiffening attributes, for example, networks of actin, fibrin, collagen, vimentin and microtubules[7]. Actin and fibrin are the two best candidates for our study. Collagen network formation and morphology of constituent components is affected by temperature[10], and there are conflicting scaling theories that attempt to relate network modulus to concentration[11,12]. Moreover, probe

‡ Results presented in this chapter were previously published in: Bharadwaj N. A. K.[†], Kang, J. G.[†], Hatzell, M. C.[†], Schweizer, K. S., Braun, P. V. & Ewoldt, R. H. *Soft Matter* **13**, 1430-1443, doi:10.1039/C6SM02141G (2017). [†] Equally contributing authors.

diffusion studies report a smaller mesh size for collagen networks, even at relatively low concentrations[13]. Additionally, networks of vimentin and microtubules have not been as extensively studied as actin and fibrin and are not suitable choices as a model material. Crosslinked filamentous actin has a reasonably large mesh size and shows strain-stiffening, and could be used. Here we choose bovine fibrin[14,15] as a model large mesh network. Bovine fibrin is easier and safer to handle (it is absent of human pathogens and thus requires a lower biosafety level) and has similar properties to human fibrin, which has been extensively studied[16-19].

Fibrin is a known active ingredient in a blood clot, which is a shear flow driven (bio)polymer-colloid (platelet) composite. This has inspired studies of shear driven assemblies of polymer-colloid composites[20], and studies of fibrin integrated with soft deformable thermally responsive microgels that resemble platelets[21]. Fibrin matrix porosity is known to increase with microgel inclusion, allowing for better cell spreading and migration[22]. Fibrin based composites have also been considered for several biomedical applications[23,24]. Yet, fundamental studies of the resulting structure of engineered composites, and the relation of structure to mechanical properties, are incomplete.

A network of fibrin is composed of very long fibrils of thickness $d \sim$ 20-40 nm[16,25] that form controllable meshes of pore size $\xi \sim$ 1-10 μm[26]. Semi-flexibility in fibrin results from the large persistence length of constituent fibers, typically around 500 nm[7,27], of the same order of magnitude as the fiber contour length. This produces nonlinear elastic stiffening of the network[7,28-30]. Fibrin network elasticity is also well studied, both macroscopically[18,31-35] and on the molecular scale[19,36]. It is also a versatile biomaterial that finds use in a variety of applications[37]. Fibrin gels have been used as skin grafts to treat injuries[38], fibrin sealants[39] have found great use in drug delivery, stem cell delivery, wound healing, tissue engineering and regeneration[40-45].

As model colloids, we use carboxylate modified polystyrene/latex (CML) particles of diameter $d \approx$ 200 nm and $d \approx$ 1000 nm[46-49]. The larger size coincides with the expected size range for other stimuli responsive colloids in a polymer matrix, for example, magnetically susceptible particles in a matrix of carrageenan[50] and thermally sensitive microgels in fibrin[21]. Fibrin network formation around colloids has been attempted before[21], but a systematic study of the limits of colloid inclusion, and the resulting phase behavior of such composites is pending. Fibrin formation in a colloidal environment is of significant interest in medicine. Natural and artificial colloids are

increasingly administered as intravenous fluids[51] and they are known to interfere with fibrin polymerization, resulting in reduced clot firmness and strength[52-56]. Unmodified ultrafine polystyrene particles are known to not interfere in a blood clot, but carboxylate treated particles of the same dimension adversely affect thrombus formation[57]. A successful composite is therefore one that preserves network integrity and strength, combined with minimal colloid clustering and phase separation. With these goals, we aim to identify practical and useful experimental methods of general relevance for large mesh strain-stiffening network-colloid composites, which requires solving non-trivial materials selection and fabrication challenges (**Figure 5.1**).

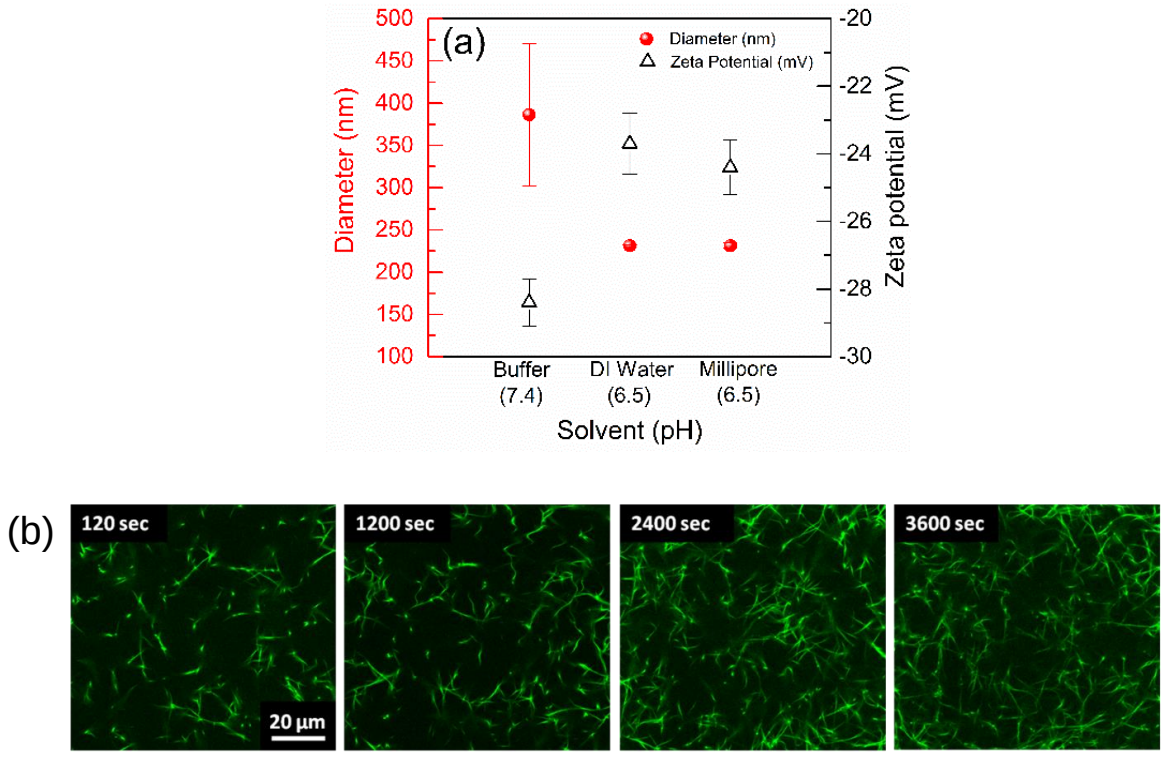

Figure 5.1 – Components of the colloid-polymer composite system. (a) Carboxylate modified latex (CML) particle size characterization, dynamic light scattering information suggests colloid aggregation in buffer (pH = 7.4). (b) Biopolymer fibrin network, confocal images showing fibrin network evolution with time.

We have developed two scenarios for realizing CML colloid-fibrin composites. **Method I**: colloids and fibrinogen are combined in solution before thrombin-initiated polymerization, and the network is formed in the presence of the colloid particles. In **Method II**: colloids are driven into a pre-formed fibrin network via external electric field. The latter is the protocol in the spirit of the "quenched annealed" (QA) scenario analyzed theoretically[1]. **Figures 5.2a** and **b** show the schematic representation of each scenario. For both methods, we characterize the morphological

features using two-color laser scanning confocal microscopy and scanning electron microscopy. A highly relevant property is the resulting composite viscoelasticity. We report linear and nonlinear shear and extensional rheology of these composites. We will show that **Method I** offers more control of colloid concentration, but the maximum concentration attainable is limited by the ability of fibrinogen to polymerize into fibrin in the presence of the colloids, a difficult to control non-equilibrium process (see sections **5.3** and **5.4**). **Method II** offers less control of colloid concentration, but allows much better structural control, improved dispersion of colloids in the wet gel matrix and demonstrates colloidal templating on the low-dimensional fibrin network (see section **5.5**).

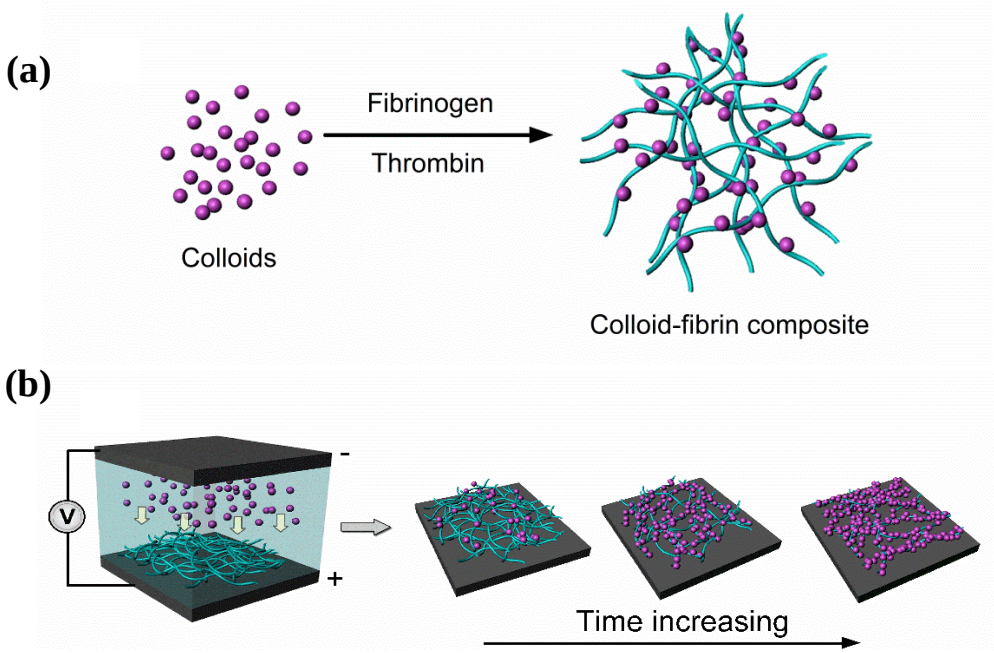

Figure 5.2 – Methods of forming fibrin–CML colloid composites. (a) **Method I**: fibrin polymerization and network formation around CML colloids. (b) **Method II**: CML colloids driven electrophoretically (at 1 V for 1, 3, 5 minutes) into a pre-existing fibrin network.

5.2 Experimental Methods

5.2.1 Materials

To minimize ionic species in solution, deionized water with a resistivity of 18.2 MΩ·cm (at 25 ^{o}C) was employed for the all experiments. A pH 7.4 aqueous buffer solution was prepared by mixing 25 mM HEPES, 150 mM NaCl, and 20 mM $CaCl_2$ in Type I water.

As model hard sphere colloids, we use commercially available suspensions of carboxylate modified polystyrene/latex (CML) colloids in water (4 % by weight, as supplied by Thermo Fisher Scientific, U.S.A). These are a suitable choice of colloids for our study since they can be tagged to fluoresce in a laser scanning microscope that enables wet state imaging, and compared to other surface treated colloids (sulfate-polystyrene), aggregate less under conditions of high ionic strength (up to 1 M). It is noteworthy that the fluorescent wavelength of the colloids is different than that of fibrin, allowing for non-intrusive two-color fluorescent imaging. They are monodisperse in nonionic solvents and also available in a wide range of sizes thereby serving as a suitable model choice of colloids with varying size. They also show well studied phase behavior that depends on the pH and ionic strength of the suspending medium[58], factors important in our study. Dictated by these conditions, particles can either aggregate or stay dispersed in solution. Such conformations in combination with particle interaction with fibrin network elements can result in different microstructural states for the composite with different rheological properties.

According to manufacturer specifications, the average particle diameter in water is 200 nm. We validate the hydrodynamic diameter (d_c) (see **Figure 5.1**) and the zeta-potential of these colloidal particles in an aqueous environment using dynamic light scattering (Malvern, Zetasizer Nano ZS, U.K). CML suspensions in three different aqueous solutions are studied, i) buffer solution (HEPES), ii) deionized water and iii) Type 1 water. The diluted CML suspensions were then introduced into two different kinds of cuvettes for measuring the diameter and zeta-potential, respectively. The data was analyzed using the manufacturer provided Zetasizer software.

Bovine fibrinogen (free of plasminogen and fibronectin) and thrombin were acquired commercially (Enzyme Research Laboratories, South Bend, IN, USA), and stocked at -60^{o}C before use. Fibrinogen was thawed at 37^{o}C and diluted to desired concentrations in the pH 7.4 HEPES buffer. Factor XIII is present in fibrinogen and results in a covalently crosslinked network after thrombin initiated gelation. Thrombin was thawed in ice and diluted in the same buffer. Fibrin hydrogels were formed by mixing fibrinogen and thrombin to achieve the desired final concentrations of fibrinogen [F] and thrombin [T], and letting them react for an hour under near isothermal (temperature controlled) conditions.

5.2.2 Microstructure visualization

Scanning electron microscopy

The internal structure of the dried samples were characterized with a field emission scanning electron microscope (FESEM; Hitachi, S-4700, Japan). Samples were prepared similar to existing studies[59,60]. Prior to imaging, the structure of fibrin (network) was preserved by fixing it overnight in a 2 % v/v glutaraldehyde solution in water. The samples were then dehydrated serially in 10, 30, 50, 70, 90, and then 100 % ethanol-in-water mixtures for 20 minutes in each solution. The treated samples were then dehydrated in a critical point drier (Tousimis, Autosamdri-931, U.S) and coated with sputtered Au-Pd alloy to make them conductive. Samples observably shrank during the dehydration step. For SEM visualization of CML particles, dilute suspensions (1 % v/v in Type I water) were added dropwise onto a silicon wafer and dried in ambient conditions.

Confocal microscopy

A two-color laser scanning confocal microscope (Zeiss, LSM 700, Germany) was employed to observe the structure of hydrogels and their composites in their wet state. A 63x oil-immersion objective lens (NA 1.4) was used. To facilitate non-intrusive two-color imaging of features in the fibrin-colloid composite, the emission wavelengths of individual components were separated by 60 nm. We purchased commercial fluorescently tagged CML suspensions (Thermofisher Scientific, U.S) with a 505/515 nm excitation/emission wavelength, respectively. Fibrinogen labeling was carried out in house with 5-carboxytetramethylrhodamine succinimidyl ester (TAMRA-SE; Thermofisher Scientific, U.S) having emission/excitation wavelengths of 547/576 nm respectively. The fibrinogen labeling process is well described elsewhere[61]. For both techniques mentioned above, images are acquired at multiple (at least three) locations on a sample. SEM and confocal images shown here are selected to represent morphologies captured in individual image/micrographs.

5.2.3 Rheology: shear and extension

Shear rheology was performed on a separated motor-transducer (a.k.a. strain-controlled) rotational rheometer (ARES-G2, TA Instruments). Geometries used were 25 mm diameter stainless steel. A serrated plate was used to avoid slip with already-gelled samples. A cone, with smooth surface and one degree cone angle, was used for samples gelled while in contact with the

rheometer geometry, in which case slip was not observed. The bottom (flat) plate was maintained at 25°C by a water recirculating Peltier system. A solvent trap was also used to encapsulate the sample in a humid environment.

For cone-plate rheometry (fibrin gelation occurring on the rheometer), precise volumes of fibrinogen and thrombin were mixed and pipetted onto the bottom plate, and the upper cone geometry was slowly lowered to squeeze into the sample. Care was taken to hold the bottom plate fixed as the sample was being squeezed.

For parallel disk rheometry (fibrin gelation occurring prior to rheometry), a custom made mold (latex rubber, 1.8 mm thick, with 25 mm diameter hole cut out) was placed on the bottom plate. Required volumes of fibrinogen and thrombin were mixed and pipetted into the well, and fibrin polymerization and gel formation allowed to proceed for one hour. Constant voltage (1 V) electric fields are applied at this point for a fixed duration (1, 3 and 5 minutes). The top serrated geometry was then lowered to grip the sample, the surrounding well was then removed, and the sample was coated with mineral oil on the exposed edges to curb evaporation during the experiment. In total, we consider 16 combinations of fibrinogen and thrombin concentrations, 11 of which with various colloid concentrations, totaling 54 total composition variations tested. All rheological measurements are repeatable to within ± 5 % accuracy, determined with duplicate measurements on all neat samples (without colloids) and select samples with colloids.

Extensional rheology was performed using a dual-drum fixture (Sentmanat Extensional rheometer (SER)) on a combined-motor transducer (a.k.a. torque-controlled) rotational rheometer (DHR-3, TA Instruments). The SER fixture has counter rotating dual cylindrical drums that impose tensile loading on samples attached to them. We wrapped the cylinders in sand paper (600 grit) to prevent slip during deformation. We prepare samples following the method described in Wufsus et al.[62]. Fibrin gels (6.4 mg ml^{-1}) and colloidal composites were formed in rectangular molds (20 mm x 10 mm) on glass slides separated by polypropylene spacers (thickness 0.45 mm). To prevent sample adhesion, the glass slides were coated with 25 % Triton X-100 solutions in Tris-buffered saline (TBS). The thickness varied by < 1 % across the sample. The drums were rotated at a fixed velocity to maintain a constant, slow extensional deformation rate ($\dot{\varepsilon} = 0.1\, s^{-1}$). The sample thickness was not independently measured, and we therefore report the engineering extensional stress. As an estimate of the potential true stress, if the material is incompressible, then at true

strains $\varepsilon = 1$ (near the maximum imposed), the true stress would be 2.7x the engineering stress reported. This is a minor difference on the log scale used to report the stress.

5.2.4 C-H-N elemental Analysis

We use the carbon (C), hydrogen (H), nitrogen (N) elemental analysis technique to determine colloid volume fractions in the gel after electrophoretic deposition (for 1, 3 and 5 minutes). Fixed sample volume gel-colloid composites were prepared (0.2 ml) and fixed, dehydrated, and critical point dried (identical to samples for SEM imaging). After determining the dry mass of each sample, they were stored in a desiccator to prevent moisture absorption. The weight percent (wt %) of C, H and N in each sample was then obtained using a CHN analysis instrument (Exeter Analytical, 440 CHN Analyzer). This instrument combusted samples, and gases corresponding to each element were then detected. Considering that nitrogen exists in fibrin ($C_5H_{11}N_3O_2$) and not in polystyrene, $(C_8H_8)_n$, we could deduce the exact weight of C and H in fibrin from the experimentally determined wt % of N, the total weight of the dried sample, and the chemical formula of fibrin. From the exact weight of C and H in fibrin, the total weight of the dried sample, and the wt % of C and H in the dried sample, we obtain the exact amount of C and H in polystyrene, which eventually gives us the total weight of polystyrene present in the composites. Using the density of polystyrene (1.05 g ml^{-1}), we convert the calculated weights of polystyrene into volumes in mL, and determine their volume fraction by dividing them by the starting volume of the wet-state hydrogels (0.2 ml). Duplicate measurements are performed to ensure reproducibility.

5.3 Fibrin Composition Effects

We discuss two scenarios for realizing CML colloid-fibrin gel network composites: one where colloids are present as the fibrinogen evolves into the fibrin network (**Method I**), and in another where we drive colloids into a fully evolved gel network (**Method II**). **Figure 5.2a** shows the case where we polymerize fibrinogen in the presence of CML particles, by adding thrombin to the fibrinogen-colloid mixture in the buffer solution. **Figure 5.2b** illustrates the other extreme, where we use external stimuli (electric fields) to drive CML particles into a pre-formed fibrin network. We study the morphology of the resulting composites using scanning electron

microscopy and two-color laser scanning confocal microscopy, and characterize them using linear and nonlinear shear and extensional rheology. We compare each technique for its efficacy in accommodating colloids into the gel matrix, in terms of the attainable range of colloid volume fraction, and the ability to retain strain-stiffening behavior that is present in the neat fibrin network.

Fibrin polymerization involves a cascade of events, starting with thrombin-initiated formation of fibrinogen into protofibrils and culminating into a fully evolved three-dimensional network structure. This mechanism is described from a molecular perspective in Weisel & Litvinov[63], and the final network morphology is known to depend on chemical conditions (especially pH and ionic strength, and in our case this may depend on colloid state of charge) and the starting concentrations of fibrinogen and thrombin.

Figure 5.3a maps out the two-dimensional composition space of fibrinogen-thrombin concentrations considered for fibrin network formation in this analysis. The timescale of network formation and resulting network elasticity depend on the composition, as shown in **Figure5.3b** (varying only fibrinogen concentration [F]) and **Figure 5.3c** (varying only thrombin concentration [T]). Some of the trends seen in **Figure 5.3** can be found scattered in old literature, e.g. varying only thrombin[64] or varying only fibrinogen[34] with bovine fibrinogen. The qualitative trends shown in **Figure 5.3** might also be expected from studies on human fibrin, which has received more attention[7], as human and bovine fibrin are known to be similar[9,19].

The relevant length scales of the fibrin network are the length of a network fiber strand L, mesh size ξ, and fiber diameter D. For our system, we make estimates for these length scales using confocal microscopy, SEM imaging, dynamic light scattering and macroscopic shear rheology. For the fibrin gels we work with, we estimate the fiber diameter (D_f) to a few tens of nanometers, but not exceeding 100 nm in any case (SEM imaging). The fiber diameter (D_f) and fiber length (L_f) are dependent on the concentration of fibrinogen and thrombin. An increase in fibrinogen concentration results in fibers with smaller diameter without altering fiber length. Increasing thrombin concentration decreases both the diameter and length of the fibers[16].

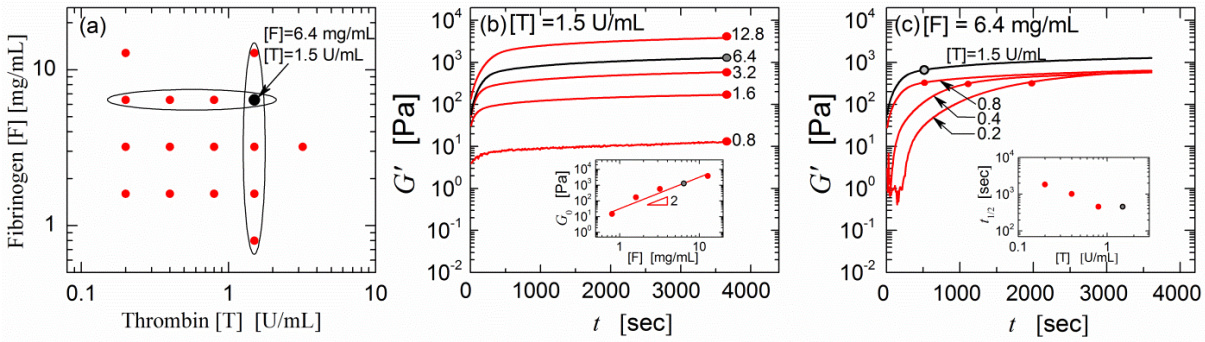

Figure 5.3 – Fibrin network formation depends on the solution mixture composition; the network stiffness and transient gel formation timescale are determined by the concentration of fibrinogen [F] and thrombin [T]. (a) Two dimensional fibrinogen-thrombin composition space showing compositional formulations considered. Emphasis is on a particular combination of [F] = 6.4 g mL^{-1} and [T] = 1.5 U mL^{-1}, used throughout this work (shown in black). (b) Fibrinogen concentration (in units of mg mL^{-1} for each case shown) primarily changes the network shear elastic modulus for a fixed [T] = 1.5 U mL^{-1}; power law scaling is shown as inset. (c) Thrombin concentration primarily changes the timescale of network formation, shown at a fixed [F] = 6.4 mg mL^{-1}. Inset shows the half time (time to reach ½ of elasticity at 3600 s) decreasing with increasing [T], suggesting faster gelation for lager [T].

We study a range of fibrinogen concentrations in **Figure 5.3a** ranging from 0.8 mg mL^{-1} to 12.4 mg mL^{-1}, but use results for 1.6 mg mL^{-1} and 6.4 mg mL^{-1} fibrin for the purpose of comparison here. The network mesh size (ξ) decreases with increasing fibrinogen concentration and scales as $\xi \sim [F]^{-2}$ as estimated by visualization experiments[26].Using this relation, we estimate $\xi_{1.6\ mg\ ml^{-1}} \sim 2\,\xi_{6.4\ mg\ ml^{-1}}$. The change in mesh size can also be estimated from the network elastic shear modulus G_0 (see **Figure 5.3b** inset). Assuming no significant change in other structural parameters (fiber diameter and length), we deduce $G_0 \sim \xi^{2}$ from entropic models for semi-flexible networks[65]. Combining this relation with our measured values of $G_0 \approx 200$ Pa for 1.6 mg mL^{-1} and $G_0 \approx 1200$ Pa for 6.4 mg mL^{-1} fibrinogen (**Figure 5.3b**), we would expect $\xi_{1.6\ mg\ ml^{-1}} = 2.5\,\xi_{6.4\ mg\ ml^{-1}}$. From confocal imaging, we further identify that the mesh size varies between 1 to 3 μm, and the fiber length ranges a few tens of microns (SEM images) for the fibrinogen concentrations considered in **Figure5.3a**. These estimates are consistent with earlier observed length scales in fibrin networks[26].

Our systematic experiments in **Figure 5.3** serve as an important baseline before considering the addition of colloids to the system. The network morphology is also known to show strong dependence on calcium ion concentration[66] and pH[67], which we fix before gelation.

For a fixed thrombin concentration [T] = 1.5 NIH U mL^{-1}, **Figure 5.3b** illustrates that fibrinogen content [F] increases the resulting elastic modulus of the network. Oscillatory time sweeps (γ_0 = 1%; ω = 1 rad s^{-1}) track gel evolution up to a point where the elastic modulus is nearly a constant (3600 s), at which point we define an elastic (quasi-equilibrium) shear modulus G_0. The gel elasticity is fit by the power law $G_0 \sim [F]^2$ (see inset of **Figure 5.3b**). This is close to earlier observed scaling of $G_0 \sim [F]^{2.2}$ for human fibrin[68], and solutions of entangled semi-flexible fibers[69].

Figure 5.3c emphasizes the role of thrombin in the kinetics of gelation. Gelation kinetics are tracked using a half-time, $t_{1/2}$, defined as the time for the gel to attain half its quasi-equilibrium elasticity ($G'(t_{1/2}) = \frac{1}{2}G_0$). Illustrated here for a fixed fibrinogen concentration [F] = 6.4 mg mL^{-1}, $t_{1/2}$ progressively drops with increasing [T], indicating faster gelation for larger thrombin concentration [T]. The thrombin concentration does not significantly affect the gel elastic modulus, indicating that small amounts of thrombin are sufficient to facilitate initiation of protofibrils and subsequent gelation[70]. The concentration of thrombin [T] however provides a significant improvement on the ability of fibrin to form in the presence of colloids, as shown in the following section.

5.4 Fibrin Polymerized in a Colloidal Suspension (Method I)

In this method, fibrin network formation occurs in the presence of different concentrations of CML colloids. We vary the concentrations of fibrinogen (0.8 mg mL^{-1} to 12.4 mg mL^{-1}) and thrombin (0.2 U ml^{-1} to 1.5 U mL^{-1}) and systematically identify the range of achievable colloid volume fraction across the fibrin composition space (**Figure 5.3a**). This range of fibrinogen concentration includes physiological conditions (~ 2.4 mg mL^{-1}), but our interests go beyond just physiological conditions. Our analysis is based on rheological measurements, observations from bi-fluorescent confocal imaging, and visual inspection of the resulting gel-colloid composite system.

Colloid-fibrin composites are formed by thrombin-initiated gelation of a solution containing fibrinogen and colloids (see schematic in **Figure 5.2a**). For a desired volume fraction of colloids in the gel, required volumes of the colloidal solution are introduced into the fibrinogen buffer. In this solution, colloids are at an aggregated state with a larger average diameter, as seen

in the dynamic light scattering data in **Figure 5.1a**, and the confocal image in **Figure 5.4a**. The aggregation of colloids results from two simultaneously occurring events: a reduced screening length due to a high ionic strength buffer (20 mM $CaCl_2$ and 150 mM NaCl), and van der Waals (vdW) attraction between high refractive index (n ~ 1.55) polystyrene particles[71].

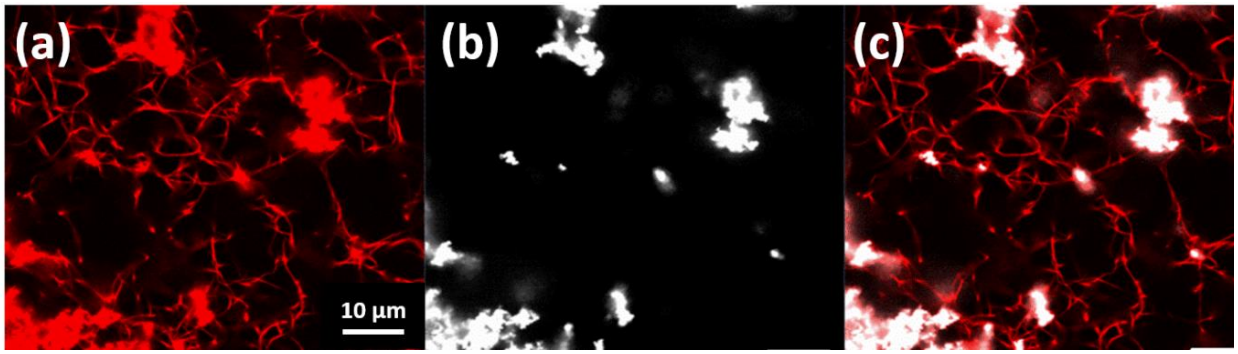

Figure 5.4 – Representative microstructure of a composite formed with **Method I**: fibrin (1.6 mg mL^{-1}) network evolution in the presence of CML colloids (f = 0.025 %). Two-color single plane confocal imaging shows signals from (a) fibrin (b) colloids (c) fibrin + colloids. Colloid clustering is evident in (b), fibrinogen recruitment is observed along colloidal clusters in (a), also seen in the combined image in (c).

Network formation is initiated by adding thrombin (also in the same buffer) to the fibrinogen-colloid solution. **Figure 5.4** shows the evolved fibrin network around colloidal clusters, for [F] = 1.6 mg mL^{-1} and [T] = 1.5 U mL^{-1}. The (aggregated) colloids appear to attract fibrinogen present in solution, and the cluster size varies anywhere from 10 ~ 20 µm. The confocal image in **Figures 5.4a** and **b** provide evidence of fibrinogen recruitment to the colloid locations. Although this stops some of the fibrinogen from participating in network formation, the thrombin enzymatic reaction on fibrinogen still occurs in the presence of colloids. The affinity of fibrinogen to polystyrene is well known, and quantitative methods to estimate the extent of absorption are also well established[72]. This interaction can also be quantified by other experimental techniques such as dynamic light scattering and zeta experiments[73], however this is beyond the scope of this work. Colloid clustering is observed for larger fibrinogen concentrations as well. The success of composite formation is tracked using oscillatory shear rheology, and in some cases, visual inspection is sufficient to capture macroscopic colloid phase separation. A higher fibrinogen concentration of 6.4 mg mL^{-1} has a larger elastic modulus (see **Figure 5.3b**) and changes to the network elasticity are more easily measured as a function of colloid volume fraction. For these

reasons, we use this higher concentration for the more detailed study of nonlinear rheological properties.

Figure 5.5 demonstrates that larger colloidal diameters allow for a higher maximum volume fraction, based on measurements of fibrin network elasticity ([F] = 6.4 mg mL^{-1}, [T] = 1.5 U mL^{-1}). The network evolves around CML colloids with diameters of 200 nm (**Figure 5.5a**) and 1000 nm (**Figure 5.5b**). The larger diameter colloids permit larger colloid volume fractions to be accommodated in the gel matrix.

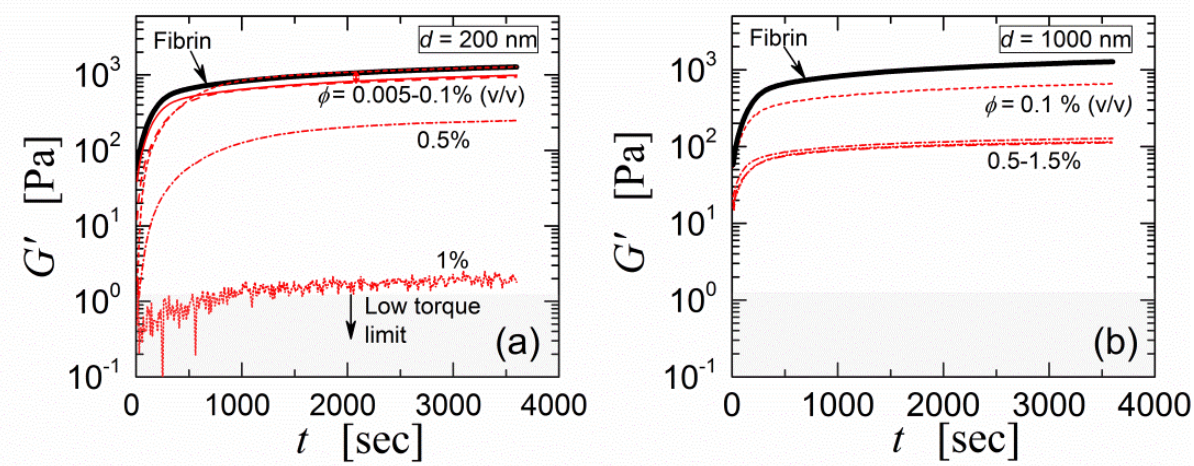

Figure 5.5 – Larger colloid diameters allow for higher volume fractions of particles to be achieved in the composite (using **Method I**). Fibrin ([F] = 6.4 mg mL^{-1}; [T] = 1.5 U mL^{-1}) network elasticity in the presence of varying concentration of (a) 200 nm and (b) 1000 nm diameter colloids, probed by oscillation time sweeps at γ_0 = 1 % and ω = 1 rad s^{-1}. The composite with 1000 nm particles accommodates a larger colloid volume fraction (up to ϕ = 1.5 %). The 200 nm particles significantly interfere with fibrin formation at ϕ = 1 %. Shaded light gray region corresponds to the minimum instrument torque resolution (0.05 μN m) which translates to G'_{min} = 1.25 Pa.

We rationalize this based on the attraction of fibrinogen to the colloids, and the different surface area to volume ratio of the differently sized colloids. For the same volume fraction, smaller colloids have a larger surface area and tend to absorb more fibrinogen in solution (compared to larger colloids). This reduces the number of fibrinogen units available for participation in network formation and disrupts network elasticity. This effect is shown in **Figures 5.5a** and **b**, where the 1000 nm colloid composite displays measurable elasticity up to ϕ = 1.5 %, whereas the composite with 200 nm colloids shows significant loss of elasticity at ϕ = 1 %. The upper bound of ϕ = 1.5 % (for the 1000 nm colloids) was set by the concentration of colloids in solution as supplied by the manufacturer. This indicates that fibrin accommodates larger particles better than smaller ones,

at least for these diameters for which the particles stay suspended in solution before the onset of gelation.

The success of composite formation depends on the composition of the fibrin network. For a fixed thrombin concentration, [T] =1.5 U mL^{-1}, **Figure 5.6** shows the accessible range of volume fraction for 200 nm colloids in fibrin networks at different fibrinogen concentrations.

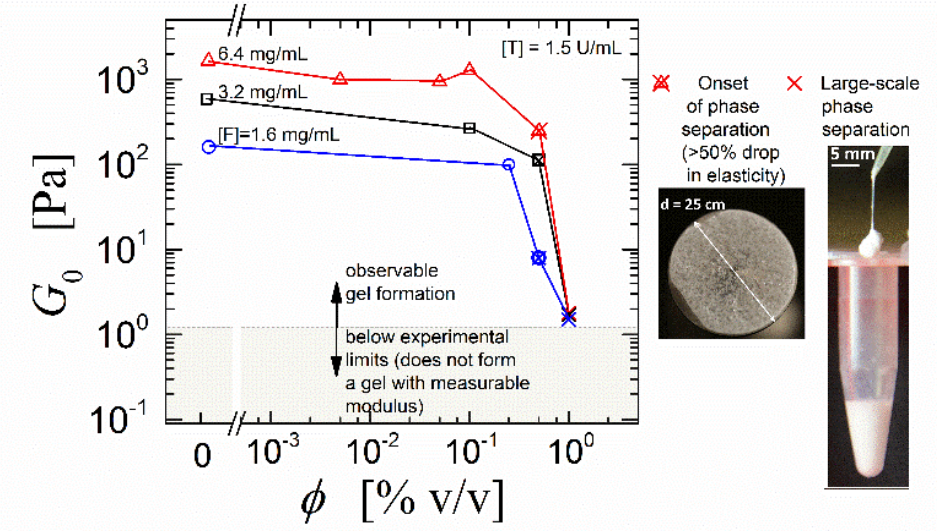

Figure 5.6 – Maximum achievable colloid volume fraction based on **Method I** depends on the fibrin network composition. Fibrin network forming in the presence of colloids (d = 200 nm), showing composite elasticity at 3600 s for fixed thrombin concentration [T] = 1.5 U mL^{-1}. The composite elasticity decreases with colloid inclusion; higher fibrinogen concentration allows for a slightly larger colloid concentration. At 1 % colloids, all composites have elasticity that approaches instrument measurement limits.

For the considered systems, the general trend is a decreasing composite elasticity with colloid inclusion, but a higher fibrinogen concentration accommodates slightly larger colloid volume fractions without much loss in network elasticity. This is true up to the point where colloid volume fractions are large enough to cause macroscopic phase separation (at ϕ = 0.5%), and significant colloid clustering around fibrinogen (ϕ = 1%) (shown in the photographs in **Figure 5.6)**. At ϕ = 0.5%, gelation occurs but results in a heterogeneous composite with a significantly reduced network elasticity (shown as ⊗ in **Figure 5.6**). At ϕ = 1%, noticeable colloid-fibrinogen aggregation occurs and interferes drastically with gelation. In this case, the elasticity of all composites approaches instrument measurement limits (shown as x in **Figure 5.6**)

We observe that the extent of colloid accommodation in fibrin also depends on thrombin concentration, and **Figure 5.7** shows this dependence for three different fibrinogen concentrations with 200 nm colloids. The upper limits on successful composite formation are marked by the boundaries of shaded regions in the fibrinogen-thrombin-colloid regime map in **Figure 5.7**.

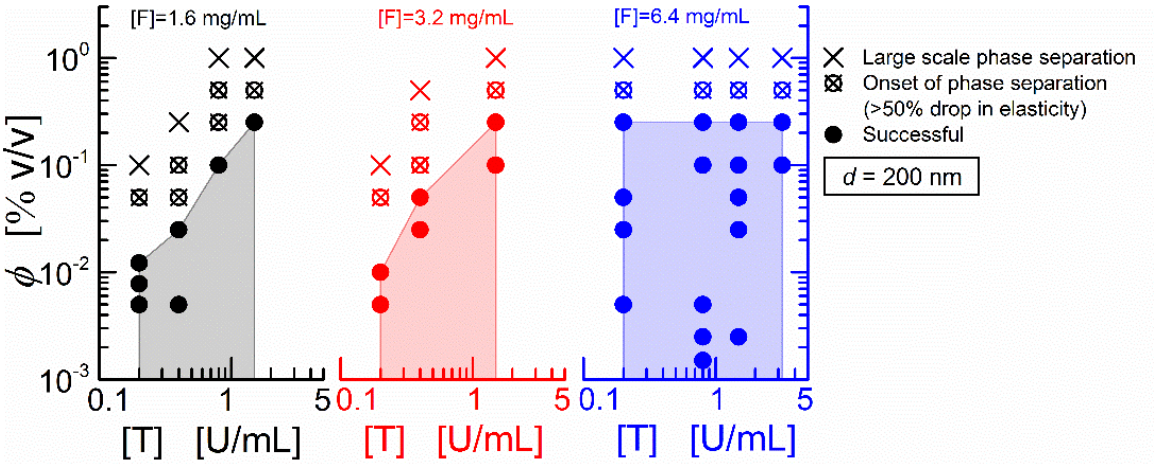

Figure 5.7 – Regime map of successful composite formation using Method I, in the three-parameter composition space {[F], [T], ϕ}; colloid diameter d = 200 nm. The limits on the regimes are determined by rheological measurements (Figure 5.6) and/or visual inspection.

For smaller fibrinogen concentrations, [F] = 1.6 mg mL^{-1} and 3.2 mg mL^{-1}, a larger thrombin concentration helps to accommodate more colloids. This is a surprising result, suggesting that the competition between fibrinogen association to the colloids and fibrinogen network formation seems to be governed by the presence of thrombin. At sufficient colloid concentration, macroscopic phase separation still occurs (outside the shaded region). At larger fibrinogen concentration, [F] = 6.4 mg mL^{-1}, the ability of the network to accommodate colloids does not depend on the thrombin concentration; accelerated gelation kinetics still occur, as with the neat fibrin, for larger thrombin concentration For successfully attained composites **Figure 5.7** (within the shaded region), the linear viscoelastic properties show statistically insignificant variations from those of fibrin (**Figure 5.5**).

Figure 5.8 presents the measured shear and extensional nonlinear mechanical properties of the composites with different colloid volume fractions compared to neat fibrin (all at [F] = 6.4 mg mL^{-1}; [T] = 1.5 U mL^{-1}). In **Figure5.8a**, the stress-strain hysteresis curves (also known as Lissajous-Bowditch curves) represent the response to large amplitude oscillatory shear (LAOS) experiments at imposed frequency ω = 1 rad s^{-1}. These raw data waveforms show a primarily

elastic network (little hysteresis) and intra-cycle strain stiffening, indicated by the upturn of stress at large positive strain.

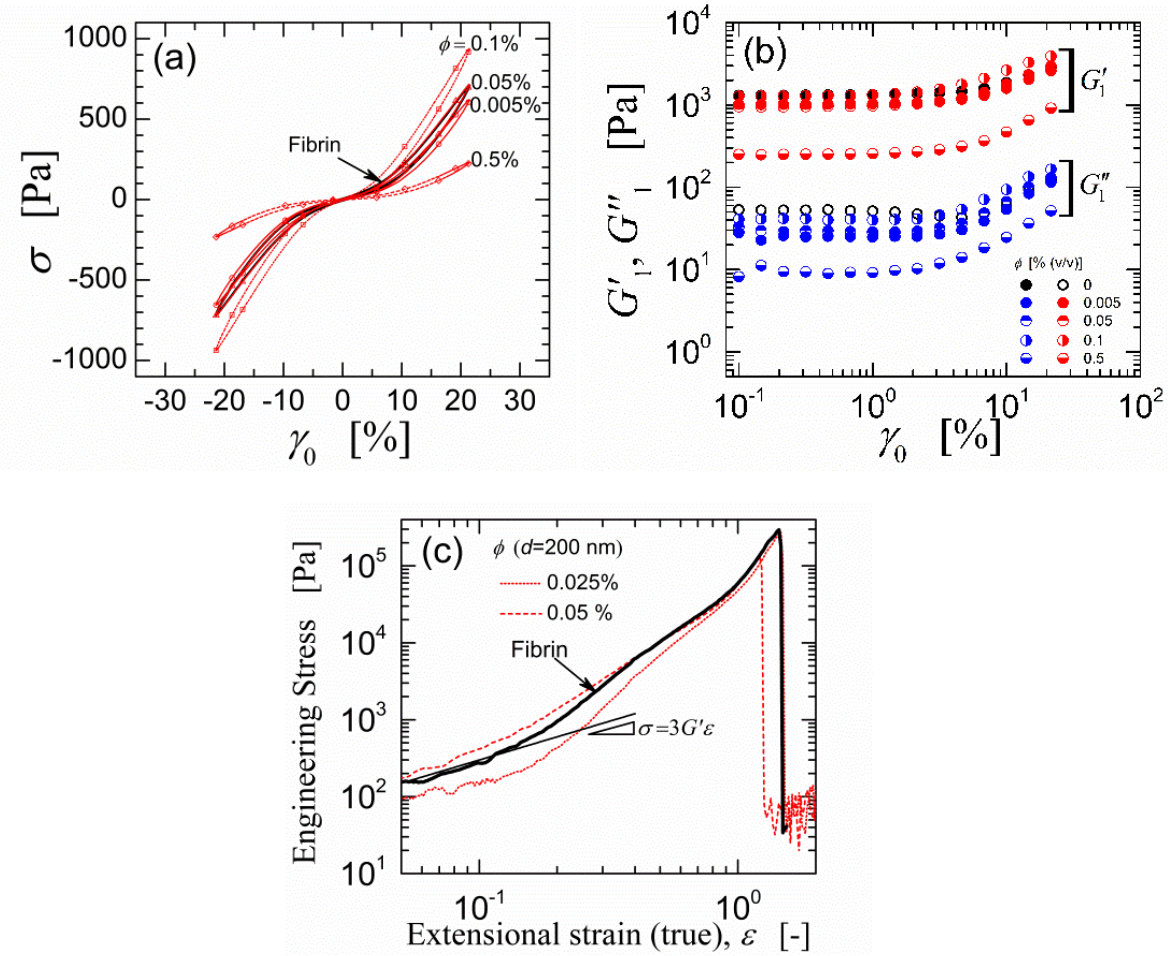

Figure 5.8 – Nonlinear oscillatory shear rheology at ω = 1 rad s^{-1} for fibrin ([F] = 6.4 mg mL^{-1}; [T] = 1.5 U mL^{-1})-colloid (d = 200 nm) composites, formed using **Method I**, shows (a) strain-stiffening in the shear stress-strain Lissajous curves and, (b) strain stiffening and rate thickening in the viscoelastic moduli. (c) Nonlinear extensional rheology ($\dot{\varepsilon} = 0.1\ s^{-1}$) shows strain stiffening and insignificant changes to the network fracture strength with colloid inclusion. Linear extensional stress is calculated from linear shear modulus G' (for fibrin), and shown for reference.

The waveform data can be described in many different ways[74]. Here, for brevity, we show only the first-harmonic moduli (**Figure 5.8b**), which are average measures of energy storage and loss during the nonlinear deformation. Inter-cycle strain stiffening, dependent on the strain amplitude, is evident from an increase in the first-harmonic viscoelastic moduli in **Figure 5.8b**. Strain stiffening in fibrin networks has been observed in experiments[7,28,30,75] and predicted by theoretical models for isotropic semi-flexible polymer networks and networks of rigid filaments[75]. Notably, colloidal composites formed here also exhibit intra- and inter-cycle strain-stiffening,

shown in (**Figures 5.8a** and **b**). This provides evidence that colloid inclusion does not interfere with the fibrillar properties of fibrin that are the origin of its strain-stiffening properties. It is also worth noting that the critical strain amplitude to see the onset of shear nonlinearity does not change with colloid inclusion under these conditions. These results can be explained with knowledge of morphology of the fibrin network (mesh size, fiber length and diameter) as a function of colloid concentration. This calls for future work with in situ high-resolution imaging of the microstructural elements of the fibrin network as they interact with colloids in the deformation field. Such a study will be illuminating and is possible in light of recent developments combining high resolution confocal imaging with rheometry[76,77].

The nonlinear properties of homogeneous gel-colloid composites are also probed in uniaxial extension (**Figure 5.8c**). Extensional stiffening is observed for fibrin and fibrin-colloid composites, indicated by the upturn of the stress-strain curves in **Figure 5.8c** compared to the linear reference. Gel fracture occurs around a true strain of ε = 100 %, and it is noteworthy that colloid inclusion in the gel matrix does not affect the composite fracture strength adversely. The homogeneity in the distribution of colloids within the fibrin matrix allows for extensional testing of composites prepared with this method, but this was not true for the other fabrication methods that follow.

5.5 Colloids Driven into an Evolved Fibrin Network (Method II)

In this section, we investigate the possibility of introducing 200 nm colloids into a pre-formed fibrin network, both passively by diffusion (unsuccessful) and actively by imposing an electric field (successful). When successful, the network fibers act as a template for low-dimensional assembly of colloids. We characterize the morphology of the resulting gel-colloid composite using cross-sectional SEM imaging and two-color confocal imaging, and use shear rheology to study its mechanical properties (extensional rheology was not performed with samples prepared by **Method II** due to heterogeneous colloid distribution through the sample). In suitable cases, we use the technique of elemental analysis to calculate the colloid volume fraction in the composite.

Attempts to passively introduce colloids through diffusion were unsuccessful, as confirmed by SEM images as shown in **Figure 5.9**. In these experiments, fibrin gels with known volume were prepared in a cylindrical mold (inner diameter 25 mm, height 1.5 mm), with the top surface

exposed to atmosphere. After gel formation, a circular wall (cut tube with inner diameter 50 mm, height 35 mm) is glued to the plate containing the gel, forming a well. Colloidal solution (1 % v/v in water) is filled into the well enclosing the inner well (with the fibrin gel) and left undisturbed for 24 hours. After 24 hours, the gel is carefully sliced into two halves along the diameter, and dried for SEM imaging. **Figure 5.9** shows the cross-sectional SEM images of dried gels at three different locations along the cut cross section: top, middle and bottom. The absence of colloids in the SEM micrographs provides conclusive evidence that colloids do not diffuse through the gel after 24 hours.

By imposing an electric field at a constant voltage of 1 V, the (charged) colloids were successfully driven into the gel matrix. The carboxylate groups in the CML particles carry a net negative charge ($RCOO^-$) in solution and thus respond to the imposed electric field. We used an electrochemical cell setup (see schematic in **Figure 5.2b**), with conductive top and bottom surfaces serving as the counter and working electrodes, respectively. Known volumes of fibrin are pre-formed onto the bottom surface and the cell is filled with the colloid solution. The charged colloids in solution are then electrophoretically driven into preformed fibrin gels ([F] = 6.4 mg mL^{-1}; [T] = 1.5 U mL^{-1}) under conditions of constant voltage (1 V) held for three different time intervals, namely, one, three and five minutes, using a potentiostat/galvanostat (BioLogic, VMP3, France). The composite morphology is studied using confocal imaging in wet conditions and cross-sectional SEM imaging in a dry state of the composite. Using the SEM micrographs in **Figure 5.10c**, we estimate a mean mesh size of 1 ~ 3 μm, fiber diameter ~ 100 nm and a fiber length greatly exceeding the mesh size (difficult to quantify since fiber ends are not apparent in the image).

The successful integration of colloids in the network, and a morphology of distributed, rather than aggregated, colloidal particles is validated by SEM images, shown in **Figure 5.10** for different locations along the cross-section (top, middle and bottom) of dried gels for different intervals of deposition. The "top" surface indicates the location where fibrin contacts the colloidal suspension during electrophoresis, and the "bottom" where the gel contacts the metal substrate they rest on. The extent of colloid penetration into the gel varies directly with the duration of electro-deposition, and deeper regions require more time for colloids to penetrate. Three and five minute intervals for electro-deposition result in superior colloid penetration into the gel, in contrast to the one minute case where the colloids fail to penetrate beyond the top portions of the gel.

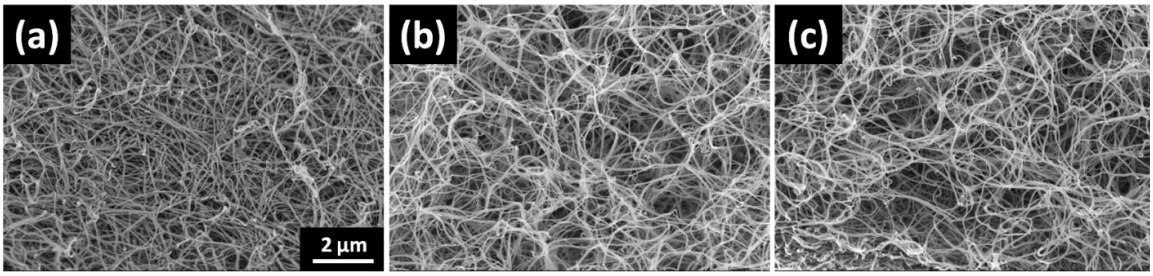

Figure 5.9 – Hydrostatic loading of colloids into fibrin. Cross-section SEM images at (a) top, (b) middle, (c) bottom sections of the fibrin sample exposed to a hydrostatic head of a 1 % v/v CML colloid suspension for 24 hours. Colloids do not diffuse/penetrate into the gel.

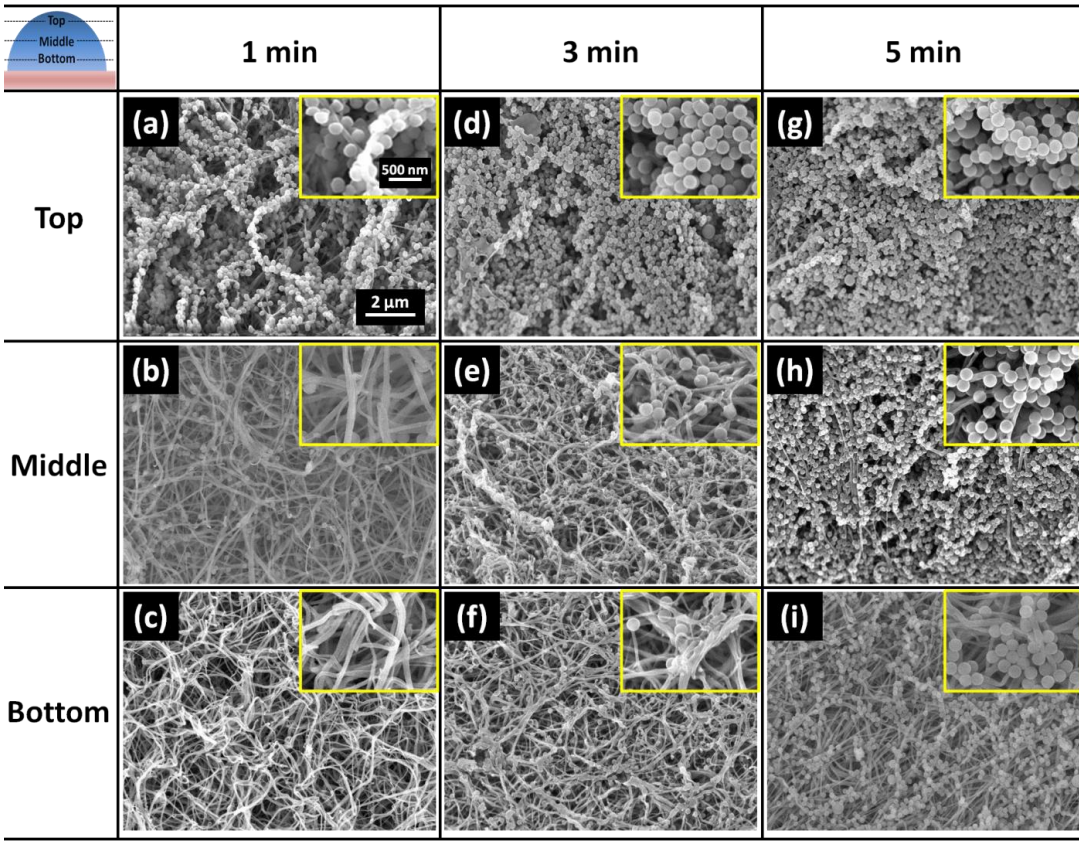

Figure 5.10 – Colloid penetration into the network depends on duration of electric field exposure. Cross-section SEM images of dried composites fabricated in 1 % (v/v) colloidal suspensions exposed to 1 V for 1 min (a-c), 3 mins (d-f), and 5 mins (g-i), respectively. Dense distribution observed in the 3 and 5 mins cases. Colloids tend to be distributed along fibers.

The SEM images show colloids assembled along the fibrous structure of the network. We hypothesize the following assembly process. Upon application of the electric field, negatively charged CML particles are driven into the fibrin matrix. Even though the colloids and the fibrin network are both negatively charged (the isoelectric point of fibrin is 5.6, implying that the fibers

are negatively charged in the pH 7.4 buffer), due to the high ionic strength of the buffer (~ 200 mM) the screening length is short, and van der Waals attraction between the fibers and the colloids leads to assembly of the colloids on the network. At this point, we do not know if the colloids are free to translate or not during the electrophoretic infilling. Regardless, the process is not self-clogging, as colloids continue to penetrate beyond the top portions of the gel.

The colloid volume fractions in the composites are estimated using elemental (C-H-N) analysis (**Table 5.1**). Approximate volume fraction estimates can also be obtained from SEM and confocal images and these calculations are summarized in the supplemental information.

Table 5.2 summarizes estimated colloid volume fractions for different field exposure times (1, 3, 5 mins). The colloid volume fraction increases monotonically with field exposure time. It is interesting that the maximum achieved colloid volume fraction in the gel is approximately the same as that of **Method I** (where fibrin was formed around colloids). However, in contrast to **Method I**, the composites fabricated using this method show little phase separation at the larger volume fractions. This can be explained by the electric field facilitated affinity of colloids to the fibrin template and the fact that a sticky fibrin network has been pre-formed, in contrast to the colloid-colloid attractions that resulted in aggregation and phase separation in **Method I**.

Table 5.1 – Calculation of volume fraction of colloids in composites attained by electrophoretic deposition of colloids in fibrin. To ensure reproducibility, two samples were analyzed for each exposure time. (t: deposition time, W_{dried}: weight of the dried sample, W_C: total weight of carbon, W_H: total weight of hydrogen, W_N: total weight of nitrogen, $W_{Colloids}$: weight of colloids, $V_{Colloids}$: volume of colloids, V_T: total volume of the wet composite hydrogels (fixed to 0.2 ml))

t (m)	W_{dried} (mg)	C (wt%)	H (wt%)	N (wt%)	W_C (mg)	W_H (mg)	W_N (mg)	$W_{Colloids}$ (mg)	$V_{Colloids}$ (ml)	$V_{Colloids}/V_T$
1	1.1	48.93	5.73	13.14	0.5382	0.0630	0.1445	0.3569	3.399E-04	**1.700E-03**
1	1.1	48.51	6.15	13.13	0.5336	0.0677	0.1444	0.3571	3.401E-04	**1.700E-03**
3	1.3	49.01	5.81	13.29	0.6371	0.0755	0.1728	0.4206	4.006E-04	**2.003E-03**
3	1.3	49.07	5.87	13.25	0.6379	0.0763	0.1723	0.4230	4.029E-04	**2.014E-03**
5	1.5	48.66	5.89	13.66	0.7299	0.0884	0.2049	0.4719	4.494E-04	**2.247E-03**
5	1.5	48.62	6.20	13.07	0.7293	0.0930	0.1961	0.4909	4.675E-04	**2.338E-03**

Table 5.2 – C–H–N analysis colloid volume fraction estimates for fibrin-colloid composites prepared by electro-deposition.

Duration	1 min	3 min	5 min
Colloid volume fraction (%)	0.17	0.20	0.23

Viscoelastic properties of electrodeposited fibrin-colloid composites are measured from linear and nonlinear shear rheology with serrated parallel plates. Serrated plates are used because slip is a major issue with hydrated gels that are formed before contact with the rheometer fixture, as in this **Method II**. Gels were prepared on the rheometer as per the protocol described in Section 2, and the serrated plates were lowered to maintain sample contact Oscillatory time sweeps at ω = 1 rad s^{-1} and strain amplitude γ_0 = 1% probe the linear viscoelastic properties in shear, and the response is well illustrated in **Figure 5.11**. When compared with the properties of the neat fibrin matrix, the linear viscoelastic shear moduli decrease with inclusion of colloids into the matrix. This is contrary to the general continuum mechanics prediction that particle inclusions result in an increase in the elastic modulus, as seen with particle inclusions in hydrogel composites[78-80]. Assuming a no-slip scenario at the geometry boundary, we attribute the decrease in elastic modulus to the loss/straining of physical bonds between fibers that now favor attractive interactions with colloids.

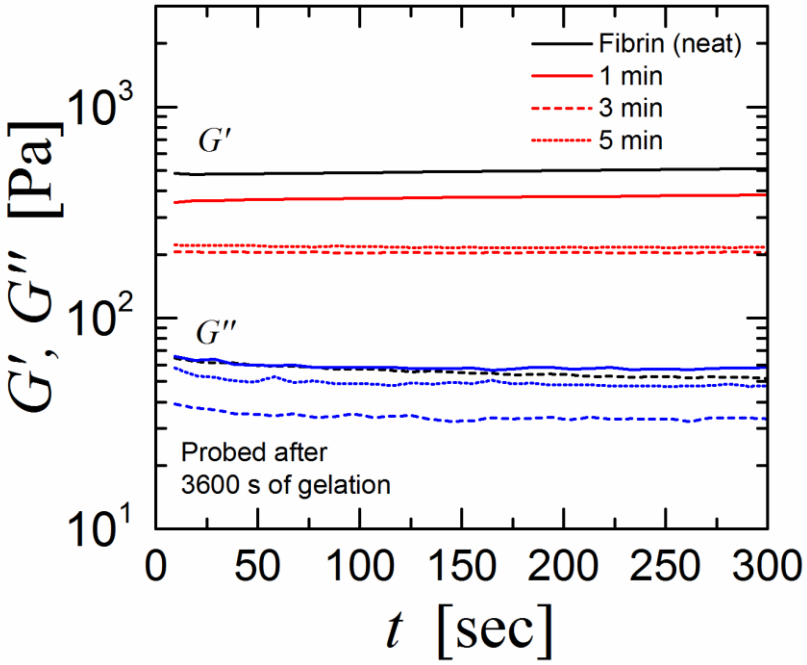

Figure 5.11 – Linear oscillatory shear rheology (ω = 1 rad s^{-1}, γ_0 = 1%) of fibrin ([F] = 6.4 mg ml^{-1}; [T] = 1.5 U mL^{-1}) and CML colloid (d = 200 nm) composites prepared under a constant voltage electric field (1 V) for different exposure times, namely 1 min, 3 min and 5 min.

Nonlinear rheology gives further insight to the structure and properties of the resulting composites. Using large amplitude oscillatory shear rheology (ω = 1 rad s^{-1}), the resulting stress-strain hysteresis curves show local intra-cycle stiffening for fibrin, both with and without exposure

to electric fields (**Figure 5.12a**). The maximum shear stress (corresponding to the maximum shear strain; $\gamma_0 \approx 20\%$) decreases with colloid inclusion in the matrix (with electric fields), and is smallest for the case with maximum field exposure time (five minutes). Attributes of intra-cycle stiffening are progressively lost with exposure to electric fields, and this effect is quite pronounced for field exposure times of three and five minutes.

Averaged viscoelastic moduli G'_1 and G''_1 (from the stress-strain curves) in **Figure 5.12b** reveals inter-cycle strain-dependent properties. The elastic modulus shows weak strain-softening and, at leading order, rate-thickening for fibrin. With field driven colloid inclusion in the gel, these effects are accentuated with a smaller critical strain to observe the onset of these nonlinearities. These signatures generally indicate yield or slip of the material, and we attribute this behavior to insufficient contact of fibrin to the serrated geometry (even though the serrations are a counter measure to avoid slip, they are insufficient under these conditions). For the composites, there may be contact with a thin layer of deposited colloids on the surface. The key take away is that the electrodeposition technique creates a material that is slippery, and fragile; as mentioned above, extensional rheology was not performed on these systems owing to the difficulty of sample handling and the heterogeneity in the distribution of colloids within the gel (illustrated in SEM images in **Figure 5.10**).

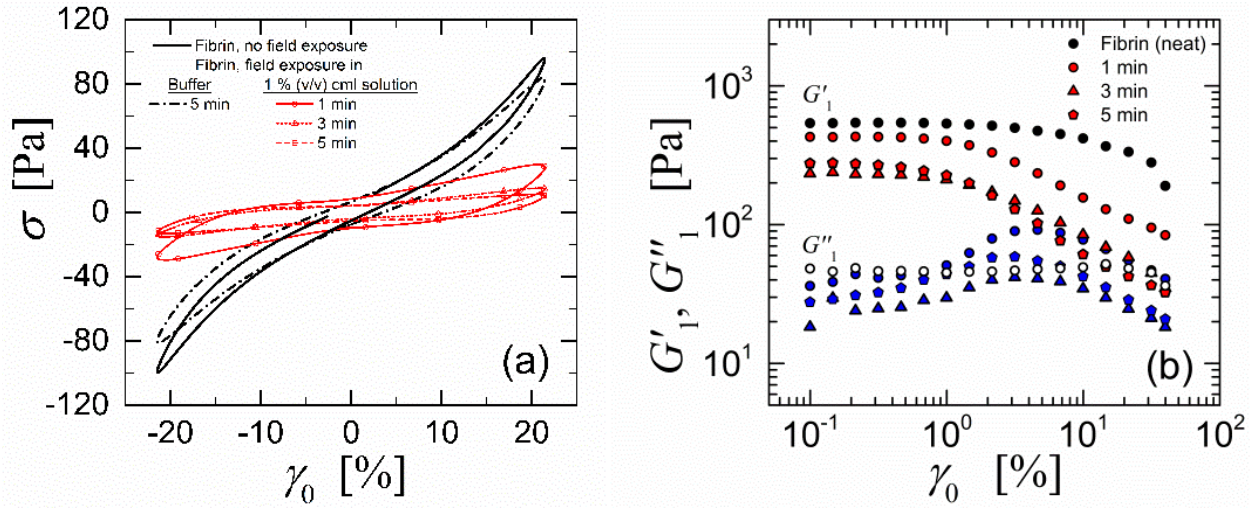

Figure 5.12 – **Method II**, nonlinear oscillatory shear rheology (ω = 1 rad s^{-1}) for electric field enabled fibrin-colloid (200 nm) composites shows (a) intra-cycle stiffening at large strain amplitude γ_0 = 20% and, (b) strain softening average elasticity G'_1, and local maximum of loss modulus G''_1, which suggest a yielding or slip response under these conditions.

5.6 Conclusions

We have developed and studied two methods of combining 200 nm diameter carboxylate modified latex (polystyrene) particles with a semi-flexible biopolymer network of bovine fibrin. One method induces the fibrin network to polymerize and evolve in the presence of colloids in solution (**Method I**), and the other method electrophoretically drives colloids into a pre-formed fibrin network (**Method II**). For each method, **Table 5.3** summarizes key observations from microstructure and mechanical property characterization of the resulting composites. For both methods, the CML colloids tend to associate with the fibrin template indicating colloid-fiber attractions beyond an adsorption threshold. This is significant in the context of recent replica integral equation statistical mechanical theory work which predicts beyond the threshold adsorption degree of fiber-colloid attraction, macroscopic colloid phase separation in pre-formed fiber networks is destroyed due to quenched disorder physics[81].

Table 5.3 – Summary of results from methods for preparing fibrin-CML colloid composites.

	Principle	**Morphology/ features**	**Mechanical properties**	**Composition limit, ϕ_{max}**
Method I	Colloids added *before* polymerization of fibrin	Fibrinogen recruitment in regions of aggregated colloids.	Softer composites with colloid inclusion. Strain stiffening preserved.	0.5 % (d = 200 nm) 1.5 % (1000 nm)
Method II	Colloids added *after* fibrin polymerization, driven by electric field	Colloid deposition along fibers. Depth dependent heterogeneity in colloid distribution.	Softer composites with colloid inclusion. Loss of strain stiffening.	~ 0.2 % (elemental analysis)

The composites prepared using **Method I** showed colloid clustering before and after network formation, accompanied by fibrinogen recruitment in these regions. This implies the presence of competing colloid-colloid and colloid-fiber attractive interactions. The consequences of the latter is very complicated and hard to control since fibrin polymerization is occurring simultaneously with aggregation and adsorption processes. This is a general challenge to integrating colloids into 'sticky' networks of semi-flexible biopolymers. This might be overcome

by using surface treated particles, for example, poly-(ethylene glycol) (PEG)-coated surfaces that resist protein adsorption[82], including fibrinogen[72].

Mechanical, linear viscoelastic properties of these composites showed strong dependence on the concentration of fibrinogen and thrombin, colloid size and volume fraction. In general, colloid inclusion in the matrix resulted in composites with a smaller elastic modulus than the neat fibrin network, which from our two-color confocal images we attribute to limited fibrinogen participation in network formation. For a given fibrinogen–thrombin combination, a minimum measurable elastic modulus and/or large scale phase separation identifies the maximum accommodable colloid volume fraction in which fibrinogen successfully forms a sample-spanning fibrin network. Fibrinogen polymerized in the presence of larger colloids (d = 1000 nm) is successful up to larger colloid volume fractions compared to those formed with smaller ones (d = 200 nm), which we attribute to colloidal surface interactions with the fibrinogen and thrombin. Much like neat fibrin, nonlinear viscoelasticity from large-amplitude oscillatory shear (LAOS) and extensional experiments showed strain-stiffening in these composites formed by **Method I**. The composites formed using **Method II** showed templated assembly of colloids along fibers, and no macroscopic demixing or large colloid aggregates in the pore space of the fibrin network. This behavior is qualitatively different than the system fabricated using **Method I**, despite the fact that the sticky colloids are the same particles. The observed behavior based on **Method II** is thus qualitatively consistent with the theoretical idea[81] that an effectively quenched fiber network, which attracts colloids beyond a critical adsorption threshold frustrates colloid macrophase separation. The resulting composite was not spatially homogeneous, but rather showed depth dependent heterogeneity, a signature it is not fully equilibrated. Such heterogeneity seems unsurprising given the field-driven protocol used to insert colloids into the fibrin gel and the likely situation that the attractions are quite strong. The heterogeneity and colloid volume fraction also depend on the electric field exposure time, consistent with the presence of non-equilibrium aspects of **Method II** based assembly. A larger exposure time permits superior colloid penetration into gel, and results in composites with larger volume fraction. The colloid volume fractions were estimated using elemental analysis. The volume fraction estimates in a wet state are close to those studied in **Method I**.

Mechanical properties of these composites were probed using shear rheology. The composites showed progressively smaller linear viscoelastic moduli with increased colloid inclusion in the gel, and displayed nonlinear strain-softening behavior in LAOS. However, slip at the surface cannot be completely ruled out despite the use of serrated plates in these measurements. This calls for characterization of these composites using other techniques like active[83,84] and passive microrheology[85], and tools for measurement of local viscoelastic properties[86]. However, if this were a true material signature (free of experimental artifacts), the strain-softening may be a consequence of a weakened state of physical crosslinks between fibrin elements that now favor attractive interactions with colloids.

We have chosen a particular colloid-biopolymer combination for this study, but the implications of our results extend beyond this combination. We are currently developing composites that combine the strain stiffening properties of the fibrin network with colloids that respond to external stimuli (e.g. temperature and magnetic fields). The principles for composite formulation in this study will be paramount in determining the optimum and obtainable colloid volume fraction in these other composites. We also believe that applications with these composites could be more useful with tunable interactions between colloids and the network[87,88]. This could be achieved either by tuning the colloid chemistry to attach/detach from the network elements, or alternately choosing a synthetic polymer network that can enable such transitions.

Recent theoretical advances[81] have also considered such large mesh composite systems where the fibrils form a quenched network. To suppress colloid macrophase separation, and realize massive structural re-configuration and property change (e.g., bulk modulus, electrical conductivity) requires control over the competing effects of fiber-colloid and colloid-colloid attractions and the many length scales that define the hybrid system. A bistable or switch-like equilibrium reconfiguration between a relatively dilute suspension of colloids in the network pores to diverse strongly adsorbed and percolated colloidal microstructures is predicted to be achievable under conditions of separated length scales: $L > \xi >> d >> D$, where L is the length of a network fiber strand, ξ is the mesh size, d is the colloid diameter, and D is the fiber diameter. Our material choices satisfy such separation of length scales and holds the potential for allowing rational manipulation of intermolecular attractions. Specifically, the ability to control over a significant range the attractive interactions is critical to realize the novel microstructures theoretically

predicted[81], and the theory at present assumes the fiber network is effectively quenched in place. Thus, fibrin is a useful system since it experiences very strong inter-fiber attractions and hence strong physical (and chemical) crosslinks, and colloid chemistry can potentially be manipulated to realize variable degrees of adsorption on the fiber network.

Rich opportunities also exist for theoretical model development that can predict the structure and dynamics of semi-flexible polymer-colloid composites. Scaling relations have been proposed to capture the diffusion of spherical particles in a matrix of dynamically configurable networks of rod-like particles[89]. These studies are of practical importance and mimic vital in vivo features like the mass transport of proteins in a cell environment or their self-diffusion in a network of filamentous actin[90,91] and nucleosomes in dispersions of DNA[92]. Other studies have considered colloidal spheres in xanthan dispersions[93], solutions of living polymers[94] and dilute suspensions of tobacco mosaic virus[95]. Such scenarios can be experimentally realized with the material choices in this work. For instance, removing factor XIIIa from fibrinogen prior to fibrin polymerization[30] will result in a composite where the fibrin network is transiently crosslinked. Beyond this, such composites can also be expected to show interesting transient dynamics under oscillatory shear deformation[30]. Fibrin-colloid composition space developed here is for conditions of constant buffer pH and ionic strength. Phase space can be expanded by controlling these parameters, permitting richer morphologies and phase behavior with this combination.

5.7 References

1 Margaret, R. & Annette, F. T. Colloidal dispersions. Edited by W. B. Russel, D. A. Saville & W. R. Schowalter, Cambridge University Press, Cambridge, UK, 1989, xvii + 506 pp., price: £60.00. ISBN 0 521 34188 4. *Journal of Chemical Technology & Biotechnology* **54**, 201-202, doi:doi:10.1002/jctb.280540216 (1992).

2 Solomon, M. J. & Spicer, P. T. Microstructural regimes of colloidal rod suspensions, gels, and glasses. *Soft Matter* **6**, 1391-1400, doi:10.1039/B918281K (2010).

3 Broedersz, C. P. *et al.* Measurement of nonlinear rheology of cross-linked biopolymer gels. *Soft Matter* **6**, 4120-4127, doi:10.1039/C0SM00285B (2010).

4 Ofir, Y., Samanta, B. & Rotello, V. M. Polymer and biopolymer mediated self-assembly of gold nanoparticles. *Chemical Society Reviews* **37**, 1814-1825, doi:10.1039/B712689C (2008).

5 Rubinstein, M. & Colby, R. H. *Polymer Physics*. (Oxford University Press, 2003).

6 George, M. & Weiss, R. G. Molecular Organogels. Soft Matter Comprised of Low-Molecular-Mass Organic Gelators and Organic Liquids. *Accounts of Chemical Research*

39, 489-497, doi:10.1021/ar0500923 (2006).
7 Storm, C., Pastore, J. J., MacKintosh, F. C., Lubensky, T. C. & Janmey, P. A. Nonlinear elasticity in biological gels. *Nature* **435**, 191, doi:10.1038/nature03521 (2005).
8 Crow, A. *et al.* Contractile Equilibration of Single Cells to Step Changes in Extracellular Stiffness. *Biophysical Journal* **102**, 443-451, doi:https://doi.org/10.1016/j.bpj.2011.11.4020 (2012).
9 Kollmannsberger, P., Mierke, C. T. & Fabry, B. Nonlinear viscoelasticity of adherent cells is controlled by cytoskeletal tension. *Soft Matter* **7**, 3127-3132, doi:10.1039/C0SM00833H (2011).
10 Lai, G., Li, Y. & Li, G. Effect of concentration and temperature on the rheological behavior of collagen solution. *International Journal of Biological Macromolecules* **42**, 285-291, doi:https://doi.org/10.1016/j.ijbiomac.2007.12.010 (2008).
11 Yang, Y.-l., Leone, L. M. & Kaufman, L. J. Elastic Moduli of Collagen Gels Can Be Predicted from Two-Dimensional Confocal Microscopy. *Biophysical Journal* **97**, 2051-2060, doi:https://doi.org/10.1016/j.bpj.2009.07.035 (2009).
12 M., S. A., A., V. D., A., W. D. & M., S. L. The micromechanics of three-dimensional collagen-I gels. *Complexity* **16**, 22-28, doi:doi:10.1002/cplx.20332 (2011).
13 Arne, E., Nortvedt, A. H., Nalum, N. S., Pawel, S. & Lange, D. C. d. Physical and chemical modifications of collagen gels: Impact on diffusion. *Biopolymers* **89**, 135-143, doi:doi:10.1002/bip.20874 (2008).
14 Fukada, E. & Kaibara, M. Rheological measurements of fibrin gels during clotting. *Thrombosis Research* **8**, 49-58, doi:https://doi.org/10.1016/0049-3848(76)90047-5 (1976).
15 Copley, A. L., King, R. G. & Scheinthal, B. M. Rigidity moduli of bovine fibrin gels initiated by thrombin1. *Biorheology* **7**, 81-84, doi:10.3233/bir-1970-7201 (1970).
16 Ryan, E. A., Mockros, L. F., Weisel, J. W. & Lorand, L. Structural Origins of Fibrin Clot Rheology. *Biophysical Journal* **77**, 2813-2826, doi:https://doi.org/10.1016/S0006-3495(99)77113-4 (1999).
17 Weisel, J. W. The mechanical properties of fibrin for basic scientists and clinicians. *Biophysical Chemistry* **112**, 267-276, doi:https://doi.org/10.1016/j.bpc.2004.07.029 (2004).
18 Shen, L. L., McDonagh, R. P., McDonagh, J. & Hermans, J. Fibrin gel structure: Influence of calcium and covalent cross-linking on the elasticity. *Biochemical and Biophysical Research Communications* **56**, 793-798, doi:https://doi.org/10.1016/0006-291X(74)90675-5 (1974).
19 Lim, B. B. C., Lee, E. H., Sotomayor, M. & Schulten, K. Molecular Basis of Fibrin Clot Elasticity. *Structure* **16**, 449-459, doi:https://doi.org/10.1016/j.str.2007.12.019 (2008).
20 Chen, H. *et al.* Blood-clotting-inspired reversible polymer–colloid composite assembly in flow. *Nature Communications* **4**, 1333, doi:10.1038/ncomms2326 (2013).
21 Brown, A. C. *et al.* Ultrasoft microgels displaying emergent platelet-like behaviours. *Nature Materials* **13**, 1108, doi:10.1038/nmat4066 (2014).
22 Douglas, A. M. M., B.; Fernandez-Nieves,A.; Lyon, L. A.; Barker, T. H. in *TERMIS-Americas Annual Conference and Exposition.*
23 Lee, C. R. *et al.* Fibrin–Polyurethane Composites for Articular Cartilage Tissue Engineering: A Preliminary Analysis. *Tissue Engineering* **11**, 1562-1573, doi:10.1089/ten.2005.11.1562 (2005).
24 Brown, E. E., Hu, D., Abu Lail, N. & Zhang, X. Potential of Nanocrystalline Cellulose–Fibrin Nanocomposites for Artificial Vascular Graft Applications. *Biomacromolecules* **14**,

1063-1071, doi:10.1021/bm3019467 (2013).
25 Carr, M. E. & Hermans, J. Size and Density of Fibrin Fibers from Turbidity. *Macromolecules* **11**, 46-50, doi:10.1021/ma60061a009 (1978).
26 Lang, Nadine R. *et al.* Estimating the 3D Pore Size Distribution of Biopolymer Networks from Directionally Biased Data. *Biophysical Journal* **105**, 1967-1975, doi:https://doi.org/10.1016/j.bpj.2013.09.038 (2013).
27 Qi, W., Anindita, B., Jessamine, P. W., Arjun, Y. & Paul, A. J. Local and global deformations in a strain-stiffening fibrin gel. *New Journal of Physics* **9**, 428 (2007).
28 Shah, J. V. & Janmey, P. A. Strain hardening of fibrin gels and plasma clots. *Rheologica Acta* **36**, 262-268, doi:10.1007/bf00366667 (1997).
29 Janmey, P. A., Winer, J. P. & Weisel, J. W. Fibrin gels and their clinical and bioengineering applications. *Journal of The Royal Society Interface* **6**, 1-10, doi:10.1098/rsif.2008.0327 (2009).
30 Münster, S. *et al.* Strain history dependence of the nonlinear stress response of fibrin and collagen networks. *Proceedings of the National Academy of Sciences* **110**, 12197-12202, doi:10.1073/pnas.1222787110 (2013).
31 Roberts, W. W., Kramer, O., Rosser, R. W., Nestler, F. H. M. & Ferry, J. D. Rheology of fibrin clots. I.: Dynamic viscoelastic properties and fluid permeation. *Biophysical Chemistry* **1**, 152-160, doi:https://doi.org/10.1016/0301-4622(74)80002-5 (1974).
32 Gerth, C., Roberts, W. W. & Ferry, J. D. Rheology of fibrin clots II: Linear viscoelastic behavior in shear creep. *Biophysical Chemistry* **2**, 208-217, doi:https://doi.org/10.1016/0301-4622(74)80046-3 (1974).
33 Ferry, J. D., Miller, M. & Shulman, S. The conversion of fibrinogen to fibrin. VII. Rigidity and stress relaxation of fibrin clots; effect of calcium. *Archives of Biochemistry and Biophysics* **34**, 424-436, doi:https://doi.org/10.1016/0003-9861(51)90021-5 (1951).
34 Glover, C. J., McIntire, L. V., Brown, C. H., 3rd & Natelson, E. A. Rheological properties of fibrin clots. Effects of fibrinogen concentration, Factor XIII deficiency, and Factor XIII inhibition. *J Lab Clin Med* **86**, 644-656 (1975).
35 Janmey, P. A., Amis, E. J. & Ferry, J. D. Rheology of Fibrin Clots. VI. Stress Relaxation, Creep, and Differential Dynamic Modulus of Fine Clots in Large Shearing Deformations. *Journal of Rheology* **27**, 135-153, doi:10.1122/1.549722 (1983).
36 Falvo, M. R., Gorkun, O. V. & Lord, S. T. The molecular origins of the mechanical properties of fibrin. *Biophysical Chemistry* **152**, 15-20, doi:https://doi.org/10.1016/j.bpc.2010.08.009 (2010).
37 Brown, A. C. & Barker, T. H. Fibrin-based biomaterials: Modulation of macroscopic properties through rational design at the molecular level. *Acta Biomaterialia* **10**, 1502-1514, doi:https://doi.org/10.1016/j.actbio.2013.09.008 (2014).
38 Tidrick, R. T. & Warner, E. D. Fibrin fixation of skin transplants. *Surgery* **15**, 90-95, doi:10.5555/uri:pii:S0039606044900528 (1944).
39 Spotnitz, W. D. Fibrin sealant in the United States: clinical use at the University of Virginia. *Thromb Haemost* **74**, 482-485 (1995).
40 Spicer, P. P. & Mikos, A. G. Fibrin glue as a drug delivery system. *Journal of Controlled Release* **148**, 49-55, doi:https://doi.org/10.1016/j.jconrel.2010.06.025 (2010).
41 Wong, C., Inman, E., Spaethe, R. & Helgerson, S. *Fibrin-based biomaterials to deliver human growth factors*. Vol. 89 (2003).
42 Yücel, E. A., Oral, O., Olgaç, V. & Oral, C. K. Effects of fibrin glue on wound healing in

oral cavity. *Journal of Dentistry* **31**, 569-575, doi:https://doi.org/10.1016/S0300-5712(03)00113-1 (2003).
43 He, M. *et al.* The effect of fibrin glue on tendon healing and adhesion formation in a rabbit model of flexor tendon injury and repair. *Journal of Plastic Surgery and Hand Surgery* **47**, 509-512, doi:10.3109/2000656X.2013.789037 (2013).
44 Currie, L. J., Sharpe, J. R. & Martin, R. The Use of Fibrin Glue in Skin Grafts and Tissue-Engineered Skin Replacements: A Review. *Plastic and Reconstructive Surgery* **108**, 1713-1726 (2001).
45 C., V. *et al.* Nasal chondrocytes and fibrin sealant for cartilage tissue engineering. *Journal of Biomedical Materials Research Part A* **89A**, 176-185, doi:doi:10.1002/jbm.a.31988 (2009).
46 Ottewill, R. H. & Shaw, J. N. Studies on the preparation and characterization of monodisperse polystyrene latices. *Kolloid-Zeitschrift und Zeitschrift für Polymere* **215**, 161, doi:10.1007/bf01520398 (1967).
47 Goodwin, J. W., Hearn, J., Ho, C. C. & Ottewill, R. H. Studies on the preparation and characterisation of monodisperse polystyrene laticee. *Colloid and Polymer Science* **252**, 464-471, doi:10.1007/bf01554752 (1974).
48 de Rooij, R., van den Ende, D., Duits, M. H. G. & Mellema, J. Elasticity of weakly aggregating polystyrene latex dispersions. *Physical Review E* **49**, 3038-3049, doi:10.1103/PhysRevE.49.3038 (1994).
49 Martin, L. H. Rheological properties of aqueous polymer dispersions. *Die Angewandte Makromolekulare Chemie* **123**, 335-359, doi:doi:10.1002/apmc.1984.051230115 (1984).
50 Mitsumata, T., Honda, A., Kanazawa, H. & Kawai, M. Magnetically Tunable Elasticity for Magnetic Hydrogels Consisting of Carrageenan and Carbonyl Iron Particles. *The Journal of Physical Chemistry B* **116**, 12341-12348, doi:10.1021/jp3049372 (2012).
51 Mitra, S. & Khandelwal, P. Are All Colloids Same? How to Select the Right Colloid? *Indian Journal of Anaesthesia* **53**, 592-607 (2009).
52 G., N. V. Colloids decrease clot propagation and strength: role of factor XIII-fibrin polymer and thrombin–fibrinogen interactions. *Acta Anaesthesiologica Scandinavica* **49**, 1163-1171, doi:doi:10.1111/j.1399-6576.2005.00733.x (2005).
53 Mittermayr, M. *et al.* Effects of colloid and crystalloid solutions on endogenous activation of fibrinolysis and resistance of polymerized fibrin to recombinant tissue plasminogen activator added ex vivo. *British Journal of Anaesthesia* **100**, 307-314, doi:https://doi.org/10.1093/bja/aem363 (2008).
54 Kozek-Langenecker, S. A. Effects of hydroxyethyl starch solutions on hemostasis. *Anesthesiology* **103**, 654-660 (2005).
55 Schramko, A. *et al.* Hydroxyethylstarch and gelatin solutions impair blood coagulation after cardiac surgery: a prospective randomized trial. *British Journal of Anaesthesia* **104**, 691-697, doi:https://doi.org/10.1093/bja/aeq084 (2010).
56 K., E., L., A., M., V., J., B. J. & O., E. The in vitro effects of crystalloids and colloids on coagulation. *Anaesthesia* **57**, 1102-1108, doi:doi:10.1046/j.1365-2044.2002.02782_1.x (2002).
57 Nemmar, A. *et al.* Ultrafine Particles Affect Experimental Thrombosis in an In Vivo Hamster Model. *American Journal of Respiratory and Critical Care Medicine* **166**, 998-1004, doi:10.1164/rccm.200110-026OC (2002).
58 Behrens, S. H., Christl, D. I., Emmerzael, R., Schurtenberger, P. & Borkovec, M. Charging

and Aggregation Properties of Carboxyl Latex Particles: Experiments versus DLVO Theory. *Langmuir* **16**, 2566-2575, doi:10.1021/la991154z (2000).

59 Davis, H. E., Miller, S. L., Case, E. M. & Leach, J. K. Supplementation of fibrin gels with sodium chloride enhances physical properties and ensuing osteogenic response. *Acta Biomaterialia* **7**, 691-699, doi:https://doi.org/10.1016/j.actbio.2010.09.007 (2011).

60 Winer, J. P., Oake, S. & Janmey, P. A. Non-linear elasticity of extracellular matrices enables contractile cells to communicate local position and orientation. *PloS one* **4**, e6382, doi:10.1371/journal.pone.0006382 (2009).

61 Jawerth, L. M. *The mechanics of fibrin networks and their alterations by platelets* Ph.D thesis, Harvard Universit, (2013).

62 Wufsus, Adam R. *et al.* Elastic Behavior and Platelet Retraction in Low- and High-Density Fibrin Gels. *Biophysical Journal* **108**, 173-183, doi:https://doi.org/10.1016/j.bpj.2014.11.007 (2015).

63 Weisel, J. W. & Litvinov, R. I. Mechanisms of fibrin polymerization and clinical implications. *Blood* **121**, 1712-1719, doi:10.1182/blood-2012-09-306639 (2013).

64 Rowe, S. L., Lee, S. & Stegemann, J. P. Influence of thrombin concentration on the mechanical and morphological properties of cell-seeded fibrin hydrogels. *Acta Biomaterialia* **3**, 59-67, doi:https://doi.org/10.1016/j.actbio.2006.08.006 (2007).

65 Gardel, M. L. *et al.* Elastic Behavior of Cross-Linked and Bundled Actin Networks. *Science* **304**, 1301-1305, doi:10.1126/science.1095087 (2004).

66 Brass, E. P., Forman, W. B., Edwards, R. V. & Lindan, O. Fibrin formation: effect of calcium ions. *Blood* **52**, 654-658 (1978).

67 Nair, C. H., Shah, G. A. & Dhall, D. P. Effect of temperature, ph and ionic strength and composition on fibrin network structure and its development. *Thrombosis Research* **42**, 809-816, doi:https://doi.org/10.1016/0049-3848(86)90117-9 (1986).

68 Weigandt, K. M., Pozzo, D. C. & Porcar, L. Structure of high density fibrin networks probed with neutron scattering and rheology. *Soft Matter* **5**, 4321-4330, doi:10.1039/B906256D (2009).

69 MacKintosh, F. C., Käs, J. & Janmey, P. A. Elasticity of Semiflexible Biopolymer Networks. *Physical Review Letters* **75**, 4425-4428, doi:10.1103/PhysRevLett.75.4425 (1995).

70 Wolberg, A. S. Thrombin generation and fibrin clot structure. *Blood Reviews* **21**, 131-142, doi:https://doi.org/10.1016/j.blre.2006.11.001 (2007).

71 Israelachvili, J. N. *Intermolecular and Surface Forces*. (Elsevier Science, 2015).

72 Karin, B. *et al.* Reduction of fibrinogen adsorption on PEG-coated polystyrene surfaces. *Journal of Biomedical Materials Research* **26**, 779-790, doi:doi:10.1002/jbm.820260607 (1992).

73 Rémy, A. *et al.* Lectins as probes for assessing the accessibility of N-linked glycans in relation to the conformational changes of fibronectin. *Journal of Molecular Recognition* **28**, 731-741, doi:doi:10.1002/jmr.2487 (2015).

74 Hyun, K. *et al.* A review of nonlinear oscillatory shear tests: Analysis and application of large amplitude oscillatory shear (LAOS). *Progress in Polymer Science* **36**, 1697-1753, doi:https://doi.org/10.1016/j.progpolymsci.2011.02.002 (2011).

75 Kang, H. *et al.* Nonlinear Elasticity of Stiff Filament Networks: Strain Stiffening, Negative Normal Stress, and Filament Alignment in Fibrin Gels. *The Journal of Physical Chemistry B* **113**, 3799-3805, doi:10.1021/jp807749f (2009).

76 Lin, N. Y. C. *et al.* A multi-axis confocal rheoscope for studying shear flow of structured fluids. *Review of Scientific Instruments* **85**, 033905, doi:10.1063/1.4868688 (2014).
77 Dutta, S. K., Mbi, A., Arevalo, R. C. & Blair, D. L. Development of a confocal rheometer for soft and biological materials. *Review of Scientific Instruments* **84**, 063702, doi:10.1063/1.4810015 (2013).
78 Wang, Q., Hou, R., Cheng, Y. & Fu, J. Super-tough double-network hydrogels reinforced by covalently compositing with silica-nanoparticles. *Soft Matter* **8**, 6048-6056, doi:10.1039/C2SM07233E (2012).
79 Yang, J. *et al.* Synthetic and viscoelastic behaviors of silica nanoparticle reinforced poly(acrylamide) core-shell nanocomposite hydrogels. *Soft Matter* **9**, 1220-1230, doi:10.1039/C2SM27233D (2013).
80 Gupta, K. K. *et al.* Polycaprolactone composites with TiO2 for potential nanobiomaterials: tunable properties using different phases. *Physical Chemistry Chemical Physics* **14**, 12844-12853, doi:10.1039/C2CP41789H (2012).
81 Jadrich, R. B. & Schweizer, K. S. Directing Colloidal Assembly and a Metal-Insulator Transition Using a Quench-Disordered Porous Rod Template. *Physical Review Letters* **113**, 208302, doi:10.1103/PhysRevLett.113.208302 (2014).
82 Zhang, F., Kang, E. T., Neoh, K. G. & Huang, W. Modification of gold surface by grafting of poly(ethylene glycol) for reduction in protein adsorption and platelet adhesion. *Journal of Biomaterials Science, Polymer Edition* **12**, 515-531, doi:10.1163/156856201300194252 (2001).
83 Mizuno, D., Head, D. A., MacKintosh, F. C. & Schmidt, C. F. Active and Passive Microrheology in Equilibrium and Nonequilibrium Systems. *Macromolecules* **41**, 7194-7202, doi:10.1021/ma801218z (2008).
84 Kotlarchyk, M. A. *et al.* Concentration Independent Modulation of Local Micromechanics in a Fibrin Gel. *PloS one* **6**, e20201, doi:10.1371/journal.pone.0020201 (2011).
85 Corrigan, A. M. & Donald, A. M. Passive Microrheology of Solvent-Induced Fibrillar Protein Networks. *Langmuir* **25**, 8599-8605, doi:10.1021/la804208q (2009).
86 Schnurr, B., Gittes, F., MacKintosh, F. C. & Schmidt, C. F. Determining Microscopic Viscoelasticity in Flexible and Semiflexible Polymer Networks from Thermal Fluctuations. *Macromolecules* **30**, 7781-7792, doi:10.1021/ma970555n (1997).
87 V., Z. M. *et al.* Influence of Temperature on the Colloidal Stability of Polymer-Coated Gold Nanoparticles in Cell Culture Media. *Small* **12**, 1723-1731, doi:doi:10.1002/smll.201503232 (2016).
88 Guo, J., Yang, W., Wang, C., He, J. & Chen, J. Poly(N-isopropylacrylamide)-Coated Luminescent/Magnetic Silica Microspheres: Preparation, Characterization, and Biomedical Applications. *Chemistry of Materials* **18**, 5554-5562, doi:10.1021/cm060976w (2006).
89 Kang, K. *et al.* Diffusion of spheres in crowded suspensions of rods. *The Journal of Chemical Physics* **122**, 044905, doi:10.1063/1.1834895 (2005).
90 Wong, I. Y. *et al.* Anomalous Diffusion Probes Microstructure Dynamics of Entangled F-Actin Networks. *Physical Review Letters* **92**, 178101, doi:10.1103/PhysRevLett.92.178101 (2004).
91 Schmidt, C. F., Baermann, M., Isenberg, G. & Sackmann, E. Chain dynamics, mesh size, and diffusive transport in networks of polymerized actin: a quasielastic light scattering and microfluorescence study. *Macromolecules* **22**, 3638-3649, doi:10.1021/ma00199a023

(1989).
92 Mangenot, S., Keller, S. & Rädler, J. Transport of Nucleosome Core Particles in Semidilute DNA Solutions. *Biophysical Journal* **85**, 1817-1825, doi:https://doi.org/10.1016/S0006-3495(03)74610-4 (2003).
93 Koenderink, G. H., Sacanna, S., Aarts, D. G. A. L. & Philipse, A. P. Rotational and translational diffusion of fluorocarbon tracer spheres in semidilute xanthan solutions. *Physical Review E* **69**, 021804, doi:10.1103/PhysRevE.69.021804 (2004).
94 van der Gucht, J., Besseling, N. A. M., Knoben, W., Bouteiller, L. & Cohen Stuart, M. A. Brownian particles in supramolecular polymer solutions. *Physical Review E* **67**, 051106, doi:10.1103/PhysRevE.67.051106 (2003).
95 Lellig, C. *et al.* Self-diffusion of rodlike and spherical particles in a matrix of charged colloidal spheres: A comparison between fluorescence recovery after photobleaching and fluorescence correlation spectroscopy. *The Journal of Chemical Physics* **121**, 7022-7029, doi:10.1063/1.1791631 (2004).

CHAPTER 6.

SWITCHABLE MECHANICAL PROPERTY OF PNIPAM COLLOIDS/FIBRIN NETWORKS HYDROGEL 3D COMPOSITES BY THERMAL ACTUATION‡

6.1 Introduction

In **Chapter 5**, we discussed the significance of integrating the colloids into large mesh (~ 100 nm to 10's μms) polymeric gels in biological and biomedical fields[1-4]. We offered two different integration methods, a polymerization around the colloids and a driving the colloids into pre-formed polymer networks[5]. Based on our methods and the findings about the relation between the structure of composites and mechanical properties, here we extend our perspectives toward the development of dynamically reconfigurable assemblies of colloids/polymeric meshes, whose optical, electrical, or mechanical properties are reversibly switchable by means of external trigger forces such as temperature, pH, ionic, strength, electric/magnetic fields, and light[6-12].

We used the fibrin as a deformable polymer network gels to exert the internal fields on the assembled functional colloids. The details on the fibrin biopolymer gels are well described in **Chapter 5** and some other references[3,13-16]. Meanwhile, we selected a thermal actuation as a trigger force that could induce the changes in the configuration and dynamic properties of colloids/polymer hybrids. Poly(N-isopropylacrylamide) (PNIPAM) is the most widely studied class of thermo-responsive soft materials, which can be fabricated as the linear chain brushes[17-19] or as the deformable microgels[11,12,20-22]. **Figure 6.1** illustrates the chemical structure to help understanding of the thermo-responsive properties of PNIPAM, where the complicated hydrophilic/hydrophobic balance exists[23]. The hydrophilic region consists of the amide side chains which can bond to water through hydrogen bonding whereas the hydrophobic region is comprised of the isopropyl group which causes structuring of water[11,23,24].

‡ The results in this chapter were obtained based on the collaborative works with Prof. Ewoldt group and Prof. Schweizer group. All the rheological measurements were performed by Gaurav Chaudhary at Prof. Ewoldt group. Confocal fluorescent imaging was performed by Dr. Bharadwaj (@ Nike), a former member of Prof. Ewoldt group, Prof. Hatzell (@ GIT), a former member of Prof. Braun group, and myself. Computational work is in progress by Ghosh Ashesh at Prof. Schweizer group.

PNIPAM shows endothermic, entropically driven phase transition from a random coil to a collapsed globule upon the external heating stimulus[25,26]. At low temperatures, PNIPAM interacts with water by hydrogen bonding primarily through the amide side chains, so that the water-polymer interactions are stronger than the polymer-polymer interactions. The polymer is well solvated with the surrounding water molecules. At temperatures above ~ 32^{o}C, the isopropyl group induces hydrophobic structuring of water and this results in entropy-controlled polymer-polymer interactions. As we ramp the solution temperatures up, the expulsion of structured water takes place due to weaker hydrogen bonding with water and polymer-polymer interactions become dominant, leading to coil-globule transition. The temperature where this phase change of non-crosslinked polymer chains occurs is known as the lower critical solution temperature (LCST). The microgels comprised of cross-linked networks, exhibit thermo-responsive behavior at a so-called volume phase transition temperature (VPTT), which is close to the LCST[27,28].

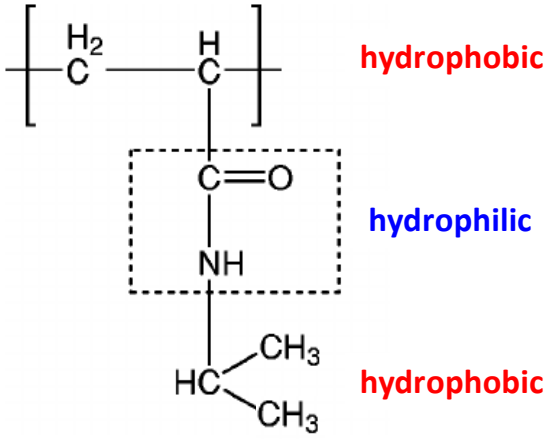

Figure 6.1 – Chemical structure of PNIPAM comprised of the hydrophilic (amide side chains) and hydrophobic (isopropyl groups) components. Adapted from ref. 23.

In this study, we have synthesized two different types of thermo-responsive colloids. First is the hard sphere SiO_2 nanoparticles of which PNIPAM linear chain brushes was grown on the surface via surface-initiated atom-transfer radical-polymerization (ATRP) method. Surface-initiated ATRP is known as a powerful tool to grow the polymer brush due to the excellent control offered over the brush homogeneity and length[17]. Second is the lightly cross-linked PNIPAM microgels, which are the soft colloids, via surfactant-free emulsion polymerization (SFEP) method. In SFEP, the continuous phase needs to have a high dielectric constant (e.g. water) and ionic initiators are employed (e.g. $K_2S_2O_8$; potassium peroxodisulfate)[29]. Even in the absence of added surfactant, the charged polymer chains created during polymerization play a role as

surfactant molecules and stabilize the growing microgel particles. SFEP is an ideally appropriate method for the preparation of PNIPAM microgels[29].

These two types of colloids were then integrated into semi-flexible networks of fibrin using the **Method I** developed in **Chapter 5**, polymerization of fibrin around the colloids[5]. The thermo-sensitive 3D colloids/fibrin meshes hybrids, kinetically transformable functional materials, were characterized by means of multiple tools to study the structure-dynamics-property relationships.

6.2 Experimental Methods

A schematic of the research design overview of this chapter is represented in **Figure 6.2**.

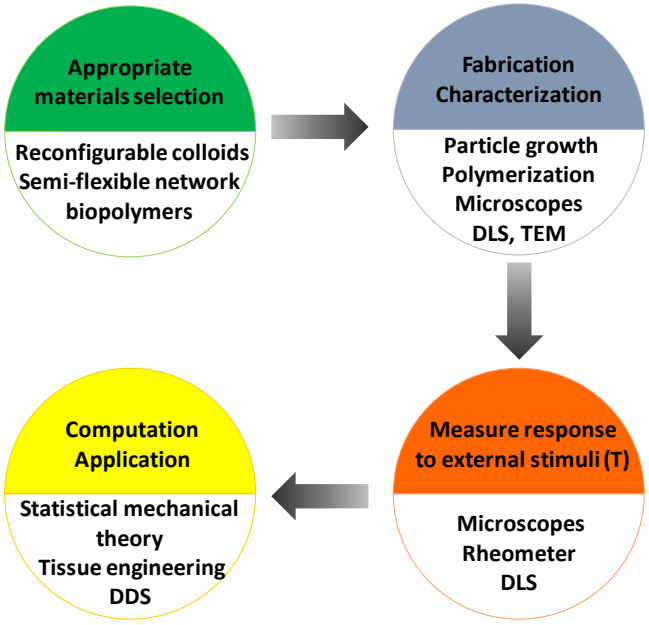

Figure 6.2 – Schematic illustrations showing the overall research processes designed for this collaborative work.

6.2.1 Synthesis of SiO_2 nanospheres

We prepared the SiO_2 hard sphere colloids by Stober method[30]. A 500 ml round bottom flask was soaked in the base bath 2 days to prevent the heterogeneous particle growth on the contaminants. After rinsed with Type 1 water, the flask was sonicated with 300 ml of ethanol for 30 mins followed by with 300 ml of isopropyl alcohol for 30 mins. At the same time, a magnetic

stirring egg bar and a stopper were also sonicated in ethanol followed by in isopropyl alcohol. Everything was rinsed with ethanol before use.

We added 100 ml of ethanol in the flask and stir at 500 rpm. 10.5 g of Type 1 water and 3 g of ammonium hydroxide (NH_4OH) were added into the solution using Norm-ject syringes. Special attention was required so that the liquids do not touch the walls of the flask. After waiting 30 mins for mixing, we added 5.2 g of tetraethyl orthosilicate (TEOS) all at once. We let the solution mix and react for 3 days. No re-growth process was performed.

6.2.2 Surface-initiated ATRP of PNIPAM brushes on SiO_2 nanospheres

The surface-initiated ATRP growth of PNIPAM chain brushes on the SiO_2 nanospheres was carried out using a previously published procedure with minor modifications[17]. The overall process is illustrated in **Figure 6.3**[17]. The bare SiO_2 nanoparticles (0.25 g) were centrifuged from aqueous suspension, and then cleaned with two cycles of centrifuge/disperse in ethanol. We sonicated the particles in 20 mL of ethanol for two days to stabilize the colloidal suspension, and then added 40 µL of aminopropyltriethoxysilane (APS, 99 %, Acros) into the suspension. The reaction proceeded for 1 day under ultrasonication.

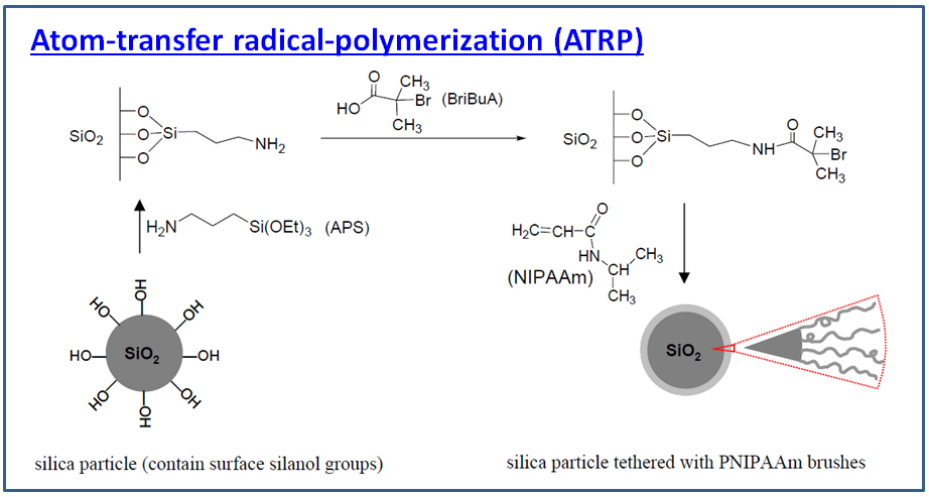

Figure 6.3 – Schematic illustrations of the surface-initiated ATRP process used for the growth of the PNIPAM chain brushes on the SiO_2 nanospheres. Adapted from ref. 17.

After two cycles of centrifuge/disperse cycles in ethanol and one cycle in dichloromethane (DCM), the SiO_2 nanospheres were transferred into a glass jar where a solution of 267 mg of 2-bromo-2-methylpropionic acid (BriBuA, 98 %, Acros) and 48 mg of 4-dimethylaminopyridine

(DMAP, 99 %, Acros) were dissolved in 30 mL of DCM. The suspension was cooled down to 0°C in an ice bath. Then, we added a solution of 413 mg of N, N'-dicylcohexylcarbodiimde (DCC, 99 %, Acros) dissolved in 5 mL of cooled DCM into the suspension. The mixture was left to reach room temperature. The reaction was allowed to continue overnight under the consistent vortexing to prevent the particle aggregations.

The initiator-grafted SiO_2 nanospheres were purified by six cycles of centrifuge/disperse in chloroform, and then dispersed in 10 mL of a 1:1 (v/v) mixture of methanol and water in a Schlenk reaction flask (capacity 100 ml, Sigma-Aldrich) under 2 hours of sonication. Meanwhile, we dissolved 6.3 g of N-isopropylacrylamide (NIPAM, 99 %, Acros), 80 mg of copper (I) bromide (CuBr, 99.999 %, Acros) and 350 µL of 1,1,4,7,7-pentamethyldiethylenetriamine (PMDETA, 99+ %, Acros) in 50 mL of 1:1 (v/v) methanol/water mixture and then degassed by two cycles of freeze-thaw processes. Using the Schlenk line setup, the solution was then transferred through a long canula into the degassed Schlenk flask containing the surface-initiator grafted SiO_2 nanoparticles. The ATRP was carried out at room temperature under a nitrogen atmosphere for 48 hours. After the completion of the reaction, we disconnected the Schlenk flask from the nitrogen line, and then cleaned the PNIPAM-functionalized SiO_2 nanospheres by five cycles of centrifuge/disperse in ethanol and water alternately.

6.2.3 Synthesis of PNIPAM microgels by SFEP

To make lightly cross-linked particles, we followed a recipe reported elsewhere with minor changes[21,22]. Type I water (100 ml) was filtered through a 0.2 µm Acrodisc syringe filter into a glass beaker. We dissolved 146 mM (1.65 g) of NIPAM monomer in the filtered water and then filtered the solution through a 0.2 µm Acrodisc syringe filter into a 3-neck round bottom flask. The solution was stirred at 500 rpm, purged with nitrogen, and heated to 45^{o}C in a temperature-controlled oil bath until the temperature of the solution became stable (1 hour typically).

We injected a solution of 2.8 mM (80 mg) potassium peroxodisulfate (KPS, 99 %+, Sigma-Aldrich) dissolved in 1 ml of the pre-filtered Type 1 water through a 0.2 µm Acrodisc syringe filter to initiate the polymerization. The temperature of the solution was ramped up to 68^{o}C at a rate of 1^{o}C min^{-1} so that more precursor radicals could be consumed for the particle growth rather than for the nucleation[22] to finally obtain the large microgel particles. The mixture was left to react under continuous stirring at 500 rpm in nitrogen atmosphere overnight. In the case of the fabrication of

dye-tagged microgels, we injected a solution of 1 mg of Rhodamine Green™ (carboxylic acid, succinimidyl ester, hydrochloride, mixed isomers, Thermo-Fisher Scientific) dissolved in 20 ul of dimethyl sulfoxide (DMSO) into the monomer solution *right before* adding the KPS initiating solution. **Figure 6.4** illustrates the entire nucleation and growth processes of the PNIPAM microgel particles[31].

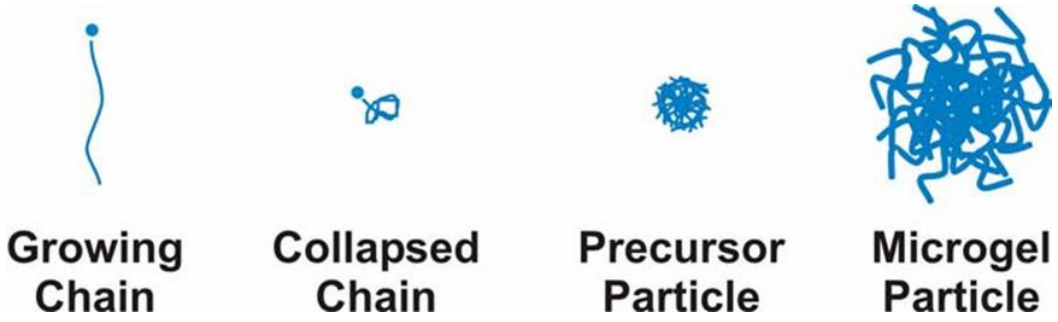

Figure 6.4 – Schematics illustrating the growth of a PNIPAM microgel during the surfactant-free emulsion polymerization. The initial PNIPAM chains are formed and then collapse upon reaching a critical chain length. The collapsed chains then serve as seeds for the further growth of the microgels. Adapted from ref. 31.

After the polymerization, we normal-cooled down the solution to the room temperature and filtered the solution with the glass wool five times to remove the large particulates. The microgel particles were thoroughly purified by five cycles of the centrifuge/dispersion processes. The centrifugation was done at 15000 xg of relative centrifugal force (RCF). The cleaned particles were then lyophilized for the purpose of further characterization. In **Figure 6.5**, the overall fabrication process of the PNIPAM microgels is visualized.

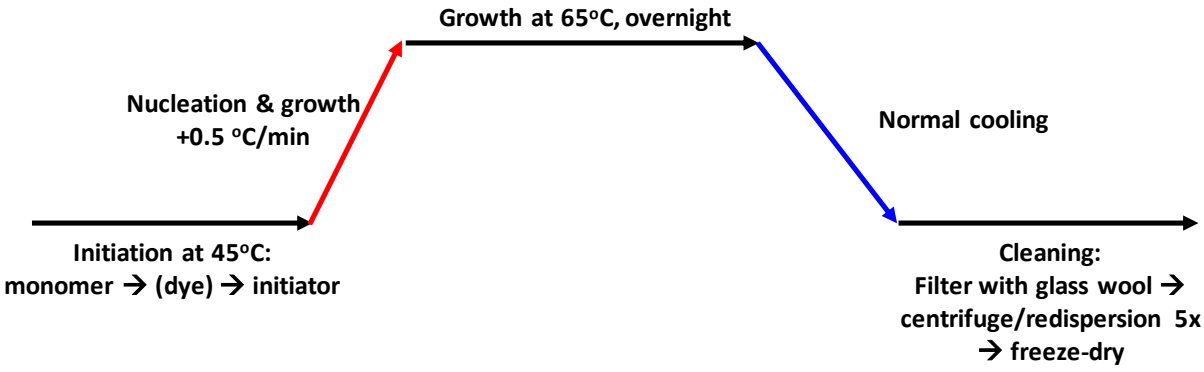

Figure 6.5 – Schematics of the overall processes for the fabrication of the µm-sized, lightly cross-linked, and highly-deformable PNIPAM microgels.

6.2.4 Characterization

SEM & TEM

The morphologies of the particles were characterized using field-emission SEM (FESEM; S-4800, Hitachi). Prior to imaging, we coated the sample using an Au-Pd sputter to enhance the imaging resolution. To image the dried state of the PNIPAM brushes on the SiO_2 nanospheres, we collected the TEM images of the bare SiO_2 nanospheres as well as the PNIPAM-SiO_2 ones using a JEOL 2010 Lab_6 TEM operated at 200 kV. Before imaging, the particles were dispersed in ethanol and then dropped onto a Holey carbon-coated Cu grid. The completely dried grid was loaded into the TEM sample holder.

Dynamic light scattering (DLS)

The diameter changes of the PNIPAM-SiO_2 hard spheres and PNIPAM soft microgels upon temperature variation swept between 25 to 40^oC, were investigated by DLS measurement (Zetasizer Nano ZS, Malvern). The temperature of the samples was controlled by automated heating/cooling system built in the Zetasizer.

Confocal Raman spectroscopy

Temperature-dependent Raman spectra of the pure PNIPAM microgels, pure fibrin hydrogels, and PNIPAM-fibrin gel composites were collected by means of a Horiba confocal Raman microscope (LabRAM HR 3D) equipped with a 532 nm laser. The temperature was changed using the same heated staged as the one used for the confocal imaging above.

Confocal fluorescence microscopy

(by Dr. Bharadwaj at Prof. Ewoldt group, Dr. Hatzell at Prof. Braun group, and myself)

The structure of the tagged hydrogels in the wet state was examined by a two-color laser scanning confocal microscope (LSM 700, Zeiss) using a 63x oil-immersion objective lens (NA 1.4). To perform two-color imaging of the PNIPAM-fibrin composites, different sets of excitation/emission wavelengths were selected. For the tagged-PNIPAM microgels, rhodamine green with 504/535 nm wavelengths was used, whereas for the tagged-fibrin, TAMRA-SE red (Thermo-Fisher Scientific) with 547/576 nm wavelengths was employed. The detailed description

of fibrinogen tagging process is well documented in a previous work[32]. The temperature was modulated from 25 to 35°C using a heated stage (Delta T, Bioptechs).

Rheological measurement

(by Gaurav Chaudhary at Prof. Ewoldt group)

Shear rheology was performed on a Discovery Hybrid Rheometer (DHR3, TA instruments) using a 20 mm flat plate with 600 grit sandpaper. The temperature of the bottom plate was controlled by a water recirculating Peltier system.

6.3 Morphology and Size of SiO_2-based Nanospheres

Figure 6.6 shows the plane-view SEM image of the bare SiO_2 nanoparticles in their dried state. They are highly monodispersed and spherical with ~ 190 nm in diameter.

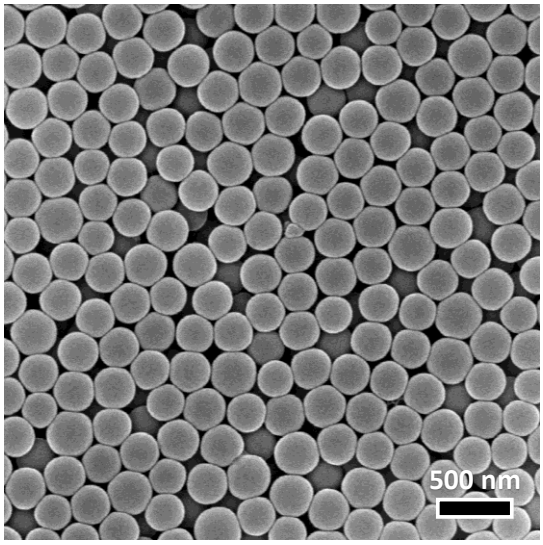

Figure 6.6 – SEM image of the bare SiO_2 nanospheres with 190 nm in diameter with high monodispersity grown by Stober method[30].

The difference in the morphology between the bare SiO_2 and PNIPAM-grafted SiO_2 nanospheres was examined by TEM imaging, as exhibited in **Figure 6.7**. In the dried state, the size of the bare particles is ~ 180 nm in diameter, which corresponds to the SEM image. We clearly see ~ 5 nm thick PNIPAM brushes grown on the SiO_2 particles in an inset of **Figure 6.7b**. This indicates that the surface-initiated ATRP successfully took place on the SiO_2 surface.

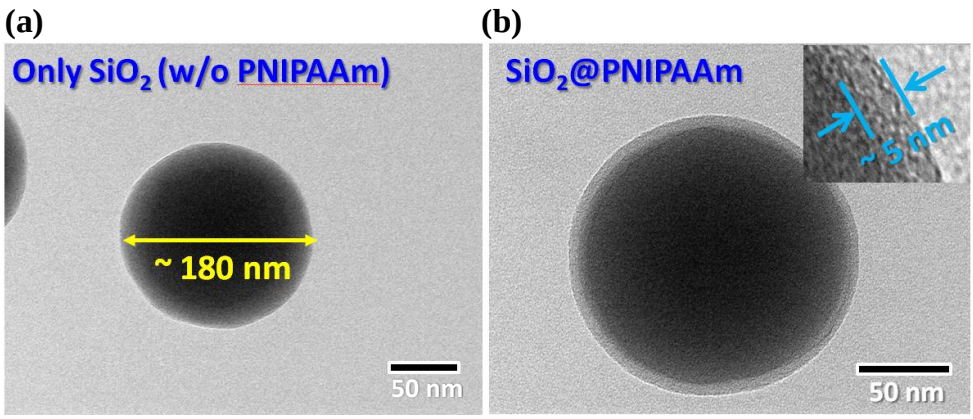

Figure 6.7 – Bright-field TEM images of the (a) bare SiO_2 and (b) PNIPAM-tethered SiO_2 particles. The PNIPAM brushes are evidently observed in an inset of (b).

Figure 6.8a represents the temperature-dependent size changes of the bare SiO_2 and PNIPAM-SiO_2 nanoparticles. The bare particles do not show any dependency on the temperature. In contrast, the hydrodynamic diameter of the PNIPAM-SiO_2 particles reversibly changed between two temperatures, 25 and 40°C.

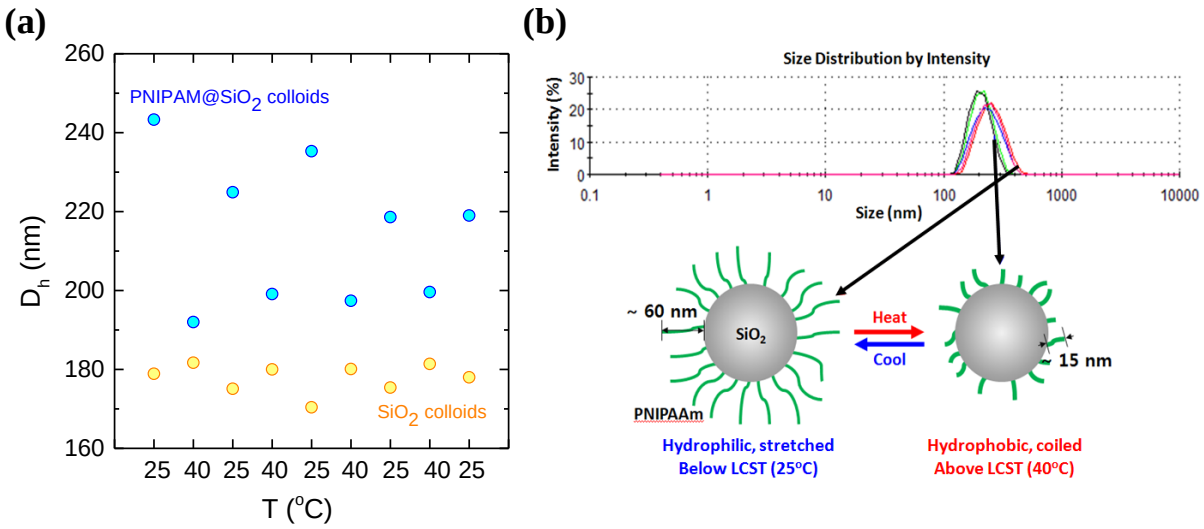

Figure 6.8 – DLS measurements on the bare SiO_2 and the PNIPAM-SiO_2 nanospheres suspended in Type 1 water. (a) Plots of the hydrodynamic diameters of two particles upon multiple cycles of heating and cooling. (b) Top graph shows that polydispersity of the particles decreases with increasing temperature. Bottom schematics briefly display the change in the particle morphology during the heating up and cooling down.

Comparing the diameter of the PNIPAM-SiO_2 particles with that of the SiO_2 particles at each temperature, we could deduce the thickness of the PNIPAM brushes in their wet state. At 25°C, the thickness of the brushes is ~ 60 nm whereas it is ~ 15 nm at 40°C, indicating that the

PNIPAM brushes undergo ~ 75 % shrinkage upon heating. In addition, the polydispersity of PNIPAM-SiO_2 nanospheres decreases as the temperature increases, as depicted in Figure **6.8b**, due to the phase transition of the PNIPAM chains to the collapsed coil[25,26].

Although the PNIPAM brushes were successfully grown on the SiO_2 hard sphere colloids and showed the thermo-responsive property in the size, we could not see any noticeable change in the mechanical performance upon thermal actuation during the rheological measurement on the PNIPAM-SiO_2/fibrin composite hydrogels. This may originate from the fact that the total amount of the PNIPAM brushes in the colloids was too small to distort the structure the fibrin networks macroscopically. Most volume of the PNIPAM-SiO_2 colloids is taken by the excluded volume of SiO_2. In addition, the thickness of the PNIPAM chains is only ~ 60 nm in their wet state. To induce the spatial reorganization of the colloids/fibrin composites and hence to reversibly switch the macroscopic mechanical properties in response to the external stimulus, we adopted the highly deformable and lightly cross-linked PNIPAM microgels[22] as an alternative colloid system.

6.4 Morphology and Size of Pure PNIPAM Microgels

The main purpose of the study in this chapter is to investigate the variations in the structure and dynamics of the PNIPAM/fibrin gel composites under a thermo-triggering force. We selected the fibrin as a viscoelastic media that has a dynamic memory and internal fields due to its large mesh size and highly deformable features[3,13,14,33]. As the mesh size of the fibrin is in the range of tens to hundreds of μms depending on the initial concentrations of the fibrinogen[34], microgel colloids on μm scale in diameter, were required to trigger the spatial organization of the fibrin.

Figure 6.9 demonstrates the confocal fluorescence (**a**) and optical microscope (**b**) images of the PNIPAM microgels in the wet state. Both indicates that the diameter of the particles range over 1.5 ~ 2.0 μm with a polydisperse nature at room temperature. To take a deeper look at the size characteristics, we carried out the DLS measurements on the microgel particles dispersed in the Type 1 water as well as in the fibrin buffer solution consisting of 25 mM HEPES, 150 mM NaCl, and 20 mM $CaCl_2$, upon sweeping the temperature over 25 ~ 35^{o}C. At each temperature, the colloidal suspension was equilibrated for 180 sec.

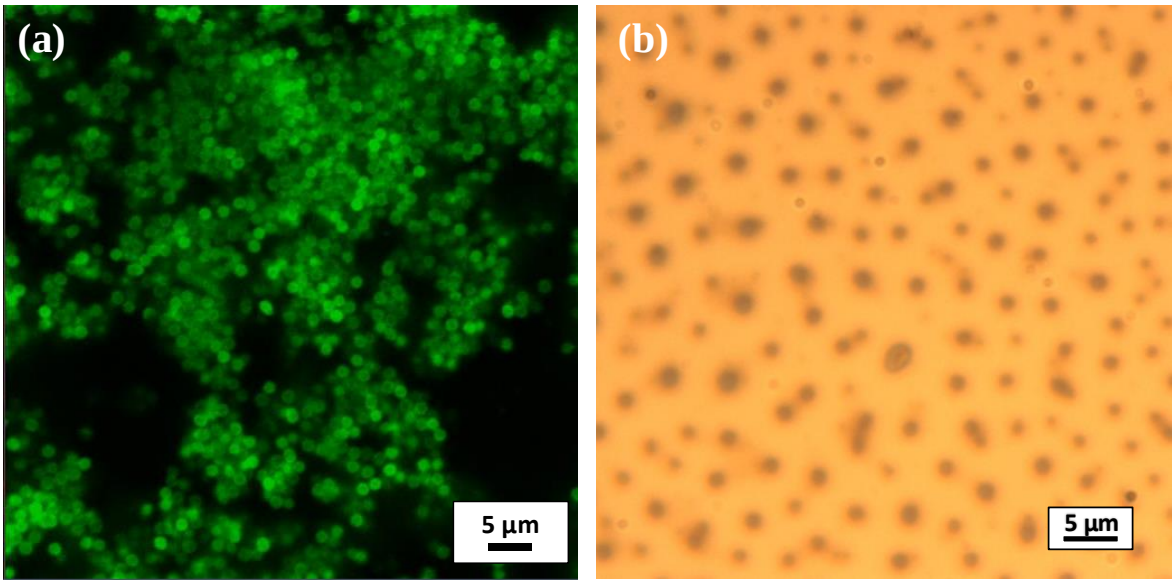

Figure 6.9 – Microstructure visualization of the pure PNIPAM microgels in their wet state. (a) Confocal fluorescence microscopy image. (b) Optical microscopy image.

In **Figure 6.10a**, we observe a typical thermo-responsive behavior of the PNIPAM microgels dispersed in deionized water[21,31], where the ionic strength of the suspension is negligible. Upon heating, the hydrodynamic diameter of the microgels dramatically decreases at 31 ~ 32°C from 1.6 µm to 500 nm, the VPTT of the PNIPAM. On cooling down, they recovered their size in a reversible manner.

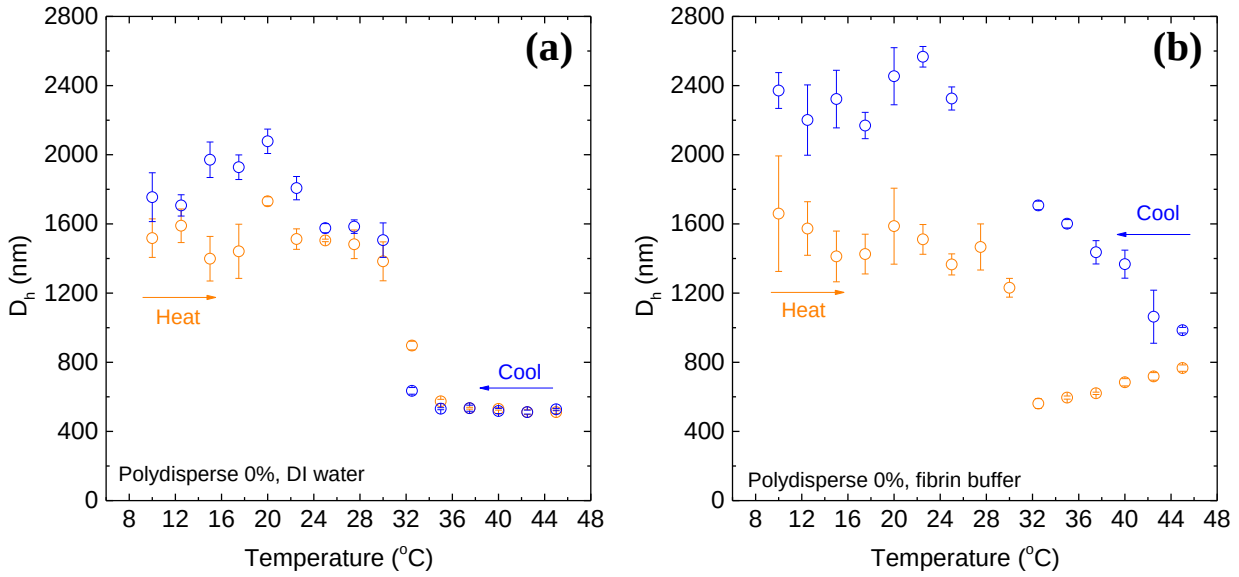

Figure 6.10 – DLS measurements on the pure PNIPAM micrgels dispersed in (a) Type 1 deionized water and (b) buffer solution of the fibrin. Continuous heating seems to make the particles get more aggregated due to reduced screening length in the fibrin buffer solution.

However, the microgels exhibit different thermo-responsive behaviors in the fibrin buffer solution from that in deionized water, as shown in **Figure 6.10b**. During the ramping up, the diameter keeps increasing above the VPTT, which was not observed in the deionized case. Besides, the particle size increases monotonically rather than drastically upon cooling down, resulting in the hysteresis.

The origin of these phenomena appears to be the high ionic strength of the buffer solution. The microgels would aggregate much more than in deionized water because the repulsive force between the particles would reduce dramatically in the presence of a large amount of ionic salts[35]. During the persistent heating above the VPTT, the microgel particles would keep suffering from the van der Waals (vdW) attractions consistently with other particles in the weak repulsive interactions[35]. On cooling, the aggregated particles would require more time to completely overcome the strong vdW interactions, leading to the detection of the larger diameters in the DLS measurement than the ramping up case.

We monitored the change in the particle diameter in the buffer solution upon continuous five cycles of the heating and cooling processes as represented in **Figure 6.11**. During the subsequent cycles (**b** to **e**), the microgels still show the reversible thermo-responsive behavior, analogous to that of the 1st cycle (**a**). Upon heating, the size of the microgel particles keep increasing above the VPTT for all cycles. The hysteresis behaviors were observed persistently during the entire cycles as well. The data collected upon heating and those collected upon cooling were separately plotted in **Figures 6.12a** and **b**, respectively. They reveal that the particle sizes at each temperature are all similar within an error regardless of the cycle number for both heating and cooling cases. This is a clear indication that our system is fully reversible.

6.5 Rheology of Pure Microgels and Microgels/fibrin Composites

(by Gaurav Chaudhary at Prof. Ewoldt group)

We first measured the rheological properties of the pure PNIPAM microgels as a control experiment. **Figure 6.13a** shows the plots of the storage modulus against the temperature at the different PNIPAM concentrations. One distinctive behavior is that the pure microgel suspensions

soften with increasing temperature due to the shrinkage of microgels above the VPTT[36,37]. We also observed the elastic response was dominant over the viscous response (not included here).

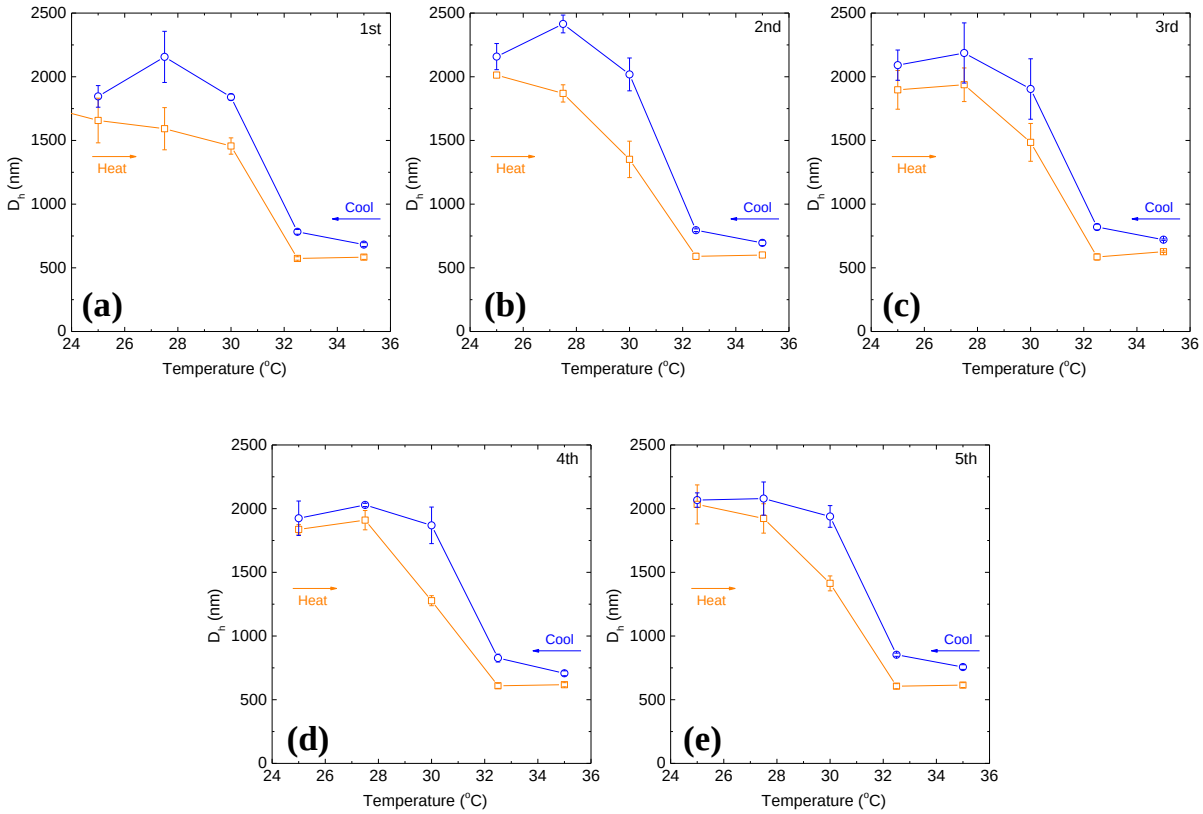

Figure 6.11 – Consistent trends of the diameter changes of the PNIPAM microgels in the buffer solution upon continuous five cycles. (a – e) correspond to first to fifth cycles, respectively.

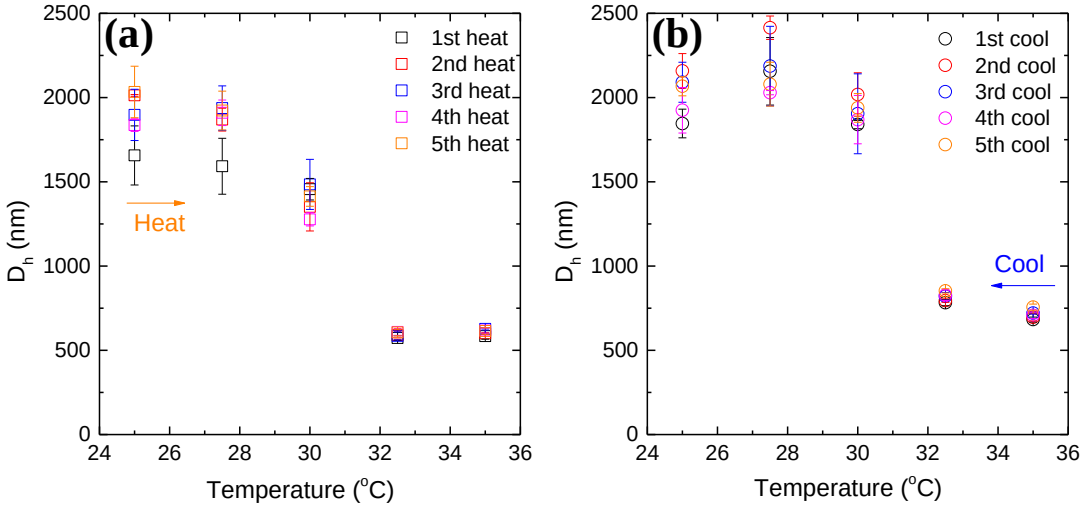

Figure 6.12 – Cycle independent behaviors of the diameter of the pure microgels in the fibrin buffer solution during five cycles of the (a) heating and (b) cooling, respectively.

Figure 6.13b demonstrates the storage modulus curves of the PNIPAM microgels/fibrin composites as a function of the temperature at the different PNIPAM concentrations from 0 ~ 3 wt %. Upon heating up, the composites exhibit multifold jump in the shear elastic modulus, which becomes more pronounced at the higher concentration of the microgels. This stiffening behavior of the composites beyond the VPTT is significant because the pure fibrin networks have a monotonic decay of modulus with increasing temperature and the pure microgels just soften upon heating up.

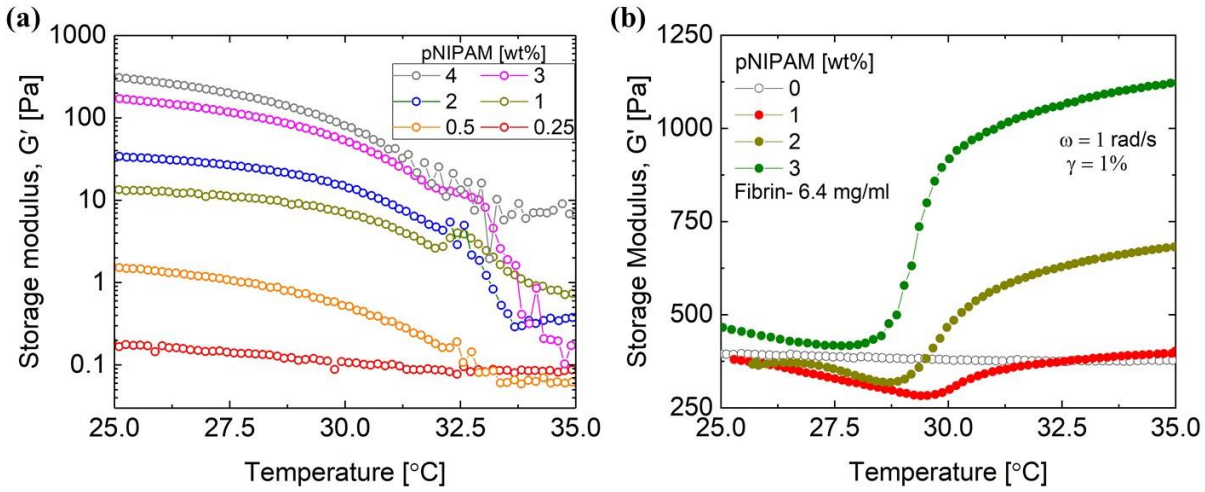

Figure 6.13 – Rheological measurements on the (a) pure PNIPAM microgels and (b) PNIPAM microgels/fibrin networks composites, respectively. The pure microgels soften with increasing temperature whereas the composites stiffen beyond the VPTT. Data were measured by Gaurav Chaudhary at Prof. Ewoldt group.

6.6 Origin of Thermo-responsive Stiffening on Microscopic Level

(by Dr. Bharadwaj at Prof. Ewoldt group, Dr. Hatzell at Prof. Braun group, and myself)

To elucidate the origin of thermally induced stiffening of the PNIPAM microgels/fibrin networks composites, we first carried out the confocal fluorescent imaging. In a two-color confocal lasers system, the total of three channel images were collected at the same time, as exhibited in **Figure 6.14**. The first, second, and last row images are acquired from the fibrins only, from the PNIPAM microgels only, and from the both, respectively. When we heated the composites starting from 25ºC, the whole structure of the composites changed dramatically beyond 29ºC, which is slightly lower than the VPTT of the PNIPAM. This seems to be caused by the shrinking behavior

of the PNIPAM microgels beyond the VPTT, where the entropically-driven phase-transition of the PNIPAM takes place[25,26].

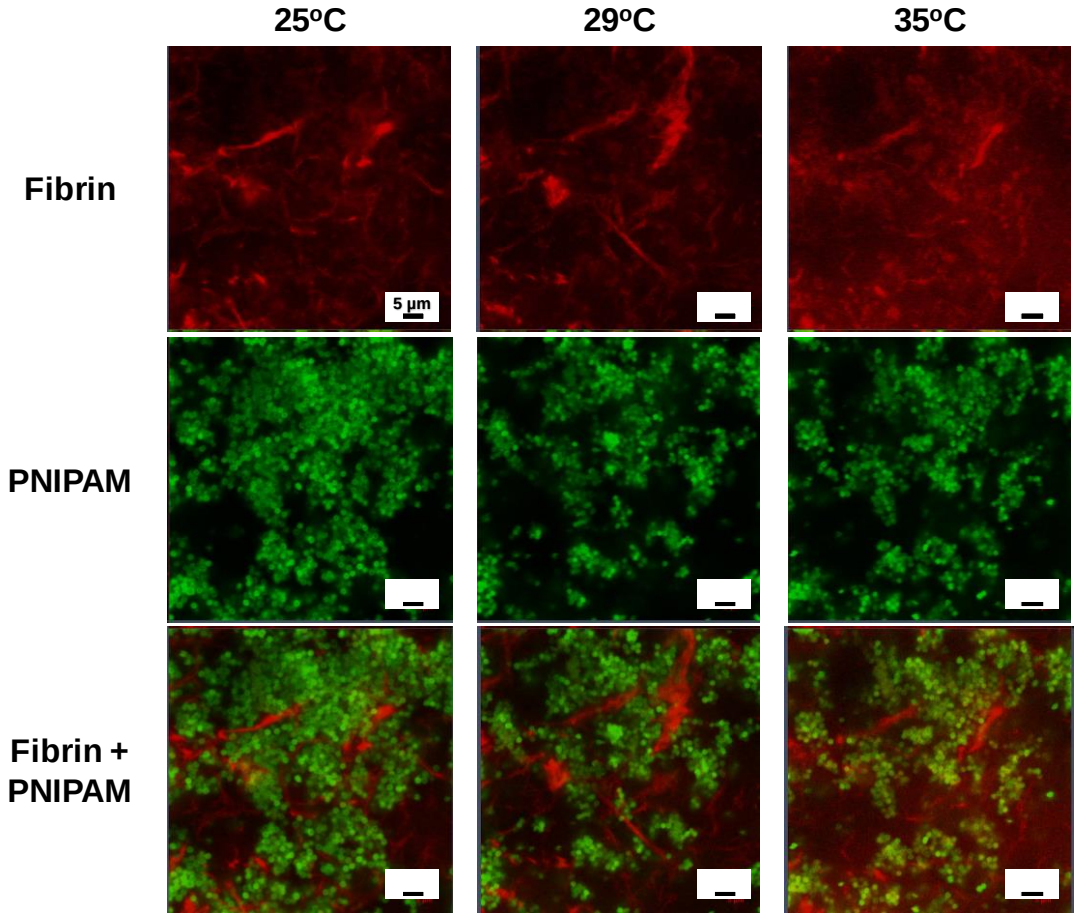

Figure 6.14 – Confocal fluorescence microscopic images of the microges/fibrin composites as a function of the temperature from 25 ~ 35ºC. Top, middle, and bottom row images correspond to the fibrin only, PNIPAM only, and combination of the two, respectively. Images were taken by Dr. Bharadwaj at Prof. Ewoldt group, Dr. Hatzell at Prof. Braun group, and myself.

Since the microgels surround the fibrin networks, the configurational changes in the former should influence on the spatial organization of the latter. Three top row images clearly show the variations in the structure of the fibrin network upon ramping up. The fibrin is a well-known material which shows the strain-induced stiffening behavior[14-16,38-40]. The polymer strands in the fibrin networks are cross-linked to each other, so they act as if they are elastic springs that attempt to go back to the original positions under any external strain[14-16]. Similarly, in our composites, thermally-induced reconfiguration of the PNIPAM microgel assemblies could generate the internal

stress in the fibrin networks, thereby leading to the stiffening of the composites. This could be considered one origin of the sudden jump in the elastic moduli upon heating.

6.7 Origin of Thermo-responsive Stiffening on Molecular Level

We additionally collected the Raman spectra of the pure fibrin, pure PNIPAM microgels, and composites at 25 and 39°C respectively so as to approach this stiffening behavior from the molecular level. **Top** curves in **Figure 6.15** show that the thermal actuation does not have any effects on the conformational changes in the molecules of the pure fibrin.

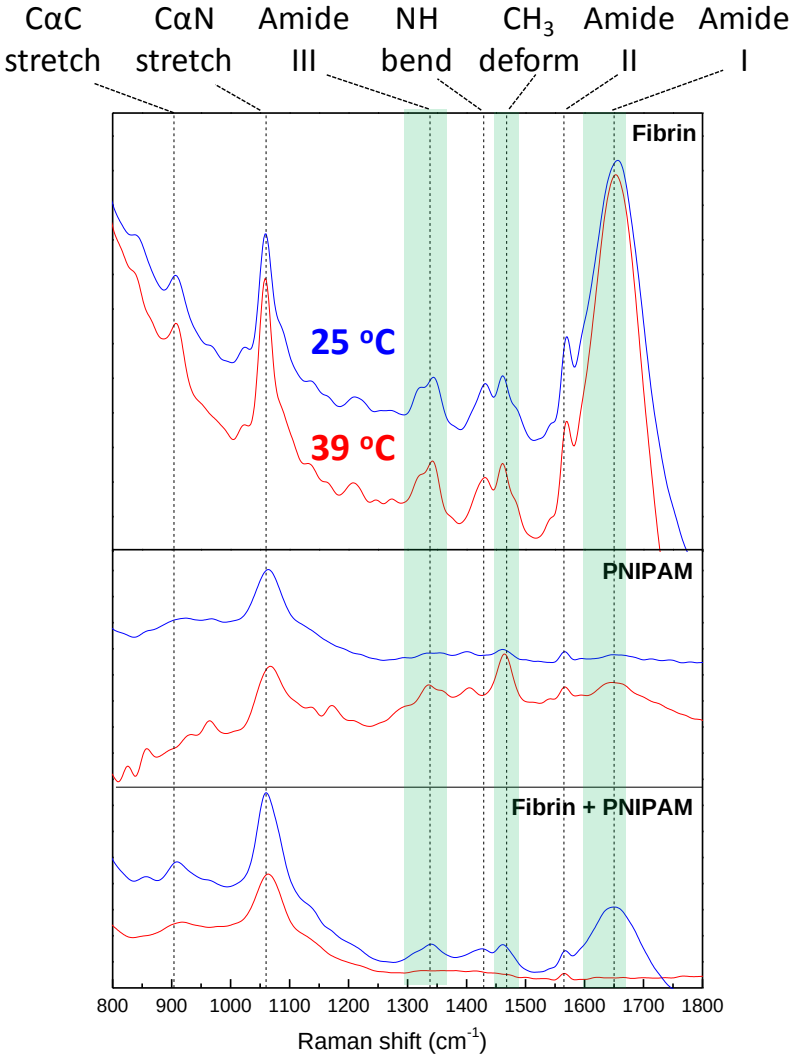

Figure 6.15 – Confocal Raman spectroscopy measurements at two different temperatures, 25 and 39°C on the (top) pure fibrin, (middle) pure PNIPAM microgels, and (bottom) PNIPAM microgels/fibrin composites, respectively.

However, the pure PNIPAM microgels exhibit the thermo-responsive Raman shift characteristics as shown in the **middle** curves. Upon heating up, three Raman shift bands corresponding to the amide III, CH_3 deformation, and amide I appear beyond the VPTT[41-43]. The evolutions of the amide I and amide III bands having hydrophilicity are attributed to the exposure of these molecular groups to the bulk suspension resulting from the breaking of the hydrogen bonding with water[41]. The CH_3 deformation band is known to be created by a non-resonant-enhanced mode of the isopropyl group[44].

The **bottom** curves indicate that the PNIPAM microgels/fibrin composites show completely different thermo-responsive behaviors from the pure fibrin and the pure microgels. At 25^{o}C, due to the presence of the fibrin, the three bands originating from the amide III, CH_3 deformation, and amide I are pronounced. However, all of them disappear beyond the VPTT, in contrary to the case of pure microgels. Presumably, as soon as those molecules in the PNIPAM are exposed by the entropically driven phase-transition to the hydrophobicity above the VPTT, they would bond immediately again with those in the surrounding fibrin networks, which could be considered polymer-polymer interactions. This would lead to the extinction of three bands in the Raman spectra. In addition, my hypothesis is that these polymer-polymer attractions taking place on the molecular scale would be another origin of the thermally-induced stiffening behaviors of the composites.

6.8 Conclusions

As an expansion of the work in **Chapter 5**, we have synthesized two different types of functional colloids including the PNIPAM brushes-tethered SiO_2 hard spheres and the lightly cross-linked PNIPAM microgels using the surface-initiated ATRP and the SFEP methods, respectively. Both colloids demonstrated the dynamically switchable behaviors in response to the temperature variations. Due to the large excluded volume of the SiO_2 nanospheres and the small amount of the PNIPAM brushes, we could not observe any changes in the storage moduli of the composites consisting of the PNIPAM-SiO_2 colloids and the fibrin networks.

However, the composites comprised of the PNIPAM microgels and the fibrin networks demonstrated multifold increase of the elastic modulus beyond the VPTT. At this moment, we

attribute this strain-stiffening behavior to the following two origins. One is the generation of the internal stress field by the macroscopic volume shrinkage of the PNIPAM microgels by an external thermal field. The other is the formation of new polymer-polymer attractions between the PNIPAM and the fibrin networks originating from the reconfiguration and rebonding at the molecular level. To understand this phenomenon more in depth, Ashesh Ghosh at Prof. Schweizer group is working on the development of the theory based on the statistical mechanical approaches.

6.9 References

1 Xu, B. Gels as Functional Nanomaterials for Biology and Medicine. *Langmuir* **25**, 8375-8377, doi:10.1021/la900987r (2009).

2 Van Vlierberghe, S., Dubruel, P. & Schacht, E. Biopolymer-Based Hydrogels As Scaffolds for Tissue Engineering Applications: A Review. *Biomacromolecules* **12**, 1387-1408, doi:10.1021/bm200083n (2011).

3 Solomon, M. J. & Spicer, P. T. Microstructural regimes of colloidal rod suspensions, gels, and glasses. *Soft Matter* **6**, 1391-1400, doi:10.1039/B918281K (2010).

4 Broedersz, C. P. *et al.* Measurement of nonlinear rheology of cross-linked biopolymer gels. *Soft Matter* **6**, 4120-4127, doi:10.1039/C0SM00285B (2010).

5 Bharadwaj, N. A. K. *et al.* Integration of colloids into a semi-flexible network of fibrin. *Soft Matter* **13**, 1430-1443, doi:10.1039/C6SM02141G (2017).

6 Solomon, M. J. Tools and Functions of Reconfigurable Colloidal Assembly. *Langmuir*, doi:10.1021/acs.langmuir.7b03748 (2018).

7 Hoffman, A. S. Stimuli-responsive polymers: Biomedical applications and challenges for clinical translation. *Advanced Drug Delivery Reviews* **65**, 10-16, doi:https://doi.org/10.1016/j.addr.2012.11.004 (2013).

8 Meng, H. & Li, G. A review of stimuli-responsive shape memory polymer composites. *Polymer* **54**, 2199-2221, doi:https://doi.org/10.1016/j.polymer.2013.02.023 (2013).

9 Geryak, R. & Tsukruk, V. V. Reconfigurable and actuating structures from soft materials. *Soft Matter* **10**, 1246-1263, doi:10.1039/C3SM51768C (2014).

10 Ahn, S.-k., Kasi, R. M., Kim, S.-C., Sharma, N. & Zhou, Y. Stimuli-responsive polymer gels. *Soft Matter* **4**, 1151-1157, doi:10.1039/B714376A (2008).

11 R., H. G., H., S. M., B., S. A. & Andrew, L. L. Design of Multiresponsive Hydrogel Particles and Assemblies. *Advanced Functional Materials* **20**, 1697-1712, doi:doi:10.1002/adfm.200902429 (2010).

12 Lyon, L. A., Meng, Z., Singh, N., Sorrell, C. D. & St. John, A. Thermoresponsive microgel-based materials. *Chemical Society Reviews* **38**, 865-874, doi:10.1039/B715522K (2009).

13 George, M. & Weiss, R. G. Molecular Organogels. Soft Matter Comprised of Low-Molecular-Mass Organic Gelators and Organic Liquids. *Accounts of Chemical Research* **39**, 489-497, doi:10.1021/ar0500923 (2006).

14 Storm, C., Pastore, J. J., MacKintosh, F. C., Lubensky, T. C. & Janmey, P. A. Nonlinear elasticity in biological gels. *Nature* **435**, 191, doi:10.1038/nature03521 (2005).

15 Crow, A. *et al.* Contractile Equilibration of Single Cells to Step Changes in Extracellular

Stiffness. *Biophysical Journal* **102**, 443-451, doi:https://doi.org/10.1016/j.bpj.2011.11.4020 (2012).
16 Kollmannsberger, P., Mierke, C. T. & Fabry, B. Nonlinear viscoelasticity of adherent cells is controlled by cytoskeletal tension. *Soft Matter* **7**, 3127-3132, doi:10.1039/C0SM00833H (2011).
17 Tu, H., Hong, L., Anthony, S. M., Braun, P. V. & Granick, S. Brush-Sheathed Particles Diffusing at Brush-Coated Surfaces in the Thermally Responsive PNIPAAm System. *Langmuir* **23**, 2322-2325, doi:10.1021/la062219i (2007).
18 Tu, H., Heitzman, C. E. & Braun, P. V. Patterned Poly(N-isopropylacrylamide) Brushes on Silica Surfaces by Microcontact Printing Followed by Surface-Initiated Polymerization. *Langmuir* **20**, 8313-8320, doi:10.1021/la049663a (2004).
19 Xue, C. *et al.* Protein Adsorption on Poly(N-isopropylacrylamide) Brushes: Dependence on Grafting Density and Chain Collapse. *Langmuir* **27**, 8810-8818, doi:10.1021/la2001909 (2011).
20 Satish, N. & Andrew, L. L. Soft Nanotechnology with Soft Nanoparticles. *Angewandte Chemie International Edition* **44**, 7686-7708, doi:doi:10.1002/anie.200501321 (2005).
21 Meng, Z., Smith, M. H. & Lyon, L. A. Temperature-programmed synthesis of micron-sized multi-responsive microgels. *Colloid and Polymer Science* **287**, 277-285, doi:10.1007/s00396-008-1986-8 (2009).
22 Bachman, H. *et al.* Ultrasoft, highly deformable microgels. *Soft Matter* **11**, 2018-2028, doi:10.1039/C5SM00047E (2015).
23 Kita, R., Kircher, G. & Wiegand, S. *Thermally induced sign change of Soret coefficient for dilute and semidilute solutions of poly(N-isopropylacrylamide) in ethanol*. Vol. 121 (2004).
24 Pich, A. & Richtering, W. *Chemical Design of Responsive Microgels*. (Springer Berlin Heidelberg, 2010).
25 Heskins, M. & Guillet, J. E. Solution Properties of Poly(N-isopropylacrylamide). *Journal of Macromolecular Science: Part A - Chemistry* **2**, 1441-1455, doi:10.1080/10601326808051910 (1968).
26 Kubota, K., Fujishige, S. & Ando, I. Single-chain transition of poly(N-isopropylacrylamide) in water. *The Journal of Physical Chemistry* **94**, 5154-5158, doi:10.1021/j100375a070 (1990).
27 Pelton, R. Temperature-sensitive aqueous microgels. *Advances in Colloid and Interface Science* **85**, 1-33, doi:https://doi.org/10.1016/S0001-8686(99)00023-8 (2000).
28 K., D. & D., P. Transition in swollen polymer networks induced by intramolecular condensation. *Journal of Polymer Science Part A-2: Polymer Physics* **6**, 1209-1216, doi:doi:10.1002/pol.1968.160060701 (1968).
29 Saunders, B. R. & Vincent, B. Microgel particles as model colloids: theory, properties and applications. *Advances in Colloid and Interface Science* **80**, 1-25, doi:https://doi.org/10.1016/S0001-8686(98)00071-2 (1999).
30 Stöber, W., Fink, A. & Bohn, E. Controlled growth of monodisperse silica spheres in the micron size range. *Journal of Colloid and Interface Science* **26**, 62-69, doi:https://doi.org/10.1016/0021-9797(68)90272-5 (1968).
31 Serpe, M. J. *Self-Assembly of Poly(N-isopropylacrylamide) Microgel Thin Films* Ph.D. thesis, Georgia Institute of Technology, (August 2004).
32 Jawerth, L. M. *The mechanics of fibrin networks and their alterations by platelets* Ph.D thesis, Harvard Universit, (2013).

33 Qi, W., Anindita, B., Jessamine, P. W., Arjun, Y. & Paul, A. J. Local and global deformations in a strain-stiffening fibrin gel. *New Journal of Physics* **9**, 428 (2007).
34 Lang, Nadine R. *et al.* Estimating the 3D Pore Size Distribution of Biopolymer Networks from Directionally Biased Data. *Biophysical Journal* **105**, 1967-1975, doi:https://doi.org/10.1016/j.bpj.2013.09.038 (2013).
35 Israelachvili, J. N. *Intermolecular and Surface Forces*. (Elsevier Science, 2011).
36 Pellet, C. & Cloitre, M. The glass and jamming transitions of soft polyelectrolyte microgel suspensions. *Soft Matter* **12**, 3710-3720, doi:10.1039/C5SM03001C (2016).
37 Menut, P., Seiffert, S., Sprakel, J. & Weitz, D. A. Does size matter? Elasticity of compressed suspensions of colloidal- and granular-scale microgels. *Soft Matter* **8**, 156-164, doi:10.1039/C1SM06355C (2012).
38 Shah, J. V. & Janmey, P. A. Strain hardening of fibrin gels and plasma clots. *Rheologica Acta* **36**, 262-268, doi:10.1007/bf00366667 (1997).
39 Janmey, P. A., Winer, J. P. & Weisel, J. W. Fibrin gels and their clinical and bioengineering applications. *Journal of The Royal Society Interface* **6**, 1-10, doi:10.1098/rsif.2008.0327 (2009).
40 Münster, S. *et al.* Strain history dependence of the nonlinear stress response of fibrin and collagen networks. *Proceedings of the National Academy of Sciences* **110**, 12197-12202, doi:10.1073/pnas.1222787110 (2013).
41 Ahmed, Z., Gooding, E. A., Pimenov, K. V., Wang, L. & Asher, S. A. UV Resonance Raman Determination of Molecular Mechanism of Poly(N-isopropylacrylamide) Volume Phase Transition. *The Journal of Physical Chemistry B* **113**, 4248-4256, doi:10.1021/jp810685g (2009).
42 Yamauchi, H. & Maeda, Y. LCST and UCST Behavior of Poly(N-isopropylacrylamide) in DMSO/Water Mixed Solvents Studied by IR and Micro-Raman Spectroscopy. *The Journal of Physical Chemistry B* **111**, 12964-12968, doi:10.1021/jp072438s (2007).
43 Dybal, J., Trchová, M. & Schmidt, P. The role of water in structural changes of poly(N-isopropylacrylamide) and poly(N-isopropylmethacrylamide) studied by FTIR, Raman spectroscopy and quantum chemical calculations. *Vibrational Spectroscopy* **51**, 44-51, doi:https://doi.org/10.1016/j.vibspec.2008.10.003 (2009).
44 Pan, Y. V., Wesley, R. A., Luginbuhl, R., Denton, D. D. & Ratner, B. D. Plasma Polymerized N-Isopropylacrylamide: Synthesis and Characterization of a Smart Thermally Responsive Coating. *Biomacromolecules* **2**, 32-36, doi:10.1021/bm0000642 (2001).

CHAPTER 7.

CONCLUSIONS AND FUTURE DIRECTIONS

7.1 Summary of Thesis Research

Through colloidal assembly, we realized two different types of the 3D functional materials. First, the self-assembled hard sphere colloidal crystals enabled us to fabricate multiple classes of inorganic 3D functional meso/nanostructures which have potential uses in the thermal management applications including thermoelectric power generation and power electronic devices. The epitaxially grown Fe_3O_4 nanostructures with the pores 40 nm in diameter were confirmed to have the superior crystal qualities and the high material filling fraction. More interestingly, these materials exhibited the ultra-low thermal conductivity and the half-metallic electrical conductivity at the same time, which could be utilized as the electrically conductive thermal insulators.

Second, the PNIPAM soft colloids in the form of the microgels, which internally have the thermo-responsive functionalities, were synthesized, and then combined with the viscoelastic fluids consisting of fibrin networks. These colloids/fiber network hydrogel composites demonstrated the dynamic switching in the mechanical properties under the thermal actuation. They showed multi-fold increase in the elastic modulus around the VPTT, which would be due to the strain-stiffening of the fibrin networks induced by the spatial reorganization of the active PNIPAM colloids.

In conclusions, this work ultimately utilized the colloidal assembly phenomena from the templating to the stimuli-responsiveness. The materials themselves and the strategies we adopted could offer new opportunities for the material engineers working in the diverse applications over the energy conversion to the microelectronics to design the advanced materials, modules, and systems that were not enabled before.

7.2 Future Directions

Above all, we could attempt to evaluate the thermoelectric zT of these epitaxial Fe_3O_4 3D nanostructures with the pores 40 nm in diameter. The remaining task is to measure the Seebeck coefficient. Similar with the thermal conductivity measurement, due to the porous features of these materials, the measurement itself would be quite challenging. However, the fabrication process should be technically based on the microfabrication platform described in **Chapter 3** developed for the 3ω measurement, with minor modifications.

Although the electroplating through the colloidal crystals grown on the epitaxial PbS film was not enabled in this study, I believe that upon the optimal conditions, the PbS should be grown through the complex 3D geometry of the colloidal crystals because the bulk electrical conductivity of the PbS and that of the Fe_3O_4 are almost similar. Besides, as the seed layer is comprised of the epitaxial PbS, not of another materials, the epitaxial nucleation process will take place much easier than the case of the Fe_3O_4 on gold layer.

From the perspectives of the practical usage of the single crystal Fe_3O_4 3D nanoporous structures, we would try to imbed this material into the power electronic devices which requires both thermally isolation and electrical conduction at the same time. When designing the current power electronics, engineers first consider the electrical performance and then take care of the thermal accommodations due to the limited choice of the materials. This tends to limit the overall system performance when the thermal barriers are met, to restrict ability to design devices that route the heat to the desired location, and to increase cost. To tackle these issues, the single crystal Fe_3O_4 3D nanostructures could be located where the thermally sensitive components in the devices need to be protected by the heat generated by circuits but still need to efficiently transfer the electric signals to the surroundings. Though the way of incorporating the materials into the modules or devices has not been fully developed yet, due to the eco-friendly and abundant components such as Fe and O, and the simple process based on the 3 steps including the colloidal self-assembly, the electroplating, and the template removal, I believe these materials would play a key role when meeting with the proper demands.

The dynamic modulation of the mechanical properties of the materials triggered by external stimuli has been a key issue in the biorobotics and biomimic applications. More specifically, for the near future application, the PNIPAM/fibrin networks composite hydrogels would be imbedded

in the biomedical devices which need to dynamically change the mechanical pressures on the living body depending on the body states. If the way of sensing the body states is using the changes in the body temperature, these composite materials would ideally suit.

The theoretical approach toward revealing the origin of the strain-stiffening behavior of the colloids/fiber composites could be another intriguing work. Once the origin is clearly identified, this will offer new opportunities of designing the different combinations of the composites by predicting their behaviors more accurately and realistically based on the statistical mechanical theories developed for the hybrid composites.